



UNIVERSITÀ DEGLI STUDI DI TRIESTE
E
UNIVERSITÀ CA' FOSCARI VENEZIA
XXXIII CICLO DEL DOTTORATO DI RICERCA IN
CHIMICA

**LIGHT-DRIVEN PROCESSES FOR FUEL PRODUCTION
AND CULTURAL HERITAGE REMEDIATION**

Settore scientifico-disciplinare: **CHIM/04**

DOTTORANDO
DANNY ZANARDO

COORDINATORE
PROF. ENZO ALESSIO

SUPERVISORE DI TESI
PROF.SSA MICHELA SIGNORETTO

CO-SUPERVISORE DI TESI
DOTT.SSA FEDERICA MENEGAZZO

ANNO ACCADEMICO 2019/2020

“Knowledge is the most democratic source of power”

Alvin Toffler

ABSTRACT

Sunlight is an appealing energy source exploitable for a sustainable and equal development of human society, being abundant, widespread and cheap, on a scenario of adaptation strategies for facing the climate change happening on Earth surface. Several kind of chemical reactions required to sustain the society, from fuel production to environmental remediation, can be potentially run exploiting the light as energy source. A light-activated catalyst (photocatalyst) is often needed to allow such reactions to occur, able to both absorb the photons and decrease the kinetic barrier. The aim of this work was to prepare some earth-abundant oxide-based semiconductor (SC) materials and assess them in some photocatalyzed reactions, using a selected SC for each process. Titanium dioxide (TiO_2) was used for H_2 production from biomass, zinc oxide (ZnO) and a mixed iron-copper oxide (CuFeO_2) in CO_2 photoreduction, while a calcium-based plaster (*marmorino*) modified with TiO_2 and ZnO , was used in cultural heritage photoremediation (self-cleaning). Different characterization techniques were exploited to achieve a comprehensive knowledge of structural, morphological, optical and surface properties of the prepared materials. Finally, the physical-chemical properties of these oxides were correlated to the photoactivity, aiming to understand how these features affect, negatively or positively, the performances of a given reaction.

CONTENTS

Abbreviations.....	4
Preface	7
1.1. Energy, society and sustainability	7
1.2. The sun power	10
1.3. Solar-to-chemicals.....	11
1.4. Fundamental of heterogeneous photo(electro)catalysis.....	12
1.5. Applications of photo(electro)catalysis.....	16
1.6. Semiconductors and material design	17
1.7. Aim of the work	23
1.8. References	24
Chapter 1: Hydrogen production by glucose photoreforming with TiO₂-based photocatalysts.....	32
1. Introduction	33
1.1. The power of hydrogen	33
1.2. Hydrogen production: strategies and challenges	33
1.3. Solar-to-hydrogen: the photocatalytic approach.....	34
1.4. Aim of the chapter	38
2. Materials and methods	39
2.1. Reagents	39
2.2. Synthesis.....	39
2.3. Characterizations.....	40
2.4. Reactivity tests	41
3. Results and discussion.....	43
3.1. Bare TiO ₂ materials.....	43
3.2. Co-catalyst-loaded TiO ₂ materials.....	46
4. Conclusions.....	53
5. Supplementary information	54
6. References	55
Chapter 2: Gas-phase CO₂ photoreduction with ZnO-based photocatalysts.....	59
1. Introduction	60
1.1. CO ₂ as source of chemicals and fuels	60
1.2. CO ₂ reduction with H ₂ O: from natural to artificial photosynthesis.....	60
1.3. Zinc oxide as photocatalyst.....	63
1.4. The issue of CO ₂ supply	66

1.5. Aim of the chapter	67
2. Materials and methods	68
2.1. Reagents	68
2.2. Synthesis	68
2.3. Characterizations.....	69
2.4. Reactivity tests	71
3. Results and discussion.....	73
3.1. Structural and morphological characterization of ZnO materials.....	73
3.2. Surface and optical characterization of ZnO materials	76
3.3. CO ₂ photoreduction with H ₂ O and hybrid CO ₂ capture/photoconversion	83
4. Conclusions.....	89
5. Supplementary information	90
6. References.....	96
Chapter 3: CO₂ photoelectrochemical reduction by photocathodes based on earth-abundant elements	101
1. Introduction	102
1.1. Insights in photoelectrochemical light-to-chemical conversion	102
1.2. CO ₂ photoelectrochemical reduction	104
1.3. The case of copper-iron delafossite (CuFeO ₂).....	107
1.4. CuFeO ₂ insights: surface states and overlayers	108
1.5. Aim of the chapter	110
2. Material and methods.....	111
2.1. Reagents	111
2.2. Synthesis	111
2.3. Structural and optical characterizations.....	112
2.4. Photoelectrochemical characterizations	113
3. Results and discussion.....	117
3.1. ZnO overlayer.....	117
3.2. CuFeO ₂ photocathode	123
3.3. ZnO/CuFeO ₂ composite photocathodes.....	127
3.4. Cu co-catalysts loaded photocathodes.....	133
4. Conclusions.....	136
5. Supplementary information	137
6. References.....	140
Chapter 4: Self-cleaning properties on ZnO and TiO₂-modified Venetian <i>marmorino</i>	145
1. Introduction	146
1.1. The surface degradation of cultural heritage	146

1.2. Cultural heritage remediation: light-driven self-cleaning	147
1.3. Case of study: Venetian <i>marmorino</i>	150
1.4. Aim of the chapter	151
2. Materials and methods	152
2.1. Reagents	152
2.2. Synthesis	152
2.3. Characterizations.....	153
2.4. Photoactivity assessment	155
3. Results and discussion.....	158
3.1. Materials characterization	158
3.4. Photocatalytic self-cleaning assessment	164
4. Conclusions.....	170
5. Supplementary information	171
6. References	172
Concluding remarks	176
Curriculum vitae.....	178
Published papers.....	179
Congresses and congress proceedings	180
Teaching and guidance activities.....	180
Acknowledgments.....	182

ABBREVIATIONS

AACVD	Aerosol-assisted chemical vapor deposition
AFM	Atomic force microscopy
AQY	Apparent quantum yield
ATR	Attenuated total reflectance
BE	Binding energy
CA	Chronoamperometry
CB	Conduction band
CSP	Concentrated solar power
CZH	Calcium zinc hydroxide hydrate
DRS	Diffuse-reflectance spectroscopy
DTA	Differential thermal analysis
E_c	Conduction band edge
E_F	Fermi level or energy
E_{FB}	Flat-band potential
E_g	Band-gap
EIS	Electrochemical impedance spectroscopy
E_{ONSET}	Onset potential
E_{SC}	Band-bending
E_U	Urbach energy
E_V	Valence band edge
GHG	Green house gas
HER	Hydrogen evolution reaction
HR-TEM	High-resolution transmission electron microscopy
ICP-MS	Inductively coupled plasma mass spectrometry
J_{ph}	Photocurrent
LSV	Linear sweep voltammetry
MB	Methylene blue
MSR	Methane Steam Reforming
N_A	Acceptor density
NBE	Near band-edge emission
nE_F^*	Electrons quasi-Fermi energy
NP	Nano-particle

OCP	Open-circuit potential
OER	Oxygen evolution reaction
O_i	Interstitial oxygen
PC	Photocatalysis
PEC	Photoelectrocatalysis
PED	Photo-electrochemical deposition
pE_F^*	Holes quasi-Fermi energy
PL	Photoluminescence
PV	Photovoltaic
RHE	Reversible hydrogen electrode
ROS	Reactive oxygen species
SC	Semiconductor
SEM	Scanning electron microscopy
$S_{H/CO}$	Stoichiometric hydrogen-to-carbon oxides ratio
SKPM	Scanning Kelvin probe force microscopy
SSA	Specific surface area
SSs	Surface states
STF	Solat-to-fuel
TCO	Transparent conductive oxide
TGA	Thermal gravimetric analysis
TOF	Turnover frequency
TOF*	Turnover frequency <i>per</i> unit specific surface area
TOF _{ph}	TOF of overall photoexcited charge carriers
VB	Valence band
V_O	Oxygen vacancy
V_{Zn}	Zinc vacancy
XPS	X-ray photoelectron spectroscopy
XRD	X-ray diffraction
Zn_i	Interstitial zinc
δ_{O-H}	O-H moiety bending vibration
$\Delta_r G^\circ_{25^\circ C}$	Free Gibbs energy of reaction (at 25°C)
ν_{CaOH}	O-H moiety stretching vibration on $Ca(OH)_2$
ν_{O-C-O}	Carbonate moiety stretching vibration

$\nu_{\text{O-H}}$

O-H moiety stretching vibration

PREFACE

1.1. ENERGY, SOCIETY AND SUSTAINABILITY

The energy is a curious concept: the standardly recognized definition as “an ability to do work” does not clearly define what this quantity is. Rather it is something that describes a given system, and particularly the energy transfer from a system to another has deep practical involvement in our society, lifestyle, as well our life itself [1]. The development of human society has had remarkably increased the energy demand: in the modern, highly organized and developed society, the daily *per capita* energy requirement is two magnitude orders higher than in the prehistoric epoch [2]. Furthermore, the huge size of human population in modern era [3] contributes to make the overall energy demand, called total primary energy supply (TPES), a real big number ($5.8 \cdot 10^{20}$ J in 2018 [4]) that grows continuously over the years as depicted in Figure 1 (green line). Fossil fuels still dominates the energy scenario of our society, supplying 87% of the total amount of consumed energy nowadays.

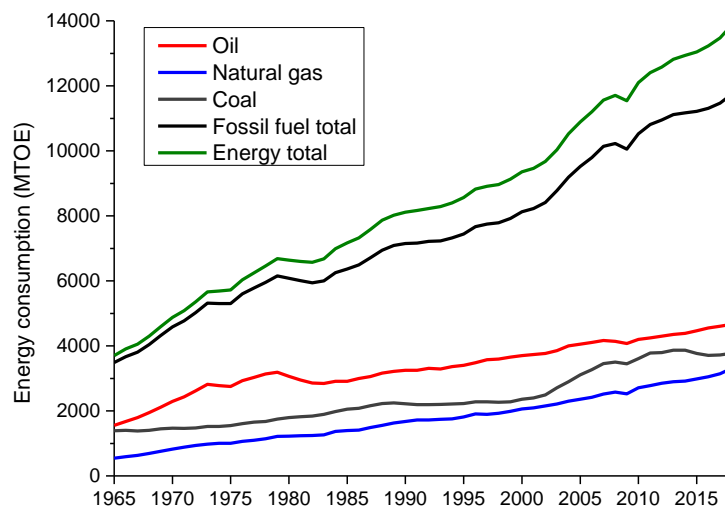


Figure 1. World energy consumption by source in millions of tonnes of oil equivalent (MTOE). Green line: total amount of consumed energy. Black line: total amount arising from fossil fuels. Red line: oil. Grey line: coal. Blue line: natural gas [Errore. Il segnalibro non è definito].

The successfulness behind fossil fuels relies on several features: their availability for the next decades [Errore. Il segnalibro non è definito.], well established extraction and production technologies [5,6], high energy return on energy invested index (EROEI) [7] and the high energy density [8]. However, the massive exploitation of these energy resources, have led to the emission of several harmful by-products for human and the environment, such as sulfur oxides (SO_x), nitrogen oxides (NO_x), polycyclic aromatic hydrocarbons (PAHs), and since the 70' several strategies have been adopted to reduce the release of such pollutants [9]. Besides that, the massive consumption of fossil fuel generates a huge amount of carbon dioxide (CO_2), which in turn cause another effect: the greenhouse effect [10]. This phenomena is related to the capability of the

so-called greenhouse gases (GHGs), to absorb the infrared (IR) fraction of the sunlight that reaches the Earth, thus warming up the planet's surface, and is mainly caused by water vapor (66%), followed by CO₂, methane (CH₄), ozone (O₃) and dinitrogen oxide (N₂O) [11]. This effect is essential to sustain the existence of liquid water on the Earth surface, and thus the life itself, but an excessive warming is detrimental for the biosphere [12]. This extra heating effect arises from anthropogenic emission of GHGs, mainly CO₂ (77% of the overall warming effect), CH₄ (16%) and N₂O (6.2%) [10]. The concentration of the GHGs, has rose remarkably in the last two centuries and, in particular, CO₂ has reached 413.30 ppm in 2020 [13], the highest recoded value in the last half-million of years [14].

Since the rate of these anthropogenic GHGs emissions exceed the natural capability of the Earth surface to buffer them [15], these gases accumulate in the atmosphere and lead to a warming of the planet surface: a + 0.84 °C increase of the average temperature has occurred from 1880 to 2012 [10]. The correlation of GHGs emissions and global warming, have been denied by some scientist in early 2000s [16], and recently with the famous letter signed in 2019 by 500 experts [17]. These admission are in opposition with the scientific community majority: as reported in Figure 2, the sole effect of natural causes (solar and volcanic activity) can be ruled out and the atmosphere warming, can be ascribed to human society activities only, in particular GHGs emissions.

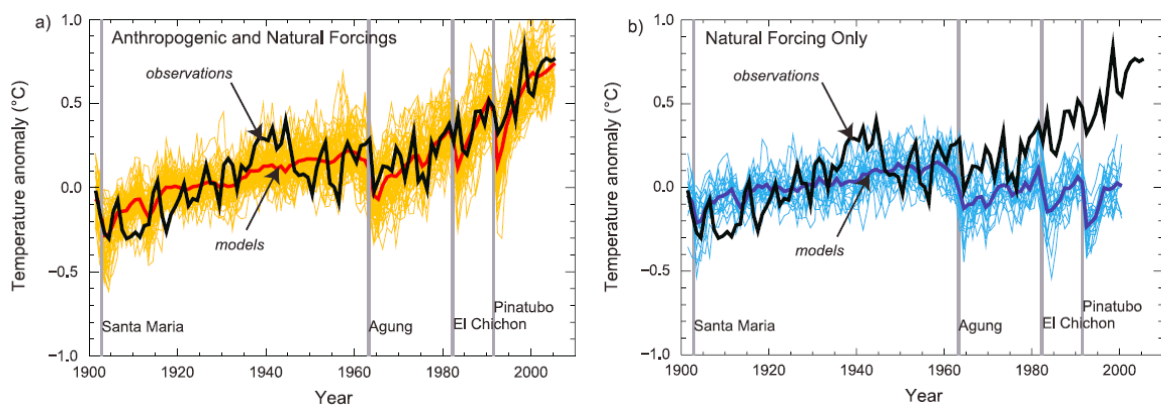


Figure 2. Measured (black line) and calculated (red and blue line) Earth surface temperature due to human-related and natural causes (left) and natural causes only (right) [14].

The global warming has several effects on Earth's climate and biosphere, such as a change in water cycle (precipitation frequency and distribution), glaciers and ice cup melting, sea level rising and ocean acidification [18], permafrost melting, cyclones, droughts, heatwaves and floods [10,19]. Predictions obtained by means of climate models suggested that, in the next decades, the human society (i.e. food and water supply, health) and the biosphere will be strongly affected by climate changes [10]. Indeed, some recent facts such as the Ophelia hurricane in 2017 [20], the Venice city floods in 2019 [21] and the dramatic 2019-2020 Australian bushfires [22], ascribable to the effects of global warming [23-26], can give us a taste of what climate change really means.

The first policy makers attempt to mitigate the detrimental effect of GHGs occurs with the Kyoto Protocol in 1997 [27]. Later, the Paris agreement (2015) stated clearer aims [28]:

1. Keep the global average temperature below 2 °C with respect to pre-industrial levels;
2. Increase the adaption to adverse effect of climate change (climate resilient development);
3. Forcing the finance toward a more sustainable economy and climate resilient development.

As answer for climate change mitigation, the scientific community also drawn its attention on CO₂, the main GHG, and specifically its capture, either from the atmosphere [29] or flue gases (i.e. power stations) [30], sequestration [31,32] and its utilization for fuels or chemical production [33,34]. Moreover, several efforts have also done on alternative energy development in order to substitute fossil fuels as main energy source, and thus directly avoid CO₂ emission [19].

However, this is not all the story. Besides warming the atmosphere, a fraction of the IR radiation in sunlight is also absorbed by waterbodies (mainly seas and oceans), rising their temperature and making them a huge thermal energy sink [14]. Due to their thermal inertia, this heat is then slowly released in the atmosphere [18], eventually affording a long-term global warming phenomenon, that continued even if all anthropogenic CO₂ (and GHGs) emissions would suddenly stop [35]. A simulation by Zickfeld *et al.*, shows it could be theoretically possible to keep the global warming below + 2.0 °C through a fast and huge effort, however this must face the socio-economical and technological inertia of human society, making it less feasible [36]. It is clear new strategies are required to face comprehensively the climate change: indeed, as pointed by Paris agreement, the human society has not only to mitigate its impact on the environment, but also to adapt to the effects of this change. This general approach has been eventually defined as climate change adaptation strategies [37].

Extreme climatic events, likely to be more and more common in the next future, should be faced with appropriate strategies [38], together with a good and effective communication to a general audience [39], in order to make such approaches effective and useful. Moreover, the equity requirement should not be forgotten: poor nations and communities will suffer more the effect of climate change [40]. On the more practical point of view, climate change adaptation involves several aspect of our society, such as agriculture and food supply [41,42], water management [43], preservation of ecosystems and biodiversity [44], healthcare [45], urban development [46,47], cultural heritage management [48], the already mentioned energy sector, as well as social and personal aspects of our lifestyle [49].

Climate change adaptation is something really complex: a network among science, policy, environment, society, economy and ethics [37]. Anyway, it is probably the only chance we, human beings, have to survive to global climate and environment alteration that we have created ourselves.

1.2. THE SUN POWER

One of the most promising alternative primary energy source to fossil fuels is certainly the solar energy [50]: the power (energy *per* unit time) irradiated by the Sun on Earth surface ($9.2 \cdot 10^{16}$ W) [18], is three magnitude order bigger than the power consumed by the entire human society in 2018 ($1.8 \cdot 10^{13}$ W) [4]. Besides the abundancy, some key features such as (i) cheapness, (ii) time-limitless and (iii) wide-spreading, even in remote areas, make solar energy an attractive energy source, required for human activities, as a tool in climate change adaptation strategies [51].

The sunlight is composed of several types of electromagnetic radiations (Figure 3): ultra-violet (UV) light (5% of overall intensity and $270 \div 400$ nm wavelength fraction); visible light (44% and $400 \div 760$ nm wavelength) and infra-red (IR) (51% and above 760 nm wavelength) [52]. The knowledge of the spectral distribution of solar energy is important since the different technologies involved in its utilization, exploit different region of solar spectra [19].

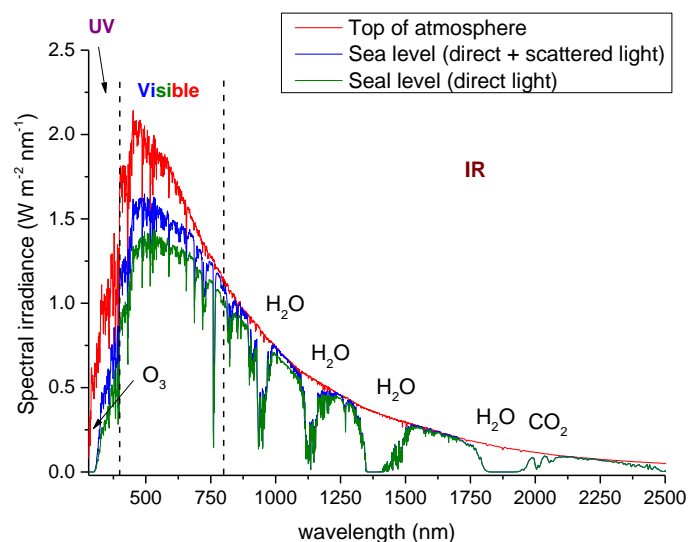


Figure 3. Solar spectrum at the top of the atmosphere (red trace), at sea level considering only direct radiations (green trace) and accounting both scattered and direct radiation (blue trace) [53]; adsorption band for the main atmospheric gases is highlighted on the spectra [54].

The solar energy utilization experienced a huge growth in the last decade [4], but it is mainly used in commercial electricity or heat production [19]. The electric power can be obtained either through a direct light-to-electricity conversion, namely photovoltaics (PV) or indirectly by means of concentrated solar power (CSP). The former use semiconductor (SC) p-n junction devices, in which a photo-induced voltage is generated upon the absorption of photons, mainly part of the visible or to the near-IR (NIR) (below ca. 1100 nm wavelength), yielding an electric current [55]. The CSP technology, on the contrary, works by exploiting the whole spectra (also the IR fraction), which is concentrated through optical devices (i.e. mirrors or lenses) to a receiver, where the energy is then transferred in form of heat to a fluid [56], and eventually used to run

thermal engines [57]. Köberle *et al.* esteemed a technically recoverable power through either CSP or PV of $2.0 \cdot 10^{13}$ W and $1.1 \cdot 10^{13}$ W, respectively [58]. Despite these values are comparable with the previously mentioned worldwide power consumption [4], social and policy issues have to be also considered, making them less feasible for large-scale project.

Besides electric power, another appealing sunlight-exploiting approach is the solar thermal energy (STE), relying on the direct utilization of solar heat, thus resembling CSP systems but without converting it into electricity. The produced heat can be then used by residential [59] and industrial [60] users, reaching in 2015, an installed capacity of $4.35 \cdot 10^{11}$ W [61]. Still concerning solar heat, another attractive exploitation approach is solar cooling, in which the heat is used to run evaporative-absorption refrigerators [62].

Solar energy can be also involved in water resource management, and this approach is very attractive since water scarcity will growly affect human society in the next future due to climate change [63]. Solar desalination is an attractive way to utilize solar energy, as both heat or electricity, to produce freshwater from seawater [64,65]. Another interesting process is solar water disinfection (SODIS) [66]. The UV fraction of sunlight is used to deactivate pathogenic microorganisms, by generating reactive chemical species within the cells, affording in the degradation of biochemical component of cells and eventually killing the microorganism [67]. The interesting feature of this method is its cheapness and simplicity, requiring only plastic bottles and sunlight, allowing its utilization in under-developed countries: in 2009 4.5 million people in 55 different countries was using this technology for their drinkable water supply [68].

SODIS is a nice example of how a renewable, abundant and free energy source like solar energy, can be exploited on a cheap and easy way, to face a social problem (water shortage) that affected mainly under-developed countries, and it is expected to become more and more serious due to climate change. Moreover, it also represent an example of how sunlight can be involved in running chemical reactions, thus paving the way on new applications for solar energy.

1.3. SOLAR-TO-CHEMICALS

The chemistry plays an important role in human society, and several chemical reactions are used for different purposes, such as the synthesis of chemical substances [6], the removal of harmful compounds from the environment [9] as well as the production of energy, nowadays mainly by burning fossil fuels. Due to the advantages of solar energy highlighted in section 1.2., the utilization of light to run chemical reactions seems an appealing approach in the contest of climate change adaptation.

Heat and electricity are widely used as energy source to run several commercial chemical processes, such as methane steam reforming (MSR), an important thermal process in hydrogen, ammonia and methanol synthesis [69], or the chlorine manufacturing through brine electrolysis [70]. Solar heat (CSP) [71] and

electricity (PV, CSP) [72] can be involved in these processes, thus indirectly utilized sunlight to run chemical reaction. However, these processes have several disadvantages such as harsh required conditions [73], bulky equipment for energy harvesting and storage [74], or expensive energy source (i.e. PV electricity) [75].

An appealing alternative is the direct light-to-chemical conversion. Specifically, in a light-driven chemical reaction (Figure 4), the light absorption by the system affords in an excited state, which eventually leads to the desired products [76]. These reactions can take place in very mild conditions (room temperature and atmospheric pressure), using light (potentially sunlight) as the only energy source. A photochemical process can be driven if the systems itself is capable to efficiently absorb the incoming light and convert the excited state to a reaction intermediate [77].



Figure 4. Reaction scheme of a photochemical reaction. R = reagent; R* = reagent in the excited state; P = product; $h\nu$ = light.

However, the reagents themselves can be unsuitable for an efficient light absorption and conversion, or require short wavelength radiation to be excited [78]: a light-activated catalyst or photo(electro)catalyst (Figure 5), in this case exhibits the key role to absorb the radiation and converts the reagents into products [77].

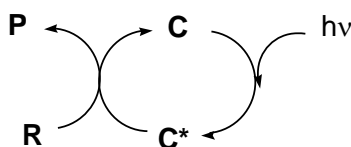


Figure 5. Reaction scheme of a photocatalyzed chemical reaction. C = catalyst; C* = catalysts in the excited state; R = reagent; P = product; $h\nu$ = light.

As in the case of traditional catalysis (thermally-activated), the use of solid materials (heterogeneous catalysts) have the significant advantage to be easily separated and recycled from the reaction medium [79].

1.4. FUNDAMENTALS OF HETEROGENEOUS PHOTO(ELECTRO)CATALYSIS

A light-activated material is essentially a SC. According to the band theory, the molecular orbitals (MOs) within a solid can be arranged in ensembles of energetically close orbitals named bands. As reported in Figure 6, three situation can be drawn, depending on how these bands are arranged [80]:

1. Conductors, in which an empty band is overlapped with an electron-occupied band.
2. Semiconductors (SCs), in which empty and filled band are energetically separated by a relatively small gap region ($1 \div 6$ eV), called bandgap (E_g).
3. Insulators, in which the empty and filled bands are separated by a wide energetic gap (> 6 eV).

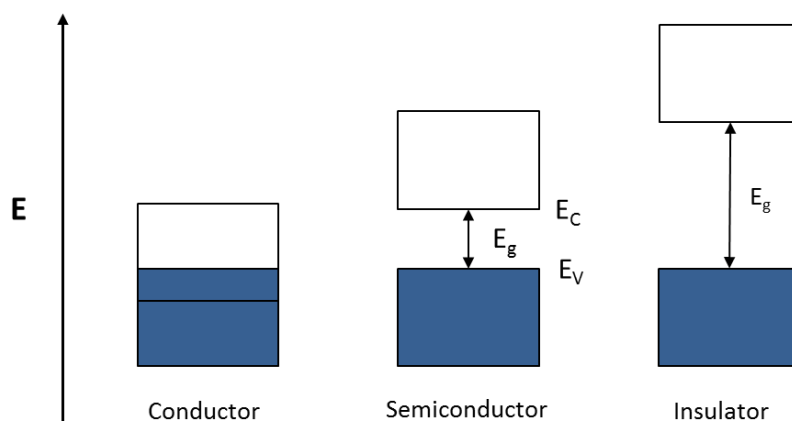


Figure 6. Energy band structure of materials. Redrawn from [80].

The band occupied by electrons is named valence band (VB), while the empty one is the conduction band (CB); the upper and lower energetic edges are named E_V and E_C , for VB and CB, respectively (Figure 6), and these band edges position depends on the type of SC [81].

A SC can be further classified depending on the charge carrier mainly contributing to the electrical conductivity, free electrons (e^-) or holes (h^+), and the relative position of the Fermi energy (E_F) [55]. E_F is an important parameter in SC science and it is defined, within the Fermi-Dirac distribution, as the energy level at which the probability to being occupied by an electron (fermion on a more general concept), is 0.5 [82]. As reported in Figure 7, three kinds of SCs can be identified [55]:

1. i-type or intrinsic, in which the conductivity is driven by both electrons and holes. E_F lies between E_C and E_V , in the middle of the energy gap. Example: non-doped Si [55].
2. n-type, in which donor impurities increase the concentration of electron, boosting the electron conductivity. These impurities induce also intra-gap energy levels or states (E_D) just below the E_C edge, and E_F is upward shifted, close to E_C . Examples: TiO_2 , ZnO, WO_3 , Fe_2O_3 , $BiVO_4$, CdS or g- C_3N_4 [83,84].
3. p-type, in which acceptor impurities improve the concentration and the conductivity of holes. These impurities induce intra-gap levels (E_A) just above E_V , and E_F is downward shifted, close to E_V . (i.e. Cu_2O , $CuFeO_2$, $Cu(In,Ga)S_2$ or WSe_2 [84]).

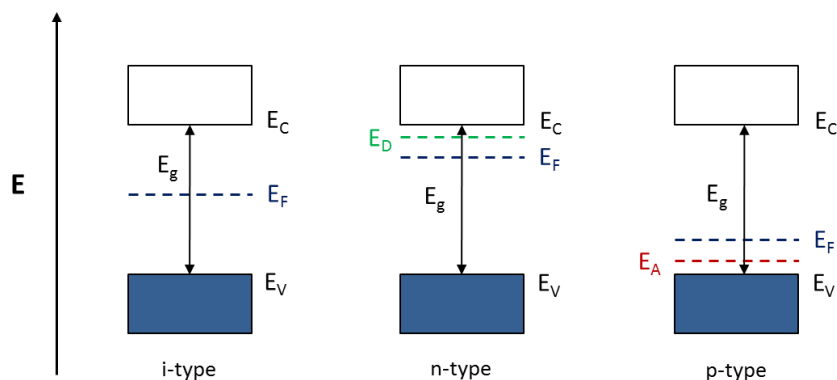


Figure 7. Energy band structure of i-type (a), n-type (b) and p-type (c) SCs. Redrawn from [55].

When a SC is irradiated by photons with energy larger or equal the E_g , electrons can be promoted from the VB to the CB, accumulating holes in the latter, and affording in two charge carrier populations. Under these non-equilibrium conditions, these can be described by two different quasi-Fermi energy (E_F^*): one for the electrons (${}_nE_F^*$) and one for holes (${}_pE_F^*$), as reported in Figure 8b. In case of n-type SC, the ${}_nE_F^*$ is almost equal to the pristine value E_F (dark conditions) while the ${}_pE_F^*$ lies closer to E_C , since the electron population does not remarkably change upon irradiation. A similar concept can be defined for p-type SC [85].

When the irradiated SC is put in contact with a liquid solution (Figure 8c) containing active redox species, a redox process can potentially occur, transferring the electron to a suitable acceptor species (A) within the solution, and filling the hole with an electron donate by a suitable donor species (D) in solution. This lead to an overall redox process to occur on the SC-solution interface [80]. On a thermodynamic point of view, this charge transfer across the SC-solution interface, requires two conditions to be fulfilled. The quasi-Fermi level of electrons (${}_nE_F^*$) has to lie above the acceptor Fermi level in solution, namely its redox potential (E°_{A/A^-}), while the quasi-Fermi level of holes (${}_pE_F^*$) has to lie below the donor redox potential (E°_{D/D^+}), as reported in Figure 8c.

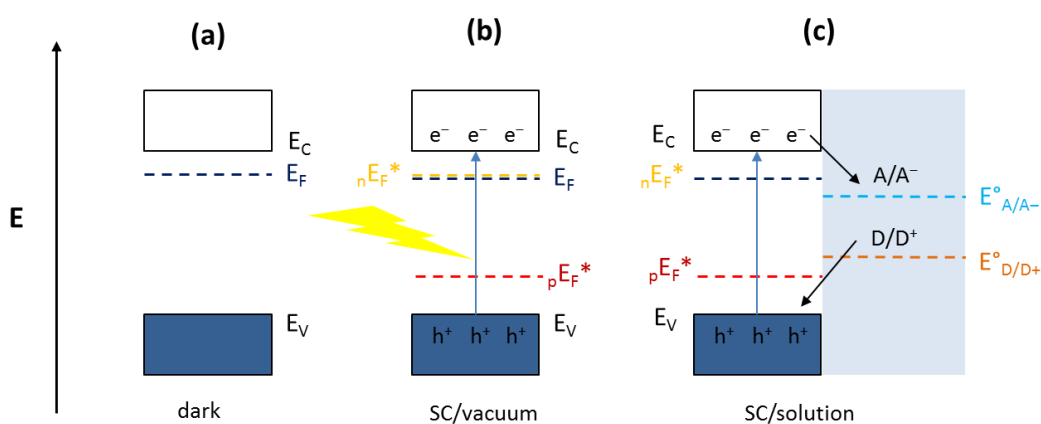


Figure 8. Energy band diagram of a n-type SC in dark (a), under irradiation in vacuum (b) and in contact with a solution (c). Redrawn for [85] and [80].

If one of the thermodynamic conditions to run the redox process cannot be fulfilled, the reaction can be run anyway. This can be achieved by supplying the extra energy as an external applied potential (ΔE), thus driving the overall redox reaction, and named photoelectrochemical (PEC) process [86]. Two main other differences can be distinguished from a photocatalytic (PC) process:

1. The two half-reaction occurs separately, thus the reaction setup requires two different components, namely a photoelectrode and a counter-electrode in the simplest setup, immersed in the solution with redox active species, and externally wired to allow electron transport as reported in Figure 9 [86].
2. The charge transfer across SC/solution interface depends on the type of SC. Specifically, oxidation processes can occur on n-type SC surfaces, while reduction processes occur on p-type SC surfaces [83].

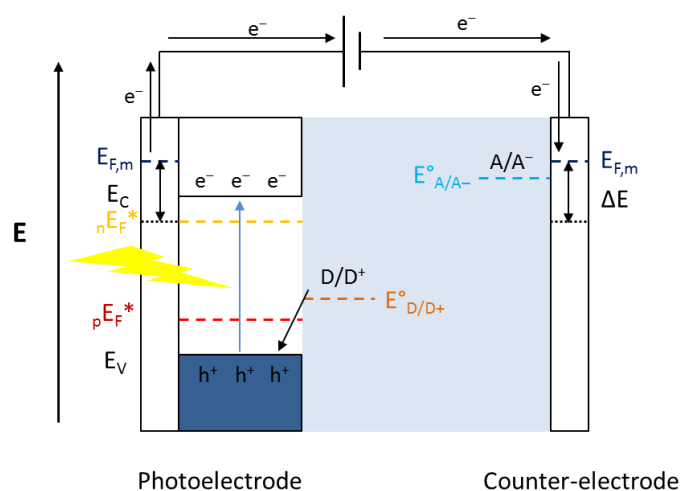


Figure 9. Energy band diagram of an n-type SC under both irradiation and applied potential in a PEC device. Electron path is reported as straight arrows.

Besides charge carrier transfer at SC/solution interface, a side process can also occur: charge carrier recombination. This phenomenon involves the reaction of a photoexcited electrons with a hole, losing the photon absorbed energy as heat (non-radiative recombination) or light (radiative recombination) [87], rather than being reacted with redox species. The process can occur through a direct band-to-band transition (Figure 10a) or, most commonly, through trap levels (E_{tr}) (Figure 10b), due to i.e. impurities or defects [55]. Such recombination process can either occurs at the surface, due to defects inducing the so-called surface states (SSs) [88,89] or within the bulk, due to poor charge carrier mobility [90] or bulk defects [91].

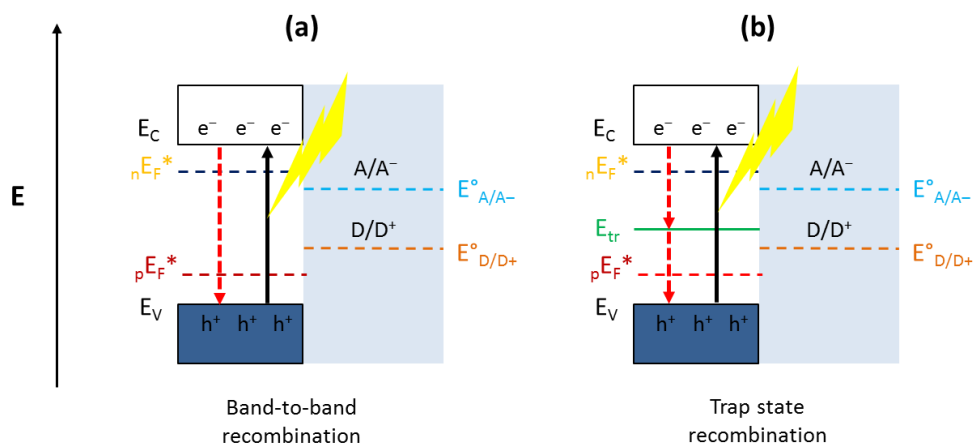


Figure 10. Charge carrier recombination (red dashed arrow) and generation (black straight arrow) in n-type SC. (a) Direct band-to-band recombination. (b) Recombination in trap state.

Besides charge and light-related processes, as in traditional heterogeneous catalysis, mass transfer of reactant and products, as well as adsorption/desorption phenomena and reaction intermediates stabilization play an important role [79] and are required to be considered in the overall catalytic phenomenon. The general mechanism of a photocatalytic process is reported in Figure 11, summarizing all the concepts previously exposed.

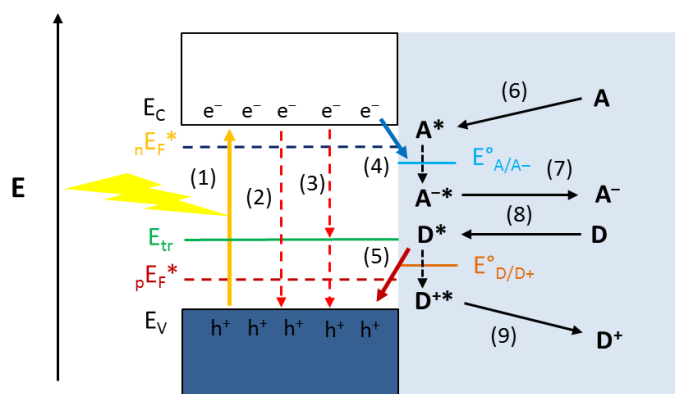


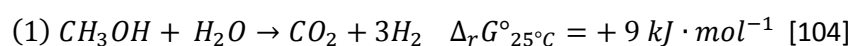
Figure 11. Overall mechanism of photocatalysis. (1) light absorption and charge carrier generation. (2) Direct band-to-band and (3) trap state recombination. (4) Electron transfer to adsorbed electron acceptor (A^*) (reduction half-reaction). (5) Electron transfer from adsorbed electron donor (D^*) (oxidation half-reaction). (6),(7) Diffusion, adsorption and desorption of electron acceptor (A) and reduction product (A^-). (8),(9) Diffusion, adsorption and desorption of electron donor (D) and oxidation products (D^+).

1.5. APPLICATIONS OF PHOTO(ELECTRO)CATALYSIS

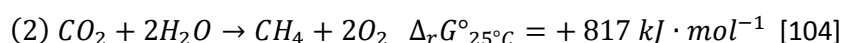
The chemical reactions that can be carried out through photo(electro)catalysis, are redox processes, and depend on the used electron acceptor (A) and donor (D). The first studied photocatalytic reactions were the oxidation, with molecular oxygen (O_2) as electron acceptor, of simple molecules such as ammonia (NH_3) [92] and carbon monoxide (CO) [93], later extended to a large variety of organic and inorganic compounds [94]. Oxidation reactions with molecular O_2 are characterized by a negative free Gibbs energy ($\Delta_r G^\circ_{25^\circ C} < 0$), and can thus easily proceed. They have been proposed as attractive tool for environmental remediation, such as

wastewater purification from pollutants [95] or pathogens [96], or air purification [97]. Others appealing applications, in virtue of the mild conditions required in PC reactions, are surfaces with PC self-cleaning and self-sterilizing properties [98]. Upon irradiation, these surfaces can remove by themselves organic deposits by oxidative degradation [99] and inactivate microorganisms [100]. Furthermore, through a non-redox light-induced phenomenon (superhydrophilicity), the water wettability is improved and dirty deposits can be further washed away [98]. These self-cleaning and self-sterilizing features can be also exploited in the field of conservation of cultural heritage [101].

When water (H₂O) is involved as electron acceptor, hydrogen (H₂) can be produced. The water splitting reaction, using water as both electron acceptor and donor (yielding respectively H₂ and O₂), was first reported by Honda and Fujishima [102], and is nowadays one of the most studied PC and PEC reaction [86,103]. The conversion of an abundant and low-value product like H₂O into more compound potentially exploitable as fuel or chemical raw material (H₂) with the sole exploitation of sunlight, is a really attractive process. This reaction, however, is characterized by a big and positive $\Delta_r G^\circ$ ($\Delta_r G^\circ_{25^\circ\text{C}} = + 237 \text{ kJ}\cdot\text{mol}^{-1}$) [104], thus requiring a large energy input to proceed. The utilization of an organic compound in place of water as electron donor species remarkably reduce the energy demand (Reaction 1), and is known to boost up the hydrogen production compared to pure water [105]. The great potentiality of H₂ production through this process, named photoreforming, is to exploit a low-cost and largely available raw material such as ligno-cellulose [106].



Besides water splitting, another appealing reaction is the conversion of CO₂ and H₂O into carbon-based fuels or chemical raw materials, namely the so-called artificial photosynthesis [107]. As for water splitting, the reaction would be able to convert abundant and low-value raw materials into marketable products, with the advantages of a wide variety of attainable useful compounds (i.e. CO, CH₄, CH₃OH) [108] and the higher energy density of carbon-based fuels, compared to H₂ [5]. However, generally the conversion of CO₂ into more valuable products requires a large energy input (Reaction 2), more than the water splitting. Furthermore, while H₂O-rich sources are readily available as waterbodies (i.e. rivers, lakes, seas), CO₂ is mainly accessible as diluted streams (i.e. atmospheric CO₂), requiring technologies to capture and enrich this gas, eventually contributing to make more expensive the overall process of large-scale CO₂ conversion [109].



Some examples of photo(electro)catalyzed reactions are reported in Table 1.

Table 1. Example of redox reactions carried out by PC or PEC processes. Products within bracket are not directly detected but supposed to be formed due to reaction pathway. †: photooxidation exploited for photocatalytic self-cleaning of surfaces.

Reference	Electron acceptor	Electron donor	Products	SC
[110]	CO ₂	H ₂ O	CH ₄ , CO, H ₂ , O ₂	BiOI/gC ₃ N ₄
[111]	CO ₂	H ₂ O	HCOOH, CO	CuO/CuFeO ₂
[112]	H ₂ O	H ₂ O	H ₂ , O ₂	Mn ₃ O ₄ /Rh-Cr ₂ O ₃ /GaN:ZnO
[113]	H ₂ O	Glycerol	H ₂ , CO ₂ , CH ₃ OH, CH ₃ COOH	Pt/TiO ₂
[114]	H ₂ O	CH ₃ OH	H ₂ , CO ₂ , HCHO,	Au/TiO ₂
[115]	H ₂ O	Benzylamine	H ₂ , n-benzylidenebenzylamine	Ti-doped Fe ₂ O ₃
[116]	O ₂	CH ₃ CHO	CO ₂ , CH ₃ COOH, (H ₂ O)	TiO ₂
[117]	O ₂	PAH (polycyclic aromatic hydrocarbons)	Aromatic hydroquinones, quinones, aldehyde, lactone, alcohols, ketones, (CO ₂), (H ₂ O)	Pt-GaN:ZnO
[118]	O ₂	PFOA (perfluoro-octanoic acid)	(CO ₂), F ⁻ , C ₇ F ₁₅ COOH, C ₆ F ₁₃ COOH, C ₅ F ₁₁ COOH, C ₄ F ₉ COOH	TiO ₂ -rGO
[119]	O ₂	MB (methylene blue), coffee and wine stains	Degradation products (not identified)†	Cu(II) porphyrin complex/ TiO ₂ immobilized on cotton fabric
[120]	O ₂	MO (methyl orange), stearic acid	Degradation products (not identified)†	TiO ₂ -SiO ₂ immobilized on stainless steel
[101]	O ₂	Rhodamine B	Degradation products (not identified)†	TiO ₂ immobilized on travertine

1.6. SEMICONDUCTORS AND MATERIAL DESIGN

Titanium dioxide (TiO_2) is the most popular semiconductor material in PC [121-123]. Besides it several other materials have been explored, such as zinc oxide (ZnO) [124], strontium titanate (SrTiO_3) [125], sodium tantalate (NaTaO_3) [126], cerium oxide (CeO_2) [127], tungsten trioxide (WO_3) [128], cadmium sulphide (CdS) [129], zinc sulphide (ZnS) [130], graphitic carbon nitride ($\text{g-C}_3\text{N}_4$) [131], tantalum nitride (Ta_3N_5) and oxynitride (TaON) [132]. Concerning material for PEC application, n-type SC employed in oxidation reactions are hematite (Fe_2O_3) [115], tungsten trioxide (WO_3) [133] and bismuth vanadate (BiVO_4) [134]. On the other hand, p-type SC such as copper (I) oxide (Cu_2O) [135], copper iron delafossite (CuFeO_2) [136], copper indium gallium sulphide ($\text{Cu}(\text{Ga},\text{In})\text{S}_2$) [137], gallium phosphide (GaP) [138] or tungsten diselenide (WSe_2) [139].

The selection of a SC material depends on the desired redox reaction. As previously mentioned, one (PEC) or both (PC) the thermodynamic requirements have to be fulfilled in order to allow the charge transfer at SC/reaction medium interface. For instance, as reported in Figure 12, the overall water splitting can potentially occur if TiO_2 or ZnO are used as PC, while it cannot if WO_3 is used. Nonetheless, WO_3 can be used in water oxidation as photoanode.

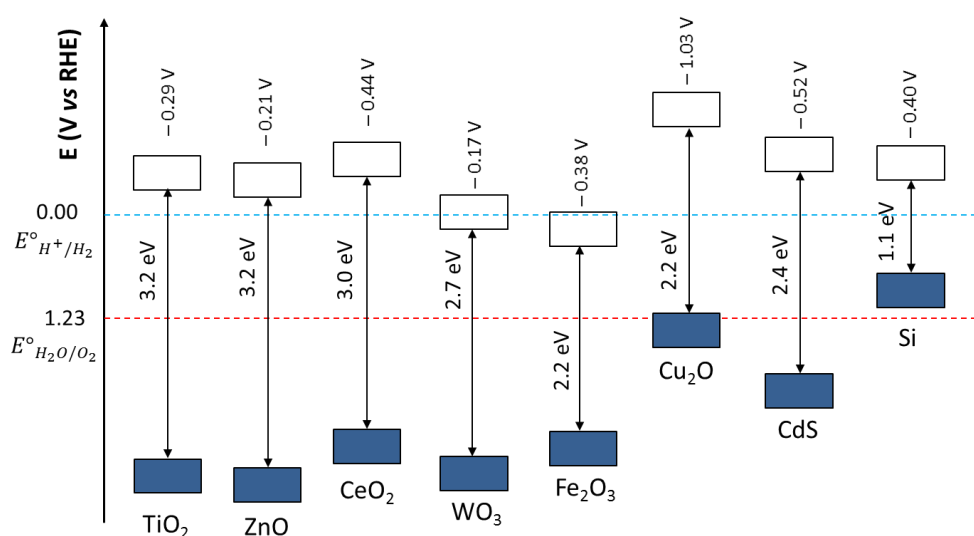


Figure 12. Band edge position vs RHE at of some SC materials, respect to the redox potential for proton reduction and water oxidation (blue and red line, respectively). Redrawn from [140,141]. CBs are represented as white boxes, while VBs as blue boxes; quasi-Fermi level position are not reported, but assumed to be close to CB and VB.

Thermodynamics is, however, just one part of the story. As reported by Li and Wu, several other parameters should be considered when selecting a SC. Indeed, a good material should have [142]:

1. A E_g as narrower as possible, in order to both maximize the harvestable photons of the solar spectrum (highly energetic UV photons compose a small fraction of the spectrum) and allow the highest solar-to-chemical energy efficiency.

2. A good light penetration within the material, namely a narrow optical penetration depth (δ_p), to maximize the generation of charge carriers in proximity of the surface.
3. An efficient transport of charge carrier, namely a charge carrier diffusion length (L_D) larger than the δ_p , in order to reduce the recombination occurring in the bulk of the SC and allow an effective transfer to the surface, where the reaction occurs.
4. A good stability in the reaction medium, in order to avoid corrosion and/or photocorrosion phenomena that induce a fast loss of activity.
5. A strong catalytic activity, namely a low reduction (η_{RED}) and/or oxidation (η_{OX}) overpotential, to exploit as much as possible the energy of the photoexcited charge carriers, in turn improving the solar-to-chemical energy efficiency. If more products can be formed, the material should also be able to selectively direct the reaction toward the desired products (selectivity).
6. Be made of earth-abundant and safe elements, in order to be cheap and safe to produce and handle.
7. Be synthesized with approaches as mild as possible, and avoiding harmful and expensive reagents, to allow a feasible large-scale production.

The ideal SC fulfilling all these requirements does not exist, and each material has some drawbacks limiting a large-scale application. TiO_2 , for instance, is a cheap, chemically and photochemically stable, non-toxic material, and due to the energetic location of E_c and E_v , a wide variety of electron acceptors and donors can potentially react on its surface [122,142]. However, given its large E_g (3.0-3.2 eV) only UV photons can excite this material, limiting the harvestable fraction of sunlight and the attainable solar-to-chemical energy efficiency [142]. Furthermore, the poor charge carrier mobility hinder an effective transfer to the surface, and further reduces its photocatalytic activity by improving recombination phenomena [143].

Besides the SC selection, several strategies can be exploited to minimize the impact of a SC drawbacks. One of the simplest strategies is the design of material morphology. The crystallinity of a material, is an important parameter to facilitate the charge carrier transfer to the surface and reduce their recombination [91]. However, a higher crystallinity is usually associated with a low specific surface area (SSA), essential to allow the reagent adsorption and subsequent interfacial charge transfer, thus a compromise between crystallinity and SSA is usually desired [144]. Other strategies rely on the shape of the material (i.e. 1D or 2D nanomaterials), which can improve the light harvesting (charge carrier generation) and maximize the charge transfer to the surface [142]. The exposed facets engineering, namely how superficial atoms are organized, can further contribute in enhancing the material activity, by exposing the most catalytically active facets (i.e. {001} facets on anatase TiO_2) [145], or even improves the material stability [146].

An important role could be played also by the presence of defects. Despite as previously stated they could facilitate the charge carrier recombination, superficial defects can be a useful tool in improving the material activity. In details, they potentially act either as charge carrier trapping sites, hampering the recombination

processes [147,148], or as adsorption site, which further facilitate the charge transfer phenomena (redox reaction) [149].

Besides the engineering of the bare material, other strategies involve the surface modification in order to improve the visible-light harvesting capability, activity, selectivity or the stability of the SC. One of the most popular strategies is to exploit a heterojunction, namely an interface between two (or more) SCs that improve the charge carrier separation and, consequently, reduce their recombination [150]. As pictured in Figure 13a, the type-II heterojunction (the most popular one), acts by a selective transfer of the photoexcited electron from the high-lying ($E_{C,1}$) to the low-lying ($E_{C,2}$) conduction band edge (pathway 1). The holes left on the first SC, cannot cross the junction due the unfavourable energetics of the valence band edges (pathway 2): being the charge carrier physically separated, their recombination is hampered and their lifetime improve, eventually potentially improving the activity as well [151]. Both E_F and quasi-Fermi levels (${}_nE_F^*$ and ${}_pE_F^*$) of the heterojunction, are different from those of the original SCs: this means the two (or more) SCs interact each other [152].

Heterojunctions have been widely exploited both in PC and PEC systems. In PC, heterojunctions have been used either to improve the sole charge carrier separation, when using SCs with comparable E_g (i.e. ZnO/SnO₂) [153], or to sensitize the material to visible photons, by using a SC with a narrow E_g (i.e. CdS/TiO₂) [154]. In PEC, heterojunctions are generated by top-coating a SC with a layer of another SC (overlayer) [155], and used to improve the charge carriers separation [137], to improve the stability of a SC in the reaction medium [156], or to passivate some defects located on the surface, which would increase the charge carrier recombination [136].

Another appealing strategy of surface functionalization is the utilization of a co-catalyst [157]. This component has two main effects, as depicted in Figure 13b:

1. Improve the charge carrier separation (pathway 6) [158]
2. Act as true reaction site, reducing the overpotential for a given reaction (pathway 7 vs pathway 5) [159]

The co-catalysts can reduce the overpotential either of the reduction [160] or of the oxidation [161] half-reactions, and often represent a key tool in enhancing the selectivity of the reaction, when more products can be obtained [162,163]. In PC application, where oxidation and reduction half-reaction occurs on the same particles, the utilization of both reduction and oxidation co-catalyst can further improve the activity by improving the rates of the two half-reactions at the same time and suppress side processes [112,164].

Finally, a key feature when dealing with surface modification such as heterojunctions or functionalization with co-catalysts, is to ensure a good quality of the solid-solid interface in term of interfacial defects, those represent an obstacle to an efficient charge transfer by improving, as for bulk SC, the recombination phenomenon [165, 166].

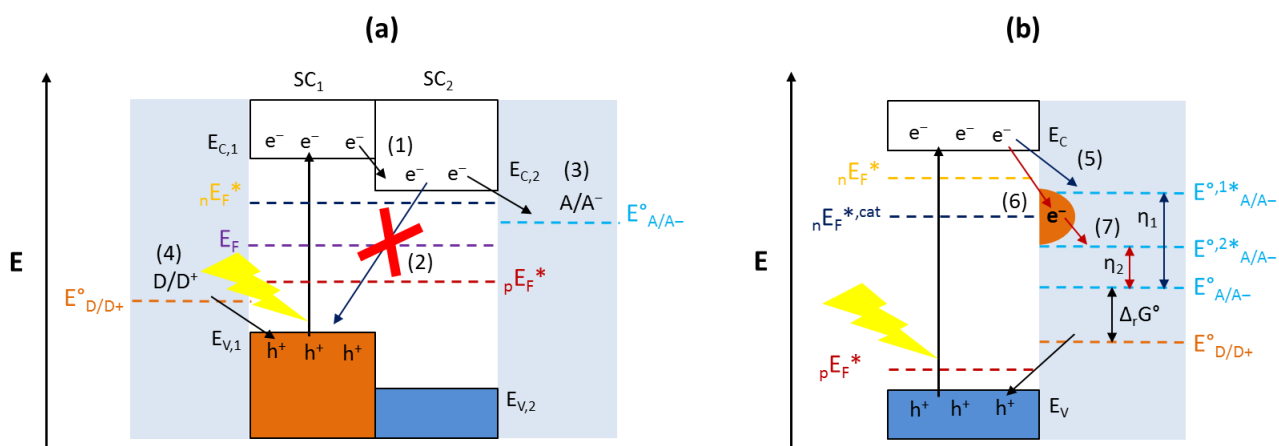


Figure 13. (a) Heterojunction scheme. SC_1 and SC_2 are the two SCs, $E_{C,1}$, $E_{C,2}$ and $E_{V,1}$, $E_{V,2}$ are the respective conduction and valence band edges. nE_F^* , pE_F^* and E_F represent the electron and holes quasi-Fermi level, and the Fermi level of the heterojunction. (1) charge carrier transfer at SC_1/SC_2 interface; (2) (hindered) interfacial charge carrier recombination; (3) and (4) SC/reaction medium charge carrier transfer. (b) Effect of a reduction co-catalyst (overpotential of the oxidation half-reaction is neglected). nE_F^* and $nE_F^{*,cat}$ are the quasi-Fermi levels of bare and co-catalyst modified SC surface. $\Delta_r G^\circ$ is the Gibbs free energy of the overall reaction and η_1 and η_2 are the co-catalyst free and co-catalyst modified overpotential of the SC surface, respectively. $E^{\circ,1*}_{A/A^-}$ and $E^{\circ,2*}_{A/A^-}$ are the redox potential of the reduction process at bare and co-catalyst modified surface. (5) direct SC-to-acceptor charge transfer; (6) SC-to-co-catalyst charge transfer; (7) co-catalyst-to-acceptor charge transfer.

1.7. AIM OF THE WORK

Climate change is a phenomenon that will strongly affect human society. To face this, the sole strategies of mitigation CO₂ emissions are not suitable alone to solve the problem, because thermal inertia of climate system will keep the global warming for a long period. The most appropriate way to face climate change is to embrace adaptation strategies. In this contest, solar energy can be a useful tool being inexpensive, unlimited and widespread all over the world. Specifically, it can be used as energy source to directly run chemical reactions, with the additional advantages of very mild operative conditions, namely room temperature and atmospheric pressure. These reactions can be potentially exploited for several purposes within the climate change adaptation concept: from fuel production, to environmental or cultural heritage application.

This work is aimed thus to study different light-driven chemical reactions, in particular fuel production and cultural heritage conservation, by using diverse SCs, characterized by different physico-chemical properties (i.e. E_g, carrier mobility, surface acidity/basicity). Specifically, earth-abundant oxide-based SC materials have been chosen for this work. Each SCs has its own drawbacks, thus aiming an improvement of the photo(electro)catalytic performances, several strategies have been exploited, ranging from the design of material morphology, to approaches of surface modification such as heterojunction formation and functionalization with co-catalyst.

In details, the work is divided into four chapters:

- Chapter 1: Ti-based powdered photocatalysts for hydrogen production from biomass.
- Chapter 2: Zn-bases powdered photocatalysts for gas-phase CO₂ reduction.
- Chapter 3: Cu- and Fe-based photocathode for CO₂ photoelectrochemical reduction.
- Chapter 4: Ti- and Zn photocatalytic-modified plaster (Venetian *marmorino*) for self-cleaning application in cultural heritage conservation.

1.8. REFERENCES

- ¹ R.L. Lehrman. Energy is not the ability to do work. *Phys. Teach.* **1973**, *11*, 15-18, doi: 10.1119/1.2349846
- ² E. Cook. The flow of energy in an industrial society. *Sci. Am.* **1971**, *225*(3), 134-147, <https://www.jstor.org/stable/2492312>. Accessed on 20/02/2020
- ³ Wordometer website: <https://worldometer.info/world-population/>. Accessed on 20/02/2020
- ⁴ BP statistical review of world energy. 2019, 68th edition. Pdf available online: <https://www.bp.com/content/dam/bp/business-sites/en/global/corporate/pdfs/energy-economics/statistical-review/bp-stats-review-2019-full-report.pdf>. Accessed on 20/02/2020.
- ⁵ G. A. Olah, A. Goepfert, G. K. Surya Prakash. *Beyond Oil and Gas: The Methanol Economy*. WILEY-VCH Verlag GmbH & Co. KGaA: Weinheim (Germany), 2009; pp. 19 – 53. ISBN: 9783527324224.
- ⁶ J. A. Moulijn, M. Makkee, A.E. Van Diepen. *Chemical Process Technology*, 2nd edition. John Wiley & Sons Ltd: Chichester (UK), 2013; pp. 41 – 168. ISBN: 9780471630623.
- ⁷ David J. Murphy, Charles A. S. Hall. Year in review—EROI or energy return on (energy) invested. *Ann. N.Y. Acad. Sci.* **2010**, *1185*, 102-118, doi: 10.1111/j.1749-6632.2009.05282.x.
- ⁸ G. Eng, I. Bywater, C. Hendtlass. *New Zealand Energy Information Handbook*, 3rd ed. New Zealand Centre for Advanced Engineering: Christchurch (New Zealand), 2008. ISBN: 9780908993444.
- ⁹ G. Ertl, H. Knozinger, J. Weitkamp. *Environmental Catalysis*. WILEY-VCH Verlag GmbH & Co. KGaA: Weinheim (Germany), 1999. ISBN: 9783527298273.
- ¹⁰ Climate Change 2014. Synthesis Report. Intergovernmental Panel on Climate Change (IPCC). Pdf available online: https://www.ipcc.ch/site/assets/uploads/2018/02/AR5_SYR_FINAL_SPM.pdf. Accessed on 20/02/2020.
- ¹¹ V. Smil. *The Earth's Biosphere: Evolution, Dynamics, and Change*. The MIT Press: Cambridge (USA), 2003. ISBN: 9780262194723.
- ¹² J. K. Casper. *Greenhouse Gases*. Facts on File: New York (USA), 2012; pp. 1 – 18. ISBN: 9780816072644
- ¹³ Trends in atmospheric carbon dioxide. National Oceanic and Atmospheric Administration (NOAA) website. <https://www.esrl.noaa.gov/gmd/ccgg/trends/>. Accessed on 24/02/2020.
- ¹⁴ S. Solomon, D. Qin, M. Manning, M. Marquis, K. Averyt, M. M. B. Tignor, Z. Chen, H. L. Miller. *Climate Change 2007: The Physical Science Basis*, published for the Intergovernmental Panel on Climate Change (IPCC). Cambridge University Press: Cambridge (UK) and New York (USA), 2007. ISBN: 9780521705967.
- ¹⁵ P. Falkowski, R. J. Scholes, E. Boyle, J. Canadell, D. Canfield, J. Elser, N. Gruber, K. Hibbard, P. Högberg, S. Linder, F. T. Mackenzie, B. Moore III, T. Pedersen, Y. Rosenthal, S. Seitzinger, V. Smetacek, W. Steffen, The global carbon cycle: a test of our knowledge of earth as a system. *Science* **2000**, *290*, 291-296, doi: 10.1126/science.290.5490.291.
- ¹⁶ A. B. Robinson, N. E. Robinson, W. Soon. Environmental Effects of Increased Atmospheric Carbon Dioxide *J. Am. Phys. Sur.* **2007**, *12*, 79-90. Pdf available online: <https://www.jpands.org/jpands1203.htm>. Accessed on 24/02/2020.
- ¹⁷ G. Readfearn. 'CO₂ is plant food': Australian group signs international declaration denying climate science. The Guardian: London (UK). Available online: <https://www.theguardian.com/environment/2019/sep/26/co2-is-plant-food-australian-group-signs-international-declaration-denying-climate-science>. Accessed on 24/02/2020.
- ¹⁸ T. F. Stocker, D. Qin, G.-K. Plattner, M. Tignor, S. K. Allen, J. Boschung, A. Nauels, Y. Xia, V. Bex, P.M. Midgley. *Climate Change 2013: The Physical Science Basis*, published for the Intergovernmental Panel on Climate Change (IPCC). Cambridge University Press: Cambridge (UK) and New York (USA) USA, 2013. ISBN: 9781107661820.
- ¹⁹ N. Armaroli, V. Balzani. *Energy for a Sustainable World*. WILEY-VCH Verlag GmbH & Co. KGaA: Weinheim (Germany), 2011. ISBN: 9783527325405.
- ²⁰ S. Moss. Weatherwatch: Storm Ophelia's trail of destruction in 2017. The Guardian. London (UK): Available online: <https://www.theguardian.com/news/2019/oct/02/weatherwatch-storm-ophelia-trail-of-destruction-2017>. Accessed on 25/02/2020.
- ²¹ J. Henley, A. Giuffrida. Two people dies as Venice floods at the highest level in 50 years. The Guardian: London (UK). Available online: <https://www.theguardian.com/environment/2019/nov/13/waves-in-st-marks-square-as-venice-flooded-highest-tide-in-50-years>. Accessed on 25/02/2020.
- ²² Australia fires: A visual guide to the bushfire crisis. British Broadcasting Corporation (BBC): London (UK). Available online: <https://www.bbc.com/news/world-australia-50951043>. Accessed on 25/02/2020.
- ²³ J. P. Kossin, K. A. Emanuel, G. A. Vecchi. The poleward migration of the location of tropical cyclone maximum intensity. *Nature* **2014**, *509*, 349-352, doi: 10.1038/nature13278.
- ²⁴ B. A. Revich, M. A. Podolnaya, Thawing of permafrost may disturb historic cattle burial grounds in East Siberia. *Glob. Health Action*. **2011**, *4*, 8482, doi: 10.3402/gha.v4i0.8482.

- ²⁵ A. Sperotto, S. Torresan, V. Gallina, E. Coppola, A. Critto, A. Marcomini. A multi-disciplinary approach to evaluate pluvial floods risk under changing climate: The case study of the municipality of Venice (Italy). *Sci. Total. Environ.* **2016**, 562, 1031-1043, doi: 10.1016/j.scitotenv.2016.03.150
- ²⁶ J. J. Sharples, G. J. Cary, P. Fox-Hughes, S. Mooney, J. P. Evans, M.-S. Fletcher, M. Fromm, P. F. Grierson, R. McRae, P. Baker. Natural hazards in Australia: extreme bushfire. *Clim. Change* **2016**, 139, 85-99, doi: 10.1007/s10584-016-1811-1.
- ²⁷ *Kyoto protocol to the United Nations Frameworks Convention on Climate Change*. The United Nations Frameworks Convention on Climate Change (UNFCCC) website. Pdf available online: <https://unfccc.int/resource/docs/convkp/kpeng.pdf>. Accessed on 24/02/2020.
- ²⁸ *The Paris Agreement*. The United Nations Frameworks Convention on Climate Change (UNFCCC) website. Pdf available online: https://unfccc.int/files/essential_background/convention/application/pdf/english_paris_agreement.pdf. Accessed on 24/02/2020.
- ²⁹ E. S. Sanz-Pérez, C. R. Murdock, S. A. Didas, C. W. Jones, Direct Capture of CO₂ from Ambient Air. *Chem. Rev.* **2016**, 116, 11840-11876, doi: 10.1021/acs.chemrev.6b00173
- ³⁰ D. Y. C. Leung, G. Caramanna, M. M. Maroto-Valer, An overview of current status of carbon dioxide capture and storage technologies. *Renew. Sustain. Energy Rev.* **2014**, 39, 426-443, doi: 10.1016/j.rser.2014.07.093
- ³¹ D. A. Voormeij, G. J. Simandl, Geological, Ocean and Mineral CO₂ sequestration options: a technical review. *Geoscience Canada* **2004**, 31(1), 11-22. Pdf available online: <https://journals.lib.unb.ca/index.php/GC/article/view/2740>. Accessed on 24/02/2020.
- ³² A. Sanna, M. Uibu, G. Caramanna, R. Kuusik, M. M. Maroto-Valer, A review of mineral carbonation technologies to sequester CO₂. *Chem. Soc. Rev.* **2014**, 43, 8049-8080, doi: 10.1039/c4cs00035h.
- ³³ H. Arakawa, M. Aresta, J. N. Armor, M. A. Barteau, E. J. Beckman, A. T. Bell, J. E. Bercaw, C. Creutz, E. Dinjus, D. A. Dixon, K. Domen, D. L. DuBois, J. Eckert, E. Fujita, D. H. Gibson, W. A. Goddard, D. W. Goodman, J. Keller, G. J. Kubas, H. H. Kung, J. E. Lyons, L. E. Manzer, T. J. Marks, K. Morokuma, K. M. Nicholas, R. Periana, L. Que, J. Rostrup-Nielson, W. M. H. Sachtler, L. D. Schmidt, A. Sen, G. A. Somorjai, P. C. Stair, B. R. Stults, W. Tumas, Catalysis Research of Relevance to Carbon Management: Progress, Challenges, and Opportunities. *Chem. Rev.* **2001**, 101, 953-996, doi: 10.1021/cr000018s.
- ³⁴ G. Centi, E. A. Quadrelli, S. Perathoner, Catalysis for CO₂ conversion: a key technology for rapid introduction of renewable energy in the value chain of chemical industries. *Energy Environ. Sci.* **2013**, 6, 1711-1731, doi: 10.1039/c3ee00056g
- ³⁵ T. M. L. Wigley, The Climate Change Commitment. *Science* **2005**, 307, 1766-1769, doi: 10.1126/science.1103934
- ³⁶ K. Zickfeld, M. Eby, A. J. Weaver, K. Alexander, E. Crespin, N. R. Edwards, A. V. Eliseev, G. Feulner, T. Fichet, C. E. Forest, P. Friedlingstein, H. Goosse, P. B. Holden, F. Joos, M. Kawamiya, D. Kicklighter, H. Kienert, K. Matsumoto, I. Mokhov, E. Monier, S. M. Olsen, J. O. P. Pedersen, M. Perrette, G. Philippon-Berthier, A. Ridgwell, A. Schlosser, T. S. Von Deimling, G. Shaffer, A. Sokolov, R. Spahni, M. Steinacher, K. Tachiiri, K. S. Tokos, M. Yoshimori, N. Zeng, F. Zhao. Long Term Climate Change Commitment and Reversibility: An EMIC Intercomparison. *J. Clim.* **2013**, 26, 5782-5809, doi: 10.1175/JCLI-D-12-00584.1
- ³⁷ J. G. Titus, Strategies for adapting to the greenhouse effect. *JAPA* **1990**, 56(3), 311-323, doi: 10.1080/01944369008975775
- ³⁸ J. Birkmann, First- and second-order adaptation to natural hazards and extreme events in the context of climate change. *Nat. Hazards* **2011**, 58, 811-840, doi: 10.1007/s11069-011-9806-8
- ³⁹ B. L. Preston, C. Brooke, T. G. Measham, T. F. Smith, R. Gorddard, Igniting change in local government: lessons learned from a bushfire vulnerability assessment. *Mitig. Adapt. Strateg. Glob. Change* **2009**, 14, 251-283, doi 10.1007/s11027-008-9163-4
- ⁴⁰ D. S. G. Thomas, C. Twyman, Equity and justice in climate change adaptation amongst natural-resource-dependent societies. *Glob. Environ. Change* **2005**, 15, 115-124, doi:10.1016/j.gloenvcha.2004.10.001
- ⁴¹ O. Mertz, C. Mbow, A. Reenberg, A. Diouf, Farmers' Perceptions of Climate Change and Agricultural Adaptation Strategies in Rural Sahel. *Environmental Management* (2009) 43:804-816 DOI 10.1007/s00267-008-9197-0
- ⁴² A. Iglesias, S. Quiroga, M. Moneo, L. Garrote, From climate change impacts to the development of adaptation strategies: Challenges for agriculture in Europe. *Clim. Change* **2012**, 112, 143-168, doi: 10.1007/s10584-011-0344-x
- ⁴³ D. Viviroli, D. R. Archer, W. Buytaert, H. J. Fowler, G. B. Greenwood, A. F. Hamlet, Y. Huang, G. Koboltschnig, M. I. Litaor, J. I. López-Moreno, S. Lorentz, B. Schädler, H. Schreier, K. Schwaiger, M. Vuille, R. Woods, Climate change and mountain water resources: overview and recommendations for research, management and policy. *Hydrol. Earth Syst. Sci.* **2011**, 15, 471-504, doi:10.5194/hess-15-471-2011
- ⁴⁴ A. H. Arthington, R. J. Naiman, M. E. McLain, C. Nilsson, Preserving the biodiversity and ecological services of rivers: new challenges and research opportunities. *Freshw. Biol.* **2010**, 55, 1-16, doi:10.1111/j.1365-2427.2009.02340.x
- ⁴⁵ J. J. Hess, J. Z. McDowell, G. Luber, Integrating Climate Change Adaptation into Public Health Practice: Using Adaptive Management to Increase Adaptive Capacity and Build Resilience. *Environ. Health Perspect.* **2012**, 120(2), 179-171, doi: 10.1289/ehp.1103515

- ⁴⁶ A. Middel, N. Chhetri, R. Quay, Urban forestry and cool roofs: Assessment of heat mitigation strategies in Phoenix residential neighborhoods. *Urban For. Urban Gree*. **2015**, *14*, 178-186, /10.1016/j.ufug.2014.09.010
- ⁴⁷ K. A. Dornelles, M. Roriz, V. F. Roriz, R. M. Caram, Thermal performance of white solar-reflective paints for cool roofs and the influence on the thermal comfort and building energy use in hot climates. *ISES Solar World Congress 2011*, Kassel (Germany), doi: 10.13140/RG.2.1.1745.5843
- ⁴⁸ C. M. Hall, T. Baird, M. James, Y. Ram, Climate change and cultural heritage: conservation and heritage tourism in the Anthropocene. *JHT* **2016**, *11(1)*, 10-24, doi: 10.1080/1743873X.2015.1082573
- ⁴⁹ F. Krebs, S. Holzhauser, A. Ernst, Modelling the Role of Neighbourhood Support in Regional Climate Change Adaptation. *Appl. Spatial Analysis* **2013**, *6*, 305-331, doi: 10.1007/s12061-013-9085-8
- ⁵⁰ O. Ellaban, H. Abu-Rub, F. Blaabjerg, Renewable energy resources: Current status, future prospects and their enabling technology. *Renew. Sustain. Energy Rev.* **2014**, *39*, 748-764, doi: 10.1016/j.rser.2014.07.113
- ⁵¹ N. Kannann, D. Vakeesan, Solar energy for future world: - A review. *Renew. Sustain. Energy Rev.* **2016**, *62*, 1092-1105, doi: 10.1016/j.rser.2016.05.022 1364-0321/&
- ⁵² B. Viswanathan, Solar Energy: Fundamental. In *Energy Sources Fundamental of Chemical Conversion Processes and Applications*, 1st ed., Elsevier: Amsterdam (The Netherlands), 2016. ISBN: 9780444563538.
- ⁵³ ASTM G173-03 Reference Spectra derived from SMARTS v 2.9.2., National Renewable Energy Laboratories (NREL) website, available on: <https://rredc.nrel.gov/solar//spectra/am1.5/ASTMG173/ASTMG173.html>. Accessed on 28/02/2020.
- ⁵⁴ E. Pallé, M. R. Zapatero Osorio, R. Barrena, P. Montañés-Rodríguez, E. L. Martín, Earth's transmission spectrum from lunar eclipse observations. *Nature* **2009**, *459*, 814-816, doi: 10.1038/nature08050
- ⁵⁵ K. Jäger, O. Isabella, A. H. M. Smets, R. A. C. M. M. van Swaaij, M. Zeman, *Solar Energy. Fundamentals, Technology, and Systems*. Uit Cambridge Ltd.: Cambridge (UK), 2016. ISBN: 9781906860325.
- ⁵⁶ H. L. Zhang, J. Baeyens, J. Degrève, G. Cacères, Concentrated solar power plants: Review and design methodology. *Renew. Sustain. Energy Rev.* **2013**, *22*, 466-481, doi: 10.1016/j.rser.2013.01.032.
- ⁵⁷ W.H. Stein, R. Buck, Advanced power cycles for concentrated solar power. *Sol. Energy* **2017**, *152*, 91-105, doi: 10.1016/j.solener.2017.04.054.
- ⁵⁸ A. C. Köberle, D. E. H. J. Gernaat, D. P. van Vuuren, Assessing current and future techno-economic potential of concentrated solar power and photovoltaic electricity generation. *Energy* **2015**, *89*, 739-756, doi: 10.1016/j.energy.2015.05.145
- ⁵⁹ Solar Heating and Cooling for Residential Application. Technology brief, 2015. Available on International Renewable Energy Agency (IRENA) website: https://www.irena.org/documentdownloads/publications/irena_etsap_tech_brief_r12_solar_thermal_residential_2015.pdf. Accessed on 01/03/2020.
- ⁶⁰ Solar Heat for Industry. Solar Payback, pdf available online: <https://www.solar-payback.com/wp-content/uploads/2017/07/Solar-Heat-for-Industry-Solar-Payback-April-2017.pdf>. Accessed on 01/03/2020.
- ⁶¹ F. Mauthner, W. Weiss, M. Spörk-Dük, Solar Heat Worldwide, 2016 edition. International Energy Agency (IEA) Solar Heating & Cooling Programme. Available online: <https://www.aee-intec.at/Uploads/dateien1105.pdf>. Accessed on 01/03/2020.
- ⁶² Abdul Ghafoor, Anjum Munir, Worldwide overview of solar thermal cooling technologies. *Renew. Sustain Energy Rev.* **2015**, *43*, 763-774, doi: 10.1016/j.rser.2014.11.073.
- ⁶³ P. Greve, T. Kahil, J. Mochizuki, T. Schinko, Y. Satoh, P. Burek, G. Fischer, S. Tramberend, R. Burtscher, S. Langan, Y. Wada, Global assessment of water challenges under uncertainty in water scarcity projections. *Nat. Sustain.* **2018**, *1*, 486-494, doi: 10.1038/s41893-018-0134-9.
- ⁶⁴ M. Shatat, M. Worall, S. Riffat. Opportunities for solar water desalination worldwide: Review. *Sustain. Cites Soc.* **2013**, *9*, 67-80, doi: 10.1016/j.scs.2013.03.004.
- ⁶⁵ A. Buenaventura Pouyfaucou, L. Garcíá-Rodríguez. Solar thermal-powered desalination: A viable solution for a potential market. *Desalination*, **2018**, *453*, 60-69, doi: 10.1016/j.desal.2017.12.025.
- ⁶⁶ M. Wegelin, S. Canonica, K. Mechsner, T. Fleischmann, F. Pesaro, A. Metzler, Solar water disinfection: scope of the process and analysis of radiation experiments. *J. Water Supply Res.* **1994**, *43(3)*, 154-169.
- ⁶⁷ M. Castro-Alfárez, M. I. Polo-López, P. Fernández-Ibáñez, Intracellular mechanisms of solar water disinfection. *Sci. Rep.* **2016**, *6*, 38145, doi: 10.1038/srep38145.
- ⁶⁸ K. G. McGuigan, R. M. Conroy, H.-J. Mosler, M. du Preez, E. Ubomba-Jaswa, P. Fernandez-Ibñez. Solar water disinfection (SODIS): A review from bench-top to roof-top. *J. Hazard. Mater.* **2012**, *235-236*, 29-46, doi: 10.1016/j.jhazmat.2012.07.053.
- ⁶⁹ R. Reimert, F. Marschner, H.-J. Renner, W. Boll, E. Supp, M. Brejc, W. Liebner, G. Schaub, *Gas Production*, 2. *Process*. Ullmann's Encyclopedia of Chemical Industry, 2012. doi: 10.1002/14356007.o12_o01.

- ⁷⁰ P. Schmittinger, T. Florkiewicz, L. C. Curlin, B. Lüke, R. Scannell, T. Navin, E. Zelfel, R. Bartsch, *Chlorine*. Ullmann's Encyclopedia of Chemical Industry, 2012. doi: 10.1002/14356007.a06_399.pub3.
- ⁷¹ S. A. M. Said, M. Waseuddin, D. S. A. Simakov, A review on solar reforming systems. *Renew. Sustain. Energy Rev.* **2016**, *59*, 149-159, doi: 10.1016/j.rser.2015.12.072.
- ⁷² K. Y. Khouzam, Electrolysis of Salt Water for Chlorine Production by Photovoltaic Power. *2008 IEEE Power and Energy Society General Meeting - Conversion and Delivery of Electrical Energy in the 21st Century*, Pittsburgh (USA), 2008, doi: 10.1109/PES.2008.4596165.
- ⁷³ E. J. Sheu, E. M. A. Mokheimer, A. F. Ghoniem, A review of solar methane reforming systems. *Int. J. Hydrogen Energy* **2015**, *40(38)*, 12929-12955, doi: 10.1016/j.ijhydene.2015.08.005.
- ⁷⁴ A. Giaconia, M. de Falco, G. Caputo, R. Grena, P. Tarquini, L. Marrelli, Solar Steam Reforming of Natural Gas for Hydrogen Production using Molten Salt Heat Carriers, *AIChE J.* **2008**, *54(7)*, 1932-1944, doi: 10.1002/aic.11510.
- ⁷⁵ Levelized Cost and Levelized Avoided Cost of New Generation Resources AEO2020. US Energy Information Administration (EIA) website, pdf available on: https://www.eia.gov/outlooks/aeo/pdf/electricity_generation.pdf. Accessed on 01/03/2020.
- ⁷⁶ M. Persico, G. Granucci, *Photochemistry. A Modern Theoretical Perspective*. Springer International Publishing AG: Cham (Switzerland), 2018. ISBN: 9783319899725.
- ⁷⁷ V. Balzani, P. Ceroni, A. Juris, *Photochemistry and Photophysics: Concepts, Research, Applications*. Wiley-VCH Verlag GmbH & Co. KGaA: Weinheim (Germany), 2015. ISBN: 9783527334797.
- ⁷⁸ M. A. Oturan, J.-J. Aaron, Advanced Oxidation Processes in Water/Wastewater Treatment: Principles and Applications. A Review. *Env. Sci. Technol.* **2014**, *44*, 2577-2641, doi: 10.1080/10643389.2013.829765.
- ⁷⁹ J. Hagen, *Industrial Catalysis*, 2nd ed. Wiley-VCH Verlag GmbH & Co. KGaA: Weinheim (Germany), 2006. ISBN: 9783527311446.
- ⁸⁰ H. Kisch, *Semiconductor photocatalysis*. Wiley-VCH Verlag GmbH & Co. KGaA: Weinheim (Germany), 2014. ISBN: 9783527335534.
- ⁸¹ Y. Xu, M. A. A. Schoonen, The absolute energy positions of conduction and valence bands of selected semiconducting minerals. *Am. Min.* **2000**, *85*, 543-556, doi: 10.2138/am-2000-0416.
- ⁸² R. E. Eisberg, R. Resnick, *Quantum Physics: Of Atoms, Molecules, Solids, Nuclei and Particles*, 2nd ed. John Wiley & Sons: New York (USA), 1985. ISBN: 9788126508181.
- ⁸³ A. J. Nozik, R. Memming, Physical Chemistry of Semiconductor-Liquid Interfaces. *J. Phys. Chem.* **1996**, *100*, 13061-13078, doi: 10.1021/jp953720e.
- ⁸⁴ K. Sivula, R. van der Krol, Semiconducting materials for photoelectrochemical energy conversion. *Nat. Rev. Mater.* **2016**, *1*, 15010, doi: 10.1038/natrevmats.2015.10.
- ⁸⁵ N. Sota, Semiconductor Photoelectrodes in *Electrochemistry at Material and Semiconductors Electrodes*. Elsevier Science B.V.: Amsterdam (The Netherlands), 1998. ISBN: 9780444828064.
- ⁸⁶ T. Hisatomi, K. Domen, Recent advances in semiconductors for photocatalytic and photoelectrochemical water splitting. *Chem. Soc. Rev.* **2014**, *43*, 7520-7535, doi: 10.1039/c3cs60378d.
- ⁸⁷ Liwu Zhang, Hanan H. Mohamed, Ralf Dillert, Detlef Bahnemann, Kinetics and mechanisms of charge transfer processes in photocatalytic systems: A review. *J. Photochem. Photobiol. C* **2012**, *13*, 263-276, doi: 10.1016/j.jphotochemrev.2012.07.002.
- ⁸⁸ F. Le Formal, S. R. Pendlebury, M. Cornuz, S. D. Tilley, M. Gratzel, J. R. Durrant, Back Electron-Hole Recombination in Hematite Photoanodes for Water Splitting. *J. Am. Chem. Soc.* **2014**, *136*, 2564-2574, doi: 10.1021/ja412058x J.
- ⁸⁹ M. S. Prévot, X. A. Jeanbourquin, W. S. Bourée, F. Abdi, D. Friedrich, R. van de Krol, N. Guijarro, F. Le Formal, K. Sivula, Evaluating Charge Carrier Transport and Surface States in CuFeO₂ Photocathodes. *Chem. Mater.* **2017**, *29*, 4952-4962, doi: 10.1021/acs.chemmater.7b01284.
- ⁹⁰ F. F. Abdi, R. van de Krol, Nature and Light Dependence of Bulk Recombination in Co-PiCatalyzed BiVO₄ Photoanodes. *J. Phys. Chem. C* **2012**, *116*, 9398-9404, doi: 10.1021/jp3007552.
- ⁹¹ J. Yan, G. Wu, N. Guan, L. Li, Z. Li, X. Cao, Understanding the effect of surface/bulk defects on the photocatalytic activity of TiO₂: anatase versus rutile. *Phys. Chem. Chem. Phys.* **2013**, *15*, 10978-10988, doi: 10.1039/c3cp50927c.
- ⁹² I.E. Den Besten, M. Qasim, Photocatalytic oxidation of ammonia on zinc oxide catalysts. *J. Catal.* **1964**, *3*, 387-389, doi:10.1016/0021-9517(64)90044-2.
- ⁹³ K. Tanaka, G. Blyholder, Photocatalytic Reaction on Zinc Oxide. II. Oxidation of Carbon Monoxide with Nitrous Oxide and Oxygen. *J. Phys. Chem.* **1972**, *76*, 1807-1814, doi:10.1021/j100657a003.
- ⁹⁴ M.R. Hoffmann, S.T. Martin, W. Choi, D.W. Bahnemann, Environmental Applications of Semiconductor Photocatalysis. *Chem. Rev.* **1995**, *95*, 69-96, doi:10.1021/cr00033a004.
- ⁹⁵ J. Herrmann, Heterogeneous photocatalysis: fundamentals and applications to the removal of various types of aqueous pollutants. *Catal. Today* **1999**, *53*, 115-129, doi: 10.1016/S0920-5861(99)00107-8.

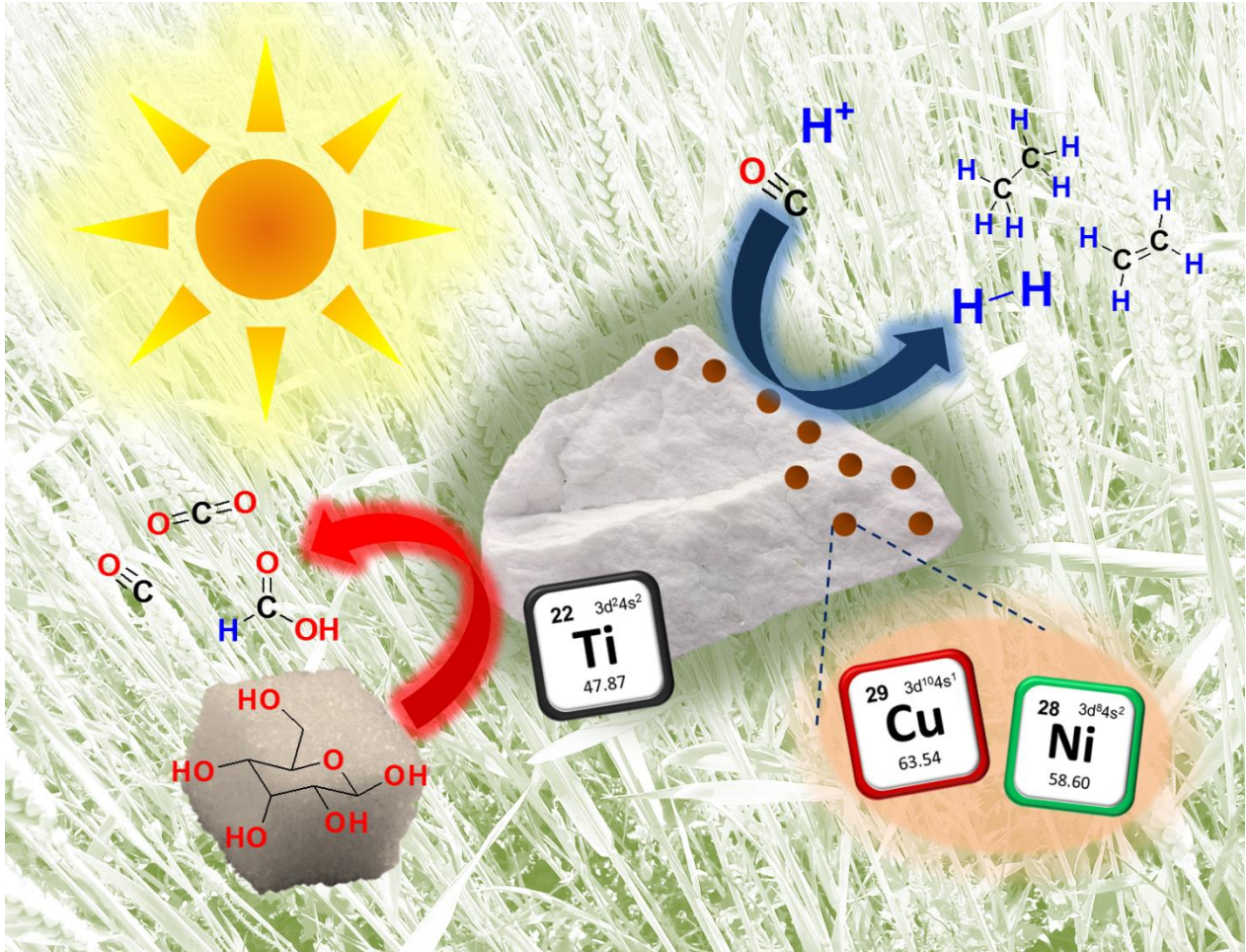
- ⁹⁶ R. Fagan, D.E. McCormack, D.D. Dionysiou, S.C. Pillai, A review of solar and visible light active TiO₂ photocatalysis for treating bacteria, cyanotoxins and contaminants of emerging concern. *Mater. Sci. Semicond. Process.* **2016**, *42*, 2-14, doi:10.1016/j.mssp.2015.07.052.
- ⁹⁷ Y. Boyjoo, H. Sun, J. Liu, V.K. Pareek, S. Wang, A review on photocatalysis for air treatment: From catalyst development to reactor design. *Chem. Eng. J.* **2017**, *310*, 537-559, doi:10.1016/j.cej.2016.06.090.
- ⁹⁸ A. Fujishima, X. Zhang, D.A. Tryk, Surface Science Reports TiO₂ photocatalysis and related surface phenomena. *Surf. Sci. Rep.* **2008**, *63*, 515-582, doi:10.1016/j.surfrep.2008.10.001.
- ⁹⁹ A. Mills, A. Lepre, N. Elliott, S. Bhopal, I.P. Parkin, S.A. O'Neill. Characterisation of the photocatalyst Pilkington Activ™: A reference film photocatalyst? *J. Photochem. Photobiol. A* **2003**, *160*, 213-224, doi:10.1016/S1010-6030(03)00205-3.
- ¹⁰⁰ K. Sunada, T. Watanabe, K. Hashimoto, Bactericidal Activity of Copper-Deposited TiO₂ Thin Film under Weak UV Light Illumination. *Environ. Sci. Technol.* **2003**, *37*, 4785-4789, doi:10.1021/es034106g.
- ¹⁰¹ E. Quagliarini, F. Bondioli, G.B. Goffredo, C. Cordoni, P. Munafò, Self-cleaning and de-polluting stone surfaces: TiO₂ nanoparticles for limestone. *Constr. Build. Mater.* **2012**, *37*, 51-57, doi:10.1016/j.conbuildmat.2012.07.006.
- ¹⁰² A. Fujishima, K. Honda, Electrochemical Photolysis of Water at a Semiconductor Electrode. *Nature* **1972**, *238*, 37-38, doi: 10.1038/238037a0.
- ¹⁰³ M.S. Prévot, K. Sivula, Photoelectrochemical Tandem Cells for Solar Water Splitting. *J. Phys. Chem. C* **2013**, *117*, 17879-17893, doi:10.1021/jp405291g.
- ¹⁰⁴ Gibbs free energy of reaction were calculated as follow: $\Delta_r G_{25^\circ C}^\circ = \left(\sum_{i=0}^n y_i \Delta_f G_{25^\circ C, i}^{oP} \right) - \left(\sum_{i=0}^n x_i \Delta_f G_{25^\circ C, i}^{oR} \right)$, where $\Delta_f G_{25^\circ C, i}^{oP}$ is the Gibbs free energy of formation of the *i*th reaction product, $\Delta_f G_{25^\circ C, i}^{oR}$ is the free Gibbs energy of formation of the *i*th reaction reagent, while *y_i* and *x_i* are the stoichiometric coefficient of, respectively, the *i*th product and *i*th reagent. The Gibbs free energy of formation are taken from: D.R. Lide, Grace Baysinger, Lev I. Berger, Robert N. Goldberg, Henry V. Kehiaian, Kozo Kuchitsu, Gerd Rosenblatt, Dana L. Roth, Daniel Zwillingner. Thermochemistry, electrochemistry and kinetics. In *CRC Handbook of Chemistry and Physics*, 6th ed., CRC press: Boca Raton (USA), 2005. ISBN: 9780849332043.
- ¹⁰⁵ T. Kawai, T. Sakata, Conversion of carbohydrate into hydrogen fuel by a photocatalytic process. *Nature* **1980**, *286*, 474-476, doi:10.1038/286474a0.
- ¹⁰⁶ D.W. Wakerley, M.F. Kuehnel, K.L. Orchard, K.H. Ly, T.E. Rosser, E. Reisner, Solar-driven reforming of lignocellulose to H₂ a CdS/CdO_x photocatalyst. *Nat. Energy* **2017**, *2*, 17021, doi:10.1038/nenergy.2017.21.
- ¹⁰⁷ X. Chang, T. Wang, J. Gong, CO₂ photo-reduction: insights into CO₂ activation and reaction on surfaces of photocatalysts. *Energy Environ. Sci.* **2016**, *9*, 2177-2196, doi: 10.1039/c6ee00383d.
- ¹⁰⁸ E. Kalamaras, M.M. Maroto-Valer, M. Shao, J. Xuan, H. Wang, Solar carbon fuel via photoelectrochemistry. *Catal. Today* **2018**, *317*, 56-75, doi:10.1016/j.cattod.2018.02.045.
- ¹⁰⁹ A. Steingrube, P. Voll, Selecting CO₂ Sources for CO₂ Utilization by Environmental-Merit- Order Curves, *Environ. Sci. Technol.* **2016**, *50*(3), 1093-1101, doi:10.1021/acs.est.5b03474.
- ¹¹⁰ J.-C. Wang, H.-C. Yao, Z.-Y. Fan, L. Zhang, J.-S. Wang, S.-Q. Zang, Z.-J. Li, Indirect Z-Scheme BiOI/g-C₃N₄ Photocatalysts with Enhanced Photoreduction CO₂ Activity under Visible Light Irradiation. *ACS Appl. Mater. Interfaces* **2016**, *8*, 3765-3775, doi: 10.1021/acsami.5b09901.
- ¹¹¹ U. Kang, S. K. Choi, Dong Jin Ham, Sang Min Ji, W. Choi, D. S. Han, A. Abdel-Wahab, H. Park, Photosynthesis of formate from CO₂ and water at 1% energy efficiency via copper iron oxide catalysis. *Energy Environ. Sci.* **2015**, *8*, 2638-2643, doi: 10.1039/c5ee01410g.
- ¹¹² K. Maeda, A. Xiong, T. Yoshinaga, T. Ikeda, N. Sakamoto, T. Hisatomi, M. Takashima, D. Lu, M. Kanehara, T. Setoyama, T. Teranishi, K. Domen, Photocatalytic Overall Water Splitting Promoted by Two Different Cocatalysts for Hydrogen and Oxygen Evolution under Visible Light. *Angew. Chem.* **2010**, *122*, 4190-4193, doi: 10.1002/anie.201001259.
- ¹¹³ V. M. Daskalaki, D. I. Kondarides, Efficient production of hydrogen by photo-induced reforming of glycerol at ambient conditions. *Catal. Today* **2009**, *144*, 75-80, doi:10.1016/j.cattod.2008.11.009.
- ¹¹⁴ G. L. Chiarello, L. Forni, E. Sellì, Photocatalytic hydrogen production by liquid- and gas-phase reforming of CH₃OH over flame-made TiO₂ and Au/TiO₂. *Catal. Today* **2009**, *144*, 69-74, doi:10.1016/j.cattod.2009.01.023.
- ¹¹⁵ R. Mazzaro, S. Boscolo Bibi, M. Natali, G. Bergamini, V. Morandi, P. Ceroni, A. Vomiero. Hematite nanostructures: An old material for a new story. Simultaneous photoelectrochemical oxidation of benzylamine and hydrogen production through Ti doping. *Nano Energy* **2019**, *61*, 36-46, doi: 10.1016/j.nanoen.2019.04.013.
- ¹¹⁶ I. Sopyan, M. Watanabe, S. Murasawa, K. Hashimoto, A. Fujishima, An efficient TiO₂ thin-film photocatalyst: photocatalytic properties in gas-phase acetaldehyde degradation. *J. Photochem. Photobiol. A* **1996**, *98*, 79-86, doi: 10.1016/1010-6030(96)04328-6.
- ¹¹⁷ J. Kou, Z. Li, Y. Guo, J. Gao, M. Yang, Z. Zou, Photocatalytic degradation of polycyclic aromatic hydrocarbons in GaN:ZnO solid solution-assisted process: Direct hole oxidation mechanism. *J. Mol. Catal. A* **2010**, *325*, 48-54, doi: 10.1016/j.molcata.2010.03.029.

- ¹¹⁸ B. Gomez-Ruiz, P. Ribao, N. Diban, M. J. Rivero, I. Ortiz, A. Urriaga, Photocatalytic degradation and mineralization of perfluorooctanoic acid (PFOA) using a composite TiO₂-rGO catalyst. *J. Hazard. Mater.* **2018**, *344*, 950-957, doi: 10.1016/j.jhazmat.2017.11.048.
- ¹¹⁹ S. Afzal, W.A. Daoud, S.J. Langford, Photostable Self-Cleaning Cotton by a Copper(II) Porphyrin/TiO₂ Visible-Light Photocatalytic System. *ACS Appl. Mater. Interfaces* **2013**, *5*, 4753-4759, doi: 10.1021/am400002k.
- ¹²⁰ B.S. Boroujeny, A. Afshar, A. Dolati, Photoactive and self-cleaning TiO₂-SiO₂ thin films on 316L stainless steel. *Thin Solid Films* **2012**, *520*, 6355-6360, doi: 10.1016/j.tsf.2012.03.051.
- ¹²¹ X. Chen, S. S. Mao, Titanium Dioxide Nanomaterials: Synthesis, Properties, Modifications, and Applications. *Chem. Rev.* **2007**, *107*, 2891-2959, doi: 10.1021/cr0500535.
- ¹²² Y. Ma, X. Wang, Y. Jia, Xiaobo Chen, H. Han, C. Li, Titanium Dioxide-Based Nanomaterials for Photocatalytic Fuel Generations. *Chem. Rev.* **2014**, *114*, 9987-10043, doi: 10.1021/cr500008u.
- ¹²³ J. Schneider, M. Matsuoka, M. Takeuchi, J. Zhang, Y. Horiuchi, M. Anpo, D. W. Bahnemann, Understanding TiO₂ Photocatalysis: Mechanisms and Materials. *Chem. Rev.* **2014**, *114*, 9919-9986, doi: 10.1021/cr5001892.
- ¹²⁴ X. Zhang, J. Qin, Y. Xue, P. Yu, B. Zhang, L. Wang, R. Liu, Effect of aspect ratio and surface defects on the photocatalytic activity of ZnO nanorods. *Sci. Rep.* **2014**, *4*, 4596, doi: 10.1038/srep04596.
- ¹²⁵ H. Tan, Z. Zhao, W.-B. Zhu, E. N. Coker, B. Li, M. Zheng, W. Yu, H. Fan, Z. Sun, Oxygen Vacancy Enhanced Photocatalytic Activity of Perovskite SrTiO₃. *ACS Appl. Mater. Interfaces* **2014**, *6*, 19184-19190, doi: 10.1021/am5051907.
- ¹²⁶ K. Shimura, S. Kato, T. Yoshida, H. Itoh, T. Hattori, H. Yoshida, Photocatalytic Steam Reforming of Methane over Sodium Tantalate. *J. Phys. Chem. C* **2010**, *114*, 3493-3503, doi: 10.1021/jp902761x.
- ¹²⁷ A. Primo, T. Marino, A. Corma, R. Molinari, H. García, Efficient Visible-Light Photocatalytic Water Splitting by Minute Amounts of Gold Supported on Nanoparticulate CeO₂ Obtained by a Biopolymer Templating Method. *J. Am. Chem. Soc.* **2011**, *133*, 6930-6933, doi: 10.1021/ja2011498.
- ¹²⁸ I. M. Szilágyi, B. Fórizs, O. Rosseler, Á. Szegedi, P. Németh, P. Király, G. Tárkányi, B. Vajna, K. Varga-Josepovits, K. László, A. L. Tóth, P. Baranyai, M. Leskelä, WO₃ photocatalysts: Influence of structure and composition. *J. Catal.* **2012**, *294*, 119-127 doi:10.1016/j.jcat.2012.07.013.
- ¹²⁹ D. W. Wakerley, M. F. Kuehnel, K. L. Orchard, K. H. Ly, T. E. Rosser, E. Reisner, Solar-driven reforming of lignocellulose to H₂ a CdS/CdO_x photocatalyst. *Nat. Energy* **2017**, *2*, 17021, doi: 10.1038/nenergy.2017.21.
- ¹³⁰ A. Kudo, M. Sekizawa. Photocatalytic H₂ evolution under visible light irradiation on Ni-doped ZnS photocatalyst. *Chem. Comm.* **2000**, 1371-1372, doi: 10.1039/b003297.
- ¹³¹ S. Yang, Y. Gong, J. Zhang, L. Zhan, L. Ma, Z. Fang, R. Vajtai, X. Wang, P. M. Ajayan, Exfoliated Graphitic Carbon Nitride Nanosheets as Efficient Catalysts for Hydrogen Evolution Under Visible Light. *Adv. Mater.* **2013**, *25*, 2452-2456, doi: 10.1002/adma.201204453.
- ¹³² M. Hara, G. Hitoki, T. Takata, J. N. Kondo, H. Kobayashi, K. Domen, TaON and Ta₃N₅ as new visible light driven photocatalysts. *Catal. Today* **2003**, *78*, 555-560, doi: 10.1016/S0920-5861(02)00354-1.
- ¹³³ C. R. Lhermitte, J. G. Verwer, B. M. Bartlett. Improving the stability and selectivity for the oxygen-evolution reaction on semiconducting WO₃ photoelectrodes with a solidstate FeOOH catalyst. *J. Mater. Chem. A*, **2016**, *4*, 2960-2968, doi: 10.1039/C5TA04747A.
- ¹³⁴ S. Kishore Pilli, T. E. Furtak, L. D. Brown, T. G. Deutsch, J. A. Turner, A. M. Herring, Cobalt-phosphate (Co-Pi) catalyst modified Mo-doped BiVO₄ photoelectrodes for solar water oxidation. *Energy Environ. Sci.* **2011**, *4*, 5028-5034, doi: 10.1039/c1ee02444b.
- ¹³⁵ A. Paracchino, N. Mathews, T. Hisatomi, M. Stefiik, S. D. Tilley, M. Grätzel, Ultrathin films on copper(I) oxide water splitting photocathodes: a study on performance and stability. *Energy Environ. Sci.* **2012**, *5*, 8673-8681, doi: 10.1039/c2ee22063f.
- ¹³⁶ M. S. Prévot, N. Guijarro, K. Sivula. Enhancing the Performance of a Robust Sol-Gel-Processed p-Type Delafossite CuFeO₂ Photocathode for Solar Water Reduction. *ChemSusChem* **2015**, *8*, 1359-1367, doi: 10.1002/cssc.201403146.
- ¹³⁷ Néstor Guijarro, Mathieu S. Prévot, Xiaoyun Yu, Xavier A. Jeanbourquin, Pauline Borno, Wiktor Bourée, Melissa Johnson, Florian Le Formal, Kevin Sivula, A Bottom-Up Approach toward All-Solution-Processed High-Efficiency Cu(In,Ga)S₂ Photocathodes for Solar Water Splitting. *Adv. Energy Mater.* **2016**, *6*, 1501949, doi: 10.1002/aenm.201501949.
- ¹³⁸ C. Liu, J. Sun, J. Tang, P. Yang, Zn-Doped p-Type Gallium Phosphide Nanowire Photocathodes from a Surfactant-Free Solution Synthesis. *Nano Lett.* **2012**, *12*, 5407-5411, doi: 10.1021/nl3028729.
- ¹³⁹ X. Yu, M. S. Prévot, N. Guijarro, K. Sivula, Self-assembled 2D WSe₂ thin films for photoelectrochemical hydrogen production. *Nat. Commun.* **2015**, *6*, 7596, doi: 10.1038/ncomms8596.
- ¹⁴⁰ J. Li, N. Wu, Semiconductor-based photocatalysts and photoelectrochemical cells for solar fuel generation: a review. *Catal. Sci. Technol.* **2015**, *5*, 1360-1384, doi: 10.1039/c4cy00974f.

- ¹⁴¹ E. Kusmierek, A CeO₂ semiconductor as a photocatalytic and photoelectrocatalytic material for the remediation of pollutants in industrial wastewater: A review. *Catalysts* **2020**, *10*, 1435, doi:10.3390/catal10121435.
- ¹⁴² J. Li, N. Wu, Semiconductor-based photocatalysts and photoelectrochemical cells for solar fuel generation: a review. *Catal. Sci. Technol.* **2015**, *5*, 1360-1384, doi: 10.1039/c4cy00974f.
- ¹⁴³ Y. Li, W. Xie, X. Hu, G. Shen, X. Zhou, Y. Xiang, X. Zhao, P. Fang, Comparison of dye photodegradation and its coupling with light-to-electricity conversion over TiO₂ and ZnO. *Langmuir* **2010**, *26*, 591-597, doi:10.1021/la902117c.
- ¹⁴⁴ W. Sun, S. Zhang, C. Wang, Z. Liu, Z. Mao, Effects of cocatalyst and calcination temperature on photocatalytic hydrogen evolution over BaTi₄O₉ powder synthesized by the polymerized complex method. *Catal. Letters* **2008**, *123*, 282-288, doi:10.1007/s10562-008-9420-x.
- ¹⁴⁵ S. Liu, J. Yu, M. Jaroniec, Anatase TiO₂ with Dominant High-Energy {001} Facets: Synthesis, Properties, and Applications. *Chem. Mater.* **2011**, *23*, 4085-4093, doi:10.1021/cm200597m.
- ¹⁴⁶ N. Kislov, J. Lahiri, H. Verma, D.Y. Goswami, E. Stefanakos, M. Batzill. Photocatalytic degradation of methyl orange over single crystalline ZnO: Orientation dependence of photoactivity and photostability of ZnO. *Langmuir* **2009**, *25*, 3310-3315, doi:10.1021/la803845f.
- ¹⁴⁷ D. Liu, Y. Lv, M. Zhang, Y. Liu, Y. Zhu, R. Zong, Y. Zhu, Defect-related photoluminescence and photocatalytic properties of porous ZnO nanosheets. *J. Mater. Chem. A* **2014**, *2*, 15377-15388, doi:10.1039/c4ta02678k.
- ¹⁴⁸ H. Tan, Z. Zhao, W. Zhu, E.N. Coker, B. Li, M. Zheng, W. Yu, H. Fan, Z. Sun, Oxygen Vacancy Enhanced Photocatalytic Activity of Pervoskite SrTiO₃. *ACS Appl. Mater. Interfaces* **2014**, *6*, 19184-19190, doi:10.1021/am5051907.
- ¹⁴⁹ L. Liu, F. Gao, H. Zhao, Y. Li, Tailoring Cu valence and oxygen vacancy in Cu/TiO₂ catalysts for enhanced CO₂ photoreduction efficiency. *Appl. Catal. B* **2013**, *134-135*, 349-358, doi:10.1016/j.apcatb.2013.01.040.
- ¹⁵⁰ H. Wang, L. Zhang, Z. Chen, J. Hu, S. Li, Z. Wang, J. Liu, X. Wang, Semiconductor heterojunction photocatalysts: Design, construction, and photocatalytic performances. *Chem. Soc. Rev.* **2014**, *43*, 5234-5244, doi:10.1039/c4cs00126e.
- ¹⁵¹ S.J.A. Moniz, S.A. Shevlin, D.J. Martin, Z.X. Guo, J. Tang, Visible-light driven heterojunction photocatalysts for water splitting—a critical review. *Energy Environ. Sci.* **2015**, *8*, 731-759, doi: 10.1039/c4ee03271c.
- ¹⁵² P. Cendula, M.T. Mayer, J. Luo, M. Grätzel, Sustainable Energy & Fuels Elucidation of photovoltage origin and charge transport in Cu₂O heterojunctions for solar energy conversion. *Sustain. Energ. Fuels* **2019**, *3*, 2633-2641, doi:10.1039/c9se00385a.
- ¹⁵³ T. Uddin, Y. Nicolas, T. Toupance, L. Servant, M.M. Mu, H. Kleebe, J. Ziegler, W. Jaegermann, Nanostructured SnO₂-ZnO Heterojunction Photocatalysts Showing Enhanced Photocatalytic Activity for the Degradation of Organic Dyes. *Inorg. Chem.* **2012**, *51*, 7764-7773, doi:10.1021/ic300794j.
- ¹⁵⁴ V.M. Daskalaki, M. Antoniadou, G. Li Puma, D.I. Kondarides, P. Lianos, Solar Light-Responsive Pt/CdS/TiO₂ Photocatalysts for Hydrogen Production and Simultaneous Degradation of Inorganic or Organic Sacrificial Agents in Wastewater. *Env. Sci. Technol.* **2010**, *44*, 7200-7205, doi: 10.1021/es9038962.
- ¹⁵⁵ N. Guijarro, M.S. Prévot, K. Sivula, Surface modification of semiconductor photoelectrodes. *Phys. Chem. Chem. Phys.* **2015**, *17*, 15655-15674, doi:10.1039/c5cp01992c.
- ¹⁵⁶ A. Paracchino, V. Laporte, K. Sivula, M. Grätzel, E. Thimsen, Highly active oxide photocathode for photoelectrochemical water reduction. *Nat. Mater.* **2011**, *10*, 456-461, doi: doi.org/10.1038/nmat3017.
- ¹⁵⁷ J. Yang, D. Wang, H. Han, C. Li, Roles of cocatalysts in photocatalysis and photoelectrocatalysis. *Acc. Chem. Res.* **2013**, *46*, 1900-1909, doi:10.1021/ar300227e.
- ¹⁵⁸ V. Subramanian, E.E. Wolf, P. V Kamat, B. Engineering, V. Uni, N. Dame, Catalysis with TiO₂/Gold Nanocomposites. Effect of Metal Particle Size on the Fermi Level Equilibration. *J. Am. Chem. Soc.* **2004**, *126*, 4943-4950, doi:10.1021/ja0315199.
- ¹⁵⁹ A. Tanaka, K. Hashimoto, H. Kominami, Visible light-induced hydrogen and oxygen formation over Pt/Au/WO₃ photocatalyst utilizing two types of photoabsorption due to surface plasmon resonance and band-gap excitation. *J. Am. Chem. Soc.* **2014**, *136*, 586-589, doi:10.1021/ja410230u.
- ¹⁶⁰ M. Baek, M. Zafar, S. Kim, D.-H. Kim, C.-W. Jeon, J. Lee, K. Yong, Enhancing Durability and Photoelectrochemical Performance of the Earth Abundant Ni-Mo/TiO₂/CdS/CIGS Photocathode under Various pH Conditions. *ChemSusChem* **2018**, *11*, 3679-3688, doi: 10.1002/cssc.201801211.
- ¹⁶¹ D. K. Zhong, M. Cornuz, K. Sivula, M. Grätzel, D. R. Gamelin, Photo-assisted electrodeposition of cobalt-phosphate (Co-Pi) catalyst on hematite photoanodes for solar water oxidation. *Energy Environ. Sci.* **2011**, *4*, 1759-1764, doi: 10.1039/c1ee01034d.
- ¹⁶² A. Li, T. Wang, X. Chang, Z.J. Zhao, C. Li, Z. Huang, P. Yang, G. Zhou, J. Gong, Tunable syngas production from photocatalytic CO₂ reduction with mitigated charge recombination driven by spatially separated cocatalysts. *Chem. Sci.* **2018**, *9*, 5334-5340, doi:10.1039/c8sc01812j.
- ¹⁶³ G.L. Chiarello, M.H. Aguirre, E. Selli, Hydrogen production by photocatalytic steam reforming of methanol on noble metal-modified TiO₂. *J. Catal.* **2010**, *273*, 182-190, doi:10.1016/j.jcat.2010.05.012.

-
- ¹⁶⁴ Q. Liu, Y. Zhou, Z. Tian, X. Chen, J. Gao, Z. Zou, Zn₂GeO₄ crystal splitting toward sheaf-like, hyperbranched nanostructures and photocatalytic reduction of CO₂ into CH₄ under visible light after nitridation. *J. Mater. Chem.* **2012**, *22*, 2033-2038, doi:10.1039/c1jm14122h.
- ¹⁶⁵ Z. Liu, Z. Zhao, M. Miyauchi, Efficient Visible Light Active CaFe₂O₄/WO₃ Based Composite Photocatalysts: Effect of Interfacial Modification. *J. Phys. Chem. C* **2009**, *113*, 17132-17137, doi: 10.1021/jp906195f.
- ¹⁶⁶ T.W. Kim, K.-S. Choi, Nanoporous BiVO₄ Photoanodes with Dual-Layer Oxygen Evolution Catalysts for Solar Water Splitting. *Science* **2014**, *343*, 990-994, doi: 10.1126/science.1246913.

CHAPTER 1: HYDROGEN PRODUCTION BY GLUCOSE PHOTOREFORMING WITH TiO₂-BASED PHOTOCATALYSTS



1. INTRODUCTION

1.1. THE POWER OF HYDROGEN

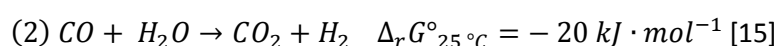
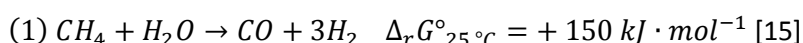
Hydrogen (H₂) is a low density and flammable gas currently used in chemical industry, mainly in ammonia (NH₃) synthesis, methanol (CH₃OH) synthesis and oil refining [1]. It has also been proposed as energy vector due to the possibility to directly produce electricity through highly efficient devices, namely fuel cells [2]. Besides the energy efficiency, modularity, static nature and prompt load can be ranked as advantageous features of fuel cell over other devices such as thermal engines or batteries [3]. Unfortunately, the utilization of hydrogen as energy vector suffers of important drawbacks:

1. Large-scale hydrogen availability [2]
2. Feasible storage and delivery methods [4]
3. Fuel cell expensiveness [5]
4. Safety issues in hydrogen handling [4]

Nonetheless, hydrogen can be indirectly used as fuel by the chemical conversion of less valuable substances into marketable fuels or fuel precursors [6]. An example is the thermocatalytic reduction of CO₂, a waste gas of human activities with a potential huge availability, into CH₃OH [7], methane (CH₄) [8] or carbon monoxide (CO) [9]. Hydrogen can be also used in the upgrading of other raw materials to valuable fuels or fuels additives, such as hydrodeoxygenation of vegetable oils [10] or bio-oils for biomass pyrolysis [11,12]. These approaches allow hydrogen to be converted into fuels directly usable into traditional thermal engine or burning equipment, avoiding the aforementioned issues of hydrogen storage and expensiveness of fuel cells. However, a large scale, feasible and cheap hydrogen source is still required in this scenario.

1.2. HYDROGEN PRODUCTION: STRATEGIES AND CHALLENGES

Currently 70 million tonnes of hydrogen are produced each year [13], mainly arising from fossil fuels (natural gas, coal, liquid hydrocarbons) [2]. Methane steam-reforming (MSR) is currently the leading technology in hydrogen production and consumes 6% of natural gas production [13]. The process relies on an endothermic high-temperature catalytic reaction (800-900 °C) that converts CH₄ into syngas, a mixture of H₂ and CO, (Reaction 1) followed by the exothermic catalytic conversion of CO through the water-gas shift reaction (WGSR) at lower temperature (200-350 °C) (Reaction 2) [14].



Several alternative processes have been developed, aiming improvement in energy efficiency, gas separation or hydrogen purity [4]. After the 1970s oil crisis, more attention has also been drawn to solid feedstocks such as coal, biomass or solid waste, which are abundant and less sensitive to market price changes, through

gasification technologies [16]. However, due to the high temperature involved in all of these processes, expensive and special equipment are often required, which increase the overall cost of the process [16]. Aqueous phase reforming (APR) has been proposed as alternative hydrogen production technology, operating at lower temperature (200-250 °C) but requiring higher pressure to maintain the liquid state (2-5 MPa) [17]. Another key advantage over the high-temperature reforming processes, is that non-vaporizable feedstock such as glucose [18], cellulose [19], raw biomass [20] as well as wet feedstock such as industrial wastewater [21], can be used. However, selected materials are required to handle high-pressure hydrogen [22]. Furthermore catalyst deactivation, reactants conversion, product selectivity and mass-transfer limitations are issues still affecting a large-scale application [17].

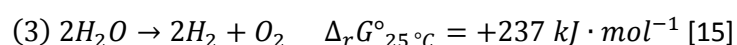
Electrocatalytic water-splitting is an interesting alternative to thermocatalytic processes because of:

1. High purity of produced hydrogen (> 99.8%) [23]
2. High energy efficiency (55-70%) [24]
3. Very mild operative conditions ($T < 90^{\circ}\text{C}$, $P < 2 \text{ MPa}$) [23]

The main drawback of this technology is the requirement of an expensive energy source (electricity), making electrolysis uncompetitive with fossil-based technologies, especially if solar or wind power are involved [25,26].

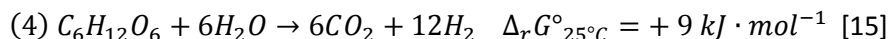
1.3. SOLAR-TO-HYDROGEN: THE PHOTOCATALYTIC APPROACH

An appealing alternative technology to water electrolysis is the photocatalytic water splitting, because still capable of operating in mild conditions ($T < 90^{\circ}\text{C}$), directly using sunlight as energy source, without the requirement of expensive electric energy [27]. In 1972 Honda and Fujishima observed a TiO_2 crystal to be able to split water into H_2 and O_2 upon irradiation of UV light on an electrochemical setup [28], opening the way for the photo(electro)chemical hydrogen production [29]. The efficiency of overall water splitting (Reaction 3) is however limited by the relatively large overpotential required for both hydrogen evolution reaction (HER) and oxygen evolution reaction (OER) [30], as well as by hydrogen and oxygen back reactions [31].



In 1980, Kawai and Sakata observed a remarkable improvement in hydrogen yield upon addition of an organic compound (carbohydrates) to the reaction medium, leading to faster oxidation kinetics because the facile oxidation of carbohydrates rather than water, and suppressing back reactions due to the lack of O_2 formation [32]. This reaction can be carried out with different organic substrates such as alcohols and polyols [33,34], organic acids [35,36], aldehydes [37], as well as more complex feedstock like fossil fuels [38], or lignocellulosic

biomass [39]. Since the complete reaction should yield CO₂ and H₂ (Reaction 4) thus resembling the thermocatalytic reforming [40,41], this reaction has been termed photoreforming [42].



Carbohydrates (i.e. glucose and cellulose) are an appealing class of organic substrates for photoreforming, because the higher intrinsic reactivity due to the large number of hydroxyl moiety [43] and the huge potential availability as relatively cheap feedstock [44].

Besides the choice of the reactant, the material design plays an important role in determining the effectiveness of the photoreforming process. Several semiconductor materials have been proposed as photocatalysts, such as strontium titanate (SrTiO₃) [45], tantalum oxynitride (TaON) [46], cadmium sulphide (CdS) [39] or graphitic carbon nitride (g-C₃N₄) [47]. Titanium dioxide (TiO₂) is certainly the most reported and studied due to its cheapness, earth-abundancy, safety, chemical and photochemical stability. This material exhibits four main crystal phases (anatase, rutile, TiO₂(B) and brookite), characterized by different physical and chemical properties [48]. The TiO₂ crystal phase strongly affects the photocatalytic activity: anatase is generally recognized as the most active one [43], due to the highest specific surface area [49] and the highest charge carrier mobility, which in turn reduces the recombination probability [50,51]. Two or more crystal phases in intimate contact, as in the case of the benchmark TiO₂ P25 (rutile-anatase mixture), are known to improve the charge carrier separation and lifetimes, thanks to the favourable band alignment [52], eventually improving the photoactivity [51]. The hydrogen yield can be remarkably increased by the addition of a co-catalyst [53,54], which acts by two mechanisms:

1. Photoexcited charge carrier sink, improving their lifetimes and reducing the recombination [55]
2. True active site, reducing the kinetic barrier for the reaction [56]

The co-catalyst usually involved in photoreforming affects the reduction pathway, thus extracting electrons from the photoexcited semiconductor (SC) [55] and acting on the hydrogen evolution reaction [56], as

pictured in Figure 1.

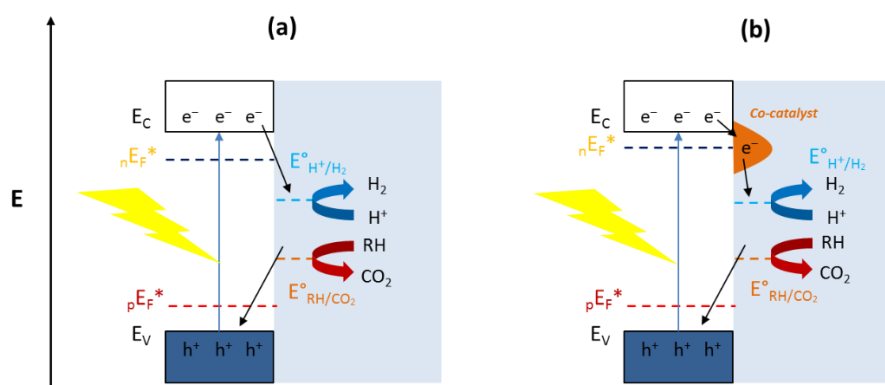


Figure 1. Energy band diagram of SC/reaction mixture interface in presence of organic electron donor (RH) (a) without and (b) with a co-catalyst. The energy levels are labelled according to the Preface section. Electron pseudo-Fermi level (nE_F^*) is shifted toward higher energy due to co-catalyst/SC band alignment according to [55].

Noble metals such as platinum (Pt) [57], palladium (Pd) [33] and gold (Au) [54] are reported to be effective co-catalysts, however their expensiveness makes them less appealing candidates for large-scale applications. Cheaper non-noble transition metals such as copper (Cu) [58] and nickel (Ni) [59] have been reported as alternative co-catalysts, maintaining a comparable activity with noble ones. Fujita *et al.* reported an improved hydrogen evolution activity, in order, $\text{CuO} > \text{NiO} > \text{CoO}_x$ on TiO_2 [60]. Besides the choice of the co-catalysts, also the loading technique plays an important role: Yoong *et al.* observed an increased photoactivity by loading CuO through precipitation rather than impregnation, because of the higher dispersion of the co-catalyst [61]. Alloying two metals was observed to be another effective approach to increase the photoactivity, thanks to the synergic role that the two involved metals can play each other [62], however such bimetallic systems usually contains at least one noble metal [63,64].

Finally, the co-catalyst affects also the selectivity of the photoreforming: the stoichiometric reaction yield H_2 and CO_2 , but in practice several side-products can be found, such as CO [65], oxygenated compounds (i.e. aldehydes) [66] or hydrocarbons [60]. Chiarello *et al.* found a decreased selectivity to CO and oxygenates, along with an increased H_2 yield, in order, $\text{Pt} > \text{Au} > \text{Ag}$ on TiO_2 [65], while Fujita *et al.* observed on CuO co-catalyst, the most active sample, the highest yield of CH_4 [60].

Some examples of TiO_2 -based photocatalysts modified with different co-catalysts are listed in Table 1.

Table 1. Examples of TiO₂-based photocatalysts used for photoreforming reactions.

Reference	Photocatalyst	Organic substrate	Reaction conditions	Comments
[57]	Pt/TiO ₂	Glycerol	40 – 60°C; 0 – 1.086 M glycerol; 0.66 – 2.66 g·L ⁻¹ photocatalyst; pH 3 – 10; Xe lamp; 3.79·10 ⁻⁷ Einstein·s ⁻¹	Effect of reaction parameters on activity.
[37]	Au/TiO ₂ ; 3-10 nm Au NPs	MeOH	r.t.; 1.0 M MeOH; 1.5 g·L ⁻¹ photocatalyst; pH 4 – 12; Xe lamp; light intensity not given	Effect of Au NPs size effect on activity and selectivity to CO
[58]	CuO/TiO ₂ ; 0-15% wt. CuO	EtOH	r.t.; 80% – 20% v/v EtOH; 0.34 g·L ⁻¹ photocatalyst; native pH; UVA lamp; 65 W·cm ⁻¹	Effect of CuO loading on activity
[63]	Pt, Pt ₃ Co, Pt ₃ Au, Pt ₃ Ni, Pt ₃ Cu on TiO ₂ and CdS	Lactic acid	r.t.; 10% v/v lactic acid; 0.2 g·L ⁻¹ photocatalyst; native pH; Xe lamp; light intensity not given	Effect of alloying metal on Pt co-catalyst on TiO ₂ and CdS
[67]	Pt, Pd, Au, Rh, Ag, Ru on TiO ₂	Glucose	30°C; 0 – 0.5 g·L ⁻¹ glucose; 0.25 g·L ⁻¹ photocatalyst; pH 1 – 13; high pressure Hg lamp; light intensity not given	Effect of reaction parameters, metal co-catalyst and catalyst thermal treatment on activity.
[32]	RuO ₂ /Pt/TiO ₂	Sucrose, Starch, Cellulose	r.t; 15 g·L ⁻¹ sucrose or 3 g·L ⁻¹ starch or a cutted cellulose filter; 7.5 g·L ⁻¹ photocatalyst; pH neutral or pH > 14 (NaOH 6 M); Xe lamp; light intensity not given	Effect of substrate and strong alkaline medium on activity.

1.4. AIM OF THE CHAPTER

The aim of this chapter is to study the activity and selectivity of glucose photoreforming with different TiO₂ materials and evaluate the effect of different non-noble metal oxide co-catalysts (CuO, NiO and their mixture) and their loading technique on the reaction performances. The reactivity results are then correlated to structural, optical and chemical properties of the synthesized materials. This work was performed in collaboration with the Chemical Plants and Industrial Chemistry Group, headed by Professor Ilenia Rossetti, of the University of Milan (Milan, Italy).

2. MATERIALS AND METHODS

2.1. REAGENTS

The following reagents were used as-received: P25 (TiO₂, Evonik), titanium (IV) oxysulphate sulphuric acid hydrate (TiOSO₄·xH₂O·yH₂SO₄, Ti assay > 29%, Sigma Aldrich), sodium hydroxide (NaOH, assay > 97%, Carlo Erba), copper nitrate trihydrate (Cu(NO₃)₂·3H₂O, assay > 99%, Sigma Aldrich), nickel nitrate trihydrate (Ni(NO₃)₂·6H₂O, assay > , Sigma Aldrich), 1,3-propanediol (C₃H₈O₂, assay > 98%, Sigma Aldrich), citric acid monohydrate (C₆H₈O₇·H₂O, assay > 99%, Sigma Aldrich) and glucose (C₆H₁₂O₆, assay > 99.5%, Sigma Aldrich).

2.2. SYNTHESIS

2.2.1. LAB-TiO₂ SYNTHESIS

Laboratory made TiO₂ was synthesized according to a previously reported procedure [68]. A 1.2 M TiOSO₄ solution was added dropwise to a beaker containing deionized water under vigorous stirring. The pH was kept constant at 7 by the addition of a 9 M NaOH aqueous solution. The as-obtained suspension was aged at 60°C for 20 hours, then vacuum filtered, washed with deionized water to remove dissolved ions and air-dried at 110°C for 18 hours. The dried product was finally annealed at 400°C for 4 hours (ramp: 2 °C·min⁻¹) in air flow (30 mL·min⁻¹). The sample is labelled LAB-TiO₂.

2.2.2. CO-CATALYST LOADING BY WETNESS IMPREGNATION.

CuO and NiO was loaded by wetness impregnation according to a previously reported procedure [69]. The metal precursors Cu(NO₃)₂·3H₂O and Ni(NO₃)₂·6H₂O were dissolved in deionized water and added dropwise to P25 powder to afford 1.0 wt. % and 0.5 wt. % metal loading for the monometallic and the bimetallic co-catalysts, respectively. The impregnated powder was air dried at 110°C for 18 hours and finally annealed at 400°C for 1 hour (ramp: 2 °C·min⁻¹) in air flow (30 mL·min⁻¹). The samples were labelled as follow:

1. ICuP25, 1.0 wt. % wt. loaded Cu
2. INiP25, 1.0 wt. % wt. loaded Ni
3. INiCuP25, 0.5 wt. % Cu and 0.5 wt. % Ni loaded

2.2.3. CO-CATALYST LOADING BY COMPLEX-ASSISTED PRECIPITATION

Complex-assisted precipitation was involved for CuO loading, according to a previously reported procedure [69]. The P25 powder was first dissolved in 200 mL of deionized water, then a solution of Cu(NO₃)₂·3H₂O with the organic ligand was added to the suspension, to afford a 1.0 wt.%. metal loading. A molar ligand/metal ratio of 3.0 was used with 1,3-propanediol, while 2.0 was used with citric acid. Then the pH of the solution was gradually risen up to 12, by the addition of a 0.5 M NaOH aqueous solution. After stirring for 1 hour the suspension, it was vacuum filtered, washed with deionized water to remove dissolved ions and residual

ligand, and air-dried at 110°C for 18 hours. Finally, the material was annealed at 400°C for 1 hour (ramp: 2 °C·min⁻¹) in air flow (30 mL·min⁻¹). The samples were labelled as follow:

1. DCuP25, 1.0 wt. % loaded copper and 1,3-propanediol as ligand
2. CCuP25, 1.0 wt. % loaded copper and citric acid as ligand

2.3. CHARACTERIZATIONS

The phase composition and crystallite size were measured by X-ray diffraction (XRD) using a Bruker D8 Advance DaVinci powder diffractometer using a sealed X-ray tube (copper anode; operating conditions, 40 kV and 40 mA) and a linear array detector (LynxEye), set to discriminate the Cu K α radiation, coupled with a Ni filter to completely remove the Cu K β component. Data scans were performed in the 2 θ range 5–90° with 0.02° step size and point-detector equivalent counting times of 5 s/step. Quantitative phase analysis and crystallite size determination were performed using the Rietveld method as implemented in the TOPAS v.5 program (Bruker AXS) using the fundamental parameters approach for line-profile fitting. The determination of the crystallite size was accomplished by the Double-Voigt approach and calculated as volume-weighted mean column heights based on integral breadths of peaks.

Specific surface area (SSA) was determined using nitrogen (N₂) physisorption with a TriStar II Plus (Micromeritics) analyzer. The samples were outgassed at 200°C in vacuum for 2 hours to clean the surface before the analysis. The N₂ adsorption-desorption isotherms were then acquired at – 196 °C and the SSA determined by the Brunauer-Emmet-Teller (BET) equation [70] fitted in the 0.04 – 0.3 P/P° range.

Sample reducibility was assessed through temperature-programmed reduction (TPR) with a lab-made equipment. The dried sample (50 mg) was heated from r.t. to 800 °C (ramp: 2 °C·min⁻¹) in a flow of 5% v/v H₂/Ar gas mixture (40 mL·min⁻¹). The outlet gases were pass through a MgClO₄ trap to remove humidity and analyzed by a Gow-Mac thermoconductivity detector (TCD).

Optical absorbance was measured through an integration sphere equipped Cary100 UV-vis spectrophotometer (Agilent). The spectra was reported through the Kubelka-Munk function (Equation 1), where R_{∞} is the reflectance at an infinite thick layer of the sample [71].

$$f(R_{\infty}) = \frac{(1 - R_{\infty})^2}{2R_{\infty}}$$

Equation 1. Kubelka-Munk function.

The bandgap (E_g) of the material was determined by the Tauc relation (Equation 2), where the Kubelka-Munk function ($f(R_{\infty})$) is used in place of the absorption coefficient (α), h the Plank constant ($6.626 \cdot 10^{-34}$ J·s), ν the photon frequency in s⁻¹, C a constant and E_g the bandgap energy. For direct allowed optical transition the exponent is set to $n = \frac{1}{2}$, while for indirect transitions is set to $n = 2$. The E_g was determined as intercept plotting $(f(R_{\infty})h\nu)^{1/n}$ vs $h\nu$ [72].

$$f(R_{\infty})hv = C(hv - E_g)^n$$

Equation 2. Tauc relation.

The Urbach energy (E_U), related to the density of states of defects [73], was assessed by the Urbach relation (Equation 3), where $f(R_{\infty})$ is used in place of the optical absorption coefficient (α), h the Plank constant ($6.626 \cdot 10^{-34}$ J·s), ν the photon frequency in s^{-1} , α_0 and E_0 are temperature-dependent constants.

$$f(R_{\infty}) = \alpha_0 \exp\left(\frac{h\nu - E_0}{E_U}\right)$$

Equation 3. Urbach relation.

The E_U is assessed from the near absorption-edge slope of $\ln(\alpha)$ vs $h\nu$ [74].

The morphology was examined through high-resolution transmission electron microscopy (HR-TEM), performed with a JOEL 3010-UHR microscope, operating at 300 kV. Digital microphotographs were acquired by a Gatan (2k x 2k)-pixel Ultrascan1000 CCD camera and processed by Gatan digital microphotograph. A copper grid coated with lacey carbon was used to support the powder samples.

Actual metal concentration of the sample was determined through flame atomic absorption spectroscopy (FAAS) with a PerkinElmer Analyts 100 analyzer. The samples were previously dissolved in boiling *aqua-regia* and the metal quantified by means of calibration curves from standard solutions.

2.4. REACTIVITY TESTS

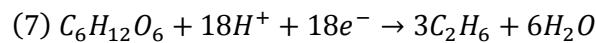
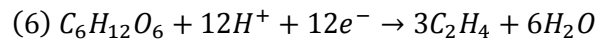
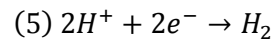
A high pressure photoreactor and optimized conditions previously reported for glucose photoreforming were used [75]. An AISI 316 stainless steel photoreactor with an internal capacity of 1.3 L and an axial UVA lamp (125 W) was used, with a spectral range from 254 nm to 364 nm and a light intensity ranged between 153 and 171 $W \cdot m^{-2}$, probed with a Delta OHM HD2012.2 photoradiometer. The vessel was filled with 1.2 L of the reaction mixture composed of 5 $g \cdot L^{-1}$ of glucose and 0.25 $g \cdot L^{-1}$ in deionized water, the stirred (400 rpm) at r.t. for 18 h to achieve a stable suspension. The system was outgassed with a N_2 flow for 15 minutes to remove dissolved air. The reaction was carried out at 80°C and 4 bar, for an overall time of 5 hours. The gaseous reaction mixture was sampled each 30 minutes and analyzed through an 7890 Agilent gas-chromatographer (GC), equipped with an HP Plot Q and molecular sieve (MS) packed columns, and a TCD. The product was quantified by means of calibration curves of H_2 , CO_2 , CO , CH_4 , ethane (C_2H_6) and ethylene (C_2H_4). The activity was expressed as turnover frequency (TOF), as reported in Equation 4, where mol_P are the detected moles of reaction product in the gas phase after 5 hours of reaction, m_{CAT} the mass of the used photocatalysts and τ the overall reaction time.

$$TOF = \frac{mol_P}{m_{CAT} \cdot \tau}$$

Equation 4. TOF determination.

The photoactivity was expressed as turnover frequency (TOF_{ph}) considering the total amount of photoexcited electrons required to run all the reductive pathways, namely two electrons for one H_2 molecule (Reaction 5), four electrons for one C_2H_4 molecule (Reaction 6) and six electrons for one C_2H_6 molecule (Reaction 7). m_{CAT} and τ are, as for TOF, the amount of used catalyst and the reaction time.

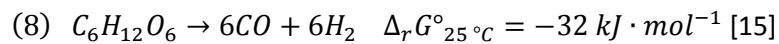
$$TOF_{ph} = \frac{mol_{H_2} \cdot 2 + mol_{C_2H_4} \cdot 4 + mol_{C_2H_6} \cdot 6}{m_{CAT} \cdot \tau}$$



The stoichiometric hydrogen-to-carbon oxides ratio ($S_{H/CO}$), was calculated from the moles of detected gas-phase products, as reported in Equation 5, taking in consideration the stoichiometry of Reaction 4 and Reaction 8.

$$S_{H/CO} = \frac{mol_{H_2}}{2 \cdot mol_{CO_2} + mol_{CO}}$$

Equation 5. $S_{H/CO}$ determination.



3. RESULTS AND DISCUSSION

3.1. BARE TiO₂ MATERIALS

The XRD analyses of the bare materials, namely LAB-TiO₂ and P25, are reported in Figure 2a. The LAB-TiO₂ is an anatase phase-pure material (ICDD PDF card no. 21-1272), with a crystallite size of 14 nm. Conversely, P25 is a mixture of anatase (89%) and rutile (11%) (ICDD PDF card no. 21-127), with an average crystallite size of 18 nm. The N₂ adsorption isotherms of the TiO₂-based photocatalysts (Figure 2b) revealed a hysteresis loop at $P/P^0 > 0.3$, feature characteristic of mesoporous materials (type IV isotherm according to IUPAC classification). Furthermore, the hysteresis loop close to $P/P^0 = 1.0$ suggested some macropores (type II isotherm according to IUPAC classification) to be present on these materials as well [76]. The SSA calculated with the BET method are reported to be 101 m²·g⁻¹ and 50 m²·g⁻¹ for LAB-TiO₂ and P25, respectively, in good agreement with the average crystallite size detected by XRD.

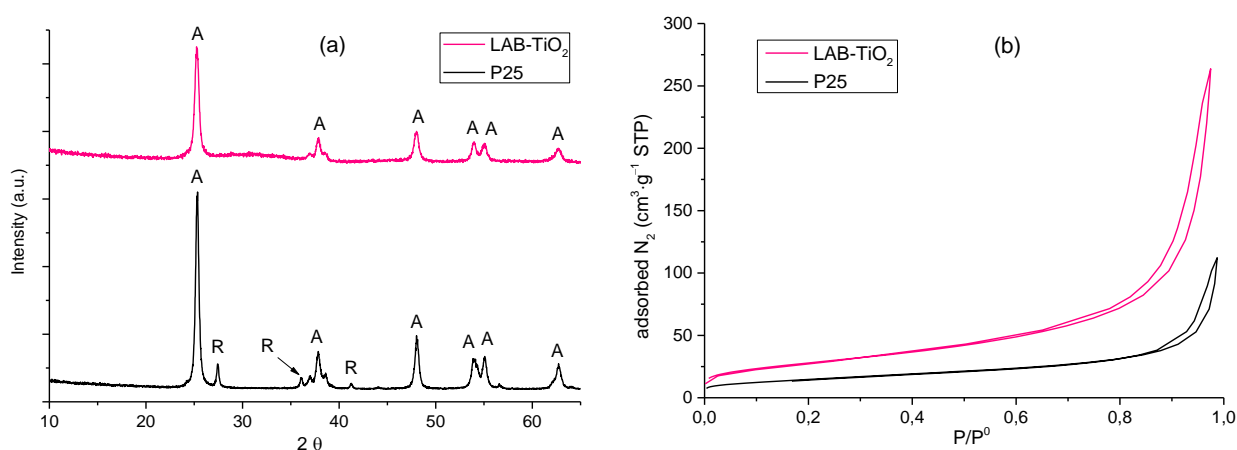


Figure 2. (a) XRD diffractograms of LAB-TiO₂ and P25; A = anatase and R = rutile. (b) N₂ physisorption isotherms of LAB-TiO₂ and P25.

The UV-vis spectra in Figure 3a reveals a blue shift of the absorption edge of LAB-TiO₂ compared to P25, further confirmed by the narrower indirect E_g of the two materials: 3.26 eV vs 3.01 eV, respectively (Figure 3b). Such blue shift can be related both to the presence of rutile in P25, which is known to have a narrower E_g than anatase [48], and to the smaller crystallites in LAB-TiO₂, potentially being affected by quantum confinement effects [77].

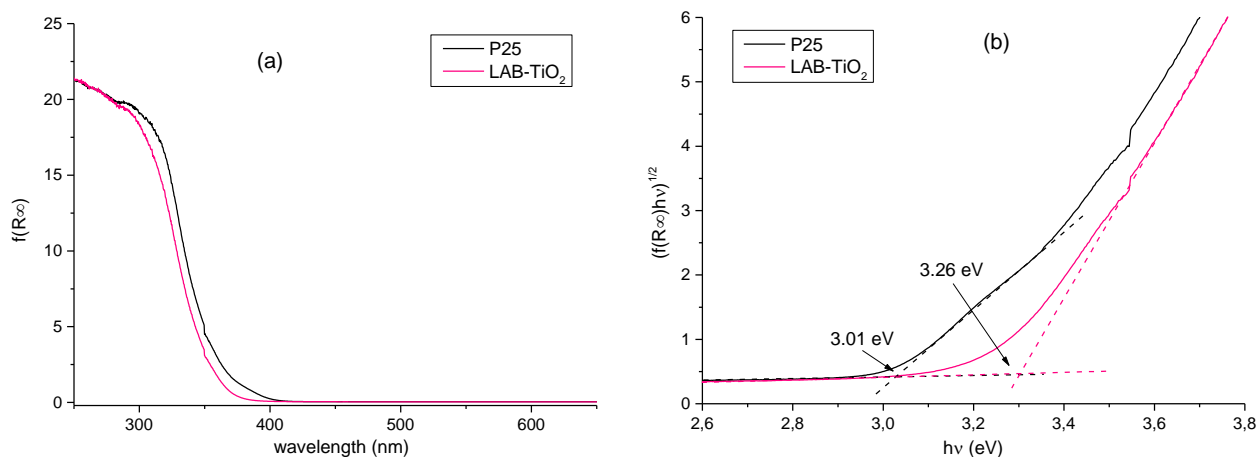


Figure 3. (a) UV-vis spectra of P25 and LAB-TiO₂. (b) Tauc plots of P25 and LAB-TiO₂.

The logarithmic plot of the absorption coefficient can give useful information regarding to the density of defect states, which in turn can affect the photoactivity by improving the recombination. The slope reciprocal of the linear part of the plot is termed Urbach Energy (E_U), and is related to intra-gap defect state density: the lower E_U , the narrower is such density [78]. The E_U assessed from Figure 4 is comparable for both samples (ca. 0.09 eV), suggesting a comparable defect state density.

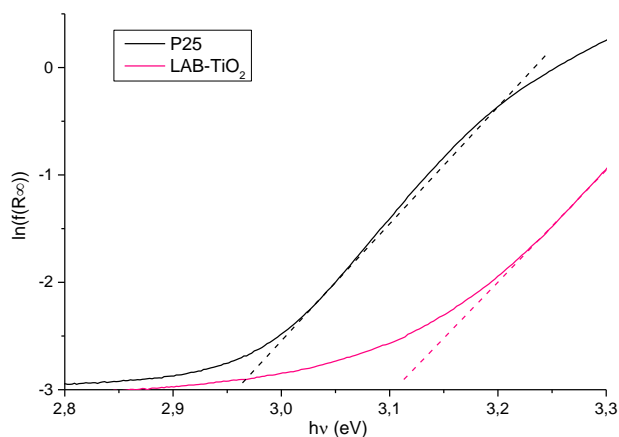


Figure 4. Urbach plots of P25 and LAB-TiO₂.

The reactivity tests were carried out in an oxygen-free aqueous solution, using glucose as organic substrate for hole scavenging, working under UVA irradiation at 80°C and 4 bar, for 5 hours [75]. The two samples revealed remarkable differences in term of both activity and selectivity. Indeed, as reported in Figure 5a, the activity toward H₂ production is higher for P25 (black bar) than for LAB-TiO₂ (pink bar). Moreover, hydrocarbons are detected in the gas phase on LAB-TiO₂, while on P25 the only carbon-based gases are CO₂ and CO (Figure 5b). The $S_{H/CO}$ ratio, involved to assess the stoichiometry of the photoreforming reaction, was almost 1.0 for P25. This suggests H₂ to be selectively produced from Reaction 4 and Reaction 8 and affording only CO₂ and CO as reaction co-products. On the contrary, the $S_{H/CO}$ ratio of 0.3 esteemed for LAB-TiO₂ points out a lower amount of H₂ to be formed, in good agreement with the detected hydrocarbon by-products:

hydrogenative side-pathways are likely to consume protons and photoexcited electrons to yield these rather than H₂ only.

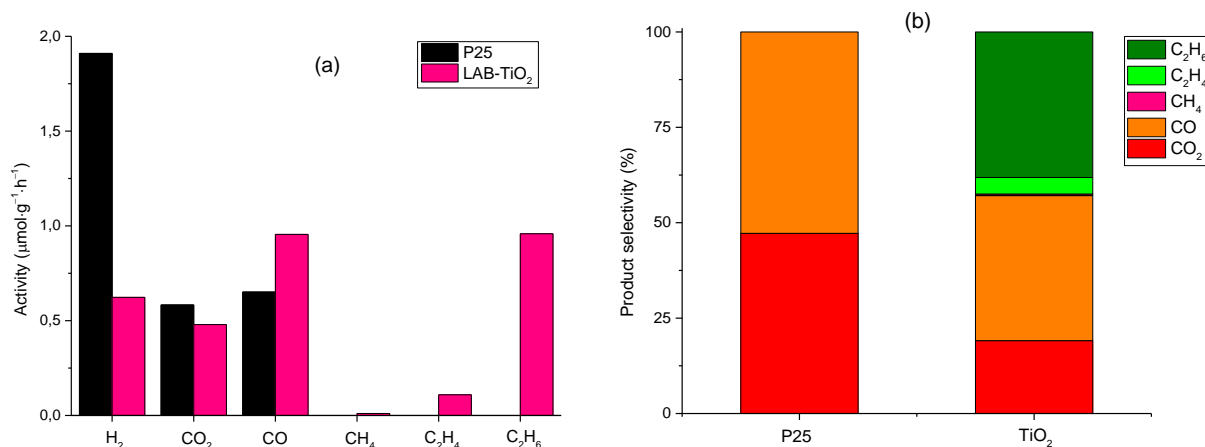


Figure 5. (a) Activity for the detected gas-phase products and (b) selectivities of C-based products in the gas phase.

Since different reduction pathways occurred at the photocatalyst surface (Reaction 5 – 7), leading to different products, the overall photoactivity should be evaluated in term of photoexcited charge carriers involved in all the redox processes. In Figure 6 this overall photoactivity (TOF_{ph}), expressed as mole of photoexcited electrons involved in reduction reactions, is compared with the activity toward H₂ evolution (TOF_{H₂}). It is clear that LAB-TiO₂, despite yielding less H₂, was actually more active in running reduction reactions.

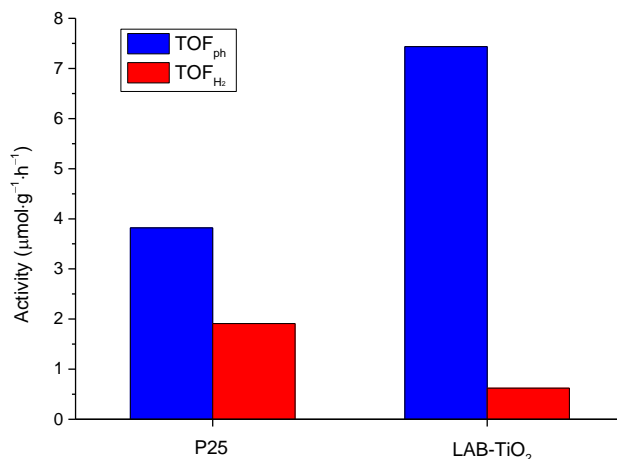


Figure 6. Activity of pristine TiO₂ photocatalysts expressed as TOF of H₂ production and TOF_{ph}.

The better performances of LAB-TiO₂ in term of overall photoactivity (TOF_{ph}) can be ascribed to its higher SSA compared to P25. Interestingly, both TOF_{ph} and SSA follow the same trend on the bare TiO₂ being doubled on LAB-TiO₂. Despite the different structural properties of the two materials (i.e. phase composition and crystallite size), the SSA seems to be the main parameter that affects the photoactivity. However, when considering the activity toward H₂ production only and the reaction stoichiometry (S_{H/CO}), P25 performed better. The two materials was observed, in a previous work, to have a different surface: P25 contains Ti⁴⁺ Lewis acid sites, while only Ti-OH moiety (free or H-bonded with water) were found on LAB-TiO₂ [68]. The Ti⁴⁺

surface sites are known to improve glucose adsorption and subsequent conversion [79], thus P25 surface is likely to catalyze more efficiently than LAB-TiO₂ the complete oxidative decomposition of glucose. This hypothesis, however, requires to be further explored.

The presence of CO as by-product in glucose photoreforming is not a big issue, since it can be easily converted into H₂ and CO₂ by a photocatalyzed water-gas shift reaction (Reaction 2) [80], still in the concept of a whole light-driven chemical process. On the contrary, hydrocarbons are less easily converted by photoreforming [81] and passively consume hydrogen and/or photoexcited electrons, thus representing an unwanted by-product in glucose photoreforming.

To summarize this section, two bare TiO₂ materials were compared, observing that LAB-TiO₂ is actually the most photoactive material due to its larger SSA, however lacking in selectivity. On the contrary, P25 despite being less active, is more selective toward H₂ production, completely suppressing hydrocarbons formation. The higher selectivity was supposed to arise from a different nature of the surface (i.e. Ti⁴⁺ Lewis acid sites), despite further studies would be required to better understand this effect.

3.2. CO-CATALYST-LOADED TiO₂ MATERIALS

Non-noble transition metal oxides, namely CuO, NiO and CuNiO_x, were selected as co-catalysts and loaded onto P25 using two different techniques, aiming at an improvement of its photoactivity. LAB-TiO₂ was excluded because, as previously observed on gas-phase ethanol photodehydrogenation, the co-catalyst was likely to become less reactive due to a strong interaction with TiO₂ as observed by TPR analyses [69]. The co-catalyst metal loading (Table 2) was assessed to be close to the theoretical value (1.0 wt. % for monometallic and for 0.5 wt. % bimetallic co-catalysts). Such low amount of metal oxides are generally undetectable by XRD [58], so the diffractograms look like the bare P25 reported in Figure 2a. Furthermore, the porosity of co-catalyst loaded samples was comparable to the pristine P25, as revealed by physisorption isotherms in Figure 7 and the SSA values reported in Table 2. Thus, the structural and morphological features of the material is almost unchanged by loading a low amount of co-catalyst.

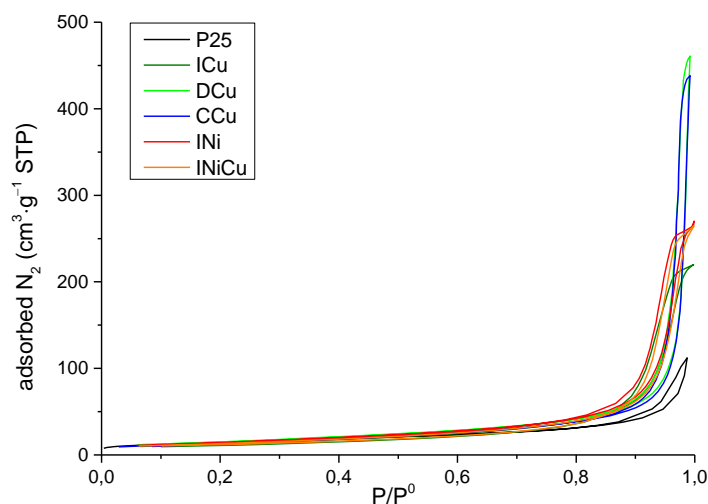


Figure 7. N_2 -physisorption isotherms of P25-based materials.

The UV-vis spectra (Figure 8a), revealed a redshift of the absorption band-edge upon loading the co-catalyst, further confirmed by the indirect E_g extrapolated from Tauc plots (not shown) and reported in Table 2. This suggests the Cu^{2+} or Ni^{2+} d orbitals of the metal co-catalyst to interact with TiO_2 band edges [82]. In the spectral region at $\lambda > 550$ nm (inset in Figure 8a), the d-d transition band of Cu^{2+} [83] and Ni^{2+} [84] species can be observed, differing from the absorption band of both bulk CuO [83] and NiO [85], suggesting the presence of narrow-sized oxides, likely to decorate the P25 surface. The 3.30 – 3.50 eV range of the Urbach plot (Figure 8b) reveals a change in the slope upon loading the metal oxide co-catalysts, and the E_U values are summarized in Table 2. The E_U was found to follow the order: $INiP25 > INiCuP25 > ICuP25 > DCuP25 \approx CCuP25 > P25$. The increased E_U upon loading the metal oxide co-catalysts, can be ascribed to the presence of the density of intra-gap states due to the co-catalysts, which in turn can affect the photoactivity [86]. UV-vis spectroscopy cannot give precise details concerning the location of such intra-gap states, so that they can be placed both close to the E_C or the E_V (conduction and valence band edge, respectively). However, as discussed later, some of them are likely to be located close to the E_C .

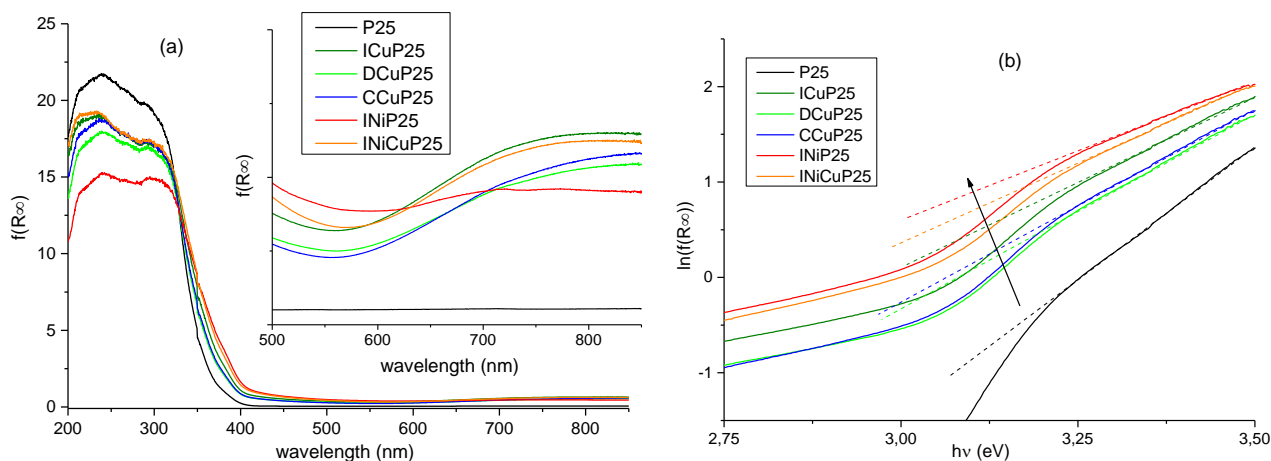


Figure 8. (a) UV-vis spectra of P25-based materials. (b) Urbach plots of P25-based materials.

The TPR analyses show a strong and sharp reduction peak for complex-precipitated samples (DCuP25 and CCuP25), while is weaker and broader for the impregnated one (ICuP25), suggesting a more reactive CuO to be present in the latter. Concerning the Ni-based samples, the bimetallic co-catalyst reveals a profile similar to the monometallic ones (INiP25 and ICuP25), and only a new weak reduction peak at 250°C was found. These observations indicate the two metal oxides to chemically interact each other only on a small extent, meaning they do not form a mixed CuNiO_x phase.

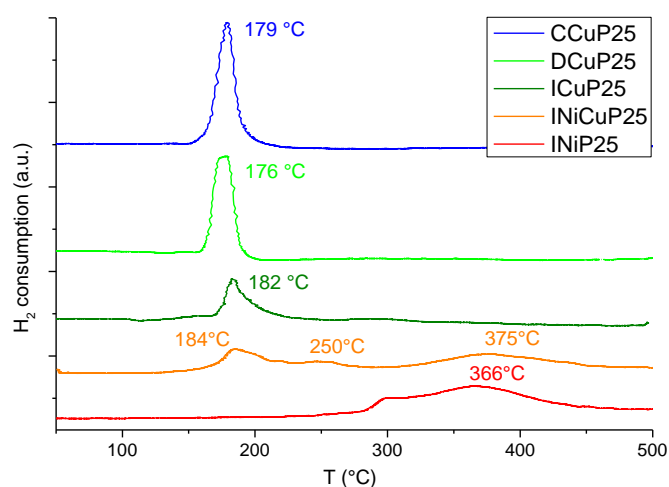


Figure 9. TPR profiles of P25-based samples.

The morphology (Figure S1), evaluated through HR-TEM, revealed no remarkable differences upon loading the Cu co-catalyst, regardless the introduction method. This suggested the presence of tiny particles of co-catalyst on the samples surface.

In Table 2 the main physico-chemical features of the P25-based photocatalysts are summarized.

Table 2. Summary of the main physico-chemical properties of the P25-based materials.

Sample	SSA ($\text{m}^2\cdot\text{g}^{-1}$)	Indirect E_g (eV)	E_u (eV)	wt. % metal loading
P25	50	3.01	0.18	-
ICuP25	46	2.89	0.28	0.9 (Cu)
DCuP25	55	2.91	0.26	1.0 (Cu)
CCuP25	49	2.91	0.26	1.0 (Cu)
INiP25	53	2.84	0.35	0.7 (Ni)
INiCuP25	48	2.86	0.31	0.5 (Cu), 0.4 (Ni)

The glucose photoreforming activity tests show a remarkable difference respect to the bare material, and further differences depending on the type of co-catalyst. As reported in Figure 10a, the highest overall photoactivity (TOF_{ph}) was achieved by loading monometallic CuO co-catalysts, which were also the most active toward H_2 production. A slight higher activity, for both TOF_{ph} and H_2 evolution, was observed on CCuP25 (blue bars). On the contrary, Ni-based co-catalysts despite still having an higher activity (both as TOF_{ph} and H_2 production) than bare P25, performed worse than the monometallic CuO. Concerning the selectivity, all the co-catalysts yielded hydrocarbons that are unwanted by-products. As pictured in Figure 10b, there are however some differences in hydrocarbon selectivity (green bars): the lowest one was achieved on DCuP25 sample, the highest one on INiP25, while the other samples gave similar selectivities.

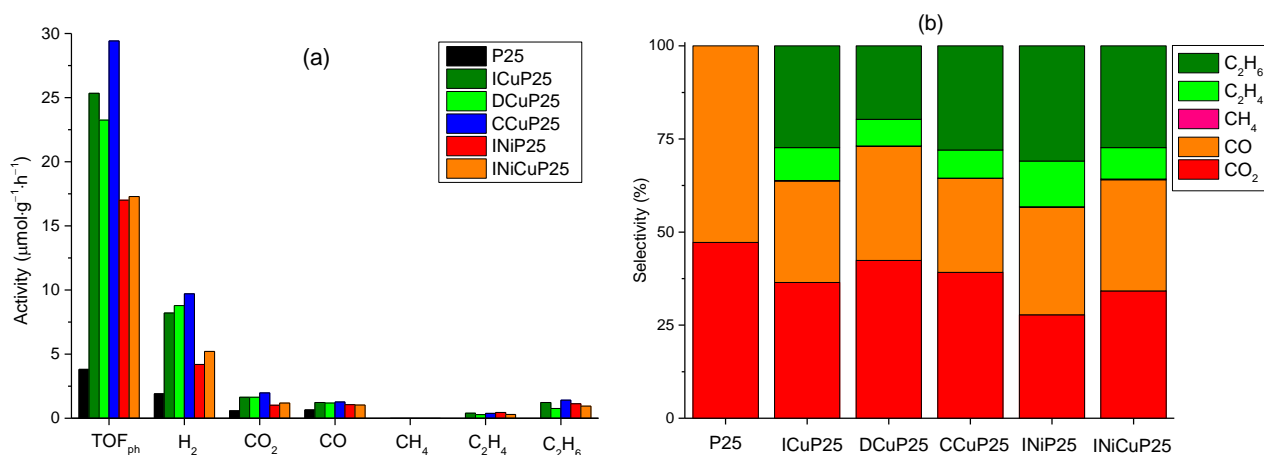


Figure 10. (a) Overall activity (TOF_{ph}) and activity toward the products in the gas phase. (b) Selectivities of C-based products in the gas phase.

The $S_{\text{H}/\text{CO}}$ reported in Table 3, exceed the unity for all the co-catalyst loaded samples. A ratio $S_{\text{H}/\text{CO}} > 1$ suggested that intermediate of glucose conversion are probably present in the liquid phase, and the photocatalyst is more active on hydrogen evolution reaction (HER) than on the glucose oxidation.

Furthermore the $S_{H/CO} > 1$, suggested hydrogenative side pathways to contribute only a little extent in consuming photogenerated electrons and protons, making HER the main reaction occurred on the co-catalyst surface.

Table 3. $S_{H/CO}$ ratio of P25-based photocatalyst.

Sample	$S_{H/CO}$
P25	1.0
ICuP25	1.8
DCuP25	1.8
CCuP25	2.0
INiP25	1.4
INiCuP25	1.5

The presence of these intra-gap states due to the co-catalyst, were useful in improving the activity, likely by improving the photoexcited charge carriers lifetime. However the most effective photocatalysts (monometallic Cu-based) revealed the lowest redshift of E_g and the lowest E_U values compared to Ni-based ones. Above an optimal density of such intra-gap states, defect-mediated recombination phenomena are likely to occur, reducing the overall activity as observed on Ni-based sample. Furthermore, besides the metal co-catalyst selection, the two strategies used for co-catalyst design, namely a different loading technique and mixing two phases, was observed to be ineffective in improving the activity. In details, the complex-precipitation used to load CuO, despite affording a more reactive co-catalyst as observed by TPR, revealed only a slight improvement in activity. The bimetallic co-catalyst did not exhibited any activity enhancement compared to the monometallic NiO, and this features is ascribable to the lack of a well mixed $CuNiO_x$ phase, as evidenced by TPR. The most relevant parameter that affects the photoactivity, in this study, is the nature of the metal co-catalyst. The effect on selectivity is more difficult to be interpreted. Generally, the highest selectivity toward hydrocarbons (Figure 10b) obtained on INiP25, can be interpreted by an improvement of side hydrogenation pathways due to Ni well-known activity as hydrogenation catalyst [14]. As for the bare TiO_2 materials, Lewis acid sites (i.e. Ti^{4+}) could potentially affect the activity and selectivity of the reaction, however further studies would be required in this direction.

The remarkable improvement of HER by loading the co-catalyst, as evidenced by $S_{H/CO} > 1$ and the data reported in Figure 10a, can suggested some of the Cu- and Ni- derived intra-gap states to be located close to the E_C , in order to allow protons to be reduced to molecular hydrogen.

On the basis of gas-phase detected products, a general mechanism of glucose conversion is proposed (Figure 11). As observed by Bellardita *et al.*, the glucose undergoes a step-by-step C-C bond cleavage (pathway 1), in which a hole (h^+) react with the sugar, leading to formic acid, protons and a sugar with one carbon atom less [87]. The formic acid can be then oxidized to CO_2 (pathway 2), or dehydrated to CO (pathway 3), which can be further oxidized with water to CO_2 (pathway 6) [37,88]. Formic acid and simpler sugars are supposed to be the intermediate of glucose conversion that accumulates in the liquid phase when using co-catalyst loaded P25. All the oxidative reaction steps yield protons, then reduced by photoexcited electrons (e^-) affording molecular hydrogen (HER, not shown). A competitive reduction reaction is the hydrogenation of adsorbed CO to C_2 hydrocarbons (pathways 4 and 5) [89], which consumes photoexcited electrons and protons.

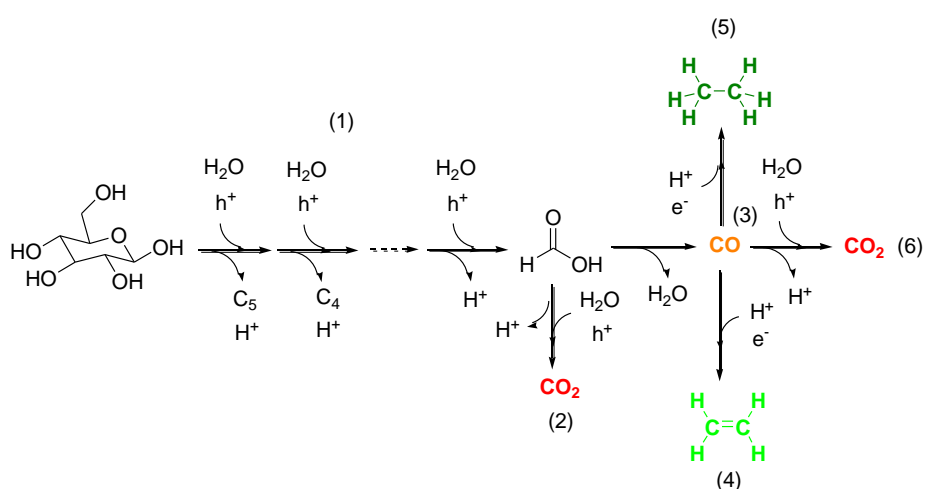


Figure 11. Mechanism of glucose conversion by photoreforming. (1) Step-by-step oxidative C-C bond cleavage. (2) Formic acid oxidation to CO_2 . (3) Formic acid dehydration to CO. (4), (5) CO hydrogenation to C_2H_4 and C_2H_6 . (6) CO oxidation to CO_2 .

To summarize this section, a general scheme of the photocatalytic process is pictured in Figure 12. In the absence of co-catalyst, glucose is oxidized to CO_2 and CO, while only H_2 is produced on the reductive side of the reaction on P25. The addition of Cu- and Ni-based co-catalysts induce some intra-gap states ($nE_{F,Cu}^*$ and $nE_{F,Ni}^*$ reported on the picture) which stabilize the photoexcited electrons and allows their transfer to electron acceptors, protons or CO, affording H_2 and hydrocarbons, respectively. Anyway, HER is likely to be the most relevant reduction pathway occurring on the photocatalyst. The oxidative pathway, besides CO and CO_2 , is likely to afford also formic acid and simpler sugars, as evidenced by the $S_{H/CO} > 1$, because the scarce ability of the co-catalyst to improve the oxidative pathway.

It can be concluded that the addition of the co-catalyst allowed a remarkable improvement the overall photoactivity, in term of photoexcited charge carriers involved in redox processes, and in particular the activity toward H_2 evolution. However, hydrocarbons and soluble by-products (i.e. formic acid and simpler sugars) were also produced, representing a limitation in the potential yield of hydrogen from glucose photoreforming.

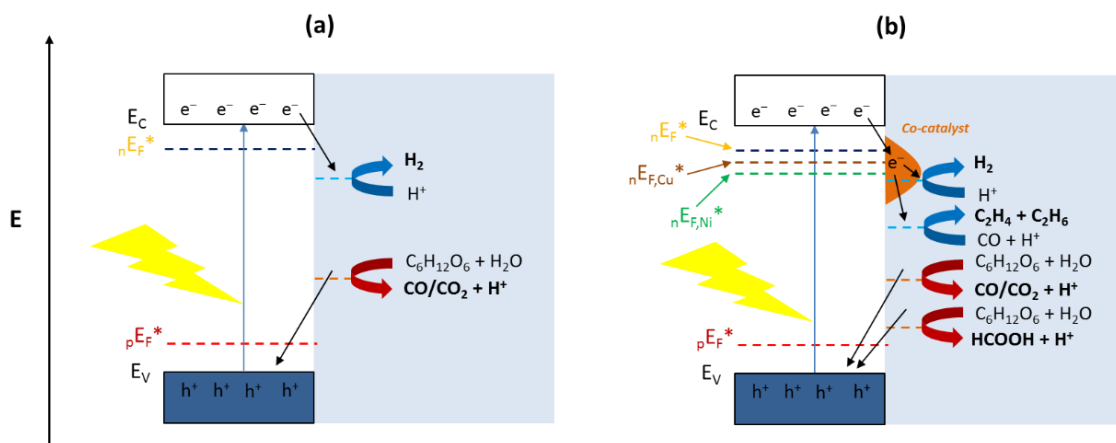


Figure 12. General scheme of the photocatalytic phenomena on (a) bare P25 and (b) co-catalyst modified P25, according to the data shown in this work. The energy levels are labelled according to the Preface section. The intra-gap states due to Cu and Ni are pictured as electron quasi-Fermi levels ($nE_{F,Cu}^*$ and $nE_{F,Ni}^*$).

4. CONCLUSIONS

Through this work, earth-abundant co-catalysts (Cu- and Ni-based) were used on TiO₂ in the glucose photoreforming reaction for a renewable H₂ production process. In details:

1. P25 was observed to be less photoactive than LAB-TiO₂ due to its lower SSA, however being more selective toward H₂ production and allowing an efficient oxidative degradation of glucose.
2. Loading the metal co-catalyst afforded a remarkable improvement of the overall photoactivity, with monometallic CuO being the most efficient co-catalyst due to a favourable intra-gap state density, likely to be partially located close to the E_c. The co-catalyst loading technique was observed to have only a slight effect on the activity, while no beneficial effect in activity improvement was obtained by mixing CuO and NiO.
3. HER was greatly enhanced upon loading the co-catalysts, and the activity toward H₂ production follows almost the same trend of photoactivity, with CuO being the most efficient one. Furthermore, the co-catalysts afforded hydrocarbons as reduction side-products in all the cases, with the highest selectivity on INiP25. Soluble intermediate of glucose oxidative degradations (i.e. formic acid and simple sugars) was also supposed to accumulate in the liquid phase.
4. A general mechanism of glucose photoreforming was proposed.

5. SUPPLEMENTARY INFORMATION

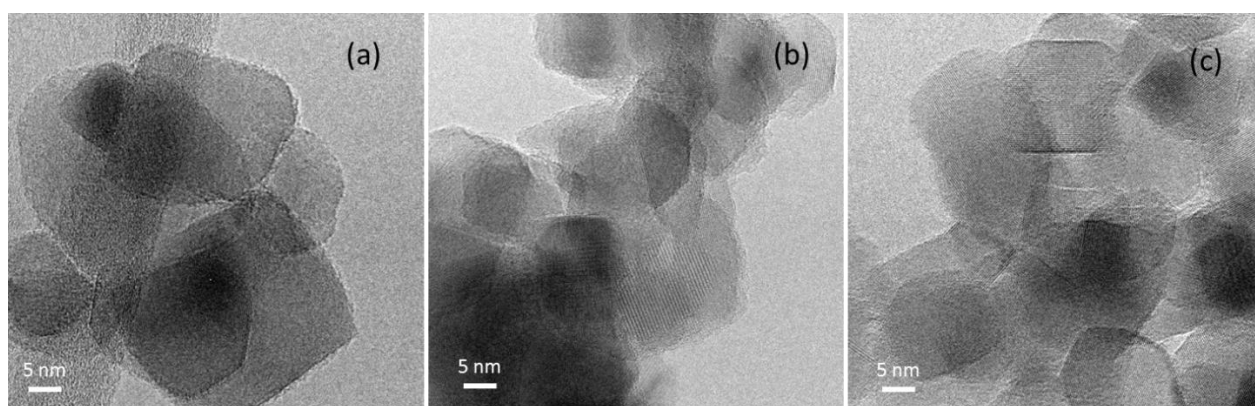


Figure S1. HR-TEM images of (a) P25, (b) ICuP25 and (c) DCuP25.

6. REFERENCES

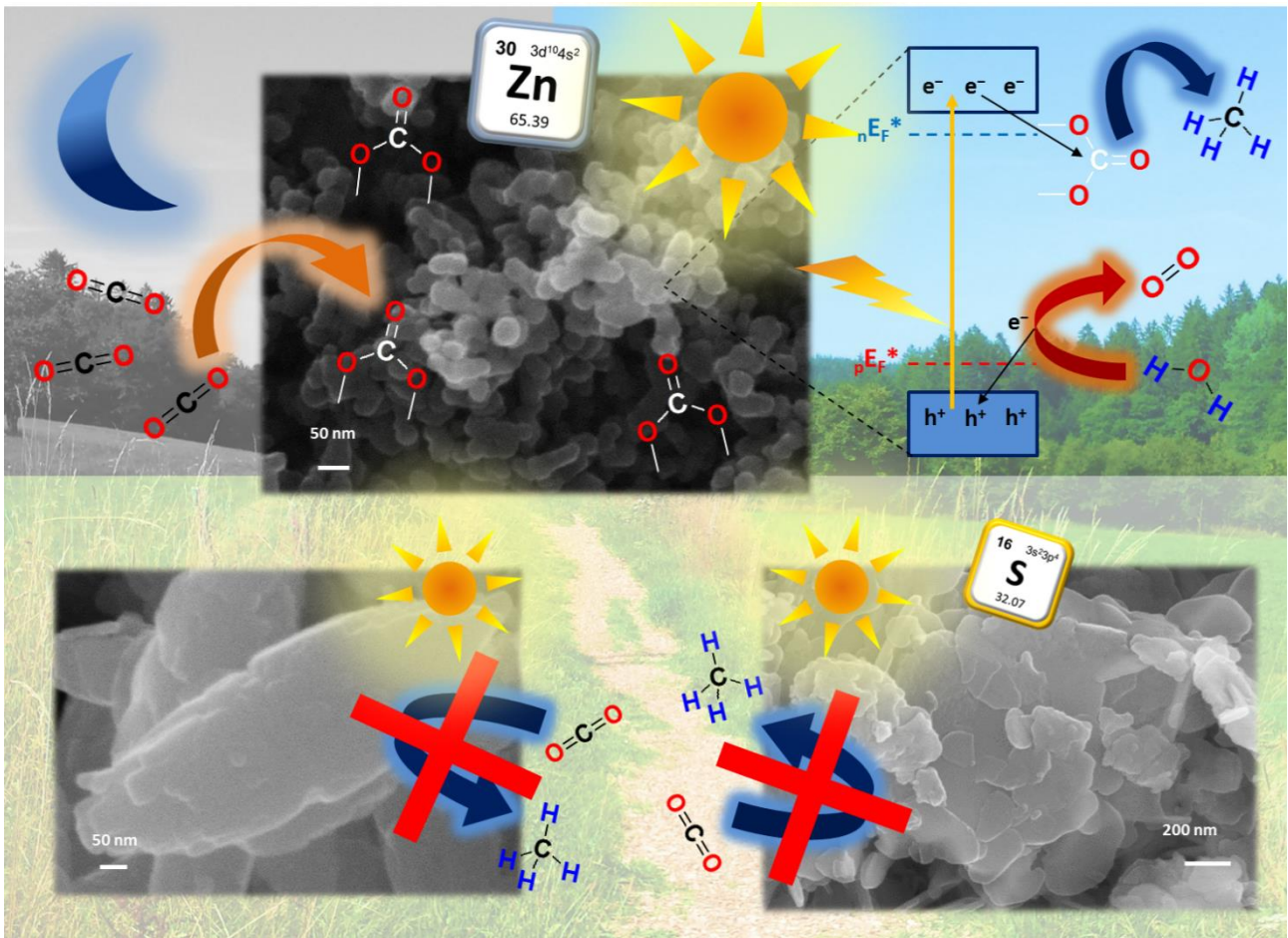
- ¹ P. Häussinger, R. Lohmüller, A. M. Watson. *Hydrogen, 6. Uses*. Ullmann's Encyclopedia of Chemical Industry, 2012. doi: 10.1002/14356007.o13_o07.
- ² N. Armaroli, V. Balzani, Hydrogen. In *Energy for a Sustainable World*. WILEY-VCH Verlag GmbH & Co. KGaA: Weinheim (Germany), 2011. ISBN: 9783527325405.
- ³ O.Z. Sharaf, M.F. Orhan, An overview of fuel cell technology: Fundamentals and applications. *Renew. Sustain. Energy Rev.* **2014**, *32*, 810-853, doi: 10.1016/j.rser.2014.01.012.
- ⁴ R.M. Gupta. *Hydrogen Fuel. Production, Transport and Storage*. Taylor & Francis Group: Boca Raton (USA), 2009. ISBN: 9781420045758.
- ⁵ N.G. Moreno, M.C. Molina, D. Gervasio, J.F.P. Robles, Approaches to polymer electrolyte membrane fuel cells (PEMFCs) and their cost. *Renew. Sustain. Energy Rev.* **2015**, *52*, 897-906, doi: 10.1016/j.rser.2015.07.157.
- ⁶ C. Graves, S.D. Ebbesen, M. Mogensen, K.S. Lackner, Sustainable hydrocarbon fuels by recycling CO₂ and H₂O with renewable or nuclear energy. *Renew. Sustain. Energy Rev.* **2011**, *15*, 1-23, doi:10.1016/j.rser.2010.07.014.
- ⁷ A. Goepfert, M. Czaun, J.-P. Jones, G.K.S. Prakash, G.A. Olah, Recycling of carbon dioxide to methanol and derived products – closing the loop. *Chem. Soc. Rev.* **2014**, *43*, 7995-8048, doi: 10.1039/c4cs00122b.
- ⁸ W.J. Lee, C. Li, H. Prajitno, J. Yoo, J. Patel, Y. Yang, S. Lim, Recent trend in thermal catalytic low temperature CO₂ methanation: A critical review. *Catal. Today* **2020**, 10.1016/j.cattod.2020.02.017.
- ⁹ Y.A. Daza, J.N. Kuhn, CO₂ conversion by reverse water gas shift catalysis: comparison of catalysts, mechanisms and their consequences for CO₂ conversion to liquid fuels. *RSC Adv.* **2016**, *6*, 49675-49691, doi: 10.1039/c6ra05414e.
- ¹⁰ M. Ameen, M.T. Azizan, S. Yusup, A. Ramli, M. Yasir, Catalytic hydrodeoxygenation of triglycerides: An approach to clean diesel fuel production. *Renew. Sustain. Energy Rev.* **2017**, *80*, 1072-1088, doi: 10.1016/j.rser.2017.05.268.
- ¹¹ M. Saidi, F. Samimi, D. Karimipourfard, T. Nimmanwudipong, B.C. Gates, M.R. Rahimpour, Upgrading of lignin-derived bio-oils by catalytic hydrodeoxygenation. *Energy Environ. Sci.* **2014**, *7*, 103-129, doi: 10.1039/C3EE43081B.
- ¹² P.M. Mortensen, J.D. Grunwaldt, P.A. Jensen, K.G. Knudsen, A.D. Jensen, A review of catalytic upgrading of bio-oil to engine fuels. *Appl. Catal. A* **2011**, *407*, 1-19, doi: 10.1016/j.apcata.2011.08.046.
- ¹³ The Future of Hydrogen. Technology report 2019. Available on International Energy Agency (IEA) website: <https://www.iea.org/reports/the-future-of-hydrogen>. Accessed on 20/08/2020.
- ¹⁴ C. H. Bartholomew, R. J. Farrauto, Hydrogen Production and Synthesis Gas Reaction. In *Fundamentals of Industrial Catalytic Processes, 2nd ed.* John Wiley & Sons, Inc.: Hoboken (USA), 2005. ISBN: 9780471457138.
- ¹⁵ Gibbs free energy of reaction were calculated as follow: $\Delta_r G^{\circ}_{25^{\circ}\text{C}} = \left(\sum_{i=0}^n y_i \Delta_f G^{\circ P}_{25^{\circ}\text{C},i}\right) - \left(\sum_{i=0}^n x_i \Delta_f G^{\circ R}_{25^{\circ}\text{C},i}\right)$, where $\Delta_f G^{\circ P}_{25^{\circ}\text{C},i}$ is the Gibbs free energy of formation of the ith reaction product, $\Delta_f G^{\circ R}_{25^{\circ}\text{C},i}$ is the free Gibbs energy of formation of the ith reaction reagent, while y_i and x_i are the stoichiometric coefficient of, respectively, the ith product and ith reagent. The Gibbs free energy of formation are taken from: D.R. Lide, Grace Baysinger, Lev I. Berger, Robert N. Goldberg, Henry V. Kehiaian, Kozo Kuchitsu, Gerd Rosenblatt, Dana L. Roth, Daniel Zwillingner. Thermochemistry, electrochemistry and kinetics. In *CRC Handbook of Chemistry and Physics, 6th ed.*, CRC press: Boca Raton (USA), 2005. ISBN: 9780849332043.
- ¹⁶ R. Reimert, F. Marschner, H.-J. Renner, W. Boll, E. Supp, M. Brejc, W. Liebner, G. Schaub, *Gas Production, 2. Processes*. Ullmann's Encyclopedia of Industrial Chemistry, 2012. doi: 10.1002/14356007.o12_o01.
- ¹⁷ I. Coronado, M. Stekrova, M. Reinikainen, P. Simell, L. Lefferts, J. Lehtonen, A review of catalytic aqueous-phase reforming of oxygenated hydrocarbons derived from biorefinery water fractions. *Int. J. Hydrogen Energy.* **2016**, *41*, 11003-11032, doi:10.1016/j.ijhydene.2016.05.032.
- ¹⁸ G. Wen, Y. Xu, Z. Xu, Z. Tian, Characterization and catalytic properties of the Ni/Al₂O₃ catalysts for aqueous-phase reforming of glucose. *Catal. Lett.* **2009**, *129*, 250-257, doi:10.1007/s10562-008-9810-0.
- ¹⁹ G. Wen, Y. Xu, Z. Xu, Z. Tian, Direct conversion of cellulose into hydrogen by aqueous-phase reforming process. *Catal. Commun.* **2010**, *11*, 522-526, doi: 10.1016/j.catcom.2009.12.008.
- ²⁰ M.B. Valenzuela, C.W. Jones, P.K. Agrawal, Batch aqueous-phase reforming of woody biomass. *Energ. Fuel.* **2006**, *20*, 1744-1752, doi: 10.1021/ef060113p.
- ²¹ A.S. Oliveira, J.A. Baeza, L. Calvo, N. Alonso-Morales, F. Heras, J.J. Rodriguez, M.A. Gilarranz, Production of hydrogen from brewery wastewater by aqueous phase reforming with Pt/C catalysts. *Appl. Catal. B* **2019**, *245*, 367-375, doi: 10.1016/j.apcatb.2018.12.061.
- ²² P. Häussinger, R. Lohmüller, A.M. Watson. *Hydrogen, 5. Handling*. Ullmann's Encyclopedia of Industrial Chemistry, 2012. doi: 10.1002/14356007.o13_o06.
- ²³ P. Häussinger, R. Lohmüller, A. M. Watson. *Hydrogen, 2. Production*. Ullmann's Encyclopedia of Chemical Industry, 2012. doi: 10.1002/14356007.o13_o03.

- ²⁴ D.P. Harrison, Sorption-enhanced hydrogen production: A review. *Ind. Eng. Chem. Res.* **2008**, *47*, 6486-6501. doi:10.1021/ie800298z.
- ²⁵ I. Dincer, C. Acar, Review and evaluation of hydrogen production methods for better sustainability. *Int. J. Hydrogen Energy* **2014**, *40*, 11094-11111, doi:10.1016/j.ijhydene.2014.12.035.
- ²⁶ J.R. Bartels, M.B. Pate, N.K. Olson, An economic survey of hydrogen production from conventional and alternative energy sources. *Int. J. Hydrogen Energy* **2010**, *35*, 8371-8384, doi:10.1016/j.ijhydene.2010.04.035.
- ²⁷ A. Olivo, D. Zanardo, E. Ghedini, F. Menegazzo, M. Signoretto, Solar Fuels by Heterogeneous Photocatalysis: From Understanding Chemical Bases to Process Development. *ChemEngineering* **2018**, *2*, 42, doi:10.3390/chemengineering2030042.
- ²⁸ A. Fujishima, K. Honda, Electrochemical photolysis of water at a semiconductor electrode. *Nature* **1972**, *238*, 37-38, doi:10.1038/238037a0.
- ²⁹ T. Hisatomi, J. Kubota, K. Domen, Recent advances in semiconductors for photocatalytic and photoelectrochemical water splitting. *Chem. Soc. Rev.* **2014**, *43*, 7520-7535, doi:10.1039/C3CS60378D.
- ³⁰ M.G. Walter, E.L. Warren, J.R. Mckone, S.W. Boettcher, Q. Mi, E.A. Santori, N.S. Lewis, Solar Water Splitting Cells. *Chem. Rev.* **2010**, *110*, 6446-6473, doi: 10.1021/cr1002326.
- ³¹ M. Yoshida, K. Takanebe, K. Maeda, A. Ishikawa, J. Kubota, Y. Sakata, Y. Ikezawa, K. Domen, Role and Function of Noble-Metal / Cr-Layer Core / Shell Structure Cocatalysts for Photocatalytic Overall Water Splitting Studied by Model Electrodes. *J. Phys. Chem. C* **2009**, *113*, 10151-10157, doi: 10.1021/jp901418u.
- ³² T. Kawai, T. Sakata, Conversion of carbohydrate into hydrogen fuel by a photocatalytic process. *Nature* **1980**, *286*, 474-476, doi:10.1038/286474a0.
- ³³ H. Bahruji, M. Bowker, P.R. Davies, F. Pedrono, Applied Catalysis B : Environmental New insights into the mechanism of photocatalytic reforming on Pd/TiO₂. *Appl. Catal. B* **2011**, *107*, 205-209, doi: 10.1016/j.apcatb.2011.07.015.
- ³⁴ Z.H.N. Al-Azri, W.T. Chen, A. Chan, V. Jovic, T. Ina, H. Idriss, G.I.N. Waterhouse, The roles of metal co-catalysts and reaction media in photocatalytic hydrogen production: Performance evaluation of M/TiO₂ photocatalysts (M = Pd, Pt, Au) in different alcohol-water mixtures. *J. Catal.* **2015**, *329*, 355-367, doi: 10.1016/j.jcat.2015.06.005.
- ³⁵ T. Sakata, T. Kawai, K. Hashimoto, Heterogeneous photocatalytic reactions of organic acids and water. New reaction paths besides the photo-Kolbe reaction. *J. Phys. Chem.* **1984**, *88*, 2344-2350, doi: 10.1021/j150655a032.
- ³⁶ A. Patsoura, D.I. Kondarides, X.E. Verykios, Photocatalytic degradation of organic pollutants with simultaneous production of hydrogen. *Catal. Today* **2007**, *124*, 94-102, doi: 10.1016/j.cattod.2007.03.028.
- ³⁷ G. Wu, T. Chen, W. Su, G. Zhou, X. Zong, Z. Lei, C. Li, H₂ production with ultra-low CO selectivity via photocatalytic reforming of methanol on Au/TiO₂ catalyst. *Int. J. Hydrogen Energy* **2008**, *33*, 1243-1251, doi:10.1016/j.ijhydene.2007.12.020.
- ³⁸ K. Hashimoto, T. Kawai, T. Sakata, Photocatalytic reactions of hydrocarbons and fossil fuels with water. Hydrogen production and oxidation. *J. Phys. Chem.* **1984**, *88*, 4083-4088, doi: 10.1021/j150662a046.
- ³⁹ D.W. Wakerley, M.F. Kuehnel, K.L. Orchard, K.H. Ly, T.E. Rosser, E. Reisner, Solar-driven reforming of lignocellulose to H₂ with a CdS/CdO_x photocatalyst. *Nat. Energy* **2017**, *2*, 17021, doi:10.1038/nenergy.2017.21.
- ⁴⁰ V. Nichele, M. Signoretto, F. Menegazzo, A. Gallo, V. Dal Santo, G. Cruciani, G. Cerrato, Glycerol steam reforming for hydrogen production: Design of Ni supported catalysts. *Appl. Catal. B* **2012**, *111-112*, 225-232, doi:10.1016/j.apcatb.2011.10.003.
- ⁴¹ R.L. Manfro, A.F. Da Costa, N.F.P. Ribeiro, M.M.V.M. Souza, Hydrogen production by aqueous-phase reforming of glycerol over nickel catalysts supported on CeO₂. *Fuel Process. Technol.* **2011**, *92*, 330-335, doi:10.1016/j.fuproc.2010.09.024.
- ⁴² I. Rossetti, Hydrogen Production by Photoreforming of Renewable Substrates. *ISRN Chem. Eng.* **2012**, *2012*, 964936, doi: 10.5402/2012/964936.
- ⁴³ A. V. Puga, Photocatalytic production of hydrogen from biomass-derived feedstocks. *Coord. Chem. Rev.* **2016**, *315*, 1-66, doi:10.1016/j.ccr.2015.12.009.
- ⁴⁴ H. Kobayashi, A. Fukuoka, Synthesis and utilisation of sugar compounds derived from lignocellulosic biomass. *Green Chem.* **2013**, *15*, 1740-1763, doi:10.1039/c3gc00060e.
- ⁴⁵ B. Zielińska, E. Borowiak-Palen, R.J. Kalenczuk, Photocatalytic hydrogen generation over alkaline-earth titanates in the presence of electron donors. *Int. J. Hydrogen Energy* **2008**, *33*, 1797-1802, doi: 10.1016/j.ijhydene.2008.02.001.
- ⁴⁶ S.S.K. Ma, K. Maeda, K. Domen, Modification of TaON with ZrO₂ to improve photocatalytic hydrogen evolution activity under visible light: influence of preparation conditions on activity. *Catal. Sci. Technol.* **2012**, *2*, 818-823, doi:10.1039/c2cy00499b.
- ⁴⁷ L. Ge, C. Han, X. Xiao, L. Guo, Synthesis and characterization of composite visible light active photocatalysts MoS₂-g-C₃N₄ with enhanced hydrogen evolution activity. *Int. J. Hydrogen Energy* **2013**, *38*, 6960-6969, doi:10.1016/j.ijhydene.2013.04.006.

- ⁴⁸ Y. Ma, X. Wang, Y. Jia, X. Chen, H. Han, C. Li, Titanium Dioxide-Based Nanomaterials for Photocatalytic Fuel Generations. *Chem. Rev.* **2014**, *114*, 9987-10043, doi: 10.1021/cr500008u.
- ⁴⁹ J. Yan, G. Wu, N. Guan, L. Li, Z. Li, X. Cao, Understanding the effect of surface/bulk defects on the photocatalytic activity of TiO₂: anatase versus rutile. *Phys. Chem. Chem. Phys.* **2013**, *15*, 10978-10988, doi: 10.1039/c3cp50927c.
- ⁵⁰ H. Tang, K. Prasad, R. Sanjinès, P.E. Schmid, F. Lévy, Electrical and optical properties of TiO₂ anatase thin films. *J. Appl. Phys.* **1994**, *75*(4), 2042-2047 doi:10.1063/1.356306.
- ⁵¹ A. Sclafani, J.M. Herrmann, Comparison of the photoelectronic and photocatalytic activities of various anatase and rutile forms of titania in pure liquid organic phases and in aqueous solutions. *J. Phys. Chem.* **1996**, *100*, 13655-13661, doi:10.1021/jp9533584.
- ⁵² D.O. Scanlon, C.W. Dunnill, J. Buckeridge, S.A. Shevlin, A.J. Logsdail, S.M. Woodley, C.R.A. Catlow, M.J. Powell, R.G. Palgrave, I.P. Parkin, G.W. Watson, T.W. Keal, P. Sherwood, A. Walsh, A.A. Sokol, Band alignment of rutile and anatase TiO₂. *Nat. Mater.* **2013**, *12*, 798-801, doi: 10.1038/NMAT3697.
- ⁵³ J. Yu, Y. Hai, M. Jaroniec, Journal of Colloid and Interface Science Photocatalytic hydrogen production over CuO-modified titania. *J. Colloid Interface Sci.* **2011**, *357*, 223-228, doi:10.1016/j.jcis.2011.01.101.
- ⁵⁴ G.L. Chiarello, L. Forni, E. Selli, Photocatalytic hydrogen production by liquid- and gas-phase reforming of CH₃OH over flame-made TiO₂ and Au/TiO₂. *Catal. Today* **2009**, *144*, 69-74, doi: 10.1016/j.cattod.2009.01.023.
- ⁵⁵ V. Subramanian, E.E. Wolf, P. V. Kamat, B. Engineering, V. Uni, N. Dame, Catalysis with TiO₂/Gold Nanocomposites. Effect of Metal Particle Size on the Fermi Level Equilibration. *J. Am. Chem. Soc.* **2004**, *126*, 4943-4950, doi:10.1021/ja0315199.
- ⁵⁶ A. Tanaka, K. Hashimoto, H. Kominami, Visible light-induced hydrogen and oxygen formation over Pt/Au/WO₃ photocatalyst utilizing two types of photoabsorption due to surface plasmon resonance and band-gap excitation. *J. Am. Chem. Soc.* **2014**, *136*, 586-589, doi:10.1021/ja410230u.
- ⁵⁷ V.M. Daskalaki, D.I. Kondarides, Efficient production of hydrogen by photo-induced reforming of glycerol at ambient conditions. *Catal. Today* **2009**, *144*, 75-80, doi:10.1016/j.cattod.2008.11.009.
- ⁵⁸ W.T. Chen, V. Jovic, D. Sun-Waterhouse, H. Idriss, G.I.N. Waterhouse, The role of CuO in promoting photocatalytic hydrogen production over TiO₂. *Int. J. Hydrogen Energy* **2013**, *38*, 15036-15048, doi:10.1016/j.ijhydene.2013.09.101.
- ⁵⁹ W.T. Chen, A. Chan, D. Sun-Waterhouse, T. Moriga, H. Idriss, G.I.N. Waterhouse, Ni/TiO₂: A promising low-cost photocatalytic system for solar H₂ production from ethanol-water mixtures. *J. Catal.* **2015**, *326*, 43-53, doi:10.1016/j.jcat.2015.03.008.
- ⁶⁰ S.-I. Fujita, H. Kawamori, D. Honda, H. Yoshida, M. Arai, Photocatalytic hydrogen production from aqueous glycerol solution using NiO/TiO₂ catalysts: Effects of preparation and reaction conditions. *Appl. Catal. B* **2016**, *181*, 818-824, doi:10.1016/j.apcatb.2015.08.048.
- ⁶¹ L.S. Yoong, F.K. Chong, B.K. Dutta. Development of copper-doped TiO₂ photocatalyst for hydrogen production under visible light. *Energy* **2009**, *34*, 1652-1661, doi:10.1016/j.energy.2009.07.024.
- ⁶² M. Jung, J.N. Hart, D. Boensch, J. Scott, Y.H. Ng, R. Amal, Hydrogen evolution via glycerol photoreforming over Cu-Pt nanoalloys on TiO₂. *Appl. Catal. A* **2016**, *518*, 221-230, doi:10.1016/j.apcata.2015.10.040.
- ⁶³ Z. Hu, J.C. Yu, Pt₃Co-loaded CdS and TiO₂ for photocatalytic hydrogen evolution from water. *J. Mater. Chem. A* **2013**, *1*, 12221-12228, doi:10.1039/c3ta12407j.
- ⁶⁴ C.E. Barrios, E. Albitar, J.M. Gracia y Jimenez, H. Tiznado, J. Romo-Herrera, R. Zanella, Photocatalytic hydrogen production over titania modified by gold – Metal (palladium, nickel and cobalt) catalysts. *Int. J. Hydrogen Energy* **2016**, *41*, 23287-23300, doi:10.1016/j.ijhydene.2016.09.206.
- ⁶⁵ G.L. Chiarello, M.H. Aguirre, E. Selli, Hydrogen production by photocatalytic steam reforming of methanol on noble metal-modified TiO₂. *J. Catal.* **2010**, *273*, 182-190, doi:10.1016/j.jcat.2010.05.012.
- ⁶⁶ E. Taboada, I. Angurell, J. Llorca, Dynamic photocatalytic hydrogen production from ethanol-water mixtures in an optical fiber honeycomb reactor loaded with Au/TiO₂. *J. Catal.* **2014**, *309*, 460-467, doi:10.1016/j.jcat.2013.10.025.
- ⁶⁷ X. Fu, J. Long, X. Wang, D.Y.C. Leung, Z. Ding, L. Wu, Z. Zhang, Z. Li, X. Fu, Photocatalytic reforming of biomass: A systematic study of hydrogen evolution from glucose solution. *Int. J. Hydrogen Energy* **2008**, *33*, 6484-6491, doi:10.1016/j.ijhydene.2008.07.068.
- ⁶⁸ A. Olivo, V. Trevisan, E. Ghedini, F. Pinna, C.L. Bianchi, A. Naldoni, G. Cruciani, M. Signoretto, CO₂ photoreduction with water: Catalyst and process investigation. *J. CO₂ Util.* **2015**, *12*, 86-94, doi:10.1016/j.jcou.2015.06.001.
- ⁶⁹ D. Zanardo, E. Ghedini, F. Menegazzo, E. Cattaruzza, M. Manzoli, G. Cruciani, M. Signoretto, Titanium dioxide-based nanocomposites for enhanced gas-phase photodehydrogenation. *Materials* **2019**, *12*, 3093, doi:10.3390/ma12193093.
- ⁷⁰ S. Brunauer, P.H. Emmett, E. Teller, Adsorption of Gases in Multimolecular Layers. *J. Am. Chem. Soc.* **1938**, *60*, 309-319, doi:10.1021/ja01269a023.
- ⁷¹ P. Kubelka; F. Munk, Ein Beitrag zur Optik der Farbanstriche. *Zeitschrift Technische Physik* **1931**, *12*, 593-601.
- ⁷² J. Tauc, A. Menth, States in the gap. *J. Non-Cryst. Solids* **1972**, *8-10*, 569-585, doi:10.1016/0022-3093(72)90194-9.

- ⁷³ W.F. Lim, H.J. Quah, Z. Hassan, R. Radzali, N. Zainal, F.K. Yam, Alteration of structural and optical properties in quaternary $\text{Al}_{0.1}\text{In}_{0.1}\text{Ga}_{0.8}\text{N}$ films using ultraviolet assisted photo-electrochemical etching route. *J. Alloys Compd.* **2015**, *649*, 337-347, doi:10.1016/j.jallcom.2015.07.114.
- ⁷⁴ I. Studenyak, M. Kranjčec, M. Kurik, Urbach Rule in Solid State Physics. *Int. J. Opt. Appl.* **2014**, *4(3)*, 76-83, doi: 10.5923/j.optics.20140403.02.
- ⁷⁵ G. Ramis, E. Bahadori, I. Rossetti, Design of efficient photocatalytic processes for the production of hydrogen from biomass derived substrates. *Int. J. Hydrogen Energy* **2020**, doi: 10.1016/j.ijhydene.2020.02.192.
- ⁷⁶ G. Leofanti, M. Padovan, G. Tozzola, B. Venturelli, Surface area and pore texture of catalysts. *Catal. Today* **1998**, *41*, 207-219, doi:10.1016/S0920-5861(98)00050-9.
- ⁷⁷ K. Madhusudan Reddy, C. V. Gopal Reddy, S. V. Manorama, Preparation, characterization, and spectral studies on nanocrystalline anatase TiO_2 . *J. Solid State Chem.* **2001**, *158*, 180-186, doi:10.1006/jssc.2001.9090.
- ⁷⁸ D. Kandi, S. Martha, A. Thirumurugan, K.M. Parida, CDS QDs-decorated self-doped $\gamma\text{-Bi}_2\text{MoO}_6$: A sustainable and versatile photocatalyst toward photoreduction of Cr(VI) and degradation of phenol. *ACS Omega* **2017**, *2*, 9040-9056, doi:10.1021/acsomega.7b01250.
- ⁷⁹ I. Abdouli, M. Eternot, F. Dappozze, C. Guillard, N. Essayem, Comparison of hydrothermal and photocatalytic conversion of glucose with commercial TiO_2 : Superficial properties-activities relationships. *Catal. Today* **2020**, doi:10.1016/j.cattod.2020.03.040.
- ⁸⁰ L. Millard, M. Bowker, Photocatalytic water-gas shift reaction at ambient temperature. *J. Photochem. Photobiol. A* **2002**, *148*, 91-95, doi:10.1016/S1010-6030(02)00077-1.
- ⁸¹ H. Yoshida, K. Hirao, J.I. Nishimoto, K. Shimura, S. Kato, H. Itoh, T. Hattori, Hydrogen production from methane and water on platinum loaded titanium oxide photocatalysts. *J. Phys. Chem. C* **2008**, *112*, 5542-5551, doi:10.1021/jp077314u.
- ⁸² T. Umabayashi, T. Yamaki, H. Itoh, K. Asai, Analysis of electronic structures of 3d transition metal-doped TiO_2 based on band calculations. *J. Phys. Chem. Solids* **2002**, *63*, 1909-1920, doi: 10.1016/S0022-3697(02)00177-4.
- ⁸³ J.J. Bravo-Suárez, B. Subramaniam, R. V. Chaudhari, Ultraviolet-visible spectroscopy and temperature-programmed techniques as tools for structural characterization of Cu in CuMgAlO_x mixed metal oxides. *J. Phys. Chem. C* **2012**, *116*, 18207-18221, doi: 10.1021/jp303631v.
- ⁸⁴ K. Hadjiivanov, M. Mihaylov, D. Klissurski, P. Stefanov, N. Abadjieva, E. Vassileva, L. Mintchev, Characterization of Ni/SiO_2 catalysts prepared by successive deposition and reduction of Ni^{2+} ions. *J. Catal.* **1999**, *185*, 314-323, doi: 10.1006/jcat.1999.2521.
- ⁸⁵ M. El-Kemary, N. Nagy, I. El-Mehasseb, Nickel oxide nanoparticles: Synthesis and spectral studies of interactions with glucose. *Mater. Sci. Semicond. Process.* **2013**, *16*, 1747-1752, doi:10.1016/j.mssp.2013.05.018.
- ⁸⁶ H. Khan, N. Usen, D.C. Boffito, Journal of Environmental Chemical Engineering Spray-dried microporous Pt/TiO_2 degrades 4-chlorophenol under UV and visible light. *J. Environ. Chem. Eng.* **2019**, *7*, 103267, doi:10.1016/j.jece.2019.103267.
- ⁸⁷ M. Bellardita, E.I. García-López, G. Marci, L. Palmisano, Photocatalytic formation of H_2 and value-added chemicals in aqueous glucose (Pt)- TiO_2 suspension. *Int. J. Hydrogen Energy* **2016**, *41*, 5934-5947, doi: 10.1016/j.ijhydene.2016.02.103.
- ⁸⁸ Q. Xu, Y. Ma, J. Zhang, X. Wang, Z. Feng, C. Li, Enhancing hydrogen production activity and suppressing CO formation from photocatalytic biomass reforming on Pt/TiO_2 by optimizing anatase-rutile phase structure. *J. Catal.* **2011**, *278*, 329-335, doi:10.1016/j.jcat.2011.01.001.
- ⁸⁹ J.H. Montoya, A.A. Peterson, J.K. Nørskov, Insights into C-C Coupling in CO_2 Electroreduction on Copper Electrodes. *ChemCatChem* **2013**, *5*, 737-742, doi:10.1002/cctc.201200564.

CHAPTER 2: GAS-PHASE CO₂ PHOTOREDUCTION WITH ZnO-BASED PHOTOCATALYSTS



1. INTRODUCTION

1.1. CO₂ AS SOURCE OF CHEMICALS AND FUELS

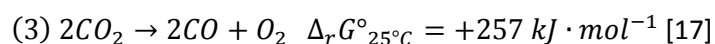
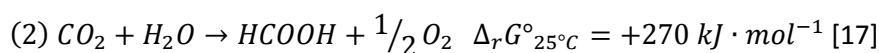
The carbon dioxide (CO₂) is the most important waste gas produced by human activities: in 2018 almost 40 billion tonnes were released in the atmosphere [1]. As already discussed in Preface, it is the main responsible of the climate changes occurring on our planet. Unfortunately, decreasing the CO₂ emissions would not mitigate on a large extent such climate changes, due to the thermal inertia of waterbody [2], and a more complex climate change adaptation strategy is required [3]. Nonetheless, due to its cheapness and large availability, CO₂ represents a potentially huge source of carbon. Currently, the largest application of CO₂ as chemical feedstock is the synthesis of urea and inorganic carbonates [4]. Furthermore, it can be also involved in the synthesis of organic carbonates, polycarbonates and carboxylic acids [5]. These reactions, however, either keep unaltered the carbon oxidation state (C⁴⁺) or require an organic compound as co-reactant, thus limiting the variety of substances potentially achievable from CO₂.

Hydrogenation is an appealing way for CO₂ valorization to a large variety of compounds, useful as fuels or chemicals [6], such as methane (CH₄) [7], methanol (CH₃OH) [8] or carbon monoxide (CO) [9]. These simple molecules can be further converted into a large variety of products: CO can be hydrogenated to liquid alkanes by Fischer-Tropsch reaction [10], while methanol can be dehydrated to olefins [11], gasoline [12] or converted into other chemicals (i.e. formaldehyde or chloromethanes) [13]. Furthermore, carbon-based fuels are more advantageous than pure hydrogen due to easier storability (higher energy density) and having less safety issues [14].

Despite CO₂ represent an appealing platform molecule for a huge variety of substances, the main bottleneck of its valorization is the current lack of a cheap and feasible hydrogen source, as highlighted in Chapter 1.

1.2. CO₂ REDUCTION WITH H₂O: FROM NATURAL TO ARTIFICIAL PHOTOSYNTHESIS

Plants and cyanobacteria are able to convert CO₂ and H₂O, abundant raw materials on Earths, into organic compounds (biomass) using sunlight as energy source [15], producing a huge amount of organic compounds. Unfortunately, the overall efficiency of this process is very low [16]. Mimicking artificially this approach, using H₂O as reductant, would avoid the requirement of H₂ for CO₂ reduction. However, the reactions are strongly endothermic (i.e. Reaction 1 – 3) and an external energy source is thus required.



Renewable thermal energy (i.e. solar) can be used in thermochemical CO₂ reduction [18], needing however special equipment due to the high temperature (T > 1000°C) involved in these processes [19]. Electrocatalytic CO₂ reduction is a potential alternative operating in mild conditions (T < 100°C) [20] and using aqueous solvent [21]. The main drawback of electrolytic technologies, as mentioned in Chapter 1 for water splitting, is the requirement of electric energy, which is usually an expensive energy source.

Resembling the natural reaction, in the artificial photosynthesis concept the CO₂ can be reduced with water in mild conditions exploiting an abundant, cheap and widespread energy source: sunlight [22,23]. Photocatalytic and photoelectrocatalytic processes have been proposed for light-driven CO₂ reduction [24], but the latter will be explained in Chapter 3. The reaction involves the oxidation of water by the photoexcited holes and the reduction of CO₂ by photoexcited electrons, as reported in Figure 1. Hydrogen evolution reaction (HER) can also occur during this process, because its redox potential is similar to those of CO₂ reduction. However, being not the main target of the reaction, HER is considered a side pathway in CO₂ photoreduction [25].

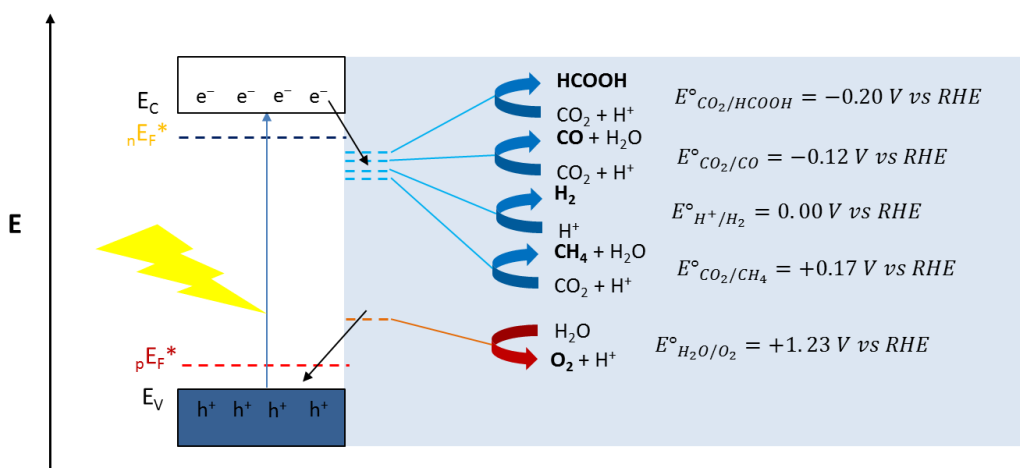


Figure 1. Energy band diagram of SC/reaction mixture interface for CO₂ photocatalytic reduction with water. The energy levels are labelled according to the Preface section. Redox potentials for CO₂ (H₂O) reduction and H₂O oxidation half-reaction are reported in the reversible hydrogen electrode (RHE) scale according to [26].

The overall CO₂ photoreduction mechanism is not still fully understood, but some proposed pathways are generally accepted. The water oxidation is supposed to take place either by surface-stabilized hydroxyl radicals (HO·) or peroxy species, those yields O₂ by a four-step electron transfer [27]. The reduction pathway is more interesting, but also more complex due to the large variety of attainable products [28,29]. Two main mechanisms are generally reported in literature for CO₂ reduction: the carbene pathway and the formaldehyde pathway [30]. The former (Figure 2a) involves the formation of an adsorbed carboxyl radical (COOH·, 1) [31], which undergoes a rapid C-O bond breaking to adsorbed CO (2), which can either desorb or be further deoxygenated to surface adsorbed carbon atoms (3), which finally are hydrogenated to CH₄ (4). The formaldehyde mechanism (Figure 2b) affords a two-step reduction of CO₂ to adsorbed formate (HCOO⁻,

7), either by a bidentate intermediate (CO_2^-) adsorbed through O atoms (6) or by a monodentate carboxyl intermediate adsorbed through C atom (5). The latter is generally recognized to be stabilized in medium with a high dielectric constant such as water [32], thus is the favored mechanism in liquid phase. The formate can be desorbed as formic acid (HCOOH) or, by further hydrogenation (8,9), converted to other oxygenates like formaldehyde (HCHO) and methanol (CH_3OH).

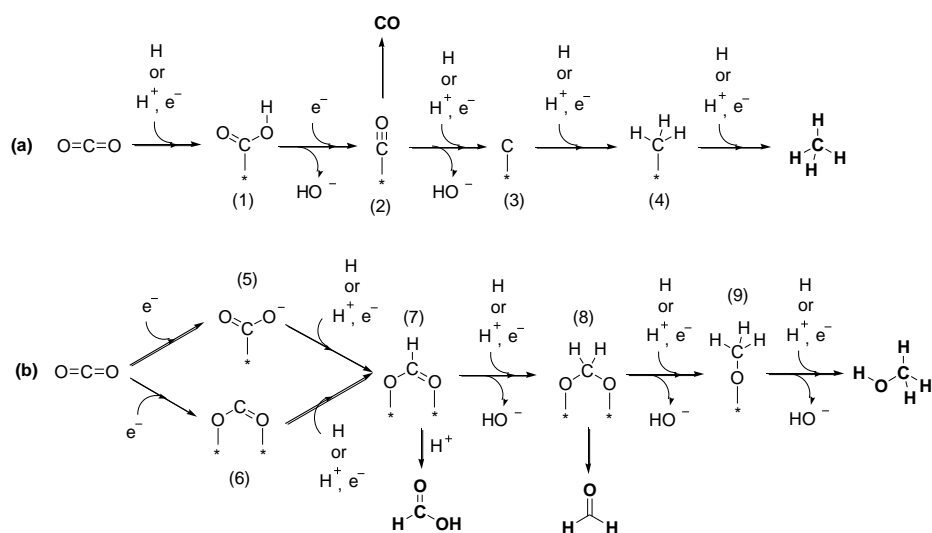


Figure 2. (a) Carbene pathway and (b) formaldehyde pathway mechanisms for CO_2 photoreduction [30]. Hydrogenation is designated to occur with both hydrogen atoms (H) or proton-electron couple (H^+ , e^-).

The activity and selectivity of CO_2 photoconversion is affected by several reaction conditions such as the reaction medium (liquid-solid vs gas-solid), the light intensity, the reaction mixture composition and the reactor geometry, in turn affecting parameters such as CO_2 availability, light and mass transfer [23]. In particular, the gas-solid reaction systems have more advantages over the liquid-solid ones, because:

1. More efficient light transfer in gas CO_2 - H_2O than liquid H_2O (lower refractive index) [33,34]
2. More efficient mass transfer of reactant or products in gas than in liquid phase (higher diffusion coefficient) [35]
3. Tunability of $\text{CO}_2/\text{H}_2\text{O}$ ratio with no solubility limits, affecting both activity and selectivity (in particular the HER) [25]
4. Easier product recovery and facile scale-up [36]

Concerning the photocatalyst, several semiconductors (SC) has been proposed for CO_2 photoreduction. The most reported materials are wide-bandgap ($E_g > 3$ eV), able to harvest only UV photons, such as titanium dioxide (TiO_2) [25], zinc oxide (ZnO) [37], gallium oxide (Ga_2O_3) [38], zinc germanate (Zn_2GeO_4) [39] or zinc sulphide (ZnS) [40]. Beside those, several narrow-bandgap materials ($E_g < 3$ eV), which are able to harvest visible photons too, like tungsten trioxide (WO_3) [41], indium tantalate (InTaO_3) [42], germanium-zinc oxynitride ($\text{Zn}_{1.7}\text{GeN}_{1.8}\text{O}$) [43] or cadmium sulphide (CdS) [40], have been studied. Furthermore, besides the choice of the photocatalyst itself, several material design strategies have been proposed to improve the

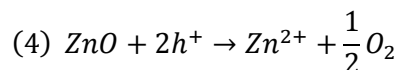
activity or the selectivity, such as heterostructures [44], surface decoration with co-catalysts [39] or base additives [45], scaffolding on porous transparent materials (i.e. mesoporous silica) [46].

Despite the huge research effort, several issues affect the large-scale application of CO₂ photoreduction. The most challenging one is certainly the activity, still very low [47].

1.3. ZINC OXIDE AS PHOTOCATALYST

Zinc oxide as a n-type SC, characterized by a large direct E_g (3.37 eV), that allows an efficient harvesting of UV photons, a large exciton binding energy (60 meV), which improves the photoexcited charge carriers lifetime [48] and electron mobility (115-205 cm²·V⁻¹·s⁻¹), that allows a fast transfer of the charge carriers across the SC [49]. These features make ZnO a promising material for electronic and optoelectronic applications such as light emitting diodes (LED) [50], thin film transistors (TFT) [51] and solar cells [52]. Photocatalysis represents another appealing application [37,53]. Some works revealed a superior photocatalytic performance of ZnO compared to TiO₂ [53,54], both being wide band-gap materials, but the latter exhibiting worse electronic properties than ZnO (excitonic binding energy and electron mobility) [55,56].

Despite its appealing properties, ZnO is known to suffer of photocorrosion, in which the lattice oxygen is oxidized by photoexcited holes (Reaction 4) [57]. This process affords in a reduced activity of the photocatalyst over time, thus limiting its re-usability [58]. Besides the photostability, ZnO is a delicate material, being consumed both in acid and strong alkaline aqueous medium [59].



Besides its intrinsic optoelectronic characteristics, other properties such as the morphology (exposed facets) and native defects, can strongly affect the photocatalytic activity. ZnO can exhibit three crystal structures: the cubic zinc-blende, which grows only on certain substrates (i.e. ZnS), the cubic rocksalt, which is stabilized by high pressure, and the most common hexagonal wurtzite, the most thermodynamically stable [49]. As reported in Figure 3, the latter is characterized by three main surfaces: the non-polar (10-10) plane, the most stable; the Zn-terminated (0001) plane and the O-terminated (000-1) plane, which are characterized by an accumulation of positive and negative charges respectively, and are defined as polar surfaces [60]. The latter are generally recognized to boost up the photocatalytic activity [61,62], thanks to the internal electric field induced by these surfaces, affording reductions reaction to occur on positively charged (0001) surfaces, while oxidations on negatively charges (000-1) surface [63]. The different surfaces also exhibited a diverse response to photocorrosion, being strong and more uniform on (000-1), where photoexcited holes are likely to accumulate, while weaker and localized on defects on (0001) and the non-polar (1010) [64].

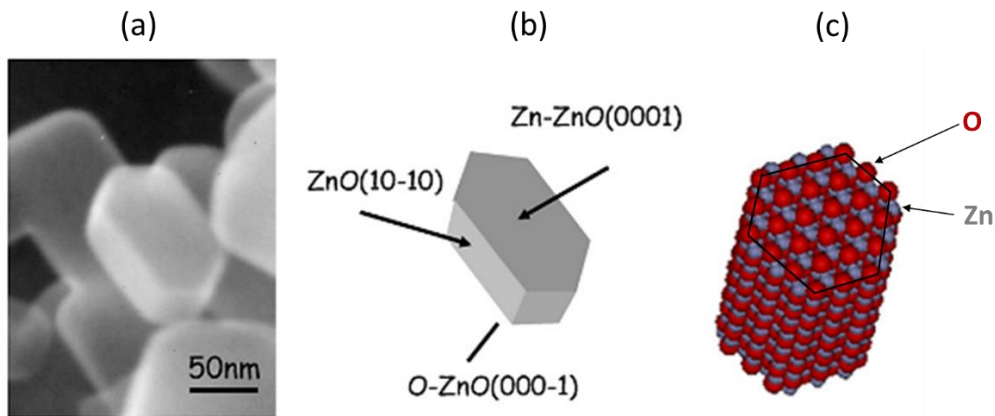


Figure 3. (a) SEM image of hexagonal ZnO morphology; (b) main surfaces of hexagonal ZnO; (c) ball and stick atomic structure of hexagonal ZnO [60].

ZnO is a material strongly affected by intrinsic point defects, due to atoms in improper position within the lattice such as vacancy, a lacking atom, and interstitial defects, atom occupying interstitial position, empty in a perfect crystal. In the specific case of ZnO, oxygen vacancy (V_O) and interstitial zinc (Zn_i) are generally favored in Zn-rich ZnO, while zinc vacancy (V_{Zn}) and interstitial oxygen (O_i) are favored in O-rich ZnO [48]. Such defects induce the formation of intra-gap energy levels, which are the responsible of the well-known luminescence of this material [49], even though the exact location of such levels is largely debated in literature and several interpretations have been proposed [65-67]. Native point defects are also recognized to play an important role on the photocatalytic activity as well [68]. Surface defects have been suggested to improve the photoexcited charge carrier lifetime by trapping, eventually allowing a facile transfer to the reactant [69]. Bulk defects, on the contrary, are supposed to mainly act as recombination center [70]. Furthermore, V_O are generally known to acts as active site for several kind of reactions, allowing the adsorption of the reactant on the surface [71,72].

ZnO was observed by Inoue et al. in 1979 to be active in the CO_2 photoreduction in aqueous suspension [73]. Few reports (Table 1) can be however found in literature concerning the utilization of ZnO in CO_2 photoconversion. However, it is known the reaction to proceed through the formation of surface carbonates, upon CO_2 adsorption, [37] furthermore both $\{0001\}$ surfaces (polar surfaces) [74] and native point defects [37] have been observed to play an important role in determining the photoactivity for CO_2 conversion, as mentioned before. Finally, ZnO was also involved in a highly photoactive heterostructure such as the Cu_2O/ZnO composite, which is able to harvest both UV and visible photons, selectively converting CO_2 to CH_4 . Such behavior has been ascribed to the favorable band alignment and the minimal lattice mismatch between ZnO and Cu_2O , which reduces the interfacial recombination probability [47].

Table 1. Example of ZnO-based photocatalysts used for CO₂ conversion.

Ref.	Material	Conditions	Products	Comments
[37]	ZnO nanoparticles (NP), nanorods (NR) and nanosheet (NS)	150-250°C; ca. 0.1 MPa; gas CO ₂ /H ₂ O (ratio not reported); UV Hg-lamp	CO, CH ₄ , H ₂	Basic zinc carbonate [Zn ₅ (OH) ₆ (CO ₃) ₂] as reaction intermediate; activity enhancement by native point defects; increased activity by increased temperature.
[47]	ZnO-Cu ₂ O heterostructure	r.t.; 0.26 MPa; CO ₂ -saturated 0.2 M Na ₂ CO ₃ aqueous solution; sunlight simulated Xe-lamp	CH ₄ (1080 μmol·g ⁻¹ ·h ⁻¹)	Apparent quantum yield (AQY) 1.5%; 100% selectivity to CH ₄ . Simultaneous excitation of ZnO and Cu ₂ O (Z-scheme) with efficient interfacial charge transfer (small lattice mismatch Cu ₂ O-ZnO)
[75]	Cu-ZnO _{1-x} N _x	50°C; 0.2 MPa; gas CO ₂ /H ₂ O (6.7 molar ratio); UV fluorescent lamp; 70 W·m ⁻²	H ₂ (0.29 μmol·g ⁻¹ ·h ⁻¹), CO (0.49 μmol·g ⁻¹ ·h ⁻¹), CH ₄ , CH ₃ OH	Combustion-synthesized ZnO performed worse than the hydrothermal one due to the lower specific surface area and higher recombination. Cu co-catalyst promotes an enhancement of products yield.
[74]	ZnO	20°C; 0.1 MPa; gas CO ₂ /H ₂ O (ratio not given); sunlight simulated Xe-lamp	CO (3.81 μmol·g ⁻¹ ·h ⁻¹)	More polar {0001} surfaces improves and larger surface area the photoactivity; effect of synthesis contaminants (organic compounds) not well assessed

1.4. THE ISSUE OF CO₂ SUPPLY

Despite the large potential availability of CO₂, large-scale utilization is limited by the fact that highly concentrated CO₂ sources (i.e. offgas from hydrogen chemical plants) are quite scarce, while the most abundant diluted sources (i.e. air or power station flue gas) require a large energy input to capture and enrich CO₂ [76]. Several technologies have been studied for CO₂ capture and purification [77,78], but all of them represent an extra step and require an extra energy input in the CO₂ utilization chain.

An appealing strategy to overcome this issue, is the coupling of both capture and conversion technologies in a same process. Reller *et al.* studied the CO₂ reduction to CH₃OH with an ethanolamine to capture CO₂ in liquid phase [79], while Min Kim *et al.* proposed a Ni-based catalyst mixed with a CaO sorbent, for the dry reforming of methane[80]. Only two cases have been reported in literature for photocatalysis. Wu *et al.* utilized a mesoporous TiO₂-SiO₂ material as photocatalyst, and an ethanolamine solution as CO₂ absorbent and reductant (hole scavenger) [81], similarly to the strategy used by Reller *et al.* This strategy, however, was limited to the liquid phase and used an organic reductant, more expensive than water. Another work reported the utilization of a composite material made of a double layer hydroxide as absorbent and TiO₂ nanoparticles as photocatalyst. CO₂ was captured from the gas-phase in dark, followed by its the photoconversion with H₂O under UV irradiation at 150-200°C [82]. ZnO represent a promising material in this contest of hybrid materials, due to its basic properties which allow CO₂ capture [83] and the previously mentioned photocatalytic activity in CO₂ reduction. To the best of our knowledge, no work has been reported yet on ZnO.

1.5. AIM OF THE CHAPTER

The aim of this chapter is to develop ZnO-based photocatalysts by wet chemistry approaches for the gas-phase CO₂ photocatalytic reduction with water. Specifically, the work is divided in three sub-sections:

1. Evaluation of the effect of the synthetic parameters (precipitation conditions, ageing, annealing and TiO₂ promotion) on the main morphological and structural properties of the materials, such as shape, size and porosity.
2. Evaluation of the effects of the synthetic parameters on the nature of the surface composition, and the optical absorption and emission features, aiming a more detailed picture of their electronic structure.
3. Assessment of the impact of the aforementioned materials properties on the activity toward gas-phase CO₂ photoreduction, and assessment of the hybrid CO₂ capturing-photoconverting behavior of ZnO.

2. MATERIALS AND METHODS

2.1. REAGENTS

The following reagents were used as-received: zinc sulphate heptahydrate ($\text{ZnSO}_4 \cdot 7\text{H}_2\text{O}$, assay > 99%, Sigma Aldrich), zinc nitrate hexahydrate ($\text{Zn}(\text{NO}_3)_2 \cdot 6\text{H}_2\text{O}$, assay > 99%, Sigma Aldrich), titanium isopropoxide ($\text{Ti}(\text{O}^i\text{Pr})_4$, assay > 97%, Sigma Aldrich), sodium carbonate (Na_2CO_3 , assay > 99.5%, Sigma Aldrich), sodium hydroxide (NaOH , assay > 97%, Carlo Erba), polyvinylpyrrolidone (PVP, MW = 40000 $\text{g} \cdot \text{mol}^{-1}$, Sigma Aldrich), isopropanol (i-PrOH, assay > 99.7%, Sigma Aldrich) and ethanol (EtOH, assay > 99.9%, VWR).

2.2 SYNTHESIS

2.2.2. WET CHEMISTRY ZnO SYNTHESIS

The pristine ZnO materials were synthesized starting from a previously reported procedure [84]. A 1.1 M ZnSO_4 aqueous solution was added dropwise to a beaker containing deionized water under vigorous stirring. The pH was kept constant at 9 by the addition of a 9.0 M NaOH or a 1.0 M Na_2CO_3 aqueous solution. The as-obtained suspension was aged at 60°C for 20 hours, then vacuum filtered, washed with deionized water to remove dissolved ions and air-dried at 110°C for 18 hours. The dried product was finally annealed at 400°C or 600°C for 4 hours (ramp: 2 °C·min⁻¹) in air flow (30 mL·min⁻¹). The annealed samples were labelled as follow:

1. 4SZ, precipitated with NaOH and air annealed at 400°C
2. 4CSZ, precipitated with Na_2CO_3 and air annealed at 400°C
3. 6CSZ, precipitated with Na_2CO_3 and air annealed at 600°C

The un-annealed sample precipitated from carbonate, was labelled CSZ.

2.2.3. LOW-TEMPERATURE HYDROTHERMAL ZnO SYNTHESIS

The hydrothermal synthesis was carried out with PVP as stabilizing agent [85]. 14.2 g of PVP were dissolved in 200 mL of a 0.18 M $\text{Zn}(\text{NO}_3)_2$ solution. The resulting solution was then added dropwise a beaker containing deionized water under vigorous stirring. The pH was kept constant at 10 by the addition of a 10.0 M NaOH solution. The as-obtained suspension was aged at 60°C for 18 h in a sealed Teflon tube, then vacuum filtered, washed with deionized water to remove residual compounds and air-dried at 110°C for 18 hours. The dried product was finally annealed at 400°C for 8 hours (ramp: 2 °C·min⁻¹) in air flow (30 mL·min⁻¹). The sample was labelled 4PNZ.

2.2.4. TiO₂-PROMOTED ZnO SYNTHESIS

The TiO₂ was loaded by wetness impregnation. The $\text{Ti}(\text{O}^i\text{Pr})_4$ precursor was dissolved in i-PrOH and added dropwise either to CSZ or to 4CSZ powder, to afford a 0.5 wt. % Ti loading. The impregnated powder was air dried at 110°C for 18 hours and finally annealed at 400°C for 1 hour or 4 hours (ramp: 2 °C·min⁻¹) in air flow (30 mL·min⁻¹). The samples were labelled as follow:

1. T4CSZ, Ti precursor loaded on 4CSZ and air-annealed at 400°C for 1 hour (post-annealing TiO₂ addition)
2. 4TCSZ, Ti precursor loaded on CSZ and air-annealed at 400°C for 4 hour (pre-annealing TiO₂ addition)

2.3. CHARACTERIZATION

The phase composition and crystallite size were measured by X-ray diffraction (XRD) using a Bruker D8 Advance DaVinci powder diffractometer using a sealed X-ray tube (copper anode; operating conditions, 40 kV and 40 mA) and a linear array detector (LynxEye), set to discriminate the Cu K α radiation, coupled with a Ni filter to completely remove the Cu K β component. Data scans were performed in the 2 θ range 5–90° with 0.02° step size and point-detector equivalent counting times of 5 s/step. Quantitative phase analysis and crystallite size determination were performed using the Rietveld method as implemented in the TOPAS v.5 program (Bruker AXS) using the fundamental parameters approach for line-profile fitting. The determination of the crystallite size was accomplished by the Double-Voigt approach and calculated as volume-weighted mean column heights based on integral breadths of peaks.

The specific surface area (SSA) was determined using nitrogen (N₂) physisorption with a TriStar II Plus (Micromeritics) analyzer. The samples were outgassed at 200°C in vacuum for 2 hours to clean the surface before the analysis. The N₂ adsorption-desorption isotherms were then acquired at – 196 °C and the SSA determined by the Brunauer-Emmet-Teller (BET) equation [86] fitted in the 0.04 – 0.3 P/P° range.

The morphology was evaluated with a Field Emission Electron Scanning Microscopy (FE-SEM) LEO 1525 ZEISS equipped with in-lense detector. The chemical composition was determined using a Bruker Quantax EDS. The samples were deposited onto conductive carbon adhesive tape and metallized with chromium.

The optical absorbance was measured by diffuse-reflectance spectroscopy (DRS), through an integration sphere equipped Cary100 UV-vis spectrophotometer (Agilent). The spectra was reported through the Kubelka-Munk function (Equation 1), where R_{∞} is the reflectance at an infinite thick layer of the sample [87].

$$f(R_{\infty}) = \frac{(1 - R_{\infty})^2}{2R_{\infty}}$$

Equation 1. Kubelka-Munk function.

The bandgap (E_g) of the material was determined by the Tauc relation (Equation 2), where the Kubelka-Munk function ($f(R_{\infty})$) is used in place of the absorption coefficient (α), h the Plank constant ($6.626 \cdot 10^{-34}$ J·s), ν the photon frequency in s⁻¹, C a constant and E_g the bandgap energy. For direct allowed optical transition the exponent is set to $n = \frac{1}{2}$, while for indirect transitions is set to $n = 2$. The E_g was determined as intercept plotting $(f(R_{\infty})h\nu)^{1/n}$ vs $h\nu$ [88].

$$f(R_{\infty})h\nu = C(h\nu - E_g)^n$$

Equation 2. Tauc relation.

The Urbach energy (E_U), related to the density of states of defects [89], was assessed by the Urbach relation (Equation 3), where $f(R_\infty)$ is used in place of the optical absorption coefficient (α), h the Planck constant ($6.626 \cdot 10^{-34}$ J·s), ν the photon frequency in s^{-1} , α_0 and E_0 are temperature-dependent constants.

$$f(R_\infty) = \alpha_0 \exp\left(\frac{h\nu - E_0}{E_U}\right)$$

Equation 3. Urbach relation.

The E_U is assessed from the near absorption-edge slope of $\ln(\alpha)$ vs $h\nu$ [90].

The optical emission (photoluminescence, PL) was measured at r.t. using a spectrofluorimeter Edinburg Instrument FLS-980 in the 350-750 nm range, using a 300 nm excitation source. The spectra were processed, after baseline correction, by means of a non-linear fitting using a Gaussian function (Origin 9.0 software).

The surface functional groups through Fourier-transform IR (FTIR) spectroscopy using attenuated total reflectance (ATR), by means of a Bruker Vertex 70 spectrophotometer equipped the Harrick MVP2 ATR cell, with resolution 4 cm^{-1} . The spectra were further processed, after baseline correction, through a non-linear fitting by means of a Gaussian function (Origin 9.0 software).

The carbonate thermal decomposition un-annealed materials, was evaluated through thermal gravimetric analysis (TGA) coupled with differential thermal analysis (DTA) with a NETZSCH STA 409 PC/PG instrument in air flow ($20 \text{ mL} \cdot \text{min}^{-1}$) in the temperature range r.t.- 1000°C (ramp: $10^\circ\text{C} \cdot \text{min}^{-1}$).

The surface composition was analyzed by X-ray photoelectron spectroscopy (XPS), using a Perkin-Elmer Φ 5600ci spectrometer. The samples were analyzed using a non-monochromatic Al $K\alpha$ radiation (1486.6 eV) in the 10^{-6} Pa pressure range. The analyzed sample area was around 0.5 mm^2 . In addition to the wide range survey spectrum, single spectra were recorded for Zn2p, ZnLMM, O1s, Ti2p and O1s regions. All the binding energy (BE) values are referred to the Fermi level. The correct calibration of the BE scale was verified by checking the position of both Au4f_{7/2} and Cu2p_{3/2} bands (from pure metal targets), falling at 84.0 eV and 932.6 eV, respectively. The raw spectra, after a Shirley-type background subtraction, were fitted using a non-linear least-square fitting program adopting Gaussian–Lorentzian peak shapes for all the peaks (XPSPEAK41 software). Because of surface charging, samples presented a shift of the bands toward higher BEs (of around 2 eV): the charging effect was corrected by using an internal reference (Zn2p_{3/2} band centered at 1021.4 eV in ZnO compound [91]). The uncertainty of the determined BE values was not larger than 0.2 eV. The atomic composition of the sample analyzed region (about 5-10 nm of thickness from the surface) was evaluated using sensitivity factors as provided by θ V5.4A software, after a non-linear least-square fitting process to calculate the area of the different XPS bands. The uncertainty of the atomic composition of the different elements is lower than 10%. A benchmark ZnO (assay > 99.99%, Carlo Erba) was used as reference material.

2.4. REACTIVITY TEST

The reactivity tests were carried out with the rig schematized in Figure 4, following a previously reported procedure [29]. A borosilicate glass flat-type photoreactor was used, with an inner volume of 1.9 mL and an exposed active area of 6 cm². The photocatalyst (10 mg) was dispersed in EtOH, then immobilized onto the inner wall of the photoreactor, by a dropwise addition of the suspension to the heated photoreactor and completing the solvent evaporation at 110°C for 1 h in an oven. The prepared photoreactor was set on the rig (c). The reaction was carried out with a 13.3 molar ratio CO₂/H₂O or He/H₂O gas mixture, obtained by flushing the gas (CO₂ or He) in a bubbler filled with milliQ water and kept at 40°C (b). After having purged the air from the rig and having reached a constant gas mixture composition, the photoreactor was closed, locking 62 μmol of CO₂ (or He) and 5 μmol of H₂O vapor within it. A Helios Italquartz 125 W medium pressure Hg lamp was used as light source (d), with a main emission line at 365 nm and an intensity of 60 W·m⁻², monitored by a Delta Ohm HD 2302.0 photo-radiometer and a LP 471 probe. No extra heating or cooling was supplied, and the inner temperature of the photocatalyst-coated photoreactor upon irradiation was ca. 70°C. The reaction was carried out for 6 h. The reaction mixture was finally analyzed through a 6890 HP gaschromatographer, equipped with a Porapak Q packed column and a thermal conductivity detector (TCD). The products were quantified by means of calibration curve of H₂, CH₄ and O₂.

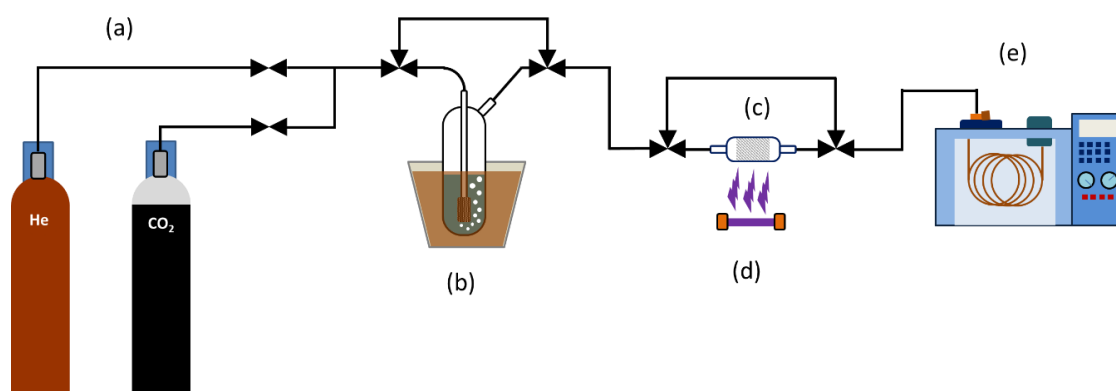


Figure 4. Scheme of the lab-made rig for gas-phase CO₂ photoreduction.

The photocatalytic activity was expressed as turnover frequency (TOF) (Equation 4), where mol_P are the detected moles of reaction product after 6 h of reaction, m_{CAT} the mass of the used photocatalyst and τ the reaction time.

$$TOF = \frac{mol_P}{m_{CAT} \cdot \tau}$$

Equation 4. TOF determination.

The photocatalytic activity was also normalized by the SSA of the photocatalyst and defined as TOF* (Equation 5), where S_{BET} is the SSA.

$$TOF^* = \frac{mol_P}{m_{CAT} \cdot \tau} \cdot \frac{1}{S_{BET}}$$

Equation 5. TOF* determination.

The efficiency of photon utilization, namely the apparent quantum yield (AQY), was expressed as reported in Equation 6. Here, mol_{CH_4} and mol_{H_2} are the detected moles of products; 8 and 2 are the photoelectrons required to reduce CO_2 to CH_4 and H_2O to H_2 , respectively; h the Plank constant ($6,626 \cdot 10^{-34}$ J·s); c the light velocity ($2,998 \cdot 10^8$ m·s⁻¹); I light intensity; A the exposed photoreactor wall and τ the reaction time.

$$AQY = \frac{mol_{CH_4} \cdot 8 + mol_{H_2} \cdot 2}{mol_{incoming\ photons}} = \frac{(mol_{CH_4} \cdot 8 + mol_{H_2} \cdot 2) \cdot h \cdot c \cdot N_A}{I \cdot A \cdot \tau}$$

Equation 6. AQY determination.

The energy efficiency, namely the solar-to-fuel efficiency (STF), was expressed as reported in Equation 7. Where mol_{CH_4} , mol_{H_2} , I , A and τ are the same values of Equation 6, while $\Delta_C H^{25^\circ C}_{CH_4}$ ($- 888$ kJ·mol⁻¹) and $\Delta_C H^{25^\circ C}_{H_2}$ ($- 241$ kJ·mol⁻¹) are the enthalpy of combustion of CH_4 and H_2 , respectively.

$$STF = \frac{E_{OUT}}{E_{IN}} = \frac{mol_{CH_4} \cdot \Delta_C H^{25^\circ C}_{CH_4} + mol_{H_2} \cdot \Delta_C H^{25^\circ C}_{H_2}}{I \cdot A \cdot \tau}$$

Equation 7. STF determination.

3. RESULTS AND DISCUSSION

3.1. STRUCTURAL AND MORPHOLOGICAL CHARACTERIZATION OF ZnO MATERIALS

The ZnO materials were synthesized by a wet-chemistry method, namely precipitation, widely used for the preparation of porous materials used in traditional heterogeneous catalysis [92]. Synthetic parameters such as the precipitating agent and the annealing temperature can strongly affect the properties of a photocatalyst [93]. For this reason the effect of two precipitating agent (NaOH vs Na_2CO_3 , samples 4SZ and 4CSZ respectively), commonly reported for wet-synthesized ZnO [94], and two annealing temperature (400°C vs 600°C , samples 4CSZ and 6CSZ respectively) were studied. Furthermore, the presence of a small quantity of a different material, named promoter, potentially affects the properties of photocatalyst (i.e. TiO_2 on ZnO) [54]. Thus, TiO_2 (0.5 wt. % of elemental Ti), chosen as promoter, was added either on annealed ZnO (post-annealing TiO_2 addition, sample T4CSZ) or on un-annealed precipitated Zn-based material (pre-annealing TiO_2 addition, sample 4TCSZ) to evaluate its effect. Eventually, a hydrothermal method was involved as comparison to precipitation, using PVP as capping agent aiming to tune the shape of ZnO (sample 4PNZ) [85].

The XRD patterns of the annealed samples are reported in Figure 5a. All the materials contained the hexagonal wurtzite ZnO structure (zincite, ICDD PDF card no. 36-1451), characterized by three main diffraction planes: (10-10), (0002) and (10-11). Two samples exhibited some more differences. 4SZ (black line) was a mixture of two phases: zincite (57 wt.%) and zinc oxide sulphate ($\text{Zn}_3\text{O}(\text{SO}_4)_2$, 43 wt. %) (ICDD PDF card no. 31-1469), the latter ascribable to the weak peaks at $2\theta < 30^\circ$. 4PNZ contained a fraction of amorphous material, related to the hump at $2\theta < 20^\circ$. No peaks ascribable to TiO_2 were detected on T4CSZ and 4TCSZ, suggesting being present as very small NPs or as amorphous material. The N_2 physisorption isotherms in Figure 5b, can be ascribed to mesoporous material (type IV isotherms according to IUPAC classification). Being the hystereses close to $P/P^0 = 1.0$, these materials contained also a fraction of macropores [95].

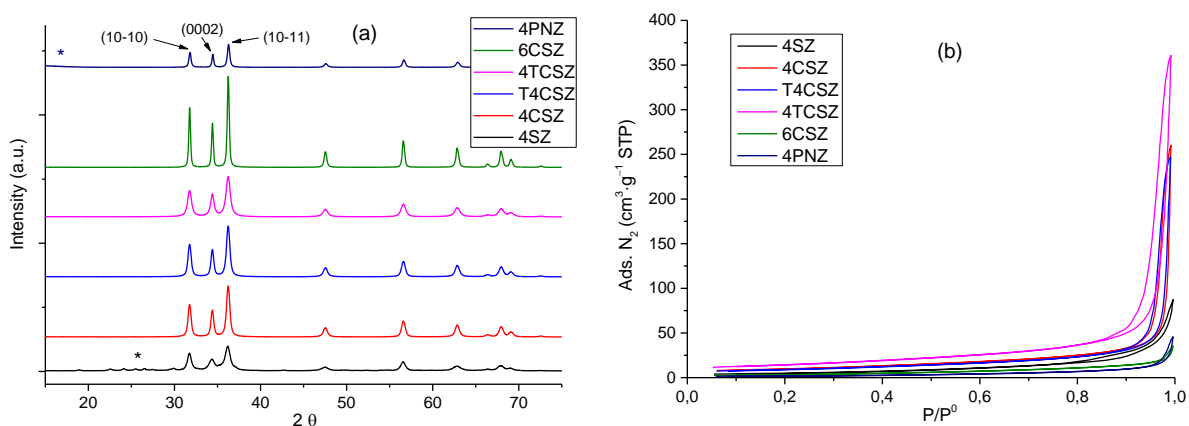


Figure 5. (a) XRD diffractograms and (b) N_2 physisorption isotherms of ZnO-based materials. The asterisks indicate the $\text{Zn}_3\text{O}(\text{SO}_4)_2$ phase (black) and the amorphous phase (blue) on the XRD diffractograms.

XRD and N₂ physisorption can give some more details on the structural properties of the material. In particular the average size of crystallites, the specific surface area (SSA) and the intensity ratio of (10-10) vs (0002) peaks ($I_{(10-10)}/I_{(0002)}$). A higher value of the latter is usually related to a larger amount of polar {0001} planes composing the material surface [74]. All these structural parameter are summarized in Table 2. Generally, the trend of crystallites size followed that of SSA: smaller crystallites, obtained by either low temperature annealing or the pre-annealing TiO₂ addition, were associated with larger SSA. Two exceptions to this trend were observed when using a different precipitating agent (4SZ) or a different synthetic procedure (4PNZ). The $I_{(10-10)}/I_{(0002)}$ ratio was observed to change. The highest values were obtained by using NaOH as precipitating agent (4SZ) or higher annealing temperature (6CSZ), while the lowest ones by means of the hydrothermal synthesis (4PNZ) or pre-annealing TiO₂ addition (4TCSZ). Finally, as expected, post-annealing TiO₂ addition (sample T4CSZ), had no appreciable effect on crystallite size, exposed facets or SSA.

Table 2. Summary of crystallite size, $I_{(10-10)}/I_{(0002)}$ and S_{BET} of ZnO-based materials.

Sample	Crystallite size (nm)	$I_{(10-10)}/I_{(0002)}$ ratio	S_{BET} (m ² ·g ⁻¹)
4SZ	11	1.50	19
4CSZ	18	1.20	35
T4CSZ	17	1.20	33
4TCSZ	14	1.15	51
6CSZ	42	1.35	13
4PNZ	37	1.15	6

The morphology was further examined through SEM. The 4SZ sample was composed of micrometer-sized flakes with a rough surface (Figure 6c), in turn forming bigger agglomerates (Figure 6a and Figure 6b). As observed by XRD, EDX, these micro flakes contains sulfur (Figure 6g), which was highly dispersed over the flakes (Figure 6f), suggesting both ZnO and Zn₃O(SO₄)₂ crystallites to be well dispersed on this microstructure.

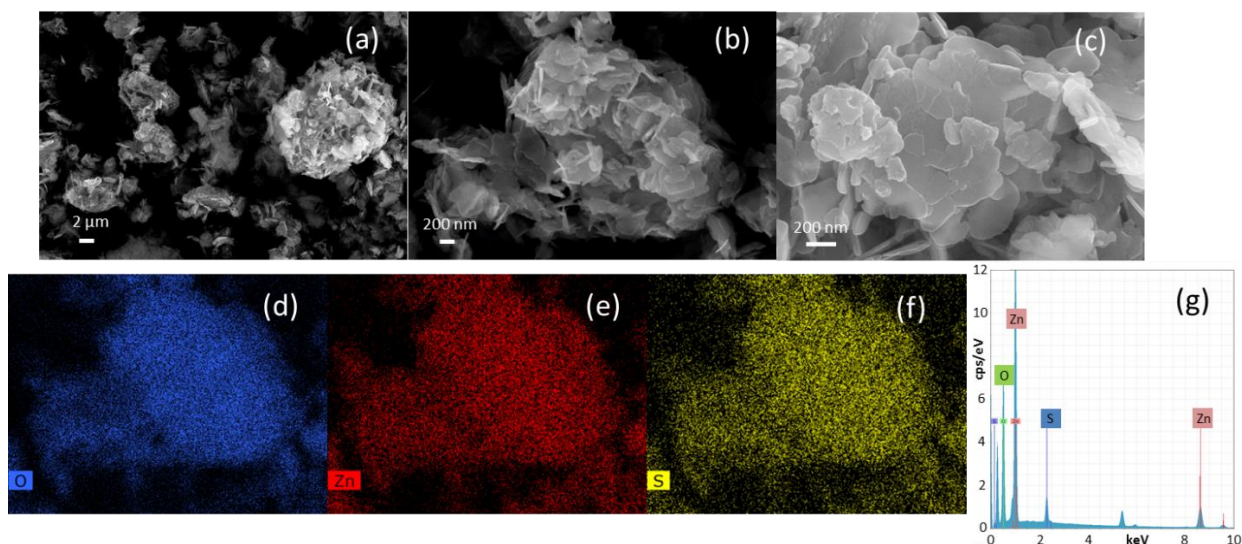


Figure 6. (a), (b), (c) SEM images of 4SZ at different magnification. (d) O, (e) Zn, (f) S EDX elemental mapping. (g) EDX spectrum.

The samples prepared using Na_2CO_3 as precipitating agent revealed a different morphology: regardless the annealing temperature or the addition of TiO_2 , the particles are boxy shaped (Figure 7). This clearly point out the role of the precipitating agent not only in determining the composition of ZnO, but also the shape. As observed for crystallite size determined through XRD analyses, the size of such boxy-shaped particles changed as well, depending on the synthetic procedure. The post-annealing TiO_2 addition keep almost unchanged the size (Figure 7b and Figure 7b). The pre-annealing TiO_2 addition, slightly reduced the particle size (Figure 7f), while increasing the annealing temperature, enlarged the NPs (Figure 7h). The amount of elemental Ti by EDX analyses in both T4CSZ (Figure S1d) and 4TCSZ (Figure S2d) was 0.5 at. %, roughly half of the expected 1.0 at. % (0.5 wt. %). Furthermore, the elemental mapping (Figure S1 and Figure S2) evidenced the TiO_2 to be highly dispersed over both the agglomerates, as supposed from XRD diffractogram.

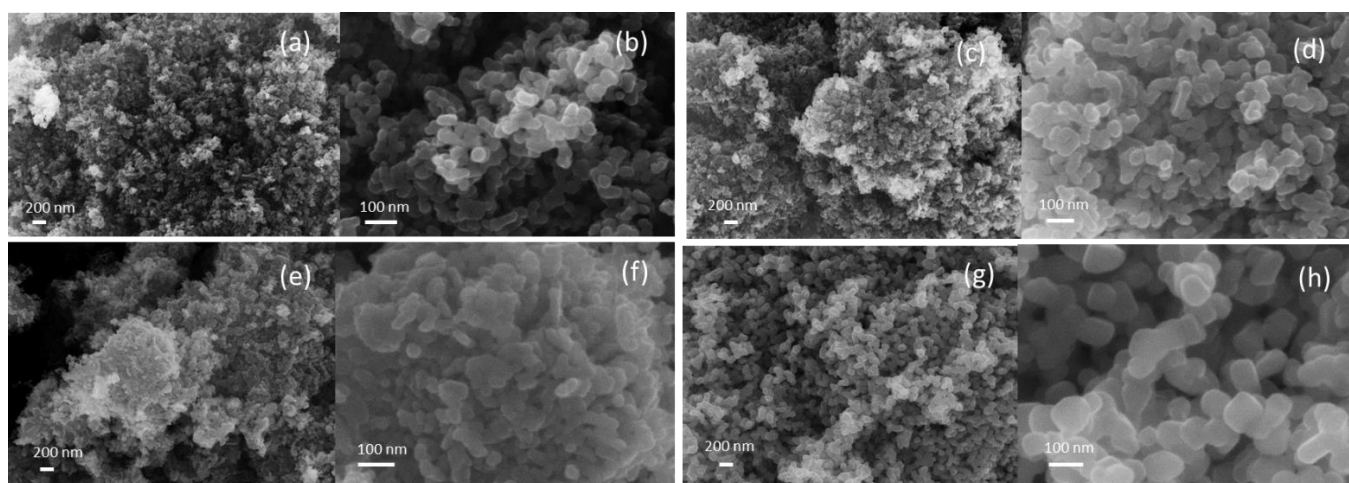


Figure 7. SEM images at different magnification of (a),(b) 4CSZ; (c), (d) T4CSZ; (e), (f) 4TCSZ; (g), (h) 6CSZ.

The hydrothermal-synthesized sample, 4PNZ, exhibited another different shape: micro-spindles ca. $1.0 \mu\text{m}$ long and 200-300 nm thick (Figure 8). Furthermore, the $I_{(10-10)}/I_{(0002)}$ ratio suggested a preferential growth

along the [0001] direction (z-axis of the hexagonal wurtzite structure), as expected by the addition of PVP as capping agent [85]. Nevertheless, as observed by XRD analysis, this elongated micro-particles was hypothesized to be composed of ZnO NPs (ca. 37 nm) mixed within an amorphous matrix.

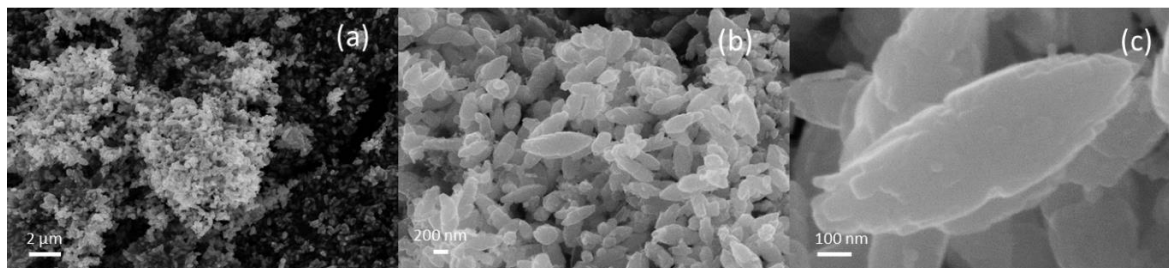


Figure 8. (a), (b), (c) SEM images at different magnification of 4PNZ.

To summarize this section, the most relevant morphological and structural difference was observed by using a different precipitating agent (4SZ) or a hydrothermal synthesis (4PNZ). The former afforded plate-like particles, with a higher fraction of {0001} surface planes but also $Zn_3O(SO_4)_2$ impurity, while the latter formed micro-sized spindle-like elongated particles, with a higher content of amorphous ZnO. On the contrary, using carbonate as precipitating agent crystalline, phase-pure, boxe-shaped ZnO NPs were obtained. Their size and porosity were easily tuned by changing the annealing temperature, affording larger NPs with a lower SSA and higher temperature, or by pre-annealing TiO_2 addition, which decreased the size of the NPs and improves the SSA. Moreover, the amount of polar {0001} planes on the surface was slightly increased by increasing the annealing temperature or decreased by pre-annealing TiO_2 promotion. Finally, post-annealing TiO_2 promotion kept almost unchanged the structural and morphological features.

3.2. SURFACE AND OPTICAL CHARACTERIZATION OF ZnO MATERIALS

The samples (except for 4SZ) were further characterized aiming a comprehensive knowledge of their surface and optical properties.

The XPS survey spectra (not shown), suggested the presence of Zn, O, C and Ti on the surface (the first 5-10 nm) of the samples. The atomic fraction of each element is summarized in Table 3. The presence of ZnO was confirmed through the Auger parameter (Equation 8), equal to 2010.0 eV for all the samples, which correspond to Zn^{2+} in ZnO lattice [96].

$$\alpha = E_K(Zn\ LMM) + E_{BE}(Zn2p_{3/2})$$

Equation 8. Auger parameter (α) relation. $E_K(ZnLMM)$ is the kinetic energy of LMM Auger electrons; $E_{BE}(Zn2p_{3/2})$ is the binding energy of $Zn2p_{3/2}$ line.

Titanium was found only on T4CSZ and 4TCSZ (Figure S3), and its BE (458.4 eV for both samples) corresponds to Ti^{4+} in TiO_2 lattice, with no appreciable presence of Ti^{3+} [97]. The atomic fraction of Ti on the surface (Table 3) was twice than those detected by EDX analyses, suggesting TiO_2 to be mainly located on the first - nm

above the surface. Along with XRD and SEM-EDX analyses, it was supposed tiny TiO_2 NPs to uniformly decorate the surface of both T4CSZ and 4TCSZ.

The surface stoichiometry of ZnO (O/Zn ratio in Table 3) was observed to be strongly affected by the annealing temperature. Indeed, despite being performed in an oxidative medium, the lower annealing temperature (4CSZ, T4CSZ, 4TCSZ, 4PNZ) afforded a Zn-rich surface (O/Zn < 1), becoming O-rich (O/Zn > 1) at higher temperature (6CSZ). On the contrary, the benchmark ZnO reference had a stoichiometric surface (O/Zn = 1).

Table 3. Atomic surface composition of ZnO samples.

Sample	% at. Zn	% at. O	% at. C	% at. Ti	O/Zn ratio
ZnO	45	45	9	-	1.00
4CSZ	52	41	7	-	0.80
T4CSZ	53	40	5	1	0.75
4TCSZ	53	40	5	1	0.75
6CSZ	44	50	5	-	1.10
4PNZ	45	42	12	-	0.90

All the samples exhibited two different types of O signals (Figure 9a), namely O_a (530.0 eV) ascribable to lattice O²⁻ ions [98], and O_b (531.7 eV) ascribable to O²⁻ ion in defective matrix [99], hydroxyl moiety, H₂O or inorganic carbonates [100]. The relative amount of these two type of oxygen atoms, evaluated by the deconvolution of the O 1s band (Figure S4 to Figure S9), was observed to be comparable for all the prepared samples, with the only exception of the reference ZnO (Table S1). This suggested a similar concentration of surface defects in all the synthesized materials.

Three types of C signals can be also observed (Figure 9b): C_a (285.0 eV) which is ascribable to adventitious hydrocarbons; C_b (286.0 eV) ascribable to organic oxygenates compounds, and C_c (289.0 eV), ascribed to inorganic carbonates (CO₃²⁻) or hydrogen carbonates (HCO₃⁻) [101]. The latter was likely to arise from the adsorption of atmospheric CO₂ over the surface of ZnO, being a material with basic properties able to react with an acid gas such as CO₂ [102,103]. The carbonate anions involved in the synthesis was less likely to contribute to the observed species, because the annealing temperature exceeded the decomposition temperature of Zn carbonate species (ca. 250-270°C) [104]. The strong endothermic peak at 265°C observed in the TG-DTA thermogram (Figure S10) of the carbonate-precipitated un-annealed material (CSZ), further confirms the carbonate removal by means of the air annealing treatments used in this work.

As for oxygen, the relative amount of these three type of carbon atoms was evaluated through the deconvolution of the C 1s band (Figure S4 to Figure S9). As reported in Table S1, the C_b component was found only on 4PNZ, suggesting an incomplete burning of the PVP used during the synthesis, while the concentration of surface (bi)carbonates (C_c) was comparable for all the sample.

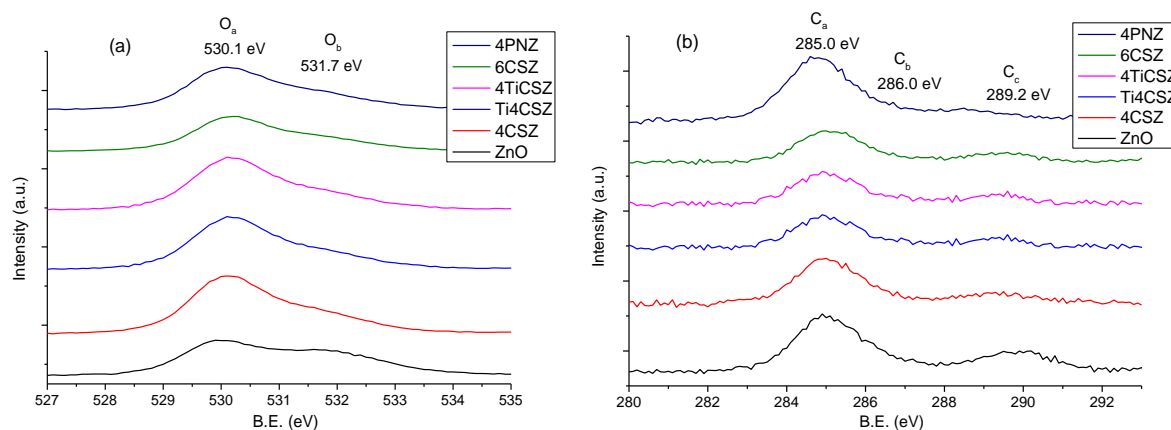


Figure 9. (a) O1s and (b) C1s XPS signals of ZnO samples.

The FTIR spectra (Figure 10a) revealed the surface to contain two different moiety. The large band at $\nu > 3000 \text{ cm}^{-1}$ (O–H stretching, $\nu_{\text{O-H}}$) [105] and the shoulder at $1630 - 1640 \text{ cm}^{-1}$ (O–H bending, $\delta_{\text{O-H}}$) [106] evidenced the presence of hydroxyl groups or adsorbed water. The two bands at $1250 - 1750 \text{ cm}^{-1}$ (symmetric and asymmetric O–C–O stretching, $\nu_{\text{O-C-O}}$) indicated the presence of carbonates [102]. Furthermore, on 4PNZ the two sharp peaks at 1327 cm^{-1} and 1520 cm^{-1} (asterisks in Figure 10a), can be generally ascribed to C–C or C–O bonds in organic compounds [107], confirming the presence of unburnt organic residues due to PVP.

The $\nu_{\text{O-H}}$ band revealed some more information concerning the nature of facets on the surface. Indeed the “truncated” shape of this band at $\nu > 3370 \text{ cm}^{-1}$ on 4PNZ and 4TCSZ (black arrows in Figure 10b) compared to the other samples, pointed out a lower fraction of polar {0001} planes to compose the surface of the formers [105], in good agreement with the XRD analyses.

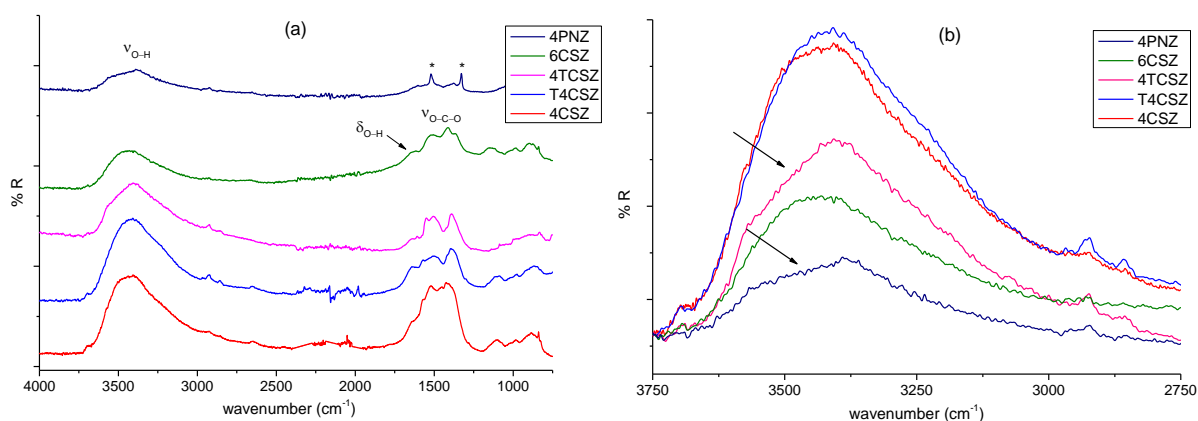


Figure 10. (a) wide-range ATR-FTIR spectra and (b) high wavenumber range ATR-FTIR spectra of ZnO-based samples.

Further details on the composition of the surface were obtained by the deconvolution of the $1200 - 1800 \text{ cm}^{-1}$ spectral region (Figure S11 to Figure S13), identifying the $\delta_{\text{O-H}}$ band ($1631 - 1644 \text{ cm}^{-1}$), the symmetric $\nu_{\text{O-C-O}}$ band ($1366 - 1407 \text{ cm}^{-1}$) and the asymmetric one ($1508 - 1536 \text{ cm}^{-1}$) [102]. The relative amount of carbonate vs hydroxyl moiety on the surface was qualitatively esteemed as ratio between the areas of $\nu_{\text{O-C-O}}$ (symmetric and asymmetric) and $\delta_{\text{O-H}}$ bands and summarized in Table 4. On 4PNZ, it was not possible to

clearly identify the $\delta_{\text{O-H}}$ band. The most relevant differences were observed by the two TiO_2 loading method. When compared to the un-promoted material (4CSZ), the post-annealing TiO_2 addition (T4CSZ) revealed a surface richer in hydroxyl groups. Since TiO_2 exhibits a lower affinity for CO_2 (carbonates) [45], this suggested TiO_2 NPs to be mainly located on the surface. On the contrary, the pre-annealing TiO_2 addition (4TCSZ) showed a surface similar to 4CSZ. This can be ascribed either to TiO_2 NPs partially buried within the sub-surface layer (10 nm), since the Ti amount found by XPS was the same regardless its loading method, or more spaced on the surface, due to the larger SSA on 4TCSZ. The intermediate value found by high temperature annealing (6CSZ) can be related to the O-rich surface, supposed to reduce the amount of O-vacancy, generally as the CO_2 adsorption sites [72].

Table 4. Areas ratio of $\nu_{\text{O-C-O}}$ (symmetric and asymmetric components) vs $\delta_{\text{O-H}}$ of ZnO-based samples.

Sample	$\nu_{\text{C-O-C}}/\delta_{\text{O-H}}$
4CSZ	8
T4CSZ	3
4TCSZ	10
6CSZ	6

The optical properties of absorption and emission of the ZnO materials were further investigated. The optical absorption revealed a sharp band in the UV region ($\lambda < 400$ nm) (Figure 11), typical of a wide-bandgap material such as ZnO.

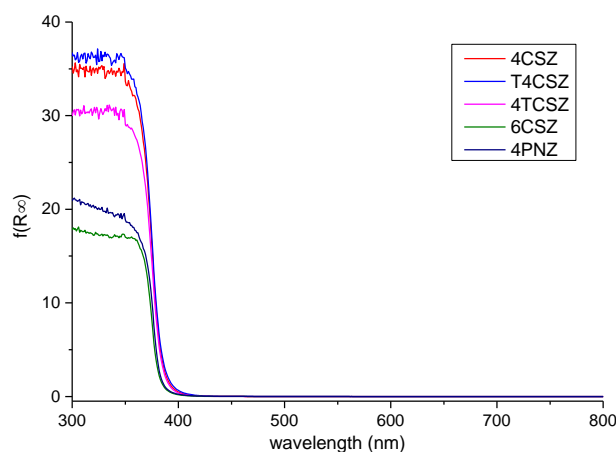


Figure 11. UV-absorption spectra of ZnO-based materials.

The E_g , esteemed from Tauc plots (Figure S14a) and summarized in Table 5, was equal to 3.27 eV for all samples, excluding quantum confinement effect to affect its value [108]. The E_U parameter, assessed from the Urbach plots (Figure S14b), was found to be comparable for all the sample, with a slightly higher value for 4PNZ (Table 5). Being related to the density of intra-band states [108], a comparable defects density for all the samples was suggested, in good agreement with the hypotheses drawn by XPS analyses. A slight higher

E_U was observed on 4PNZ, in agreement with the presence of amorphous ZnO, in turn increasing the intra-band states density.

Table 5. E_g and E_U values for ZnO-based samples.

Sample	E_g (eV)	E_U (meV)
4CSZ	3.27	69
T4CSZ	3.27	76
4TCSZ	3.27	70
6CSZ	3.28	79
4PNZ	3.27	93

The optical emission revealed two type of bands (Figure 12a). The peak at $\lambda < 400$ nm (inset in Figure 12a) is the near-band edge emission (NBE), related to the direct E_C -to- E_V radiative relaxation of photoexcited charge carriers. The weakness of this band is typical of nanomaterials, where surface defects play a major role in the luminescence [109]. Nonetheless, the strongest NBE observed on 6CSZ can be ascribed to a bigger and crystalline core of the ZnO NPs, as evidenced by XRD, compared to the other materials. The stronger emission in the visible range was ascribed, as already anticipated, to intra-gap states between E_C and E_V , arising from native point defects on the surface on the materials [66]. The spectra deconvolution of the visible region (Figure S15 to Figure S17), allowed three emission bands to be recognized: a red (1.73 – 1.80 eV), an orange (2.02 – 2.10 eV) and a green one (2.40 eV), the latter observed only on 6CSZ. The luminescence intensities for both the red and orange bands (Figure 12b), can be ranked as follows: 4PNZ > 6CSZ > 4TCSZ \approx T4CSZ > 4CSZ.

The observed visible emission of the ZnO materials were supposed to arise from a radiative transition between the same energy level, thus involving the same type of defects. Furthermore, since the density of surface defects was supposed to be comparable for all the samples, as evidenced by XPS and the E_U , it was proposed only a fraction of such defects to be involved in radiative relaxation of the photoexcited charge carriers, so that competitive non-radiative relaxation phenomenon was likely to occur. The different treatment on the samples, had different effect. The addition of TiO_2 , either on pre- or post-annealed ZnO (4TCSZ and T4CSZ, respectively), improved the emission intensity. TiO_2 was hypothesized to form a heterojunction with ZnO [110], acting as electron sink for photoexcited electrons which were then transferred to the ZnO luminescence centres, eventually reducing the non-radiative recombination probability. Increasing the annealing temperature (6CSZ), further enhanced the luminescence: as observed by the appearance of a NBE, the bigger and crystalline NPs core of ZnO was supposed to allow a more efficient charge carrier generation and subsequent transfer to the surface, where the emission take place. The strongest visible emission on ZnO (4PNZ) could be linked to the presence of the amorphous phase, likely to

induce a massive radiative recombination phenomenon in the bulk rather than on the surface. Indeed, the intra-gap states density was higher than the other samples, but the amorphous component was hypothesized to be buried within the elongated micro-particles of this material.

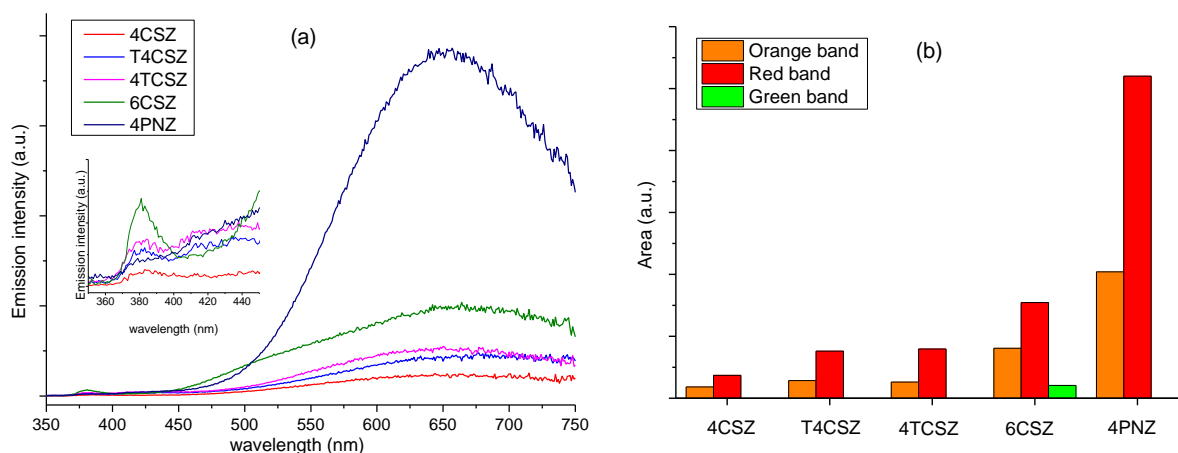


Figure 12. (a) Photoluminescence spectra ($\lambda_{EX} = 300$ nm) and (b) green, orange and red contribution to the overall visible luminescence of ZnO-based materials.

Despite a clear interpretation of the luminescence phenomena in ZnO is still debated in literature, a general energetic picture of the synthesized ZnO was proposed and represented in Figure 13. The E_C position on RHE scale can be estimated using Equation 9, where χ is the ZnO electronegativity (5.79 eV), 4.5 is the free electron energy on RHE scale and E_g the bandgap evaluated by Tauc plots [111]. Since the E_g was observed to be constant for all the samples, -0.34 V vs RHE and $+2.92$ V vs RHE were the energetic position of E_C and E_V , respectively.

$$E_C = \chi - 4.5 - 0.5E_g$$

Equation 9. Empirical equation for E_C determination.

It is generally accepted the n-type behaviour of ZnO to originate from interstitial zinc (Zn_i) states located just below (0.2 – 0.4 eV) the E_C [112], assessing their position between -0.14 V vs RHE and $+0.055$ V vs RHE. The red and orange emission was ascribed to oxygen vacancy (V_O) states (pathways 2 and 3), as proposed by some authors [65], favoured in a Zn-rich surface and supposed to be located ca. 1.75 eV below Zn_i states. Interstitial oxygen (O_i) states (pathway 4) could also induce the orange-red emission [113]. Xu *et al.* proposed such levels to be located below V_O states [114] and, despite O_i are likely to be favoured in O-rich surface (6CSZ), they could be present also in the other samples. They were supposed to be located ca. 2.05 eV below Zn_i states. The effect of TiO_2 , previously described and pictured in pathway 5, was to act as temporary photoexcited electron sink, then transferring them to Zn_i states, finally affording a radiative relaxation to V_O or O_i states. The green emission that appeared on 6CSZ was likely to arise from zinc vacancy (V_{Zn}) states (pathway 6) [67], defects favoured on O-rich surfaces and located ca. 2.40 eV below Zn_i states. According to

this proposed energetic picture, Zn_i states are always involved in the radiative transition of ZnO, supposing them to act as intermediate sink for photoexcited electrons.

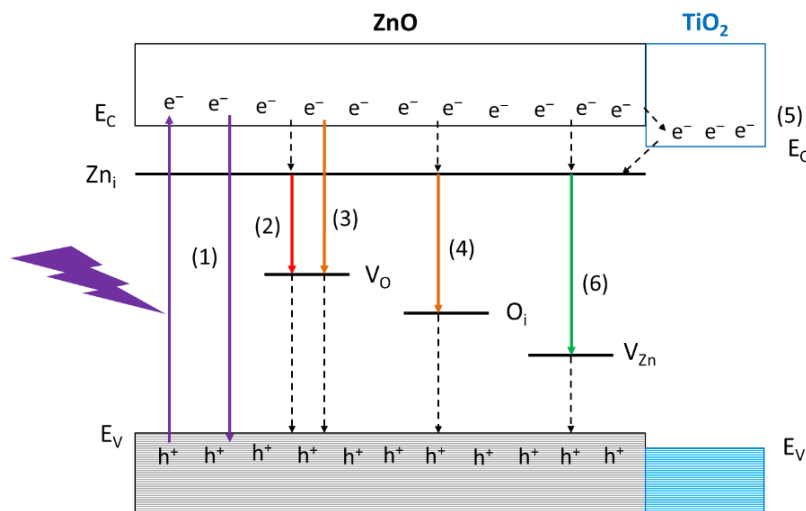


Figure 13. Energetic picture of ZnO-based materials. (1) NBE. (2) Zn_i -to- V_o red emission. (3) E_c -to- V_o orange emission. (4) Orange (red) Zn_i -to- O_i emission. (5) ZnO/TiO₂ heterojunction. (6) Zn_i -to- V_{Zn} green emission. Energy levels are qualitatively located according to [114].

Summing up this section, all the samples were observed to contain carbonates, likely to arise from the exposure to atmospheric air, and 4PNZ contains some organic impurities. A diversity on the relative amount of carbonate vs hydroxyl moiety on the surface, was also observed to depend on the synthetic approach. The samples annealed at lower temperature, revealed a Zn-rich surface, becoming O-rich by increasing the annealing temperature, while the amount of lattice oxygen vs defective oxygen is almost comparable, suggesting a similar defects content. The lower surface exposure of polar {0001} planes on 4TCSZ and 4PNZ, hypothesized in section 3.1, was further confirmed by FTIR analyses. TiO₂ was proposed to be located mainly on the surface on post-annealing TiO₂ promotion (T4CSZ), while sub-surface (up to 10 nm depth) is more likely on pre-annealing promotion (4TCSZ). The optical absorption properties were almost the same for all the samples. Concerning the optical emission, all the materials revealed a red and orange emission band, with different intensity depending on the sample, and a green band appeared after high temperature annealing (6CSZ). Finally, an energetic picture of the prepared ZnO materials was proposed and the observed improvement on the emission intensity was supposed to arise from TiO₂ in T4CSZ and 4TCSZ, acting as photoexcited electron sink, the higher crystallinity of ZnO core in 6CSZ or a massive bulk radiative recombination due to the amorphous fraction, in 4PNZ.

3.3 CO₂ PHOTOREDUCTION WITH H₂O AND HYBRID CO₂ CAPTURE/PHOTOCONVERSION

The prepared materials were finally assessed in the photocatalytic reduction of CO₂. The reactions were carried out in the gas phase, due to the advantages listed in Section 1.2. A low light intensity (60 W·m⁻²) and a flat-type photoreactor was used, aiming to maximize the overall efficiency of the reaction, as previously observed by CATMAT group [115,116].

The detected reaction products were CH₄ and O₂, while CO and H₂, despite being commonly reported reduction products in solid-gas reaction systems [28], were not found. Furthermore, as reported by Xin *et al.*, the CO₂ photoreduction on ZnO surfaces is known to proceed through carbonate species, formed by the adsorption of CO₂ on such material [37]. As reported in Figure 14a, the ZnO materials prepared by precipitation with carbonates, exhibited a comparable activity toward CH₄ production (ca. 0.2 μmol·g⁻¹·h⁻¹), while 4SZ and 4PNZ, were unactive. Another interesting parameter is the O₂ evolution, since it is both a reaction co-product (Reaction 1), from water oxidation, and comes from ZnO photocorrosion (Reaction 4). On a qualitative basis, some samples produce more O₂: 4CSZ and 4TCSZ exhibited an almost doubled yield of this gas compared to the other, while 4PNZ revealed a four-fold enhancement in O₂ evolution. Such differences can be ascribed to the ZnO photocorrosion and a general trend of photostability can be proposed: 4SZ ≈ T4CSZ ≈ 6CSZ > 4CSZ ≈ 4TCSZ > 4PNZ.

Since the sample exhibited a diverse SSA, the activity toward CH₄ evolution was also expressed as TOF *per* unit of surface (TOF*), as reported in Figure 14b. In this contest, the most active sample was 6CSZ: its surface was almost as reactive as P25. Conversely, 4CSZ and T4CSZ revealed a halved activity compared to 6CSZ, while 4TCSZ, despite having the higher SSA, has a very poorly active surface, one-fourth than 6CSZ.

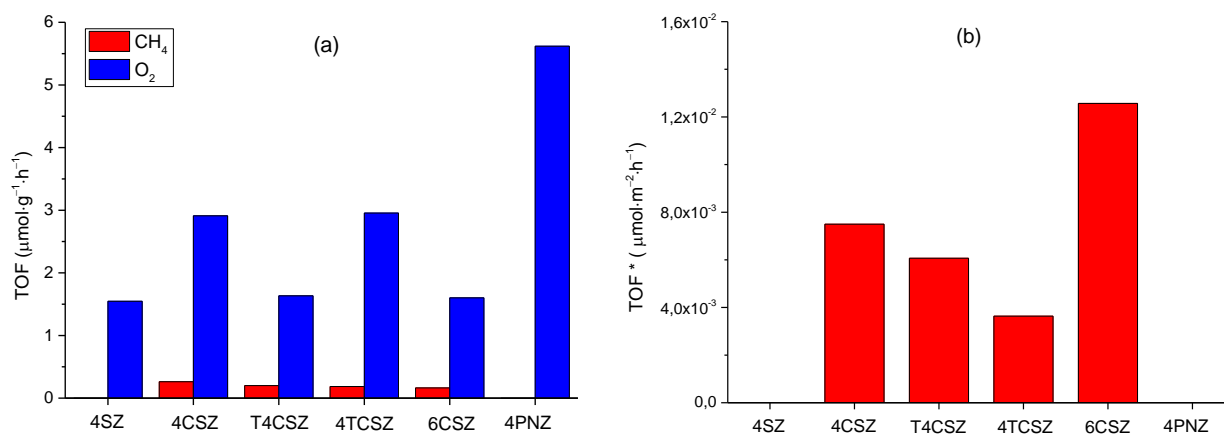


Figure 14. (a) TOF of CH₄, O₂, H₂ and (b) TOF of CH₄ normalized by the SSA (TOF*) of P25 and ZnO-based samples.

The lack of activity toward CO₂ reduction, as well as the limited photocorrosion, on 4SZ was related to the remarkable amount of sulfates in this material, supposed to act as holes scavenger or interfere with radical intermediates [84]. On 4PNZ, the inactivity was ascribed to the low SSA, the lower fraction of surface polar {0001} planes and, in particular, the presence of amorphous ZnO which boost up bulk charge carrier recombination. Furthermore, the higher intrinsic reactivity of amorphous compared to the crystalline phase, probably induce more photocorrosion to occur.

The active ZnO were crystalline and phase-pure, obtained by the carbonate-precipitation method. The addition of TiO₂, despite reducing the non-radiative recombination and allowing, in principle, more charge carriers available for the conversion of CO₂ to CH₄, had no enhancement compared to the bare material

(4CSZ). In details, the surface of T4CSZ (post-annealing TiO₂ addition) was supposed to be partially covered by tiny TiO₂ NPs, which was not able to stabilize superficial carbonates, the species formed upon CO₂ adsorption on ZnO. This was supposed to have two effects (Figure 15a): a reduced amount of carbonate moiety on the surface limited the producible CH₄, and less ZnO at the solid-gas interface allowed less O²⁻ ions to be oxidized by the photoexcited holes, improving its photostability. The surface 4TCSZ (pre-annealing TiO₂ addition) was different, because being richer in carbonates and poorer in TiO₂ NPs. The latter were probably more spaced on the surface itself, and/or partially buried within the sub-superficial layer (ca. 10 nm). As consequence TiO₂ was less effective in protecting the material against photocorrosion (Figure 15b). However, despite containing more carbonates, the material did not performed better than T4CSZ due to the lower fraction of polar {0001} planes, the most photoactive in ZnO.

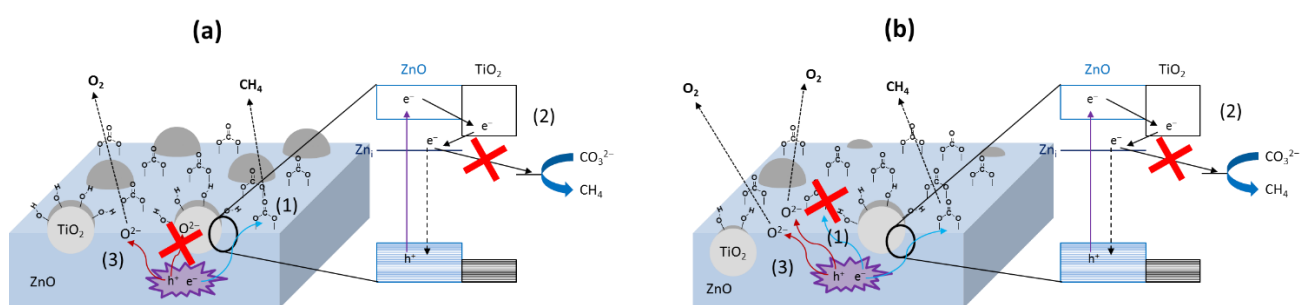


Figure 15. Effect of TiO₂ on activity and photostability in (a) T4CSZ and (b) 4TCSZ. (1) carbonate reduction pathway; (2) photoexcited charge transfer from E_c of ZnO, to E_c TiO₂ and Zn_i; (3) oxidative photocorrosion pathway.

The higher annealing temperature (6CSZ) afforded the most active surface. The superior photoactivity of this material can be either ascribed to the more efficient photoexcited charge carriers generation and transfer to the solid-gas interface, thanks to the crystalline core of the NPs, as well as by the higher fraction of superficial polar {0001} planes. The good stability toward photocorrosion was ascribed to the higher crystallinity of this material, which reduced the amount of amorphous region where this side reaction is likely to occur (surface of the NPs).

The best performing ZnO material in term of both activity and photostability, namely T4CSZ, was compared to a benchmark TiO₂, namely P25, characterized in Chapter 1. As reported in Figure 16 (red bars), the TiO₂ was three times more active than ZnO when using a CO₂/H₂O reaction mixture. This superior performance was ascribed to the absorption of CO₂ as molecular uncharged species on TiO₂ surface [117], while it formed charged carbonate upon absorption on ZnO surface, as observed by FTIR and XPS. The superficial electron transfer to a neutral acceptor molecule (CO_{2,ads}) is more favorable than negatively charged acceptor (CO₃²⁻), due to the electrostatic barrier [118], explaining the better performances of TiO₂. However, when the reaction mixture contained water vapor only, a drastic decrease in activity was observed on TiO₂, while ZnO revealed a comparable activity (Figure 16, orange bars). It is known carbon-based contaminants, to affect the products yield in CO₂ photoreduction [119]. However, on TiO₂ a contamination during the immobilization of

the catalyst (i.e. residues of the solvent or contaminants in the used gas) probably occurred, while on ZnO the surface inorganic carbonates, which in turn arose from absorption of atmospheric CO₂, was likely to be converted.

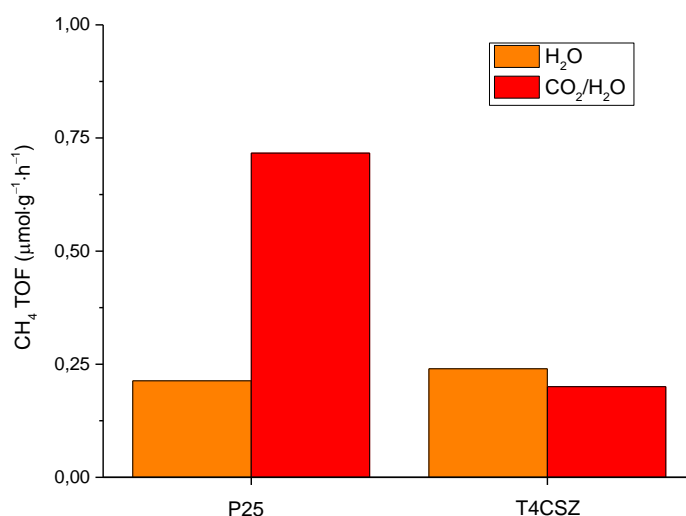


Figure 16. TOF of CH₄ on P25 and T4CSZ, in CO₂/H₂O and H₂O gas-phase reaction media.

Despite being less active than TiO₂, the supposed capability of ZnO to photoconvert air-adsorbed CO₂ in a CO₂-free reaction medium would suggest another appealing application: a hybrid CO₂ capture-photoconverting material. This would allow not only avoiding the requirement of a CO₂-rich reaction medium, but also the direct exploitation of diluted CO₂ sources.

For this reason, this property was assessed through the reaction scheme reported in Figure 17, using T4CSZ as photocatalyst. Briefly, a first reaction with H₂O vapor only was run for 6 h (1), then letting the used photocatalyst on a 10 mol. % CO₂ flow in inert gas, for 14 h in dark (2), aiming the regeneration of surface carbonates. The photoreduction with H₂O was run again (3) and regenerated with CO₂ in dark, again (4). The process was repeated for two more times (5 – 7).

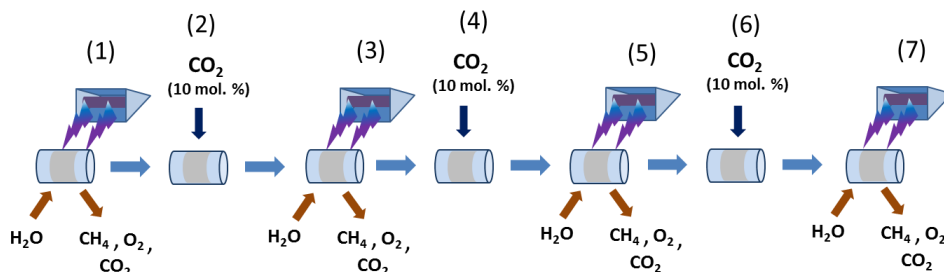


Figure 17. Hybrid CO₂ capture-photoconverting reaction scheme.

The photocatalyst successfully captured the CO₂ from a diluted stream and photoconverted it to CH₄, under irradiation with H₂O vapor (Figure 18). A slight improvement in CH₄ yield was observed after the 1st regeneration with CO₂, probably due to a surface richer in carbonates after the exposure to a 10% mol. CO₂

gas mixture. A CO_2/CH_4 ratio bigger than one was obtained in the outlet stream after every reaction run, suggesting only a fraction of the dark-adsorbed CO_2 to be photoconverted. The O_2 yield was stable over the four reaction run, pointing out a good photostability of T4CSZ after 48 h of UVA irradiation.

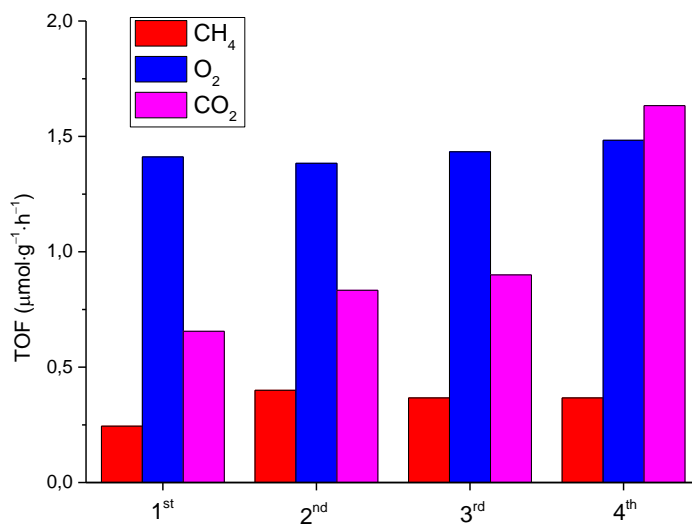


Figure 18. Recyclability of T4CSZ in gas-phase photoreduction with H_2O and dark CO_2 adsorption.

This ZnO material exhibited a poor efficiency in harvesting both photons and energy from the incoming light, affording an apparent quantum yield (AQY) of 0.008 % and a solar-to-fuel (STF) efficiency of 0.003%, despite still comparable with values usually reported in literature [120]. Despite this fact, the ZnO photocatalyst exhibited the appealing property to be a dual CO_2 capture/photoconverting material in very mild conditions. The current work, compared to recent literature [82], has some key advantages:

1. A basic semiconductor such as ZnO was used in the current work as hybrid capture/photoconverting system, while a composite of a basic insulating material and a TiO_2 photocatalyst was previously required.
2. Milder conditions ($T < 100^\circ\text{C}$) were involved in absorption and photoconversion of CO_2 in the present work, contrarily to the higher ones ($150 - 200^\circ\text{C}$) previously used with the TiO_2 composite.
3. A multi-electronic reduction pathway was favored in the present work, yielding the most reduced carbon compound (CH_4), while only CO was previously reported as reduction product.

To summarize this section, the photoactivity of ZnO-based material was assessed in the gas-phase CO_2 photoreduction with H_2O . Crystallinity and phase-purity were observed to be key parameters that allowed the photoreaction to occur and CH_4 to be produced. TiO_2 post-annealing addition was beneficial in reducing the photocorrosion. However, the scarcity of superficial carbonate, which acted as electron acceptor, do not allow an improvement in CH_4 yield. Increasing the annealing temperature, despite the reduced SSA and available active sites, had a beneficial effect due to an enhanced photoexcited charge carriers generation and transfer to the surface, as well as the favorable presence of superficial polar $\{0001\}$ planes. Finally, ZnO due

to the basic nature of its surface, it was successfully involved as hybrid material capable to absorb the CO₂ in dark, then photoconverting it in a CO₂-free reaction medium, with the sole presence of H₂O as reagent in the gas phase.

4. CONCLUSIONS

In this work, some ZnO materials were synthesized by a wet chemistry approach, and assessed in the gas-phase CO₂ photoreduction to solar fuels. The capability of hybrid CO₂ absorption/photoconversion was evaluated too. In details:

1. The structural and morphological properties of the synthesized ZnO were investigated, observing a remarkable change in shape and composition of the ZnO material when changing the precipitating agent or using a hydrothermal synthesis, while annealing temperature and promotion with TiO₂, affected mainly the size of the particles. The fraction of surface {0001} planes was also affected by the synthetic procedure.
2. The surface was observed to be composed of both carbonates and hydroxyl moieties, and their ratio changes depending on the synthetic parameter. The surface was Zn-rich at lower annealing temperature (400°C), becoming O-rich at higher temperature (600°C), while the defects concentration was comparable. Furthermore, the surface of the hydrothermal synthesized material, was observed to contain organic residues.
3. The absorption optical properties were comparable on all the samples, while the optical emission, related changed remarkably depending on the synthetic parameter. The samples had a similar concentration of surface defects, but the different emission intensity was ascribed to a different capability to reduce the non-radiative recombination phenomena, and thus a different ability to stabilize the photoexcited charge carriers.
4. An energetic picture, based on the optical properties of ZnO, was proposed.
5. The CO₂ photoreduction occurred on all the material composed of crystalline and phase pure ZnO, since the presence of impurities was detrimental. The presence of TiO₂ was not beneficial for the activity enhancement but increased stability against photocorrosion, while a large crystalline core improved the amount of photogenerated charge carriers able to run the reaction, despite having a lower active surface.
6. Thanks to the adsorption of CO₂ as superficial carbonates, ZnO was successfully used as hybrid CO₂ adsorber/photoconverter. This property avoided the requirement of a CO₂-rich reaction medium and, at the same time, allowed the exploitation of a diluted CO₂ stream as raw material.

5. SUPPLEMENTARY INFORMATION

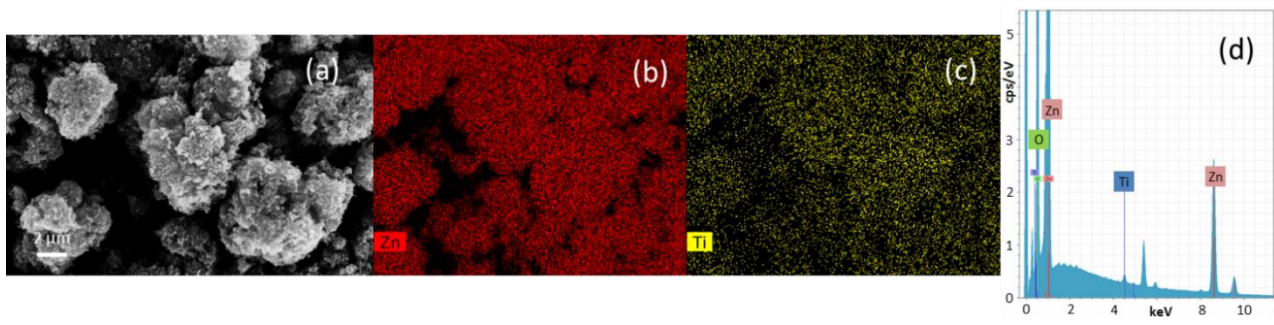


Figure S1. SEM image of T4CSZ. (b) Zn and (c) Ti EDX elemental mapping. (d) EDX spectrum.

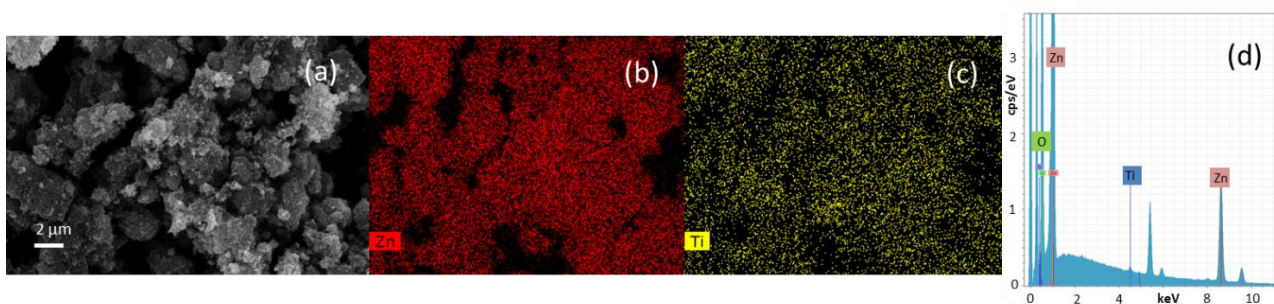


Figure S2. (a) SEM images of 4TCSZ. (b) Zn and (c) Ti EDX elemental mapping. (d) EDX spectrum.

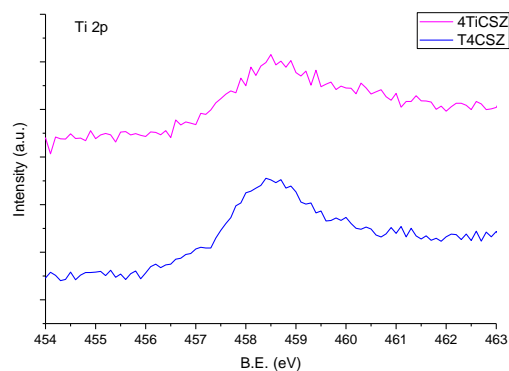


Figure S3. Ti2p XPS signal of T4CSZ and 4TCSZ samples.

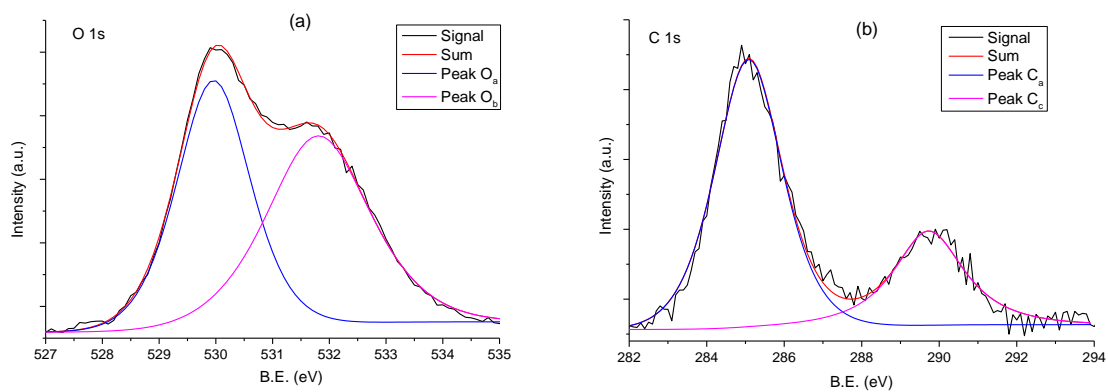


Figure S4. Deconvolution of ZnO (a) O1s and (b) C1s high-resolution XPS signals.

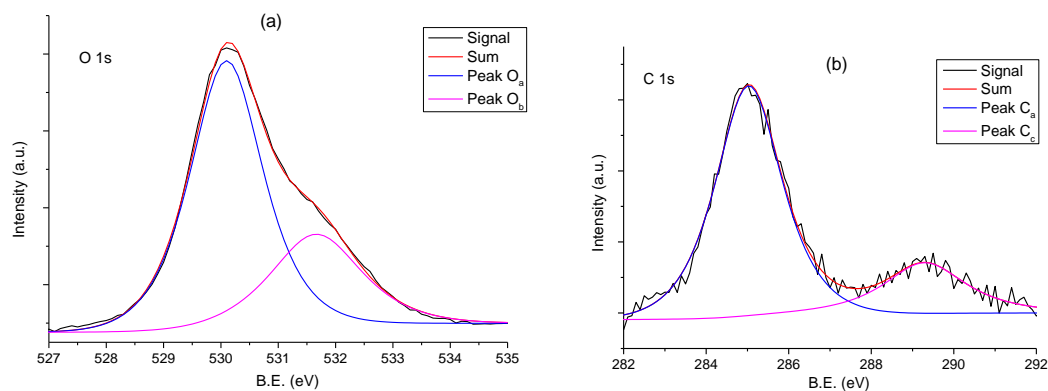


Figure S5. Deconvolution of 4CSZ (a) O1s and (b) C1s high-resolution XPS signals.

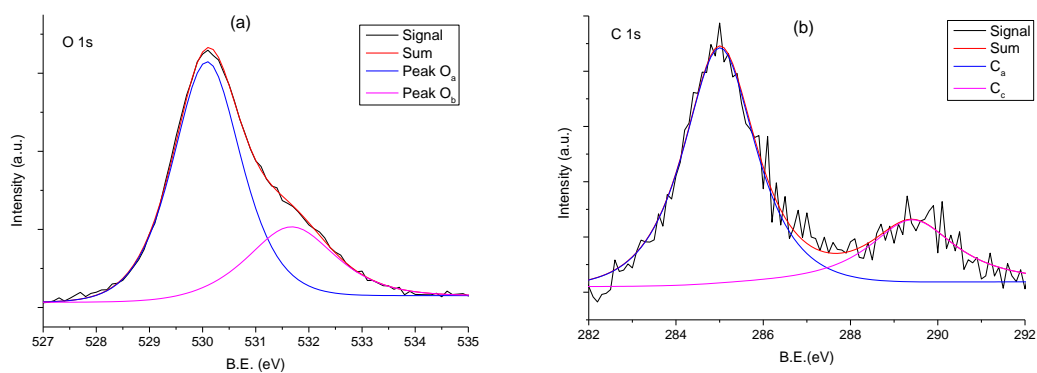


Figure S6. Deconvolution of T4CSZ (a) O1s and (b) C1s high-resolution XPS signals.

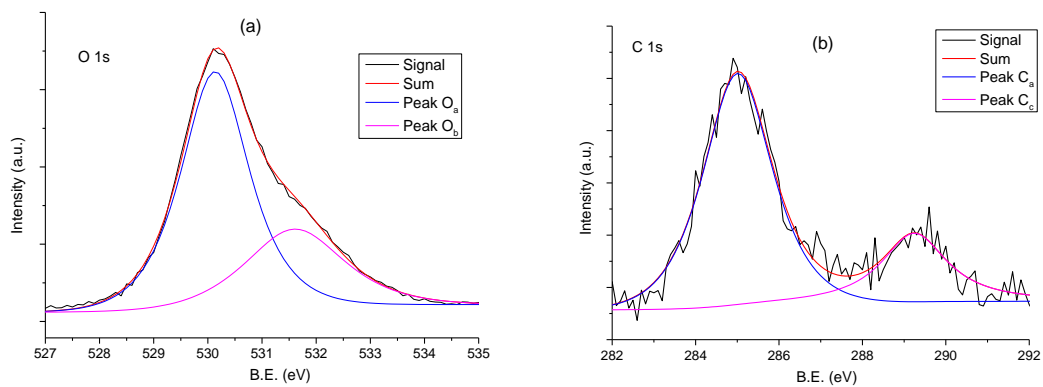


Figure S7. Deconvolution of 4TCSZ (a) O1s and (b) C1s high-resolution XPS signals.

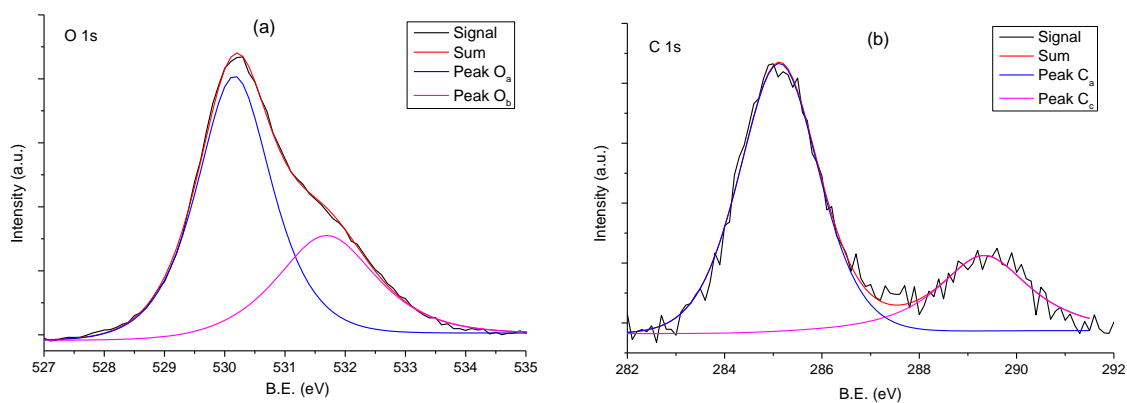


Figure S8. Deconvolution of 6CSZ (a) O1s and (b) C1s high-resolution XPS signals.

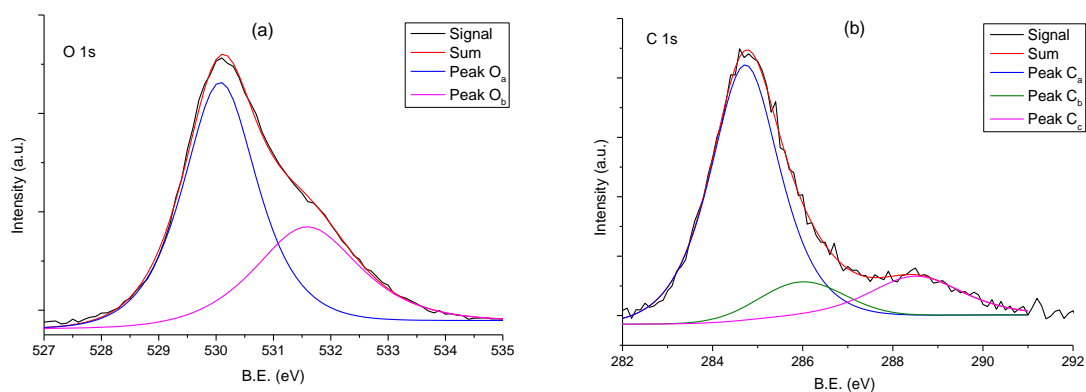


Figure S9. Deconvolution of 4PNZ (a) O1s and (b) C1s high-resolution XPS signals.

Table S1. Fraction of surface O bands (O_a , O_b) and C bands (C_a , C_b , C_c). Percentage values are reported respect to O and C at. % values in Table 3.

Sample	C_a (%)	C_b (%)	C_c (%)	O_a (%)	O_b (%)
ZnO	71	-	29	48	52
4CSZ	77	-	23	70	30
T4CSZ	74	-	26	69	31
4TCSZ	74	-	26	73	27
6CSZ	73	-	27	67	33
4PNZ	73	12	15	65	35

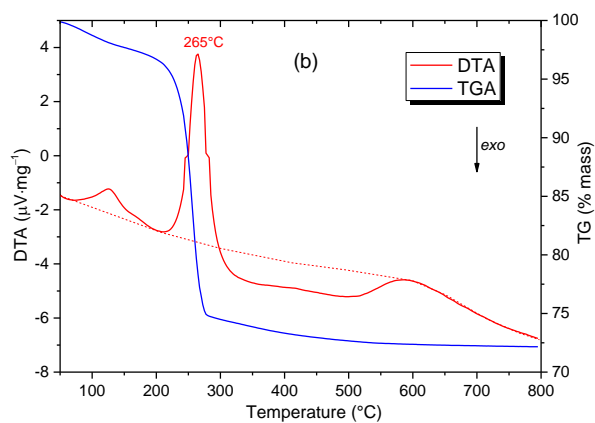


Figure S10. TGA-DTA of un-annealed CSZ.

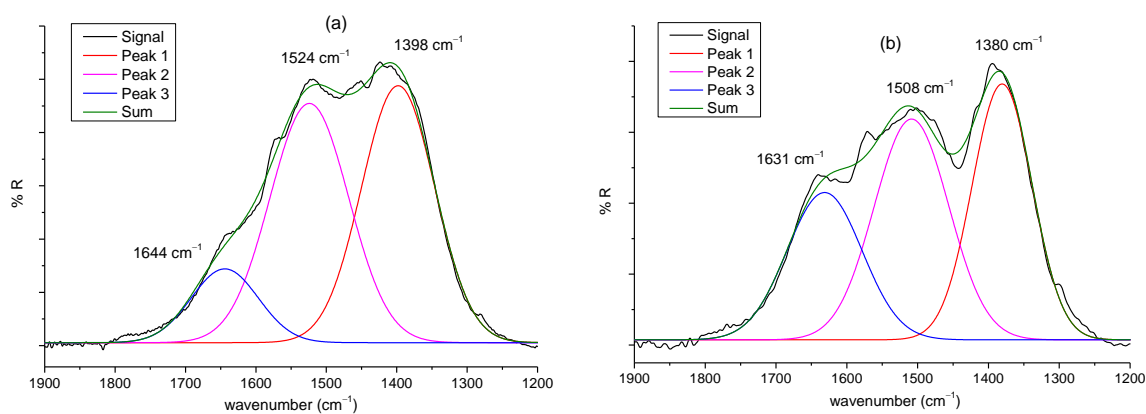


Figure S11. Deconvolution of (a) 4CSZ and (b) T4CSZ ATR-FTIR spectra.

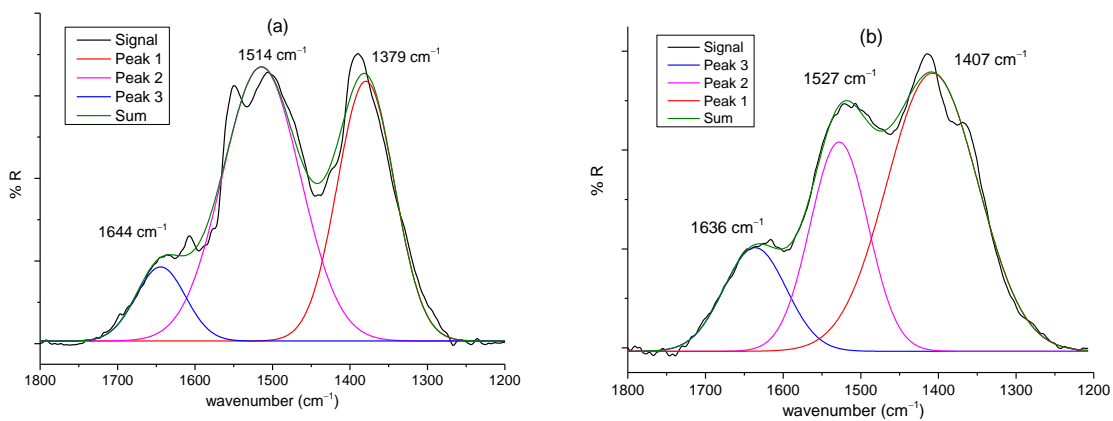


Figure S12. Deconvolution of (a) 4TCSZ and (b) 6CSZ ATR-FTIR spectra.

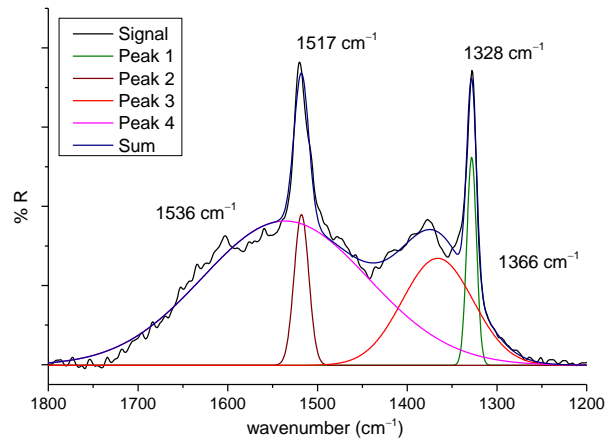


Figure S13. Deconvolution of 4PNZ ATR-FTIR spectra.

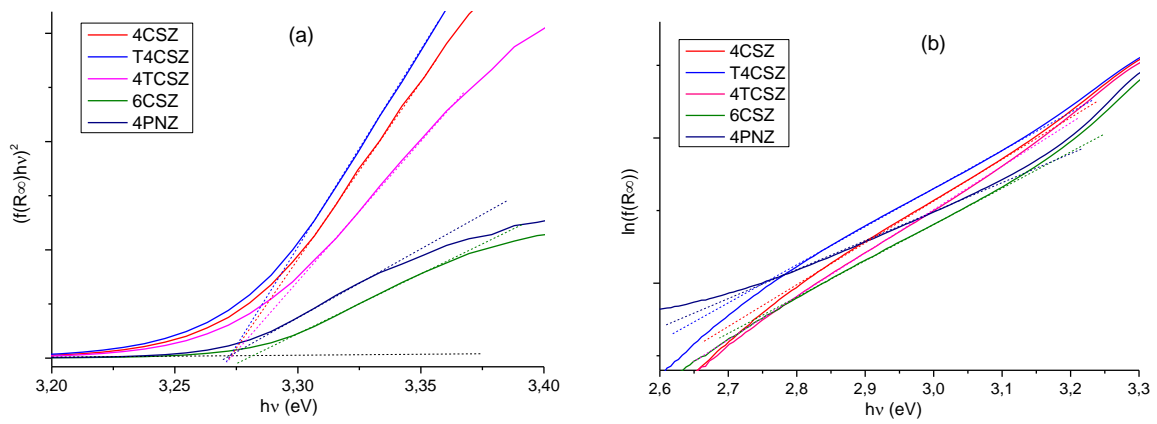


Figure S14. Tauc plot and (b) Urbach plot of ZnO-based materials. Dashed lines represent the curves tangents.

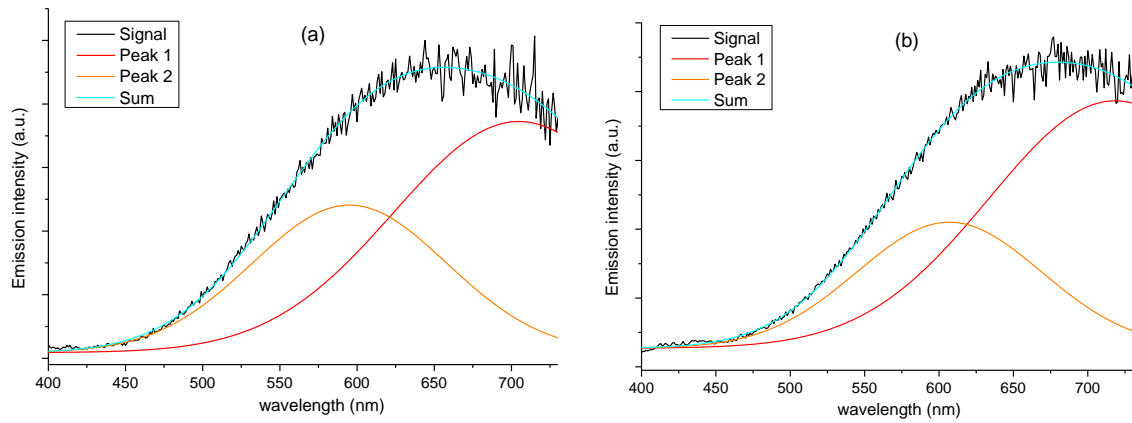


Figure S15. Deconvolution of (a) 4CSZ and (b) T4CSZ visible emission spectra.

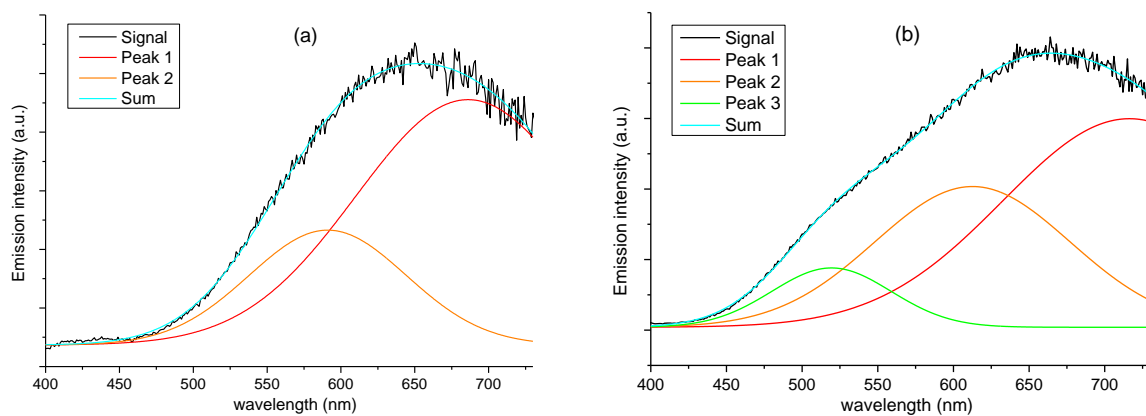


Figure S16. Deconvolution of (a) 4TCSZ and (b) 6CSZ visible emission spectra.

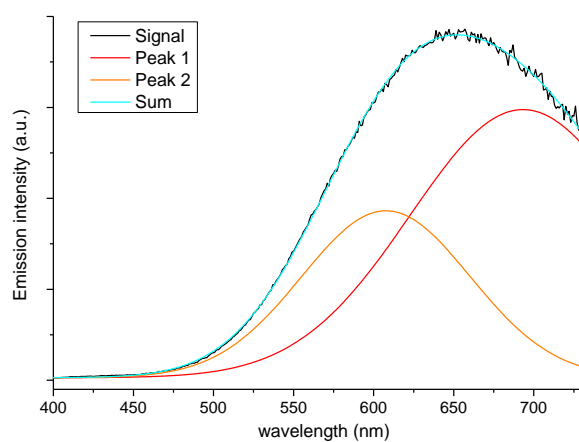


Figure S17. Deconvolution of 4PNZ visible emission spectra.

6. REFERENCES

- ¹ BP statistical review of world energy. 2019, 68th edition. Pdf available online: <https://www.bp.com/content/dam/bp/business-sites/en/global/corporate/pdfs/energy-economics/statistical-review/bp-stats-review-2019-full-report.pdf>. Accessed on 20/02/2020.
- ² K. Zickfeld, M Eby, A. J. Weaver, K. Alexander, E. Crespin, N. R. Edwards, A. V. Eliseev, G. Feulner, T. Fichet, C. E. Forest, P. Friedlingstein, H. Goosse, P. B. Holden, F. Joos, M. Kawamiya, D. Kicklighter, H. Kienert, K. Matsumoto, I. Mokhov, E. Monier, S. M. Olsen, J. O. P. Pedersen, M. Perrette, G. Philippon-Berthier, A. Ridgwell, A. Schlosser, T. S. Von Deimling, G. Shaffer, A. Sokolov, R. Spahni, M. Steinacher, K. Tachiiri, K. S. Tokos, M. Yoshimori, N. Zeng, F. Zhao. Long Term Climate Change Commitment and Reversibility: An EMIC Intercomparison. *J. Clim.* **2013**, *26*, 5782-5809, doi: 10.1175/JCLI-D-12-00584.1.
- ³ J. G. Titus, Strategies for adapting to the greenhouse effect. *JAPA* **1990**, *56*(3), 311-323, doi: 10.1080/01944369008975775.
- ⁴ N. Mac Dowell, P.S. Fennell, N. Shah, G.C. Maitland, The role of CO₂ capture and utilization in mitigating climate change. *Nat. Clim. Change* **2017**, *7*, 243-249, doi:10.1038/nclimate3231.
- ⁵ M. Mikkelsen, M. Jørgensen, F.C. Krebs, The teraton challenge. A review of fixation and transformation of carbon dioxide. *Energy Environ. Sci.* **2010**, *3*, 43-81, doi:10.1039/b912904a.
- ⁶ G. Centi, E.A. Quadrelli, S. Perathoner, Catalysis for CO₂ conversion: a key technology for rapid introduction of renewable energy in the value chain of chemical industries. *Energy Environ. Sci.* **2013**, *6*, 1711-1731, doi:10.1039/c3ee00056g.
- ⁷ W.J. Lee, C. Li, H. Prajitno, J. Yoo, J. Patel, Y. Yang, S. Lim, Recent trend in thermal catalytic low temperature CO₂ methanation: A critical review. *Catal. Today* **2020**, doi:10.1016/j.cattod.2020.02.017.
- ⁸ A. Goepfert, M. Czaun, J.-P. Jones, G.K.S. Prakash, G.A. Olah, Recycling of carbon dioxide to methanol and derived products – closing the loop. *Chem. Soc. Rev.* **2014**, *43*, 7995-8048, doi: 10.1039/c4cs00122b.
- ⁹ Y.A. Daza, J.N. Kuhn, CO₂ conversion by reverse water gas shift catalysis: comparison of catalysts, mechanisms and their consequences for CO₂ conversion to liquid fuels. *RSC Adv.* **2016**, *6*, 49675-49691, doi: 10.1039/c6ra05414e.
- ¹⁰ C. H. Bartholomew, R. J. Farrauto, Hydrogen Production and Synthesis Gas Reaction. In *Fundamentals of Industrial Catalytic Processes*, 2nd ed. John Wiley & Sons, Inc.: Hoboken (USA), 2005. ISBN: 9780471457138.
- ¹¹ P. Tian, Y. Wei, M. Ye, Z. Liu, Methanol to olefins (MTO): From fundamentals to commercialization. *ACS Catal.* **2015**, *5*, 1922-1938, doi: 10.1021/acscatal.5b00007.
- ¹² F.J. Keil, Methanol-to-hydrocarbons: Process technology. *Microporous Mesoporous Mater.* **1999**, *29*, 49–66, doi:10.1016/S1387-1811(98)00320-5.
- ¹³ K. Weissermal, H.-J. Arpe, *Industrial Organic Chemistry*, 3rd ed. Wiley-VCH Verlag GmbH & Co. KGaA: Weinheim (Germany), 1997. ISBN: 9783527614592.
- ¹⁴ G.A. Olah, A. Goepfert, G.K. Surya Prakash. The hydrogen economy and its limitation. In *Beyond Oil and Gas: The Methanol Economy*. WILEY-VCH Verlag GmbH & Co. KGaA: Weinheim (Germany), 2009; pp. 19 – 53. ISBN: 9783527324224.
- ¹⁵ D.L. Nelson, M.M. Cox, Energetics and Bioenergetics. In *Lehninger Principles of Biochemistry* 4th ed. Macmillian Publisher, New York (USA), 2005. ISBN: 9780716743392.
- ¹⁶ J. Barber, Photosynthetic energy conversion: Natural and artificial. *Chem. Soc. Rev.* **2009**, *38*, 185-196, doi:10.1039/b802262n.
- ¹⁷ Gibbs free energy of reaction were calculated as follow: $\Delta_r G^\circ_{25^\circ\text{C}} = \left(\sum_{i=0}^n y_i \Delta_f G^\circ_{25^\circ\text{C},i}\right) - \left(\sum_{i=0}^n x_i \Delta_f G^\circ_{25^\circ\text{C},i}\right)$, where $\Delta_f G^\circ_{25^\circ\text{C},i}$ is the Gibbs free energy of formation of the ith reaction product, $\Delta_f G^\circ_{25^\circ\text{C},i}$ is the free Gibbs energy of formation of the ith reaction reagent, while y_i and x_i are the stoichiometric coefficient of, respectively, the ith product and ith reagent. The Gibbs free energy of formation are taken from: D.R. Lide, Grace Baysinger, Lev I. Berger, Robert N. Goldberg, Henry V. Kehiaian, Kozo Kuchitsu, Gerd Rosenblatt, Dana L. Roth, Daniel Zwillinger. Thermochemistry, electrochemistry and kinetics. In *CRC Handbook of Chemistry and Physics*, 6th ed., CRC press: Boca Raton (USA), 2005. ISBN: 9780849332043.
- ¹⁸ R.J. Carrillo, J.R. Scheffe, Advances and trends in redox materials for solar thermochemical fuel production. *Sol. Energy* **2017**, *156*, 3-20, doi:10.1016/j.solener.2017.05.032.
- ¹⁹ W. Fuqiang, M. Lanxin, C. Ziming, T. Jianyu, H. Xing, L. Linhua, Radiative heat transfer in solar thermochemical particle reactor: A comprehensive review. *Renew. Sustain. Energy Rev.* **2017**, *73*, 935-949, doi:10.1016/j.rser.2017.01.165.
- ²⁰ J.P. Jones, G.K.S. Prakash, G.A. Olah, Electrochemical CO₂ Reduction: Recent Advances and Current Trends. *Isr. J. Chem.* **2014**, *54*, 1451-1466, doi:10.1002/ijch.201400081.
- ²¹ C. Long, X. Li, J. Guo, Y. Shi, S. Liu, Z. Tang, Electrochemical Reduction of CO₂ over Heterogeneous Catalysts in Aqueous Solution: Recent Progress and Perspectives. *Small Methods* **2019**, *3*, 1800369, doi:10.1002/smt.201800369.

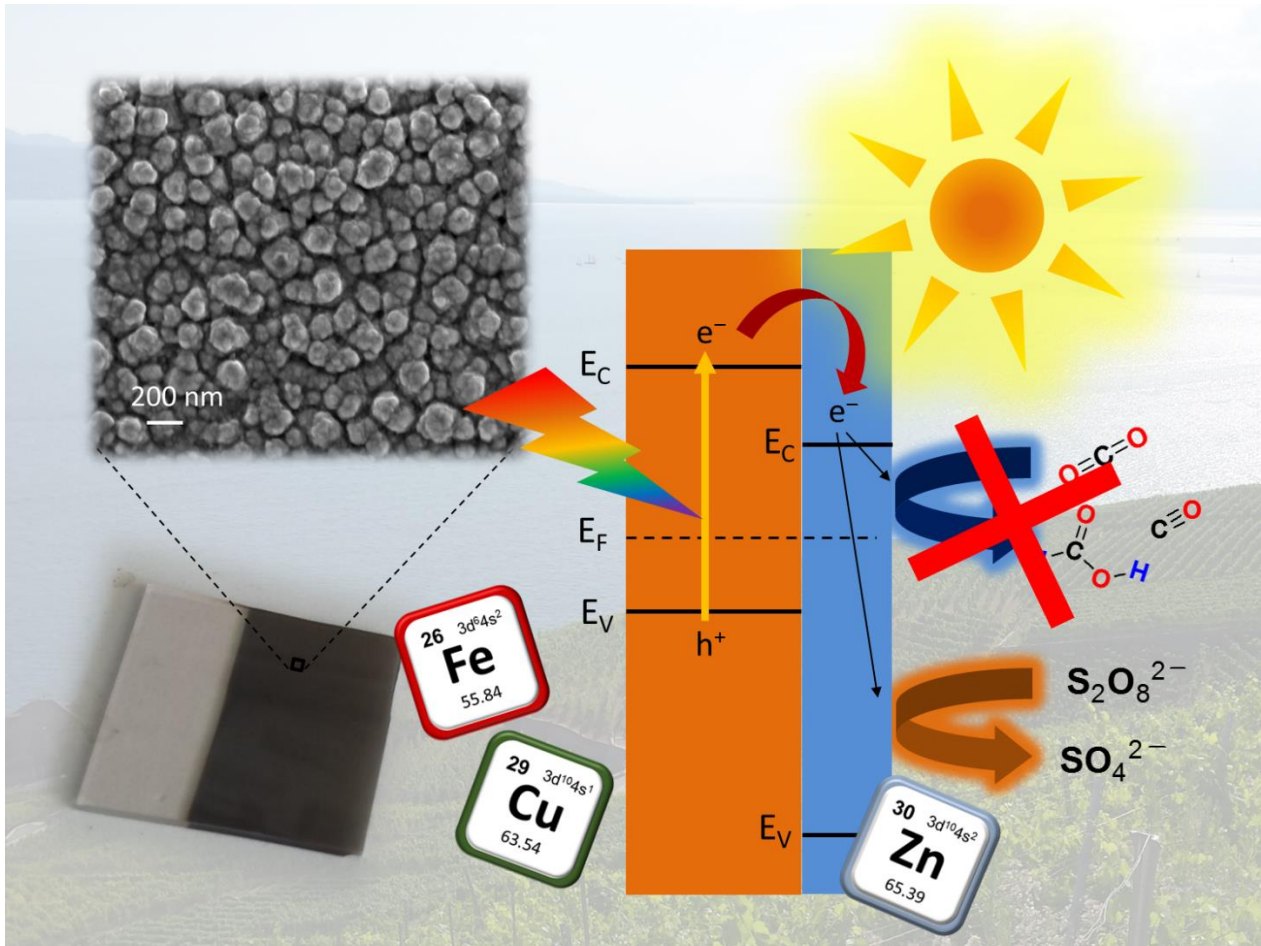
- ²² J. Barber, Photosynthetic energy conversion: Natural and artificial. *Chem. Soc. Rev.* **2009**, *38*, 185-196, doi:10.1039/b802262n.
- ²³ A. Olivo, D. Zanardo, E. Ghedini, F. Menegazzo, M. Signoretto, Solar Fuels by Heterogeneous Photocatalysis: From Understanding Chemical Bases to Process Development. *ChemEngineering* **2018**, *2*, 42, doi:10.3390/chemengineering2030042.
- ²⁴ B. Kumar, M. Llorente, J. Froehlich, T. Dang, A. Sathrum, C.P. Kubiak, Photochemical and Photoelectrochemical Reduction of CO₂. *Annu. Rev. Phys. Chem.* **2012**, *63*, 541-569, doi: 10.1146/annurev-physchem-032511-143759.
- ²⁵ A. Olivo, V. Trevisan, E. Ghedini, F. Pinna, C.L. Bianchi, A. Naldoni, G. Cruciani, M. Signoretto, CO₂ photoreduction with water: Catalyst and process investigation. *J. CO₂ Util.* **2015**, *12*, 86-94, doi:10.1016/j.jcou.2015.06.001.
- ²⁶ X. Li, J. Wen, J. Low, Y. Fang, J. Yu, Design and fabrication of semiconductor photocatalyst for photocatalytic reduction of CO₂ to solar fuel. *Sci. China Mater.* **2014**, *57*, 70-100, doi: 10.1007/s40843-014-0003-1.
- ²⁷ L. Yang, H. Zhou, T. Fan, D. Zhang, Semiconductor photocatalysts for water oxidation: Current status and challenges, *Phys. Chem. Chem. Phys.* **2014**, *16*, 6810-6826, doi:10.1039/c4cp00246f.
- ²⁸ Y. Wang, B. Li, C. Zhang, L. Cui, S. Kang, X. Li, L. Zhou, Ordered mesoporous CeO₂-TiO₂ composites: Highly efficient photocatalysts for the reduction of CO₂ with H₂O under simulated solar irradiation. *Appl. Catal. B* **2013**, *131*, 277-284, doi:10.1016/j.apcatb.2012.11.019.
- ²⁹ A. Olivo, E. Ghedini, M. Signoretto, M. Compagnoni, I. Rossetti, Liquid vs. Gas Phase CO₂ Photoreduction Process: Which Is the Effect of the Reaction Medium? *Energies* **2017**, *10*, 1394, doi: 10.3390/en10091394.
- ³⁰ S.N. Habisreutinger, L. Schmidt-Mende, J.K. Stolarczyk, Photocatalytic reduction of CO₂ on TiO₂ and other semiconductors. *Angew. Chemie* **2013**, *52*, 7372-7408, doi:10.1002/anie.201207199.
- ³¹ A. Li, T. Wang, X. Chang, Z.J. Zhao, C. Li, Z. Huang, P. Yang, G. Zhou, J. Gong, Tunable syngas production from photocatalytic CO₂ reduction with mitigated charge recombination driven by spatially separated cocatalysts. *Chem. Sci.* **2018**, *9*, 5334-5340, doi:10.1039/c8sc01812j.
- ³² X. Chang, T. Wang, J. Gong, CO₂ photo-reduction: insights into CO₂ activation and reaction on surfaces of photocatalysts. *Energy Environ. Sci.* **2016**, *9*, 2177-2196, doi:10.1039/C6EE00383D.
- ³³ R.H. Perry, D.W. Green, J.O. Maloney, *Perry's Chemical Engineers' Handbook*, 7th ed. McGraw-Hill: New York (USA), 1999. ISBN 0070498415.
- ³⁴ A. Bideau-Mehu, Y. Guern, R. Abjean, A. Johannin-Gilles, Interferometric determination of the refractive index of carbon dioxide in the ultraviolet region. *Opt. Commun.* **1973**, *9*, 432-434, doi: 10.1016/0030-4018(73)90289-7.
- ³⁵ D.R. Lide, Fluid Properties. In *CRC Handbook of Chemistry and Physics*, 6th ed., CRC press: Boca Raton (USA), 2005. ISBN: 9780849332043.
- ³⁶ C. Ampelli, C. Genovese, R. Passalacqua, S. Perathoner, G. Centi, A gas-phase reactor powered by solar energy and ethanol for H₂ production. *Appl. Therm. Eng.* **2014**, *70*, 1270-1275, doi:10.1016/j.applthermaleng.2014.04.013.
- ³⁷ C. Xin, M. Hu, K. Wang, X. Wang, Significant Enhancement of Photocatalytic Reduction of CO₂ with H₂O over ZnO by the Formation of Basic Zinc Carbonate. *Langmuir* **2017**, *33*, 6667-6676, doi:10.1021/acs.langmuir.7b00620.
- ³⁸ H.A. Park, J.H. Choi, K.M. Choi, D.K. Lee, J.K. Kang, Highly porous gallium oxide with a high CO₂ affinity for the photocatalytic conversion of carbon dioxide into methane. *J. Mater. Chem.* **2015**, *22*, 5304-5307, doi:10.1039/c2jm30337j.
- ³⁹ Q. Liu, Y. Zhou, J. Kou, X. Chen, Z. Tian, J. Gao, S. Yan, Z. Zou, High-yield synthesis of ultralong and ultrathin Zn₂GeO₄ nanoribbons toward improved photocatalytic reduction of CO₂ into renewable hydrocarbon fuel. *J. Am. Chem. Soc.* **2010**, *132*, 14385-14387, doi:10.1021/ja1068596.
- ⁴⁰ P. John, H. Kisch, Photoreduction of carbon dioxide catalysed by free and supported zinc and cadmium sulphide powders. *J. Photochem. Photobiol. A* **1997**, *111*, 223-228, doi:10.1016/S1010-6030(97)00228-1.
- ⁴¹ Y.P. Xie, G. Liu, L. Yin, H.M. Cheng, Crystal facet-dependent photocatalytic oxidation and reduction reactivity of monoclinic WO₃ for solar energy conversion. *J. Mater. Chem.* **2012**, *22*, 6746-6751, doi:10.1039/c2jm16178h.
- ⁴² Z. Wang, H. Chou, J.C.S. Wu, D. Ping, G. Mul, CO₂ photoreduction using NiO/InTaO₄ in optical-fiber reactor for renewable energy. *Applied Catal. A* **2010**, *380*, 172-177, doi:10.1016/j.apcata.2010.03.059.
- ⁴³ Q. Liu, Y. Zhou, Z. Tian, X. Chen, J. Gao, Z. Zou, Zn₂GeO₄ crystal splitting toward sheaf-like, hyperbranched nanostructures and photocatalytic reduction of CO₂ into CH₄ under visible light after nitridation. *J. Mater. Chem.* **2012**, *22*, 2033-2038, doi:10.1039/c1jm14122h.
- ⁴⁴ J.-C. Wang, L. Zhang, W.-X. Fang, J. Ren, Y.-Y. Li, H.-C. Yao, J.-S. Wang, Z.-J. Li, Enhanced Photoreduction CO₂ Activity over Direct Z-Scheme α-Fe₂O₃/Cu₂O Heterostructures under Visible Light Irradiation, *ACS Appl. Mater. Interfaces.* **2015**, *7*, 8631-8639, doi:10.1021/acsami.5b00822.
- ⁴⁵ S. Xie, Y. Wang, Q. Zhang, W. Deng, Y. Wang, MgO- and Pt-promoted TiO₂ as an efficient photocatalyst for the preferential reduction of carbon dioxide in the presence of water. *ACS Catal.* **2014**, *4*, 3644-3653, doi:10.1021/cs500648p.

- ⁴⁶ C. Zhao, L. Liu, Q. Zhang, J. Wang, Y. Li, Photocatalytic conversion of CO₂ and H₂O to fuels by nanostructured Ce-TiO₂/SBA-15 composites. *Catal. Sci. Technol.* **2012**, *2*, 2558-2568, doi:10.1039/c2cy20346d.
- ⁴⁷ C.K. Lim, K.M. Nam, H. Song, Colloidal zinc oxide-copper(I) oxide nanocatalysts for selective aqueous photocatalytic carbon dioxide conversion into methane. *Nat. Commun.* **2017**, *8*, 1156, doi:10.1038/s41467-017-01165-4.
- ⁴⁸ A. Janotti, C.G. Van De Walle, Fundamentals of zinc oxide as a semiconductor. *Rep. Prog. Phys.* **2009**, *72*, 126501, doi:10.1088/0034-4885/72/12/126501.
- ⁴⁹ Ü. Özgür, Y.I. Alivov, C. Liu, A. Teke, M.A. Reshchikov, S. Doğan, V. Avrutin, S.J. Cho, H. Morkoç, A comprehensive review of ZnO materials and devices. *J. Appl. Phys.* **2005**, *98*, 041301, doi:10.1063/1.1992666.
- ⁵⁰ S.J. Pearton, F. Ren, ZnO-based materials for light emitting diodes. *Curr. Opin. Chem. Eng.* **2014**, *3*, 51-55, doi:10.1016/j.coche.2013.11.002.
- ⁵¹ L. Petti, N. Münzenrieder, C. Vogt, H. Faber, L. Büthe, G. Cantarella, T.D. Anthopoulos, G. Tröster, C. Vogt, H. Faber, B. Lars, L. Petti, M. Niko, G. Cantarella, F. Bottacchi, T.D. Anthopoulos, Metal oxide semiconductor thin-film transistors for flexible electronics. *Appl. Phys. Rev.* **2016**, *3*, 021303, doi:10.1063/1.4953034.
- ⁵² R. Vittal, K. Ho, Zinc oxide based dye-sensitized solar cells : A review. *Renew. Sustain. Energy Rev.* **2017**, *70*, 920-935, doi:10.1016/j.rser.2016.11.273.
- ⁵³ A.A. Khodja, T. Sehili, J.-F. Pilichowski, P. Boule, Photocatalytic degradation of 2-phenylphenol on TiO₂ and ZnO in aqueous suspensions. *J. Photochem. Photobiol. A* **2001**, *141*, 231-239, doi:10.1016/S1010-6030(01)00423-3.
- ⁵⁴ Y. Li, W. Xie, X. Hu, G. Shen, X. Zhou, Y. Xiang, X. Zhao, P. Fang, Comparison of dye photodegradation and its coupling with light-to-electricity conversion over TiO₂ and ZnO. *Langmuir* **2010**, *26*, 591-597, doi:10.1021/la902117c.
- ⁵⁵ H. Tang, K. Prasad, R. Sanjinès, P.E. Schmid, F. Lévy, Electrical and optical properties of TiO₂ anatase thin films. Electrical and optical properties of TiO₂ anatase thin films. *J. Appl. Phys.* **1994**, *75*, 2042-2047, doi:10.1063/1.356306.
- ⁵⁶ J. Pascual, J. Camassel, H. Mathieu, Fine structure in the intrinsic absorption edge of TiO₂. *Phys. Rev. B.* **1978**, *18*, 5606-5614, doi:10.1103/PhysRevB.18.5606.
- ⁵⁷ J. Doménech, A. Prieto, Stability of ZnO Particles in Aqueous Suspensions under UV Illumination. *J. Phys. Chem.* **1986**, *90*, 1123-1126, doi:10.1021/j100278a031.
- ⁵⁸ J. Wang, P. Liu, X. Fu, Z. Li, W. Han, X. Wang, Relationship between oxygen defects and the photocatalytic property of zno nanocrystals in nafion membranes. *Langmuir* **2009**, *25*, 1218-1223, doi:10.1021/la803370z.
- ⁵⁹ J. Han, W. Qiu, W. Gao, Potential dissolution and photo-dissolution of ZnO thin films. *J. Hazard. Mater.* **2010**, *178*, 115-122, doi:10.1016/j.jhazmat.2010.01.050.
- ⁶⁰ C. Wöll, The chemistry and physics of zinc oxide surfaces. *Prog. Surf. Sci.* **2007**, *82*, 55-120, doi:10.1016/j.progsurf.2006.12.002.
- ⁶¹ M. Huang, Y. Yan, W. Feng, S. Weng, Z. Zheng, X. Fu, P. Liu, Controllable tuning various ratios of ZnO polar facets by crystal seed-assisted growth and their photocatalytic activity. *Cryst. Growth Des.* **2014**, *14*, 2179-2186, doi:10.1021/cg401676r.
- ⁶² R. Boppella, K. Anjaneyulu, P. Basak, S. V. Manorama, Facile synthesis of face oriented ZnO crystals: Tunable polar facets and shape induced enhanced photocatalytic performance. *J. Phys. Chem. C* **2013**, *117*, 4597-4605, doi:10.1021/jp311443s.
- ⁶³ Y. Chen, H. Zhao, B. Liu, H. Yang, Charge separation between wurtzite ZnO polar {001} surfaces and their enhanced photocatalytic activity. *Appl. Catal. B* **2015**, *163*, 189-197, doi:10.1016/j.apcatb.2014.07.044.
- ⁶⁴ N. Kislov, J. Lahiri, H. Verma, D.Y. Goswami, E. Stefanakos, M. Batzill, Photocatalytic degradation of methyl orange over single crystalline ZnO: Orientation dependence of photoactivity and photostability of ZnO. *Langmuir* **2009**, *25*, 3310-3315, doi:10.1021/la803845f.
- ⁶⁵ N.H. Alvi, K. ul Hasan, O. Nur, M. Willander, The origin of the red emission in n-zno nanotubes/p-gan white light emitting diodes. *Nanoscale Res. Lett.* **2011**, *6*, 130, doi:10.1186/1556-276X-6-130.
- ⁶⁶ R.A. Wahyuono, F. Hermann-Westendorf, A. Dellith, C. Schmidt, J. Dellith, J. Plentz, M. Schulz, M. Presselt, M. Seyring, M. Rettenmeyer, B. Dietzek. Effect of annealing on the sub-bandgap, defects and trapping states of ZnO nanostructures. *Chem. Phys.* **2017**, *483-484*, 112-121, doi:10.1016/j.chemphys.2016.12.002.
- ⁶⁷ H. Usui, Influence of Surfactant Micelles on Morphology and Photoluminescence of Zinc Oxide Nanorods Prepared by One-Step Chemical Synthesis in Aqueous Solution. *J. Phys. Chem. C* **2007**, *111*, 9060-9065, doi: 10.1021/jp071388o.
- ⁶⁸ M.Y. Guo, A.M.C. Ng, F. Liu, A.B. Djurišić, W.K. Chan, H. Su, K.S. Wong, Effect of native defects on photocatalytic properties of ZnO. *J. Phys. Chem. C* **2011**, *115*, 11095-11101, doi:10.1021/jp200926u.
- ⁶⁹ D. Liu, Y. Lv, M. Zhang, Y. Liu, Y. Zhu, R. Zong, Y. Zhu, Defect-related photoluminescence and photocatalytic properties of porous ZnO nanosheets. *J. Mater. Chem. A* **2014**, *2*, 15377-15388, doi:10.1039/c4ta02678k.
- ⁷⁰ D. Chen, Z. Wang, T. Ren, H. Ding, W. Yao, R. Zong, Y. Zhu, Influence of Defects on the Photocatalytic Activity of ZnO. *J. Phys. Chem. C* **2014**, *118*, 15300-15307, doi:10.1021/jp5033349.
- ⁷¹ G.R. Li, T. Hu, G.L. Pan, T.Y. Yan, X.P. Gao, H.Y. Zhu, Morphology-function relationship of ZnO: Polar planes, oxygen vacancies, and activity. *J. Phys. Chem. C* **2008**, *112*, 11859-11864, doi: 10.1021/jp8038626.

- ⁷² Z. Geng, X. Kong, W. Chen, H. Su, Y. Liu, F. Cai, G. Wang, J. Zeng, Oxygen Vacancies in ZnO Nanosheets Enhance CO₂ Electrochemical Reduction to CO. *Angew. Chemie* **2018**, *57*, 6054-6059, doi:10.1002/anie.201711255.
- ⁷³ T. Inoue, A. Fujishima, S. Konishi, K. Honda, Photoelectrocatalytic reduction of carbon dioxide in aqueous suspensions of semiconductor powders. *Nature* **1979**, *277*, 637-638, doi:10.1038/277637a0.
- ⁷⁴ X. Liu, L. Ye, S. Liu, Y. Li, X. Ji, Photocatalytic reduction of CO₂ by ZnO micro/nanomaterials with different morphologies and ratios of {0001} facets. *Sci. Rep.* **2016**, *6*, 38474, doi:10.1038/srep38474.
- ⁷⁵ J. Núñez, V.A. De La Peña O'Shea, P. Jana, J.M. Coronado, D.P. Serrano, Effect of copper on the performance of ZnO and ZnO_{1-x}N_x oxides as CO₂ photoreduction catalysts. *Catal. Today* **2013**, *209*, 21-27, doi:10.1016/j.cattod.2012.12.022.
- ⁷⁶ A. Steingrube, P. Voll, Selecting CO₂ Sources for CO₂ Utilization by Environmental-Merit- Order Curves, *Environ. Sci. Technol.* **2016**, *50*(3), 1093-1101, doi:10.1021/acs.est.5b03474.
- ⁷⁷ D.Y.C. Leung, G. Caramanna, M.M. Maroto-valer, An overview of current status of carbon dioxide capture and storage technologies. *Renew. Sustain. Energy Rev.* **2014**, *39*, 426-443, doi:10.1016/j.rser.2014.07.093.
- ⁷⁸ C.R. Murdock, S.A. Didas, C.W. Jones, Direct Capture of CO₂ from Ambient Air. *Chem. Rev.* **2016**, *116*, 11840-11876, doi: 10.1021/acs.chemrev.6b00173.
- ⁷⁹ C. Reller, M. Po, A. Lißner, F.O.R.L. Mertens, Methanol from CO₂ by Organo-Cocatalysis: CO₂ Capture and Hydrogenation in One Process Step. *Environ. Sci. Technol.* **2014**, *48*, 14799-14804, doi:10.1021/es503914d.
- ⁸⁰ S.M. Kim, P.M. Abdala, M. Broda, D. Hosseini, C. Cope, C. Mu, Integrated CO₂ Capture and Conversion as an Efficient Process for Fuels from Greenhouse Gases. *ACS Catal.* **2018**, *8*, 2815-2823, doi:10.1021/acscatal.7b03063.
- ⁸¹ H.Y. Wu, H. Bai, J.C.S. Wu, Photocatalytic reduction of CO₂ using Ti-MCM-41 photocatalysts in monoethanolamine solution for methane production. *Ind. Eng. Chem. Res.* **2014**, *53*, 11221-11227, doi: 10.1021/ie403742j.
- ⁸² L. Liu, C. Zhao, J. Xu, Y. Li, Integrated CO₂ capture and photocatalytic conversion by a hybrid adsorbent/photocatalyst material. *Appl. Catal. B* **2015**, *179*, 489-499, doi:10.1016/j.apcatb.2015.06.006.
- ⁸³ S. Kumar, S.K. Saxena, A comparative study of CO₂ sorption properties for different oxides. *Mater. Renew. Sustain. Energy* **2014**, *3*, 30, doi:10.1007/s40243-014-0030-9.
- ⁸⁴ W.A. Thompson, A. Olivo, D. Zanardo, G. Cruciani, M. Signoretto, F. Menegazzo, M.M. Maroto-valer, Systematic study of TiO₂/ZnO mixed metal oxides for CO₂ photoreduction. *RSC Adv.* **2019**, *9*, 21660-21666, doi:10.1039/c9ra03435h.
- ⁸⁵ M.R. Parra, F.Z. Haque, Structural and optical properties of poly-vinylpyrrolidone modified ZnO nanorods synthesized through simple hydrothermal process. *Optik* **2014**, *125*, 4629-4632, doi:10.1016/j.ijleo.2014.05.030.
- ⁸⁶ S. Brunauer, P.H. Emmett, E. Teller, Adsorption of Gases in Multimolecular Layers. *J. Am. Chem. Soc.* **1938**, *60*, 309-319, doi:10.1021/ja01269a023.
- ⁸⁷ P. Kubelka; F. Munk, Ein Beitrag zur Optik der Farbanstriche. *Zeitschrift Technische Physik* **1931**, *12*, 593-601.
- ⁸⁸ J. Tauc, A. Menth, States in the gap. *J. Non-Cryst. Solids* **1972**, *8-10*, 569-585, doi:10.1016/0022-3093(72)90194-9.
- ⁸⁹ W.F. Lim, H.J. Quah, Z. Hassan, R. Radzali, N. Zainal, F.K. Yam, Alteration of structural and optical properties in quaternary Al_{0.1}In_{0.1}Ga_{0.8}N films using ultraviolet assisted photo-electrochemical etching route. *J. Alloys Compd.* **2015**, *649*, 337-347, doi:10.1016/j.jallcom.2015.07.114.
- ⁹⁰ I. Studenyak, M. Kranjčec, M. Kurik, Urbach Rule in Solid State Physics. *Int. J. Opt. Appl.* **2014**, *4*(3), 76-83, doi: 10.5923/j.optics.20140403.02.
- ⁹¹ Zn 2p 3/2 line, NIST XPS database website, available on: https://srdata.nist.gov/xps/EngElmSrChQuery.aspx?ETType=PE&CSOpt=Retri_ex_dat&Elm=Zn. Accessed on 13/10/2020.
- ⁹² J.A. Schwarz, C. Contescu, A. Contescu, Methods for Preparation of Catalytic Materials. *Chem. Rev.* **1995**, *95*, 477-510, doi:10.1021/cr00035a002.
- ⁹³ S. Sakthivel, M.C. Hidalgo, D.W. Bahnemann, S.U. Geissen, V. Murugesan, A. Vogelpohl, A fine route to tune the photocatalytic activity of TiO₂. *Appl. Catal. B* **2006**, *63*, 31-40, doi:j.apcatb.2005.08.011.
- ⁹⁴ A. Kołodziejczak-Radzimska, T. Jesionowski, *Materials* **2014**, *7*, 2833-2881; doi:10.3390/ma7042833.
- ⁹⁵ G. Leofanti, M. Padovan, G. Tozzola, B. Venturelli, Surface area and pore texture of catalysts. *Catal. Today* **1998**, *41*, 207-219, doi:10.1016/S0920-5861(98)00050-9.
- ⁹⁶ Auger parameters for Zn, NIST XPS database website, available on: https://srdata.nist.gov/xps/EngElmSrChQuery.aspx?ETType=AP&CSOpt=Retri_ex_dat&Elm=Zn. Accessed on 13/10/2020.
- ⁹⁷ Ti 2p 3/2 line, NIST XPS database website, available on: https://srdata.nist.gov/xps/EngElmSrChQuery.aspx?ETType=PE&CSOpt=Retri_ex_dat&Elm=Ti. Accessed on 13/10/2020.
- ⁹⁸ O 1s line, NIST XPS database website, available on: https://srdata.nist.gov/xps/EngElmSrChQuery.aspx?ETType=PE&CSOpt=Retri_ex_dat&Elm=O. Accessed on 13/10/2020.
- ⁹⁹ J. C. C. Fan, J. B. Goodenough, X-ray photoemission spectroscopy studies of Sn-doped indium-oxide films. *J. Appl. Phys.* **1977**, *48*, 3524, doi: 10.1063/1.324149.

- ¹⁰⁰ G. Ballerini, K. Ogle 1, M.-G. Barthés-Labrousse, The acid–base properties of the surface of native zinc oxide layers: An XPS study of adsorption of 1,2-diaminoethane. *Appl. Surf. Sci.* **2007**, *253*, 6860–6867, doi: 10.1016/j.apsusc.2007.01.126.
- ¹⁰¹ O 1s line, NIST XPS database website, available on : https://srdata.nist.gov/xps/EngElmSrChQuery.aspx?EType=PE&CSOpt=Retri_ex_dat&Elm=C. Accessed on 13/10/2020.
- ¹⁰² A. Gankanda, D.M. Cwiertny, V.H. Grassian, Role of Atmospheric CO₂ and H₂O Adsorption on ZnO and CuO Nanoparticle Aging: Formation of New Surface Phases and the Impact on Nanoparticle Dissolution. *J. Phys. Chem. C* **2016**, *120*, 19195–19203, doi:10.1021/acs.jpcc.6b05931.
- ¹⁰³ Y. Sawada, M. Murakami, T. Nishide, Thermal analysis of basic zinc carbonate. Part 1. Carbonation process of zinc oxide at 8 and 13°C. *Thermochim. Acta* **1996**, *273*, 95–102, doi: 10.1016/0040-6031(95)02631-2.
- ¹⁰⁴ N. Kanari, D. Mishra, I. Gaballah, B. Dupré, Thermal decomposition of zinc carbonate hydroxide. *Thermochim. Acta* **2004**, *410*, 93–100, doi:10.1016/S0040-6031(03)00396-4.
- ¹⁰⁵ F. Viñes, A. Iglesias-Juez, F. Illas, M. Fernández-García, Hydroxyl identification on ZnO by infrared spectroscopies: Theory and experiments. *J. Phys. Chem. C* **2014**, *118*, 1492–1505, doi:10.1021/jp407021v.
- ¹⁰⁶ H. Jensen, A. Soloviev, Z. Li, E.G. Sjøgaard, XPS and FTIR investigation of the surface properties of different prepared titania nano-powders. *Appl. Surf. Sci.* **2005**, *246*, 239–249, doi:10.1016/j.apsusc.2004.11.015.
- ¹⁰⁷ R.M. Silverstein, F.X. Webster, D.J. Kiemle, Infrared Spectrometry. In *Spectrometric identification of organic compounds*, 7th ed. John Wiley & Sons, Inc.: Hoboken (USA), 2005. ISBN: 0471393622.
- ¹⁰⁸ R.A. Wahyuono, F. Hermann-Westendorf, A. Dellith, C. Schmidt, J. Dellith, J. Plentz, M. Schulz, M. Presselt, M. Seyring, M. Rettenmeyer, B. Dietzek, Effect of annealing on the sub-bandgap, defects and trapping states of ZnO nanostructures. *Chem. Phys.* **2017**, *483–484*, 112–121, doi: 10.1016/j.chemphys.2016.12.002.
- ¹⁰⁹ I. Shalish, H. Temkin, V. Narayanamurti, Size-dependent surface luminescence in ZnO nanowires. *Phys. Rev. B* **2004**, *69*, 245401, doi:10.1103/PhysRevB.69.245401.
- ¹¹⁰ G. Xi, S. Ouyang, J. Ye, General synthesis of hybrid TiO₂ mesoporous “french fries” toward improved photocatalytic conversion of CO₂ into hydrocarbon fuel: A case of TiO₂/ZnO. *Chem. Eur. J.* **2011**, *17*, 9057–9061, doi:10.1002/chem.201100580.
- ¹¹¹ Y. Xu, M. A. A. Schoonen, The absolute energy positions of conduction and valence bands of selected semiconducting minerals. *Am. Min.* **2000**, *85*, 543–556, doi:10.2138/am-2000-0416.
- ¹¹² K. Bandopadhyay, J. Mitra, Zn interstitials and O vacancies responsible for n-type ZnO: what do the emission spectra reveal? *RSC Adv.* **2015**, *5*, 23540–23547, doi:10.1039/c5ra00355e.
- ¹¹³ C.H. Ahn, Y.Y. Kim, D.C. Kim, S.K. Mohanta, H.K. Cho, A comparative analysis of deep level emission in ZnO layers deposited by various methods. *J. Appl. Phys.* **2009**, *105*, 1–6, doi:10.1063/1.3054175.
- ¹¹⁴ P.S. Xu, Y.M. Sun, C.S. Shi, F.Q. Xu, H.B. Pan, The electronic structure and spectral properties of ZnO and its defects. *Nucl. Instruments Methods Phys. Res. B* **2003**, *199*, 286–290, doi:10.1016/S0168-583X(02)01425-8.
- ¹¹⁵ A. Olivo, E. Ghedini, P. Pascalicchio, M. Manzoli, G. Cruciani, M. Signoretto, Sustainable Carbon Dioxide Photoreduction by a Cooperative Effect of Reactor Design and Titania Metal Promotion. *Catalysts* **2018**, *8*, 41, doi:10.3390/catal8010041.
- ¹¹⁶ A. Olivo, W.A. Thompson, E.R.B. Bay, E. Ghedini, F. Menegazzo, M. Maroto-Valer, M. Signoretto, Investigation of process parameters assessment via design of experiments for CO₂ photoreduction in two photoreactors. *J. CO₂ Util.* **2020**, *36*, 25–32, doi:10.1016/j.jcou.2019.10.009.
- ¹¹⁷ G. Martra, Lewis acid and base sites at the surface of microcrystalline TiO₂ anatase: relationships between surface morphology and chemical behaviour. *Appl. Catal. A* **2000**, *200*, 275–285, doi:10.1016/S0926-860X(00)00641-4.
- ¹¹⁸ M. Tahir, N.S. Amin, Advances in visible light responsive titanium oxide-based photocatalysts for CO₂ conversion to hydrocarbon fuels. *Energy Convers. Manag.* **2013**, *76*, 194–214, doi:10.1016/j.enconman.2013.07.046.
- ¹¹⁹ I. Grigioni, M.V. Dozzi, M. Bernareggi, G.L. Chiarello, E. Selli, Photocatalytic CO₂ reduction vs. H₂ production: The effects of surface carbon-containing impurities on the performance of TiO₂-based photocatalysts. *Catal. Today* **2017**, *281*, 214–220, doi:10.1016/j.cattod.2016.05.040.
- ¹²⁰ Z. Wang, H. Chou, J.C.S. Wu, D. Ping, G. Mul, CO₂ photoreduction using NiO/InTaO₄ in optical-fiber reactor for renewable energy. *Applied Catal. A* **2010**, *380*, 172–177, doi: 10.1016/j.apcata.2010.03.059.

CHAPTER 3: CO₂ PHOTOELECTROCHEMICAL REDUCTION BY PHOTOCATHODES BASED ON EARTH-ABUNDANT ELEMENTS



1. INTRODUCTION

1.1. INSIGHTS IN PHOTOELECTROCHEMICAL LIGHT-TO-CHEMICAL CONVERSION

A general overview of how a photo(electro)catalyst works was given in Preface. In the specific case of photoelectrochemistry, the physical fundamental behind is a bit more complex. When a solution, a liquid electrolyte in the case of PEC systems, is put in contact with a photoelectrode, an equilibration process occurs. The Fermi level (E_F) of the semiconductor (SC) equilibrates with the Fermi level of the solution (E_{redox}) (Figure 1a,b), through a charge transfer of majority carriers (holes in a p-type SC) from the SC to the solution. After reaching the equilibrium, the so-called depletion or space charge layer is formed, where the majority carriers have moved away. This layer is characterized by a width (W), usually in the range of tens or hundreds of nm, and a potential drop, also referred as band bending (E_{sc}), which inhibits further SC/electrolyte charge transfer. As reported in Figure 1b, E_{sc} is graphically represented as a bending of both conduction (E_c) and valence (E_v) band edges at SC/electrolyte interface. Interestingly, in photocatalysis the E_{sc} can be usually neglected because the nanostructured particles typically used, having a size lower than W , lie completely within the space-charge layer [1].

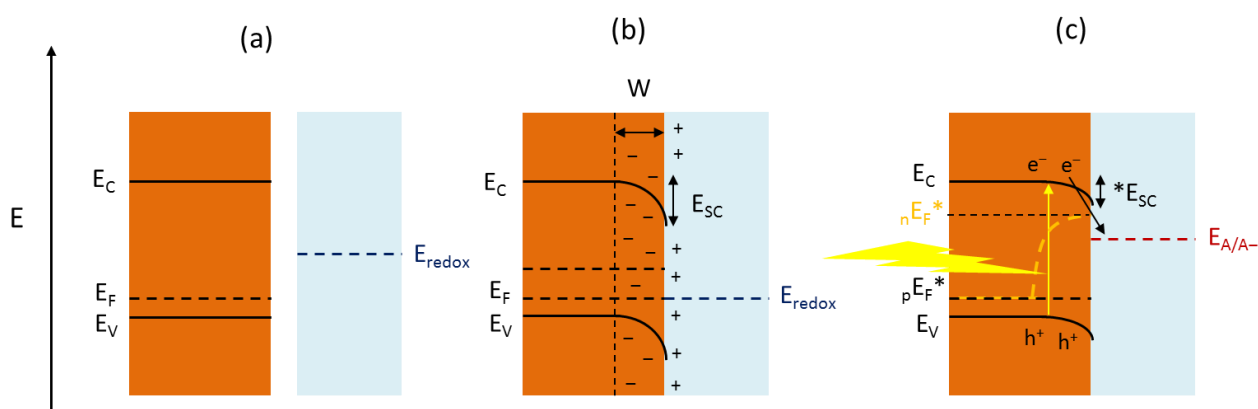


Figure 1. Band energy diagram of a p-type SC in vacuum (a); in contact with a liquid electrolyte in dark (equilibrium conditions) (b); in contact with a liquid electrolyte under irradiation (photoexcited state) (c). Redrawn from [2].

When the SC/electrolyte system is irradiated with photons having a suitable energy, electrons are promoted from the valence band (VB) to the conduction band (CB), affording photoexcited charge carriers population described by the quasi-Fermi levels (pE_F^* and nE_F^*), as already described in Preface. The limited photon penetration depth within the material, generates photoexcited charge carriers close to the SC/electrolyte interface, thus affording the photo-induced splitting of E_F in proximity of SC surface (dashed yellow line in Figure 1c). The photoexcitation at SC/electrolyte interface, induces a remarkable increase of minority charge carriers population, electrons in the case of a p-type SC, while the majority carriers are almost unchanged compared to the dark. Such increase in minority carriers lead to two effects:

1. Reduces the band bending in the excited SC ($E_{sc}^* < E_{sc}$) (Figure 1c)

- Allows the minority carrier to be transferred from SC surface to a suitable redox couple (an electron acceptor, E_{A/A^-} , in case of p-type SC), yielding a photocurrent, otherwise negligible in dark conditions.

The difference between band bending in dark and under irradiation is named photopotential or photovoltage (ΔE_{ph}), as reported in Equation 1 [2].

$$\Delta E_{ph} = |E_{SC} - E_{SC}^*|$$

Equation 1. Definition of photovoltage.

A PEC setup requires two different components to work: a photoelectrode and a counter-electrode (or another photoelectrode), where the two redox pathways take place independently [3]. As reported in Figure 2, a third component named transparent conductive oxide (TCO), usually serves as mechanical support for the photoelectrode allowing both the transmittance of the incoming light and the charge harvesting [4]. Three main kinds of PEC setup exist [3]:

- Photocathode-based cell, where a photocathode is photoexcited leading to a reduction reaction at SC/electrolyte interface, while the oxidation occurs at the counter-electrode/electrolyte interface. (Figure 2a)
- Photoanode-based cell, where a photoanode is photoexcited leading to an oxidation reaction, while the reduction occurs at the counter-electrode (Figure 2b)
- Photocathode-photoanode tandem cell, where the incoming light is first absorbed by the photoanode, affording in an oxidation reaction, then the residual light is absorbed by the photocathode, leading to a reduction reaction. It is worth to note that this configuration requires a wider band-gap (E_g) for the first absorber (photoanode) respect to the second one (photocathode) (Figure 2c).

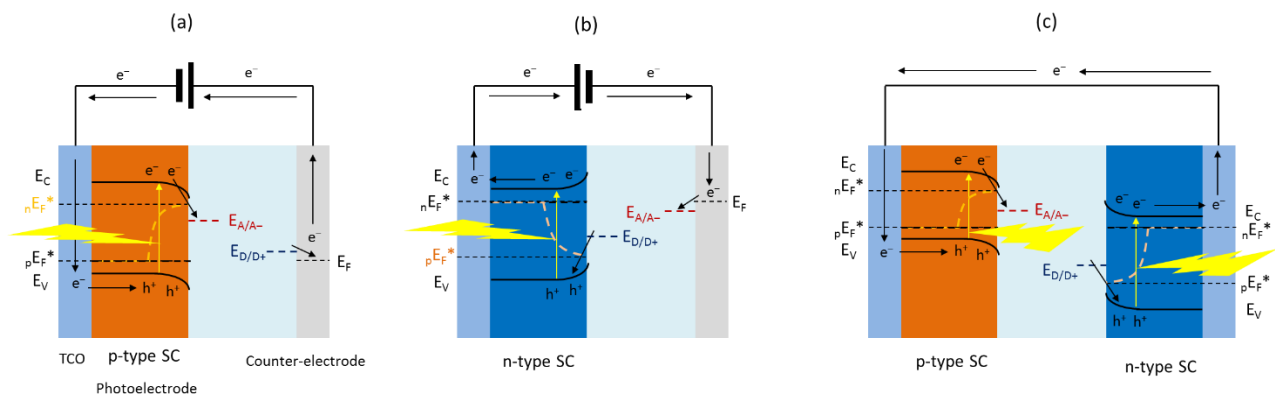


Figure 2. PEC setups. Photocathode-based cell (a), photoanode-based cell (b), photocathode-photoanode tandem cell (c). Transparent conductive oxide (TCO), photoelectrode and counter-electrode are highlighted in (a). Redrawn from [3] and [5].

The PEC tandem cells represent an ideal device to run a redox process, since the energy required is fully supplied by the incoming light, avoiding an external potential to be applied.

The development of photoanodes has been focused mainly on four oxide-based SCs: titanium dioxide (TiO_2) [6], hematite (Fe_2O_3) [7], bismuth vanadate (BiVO_4) [8] and tungsten trioxide (WO_3) [9]. Due to extensive and detailed studies over the last decades, a comprehensive knowledge about these materials is now available [10-13]. Contrary, plenty of different materials have been proposed as photocathode, ranging from oxides such as cuprous oxide (Cu_2O) [14], copper-iron delafossite (CuFeO_2) [15] or copper niobate (CuNbO_3) [16]; chalcogenides like copper gallium indium sulphide ($\text{Cu}(\text{Ga},\text{In})\text{S}_2$) [17], copper zinc tin sulphide ($\text{Cu}_2\text{ZnSnS}_4$) [18] or tungsten diselenide (WSe_2) [19]; phosphides like gallium phosphide (GaP) [20] or indium phosphide (InP) [21], as well as silicon (Si) [22]. The stability in irradiated aqueous medium is an issue affecting many p-type SCs, requiring protecting overlayers to be stable, especially among non-oxide materials [21,23], but also some oxides [24].

1.2. CO_2 PHOTOELECTROCHEMICAL REDUCTION

Historically, PEC devices have been focused mainly on hydrogen (H_2) production from water splitting [25,26]. However, as pointed in Chapter 1 and 2, H_2 suffers of two important drawbacks: the storage [27] and the expensiveness of fuel cells [28]. The CO_2 reduction affords in several C-based products such as carbon monoxide (CO), formic acid (HCOOH), formaldehyde (HCHO), methanol (CH_3OH), ethanol ($\text{C}_2\text{H}_5\text{OH}$), methane (CH_4), ethylene (C_2H_4) and ethane (C_2H_6) [29]. Some of these are already used as easily storable fuels (i.e. CH_4 , CH_3OH or $\text{C}_2\text{H}_5\text{OH}$) [30], or valuable intermediates for fuel (i.e. CO) [31] or for chemical production (i.e. C_2H_4 , HCHO , HCOOH) [32], overcoming the above mentioned issues of H_2 storage and utilization.

The variety of attainable reduction products, makes the overall reaction mechanism complex, composed of several pathways, and affected by several parameters (i.e. type of SC, nature of the electrolyte, presence and nature of a co-catalyst) [33]. The utilization of co-catalysts is a commonly involved strategy to improve CO_2 reduction activity. Indeed, such components usually decorate the SC surface and allow an efficient electron transfer to adsorbed CO_2 : this reduces the kinetic barriers to charge transfer (overpotential), making them the true catalytic active phase, while the SC works only as light harvester [34]. Different types of co-catalysts are reported in literature, like metals [35,36], metal complexes [37,38], metal oxides [39], nitrides or phosphides [40], carbon nanomaterials [41] and pyridine [42].

Different SCs have been proposed as both photoanodes and photocathodes in CO_2 PEC conversion. Despite some photoanode-based (Figure 2b) [43,44] and a tandem cell (Figure 2c) [45] has been reported for this reaction, photocathodes-based PEC cells (Figure 2a) are the most used for this application. Several p-type SC have been studied for this purpose, such as Cu_2O [38,46], Si [36, 39], InP [47], GaP [42], $\text{Cu}_2\text{ZnSnS}_4$ [48], $\text{Cu}_2\text{ZnGeS}_4$ [49], CuInS_2 [50], ZnSe [51], ZnTe [52], CuFeO_2 [53] and $\text{Cu}_3\text{Nb}_2\text{O}_8$ [54]. Despite being a promising

technology, different issues still affect the performances of photocathodes for CO₂ conversion, such as the previously mentioned photocorrosion in water-based medium [46], the still limited control in product selectivity [39,47], the competition of hydrogen evolution reaction (HER), a generally undesired reaction pathway [48,49] and the co-catalyst modification [38,53]. Nonetheless, some interesting examples of stable and selective photocathodes have been also reported [42,53], even though still far from large-scale applications. Some examples of photocathode-based devices are summarized in Table 1.

Table 1. Examples of photocathodes used for CO₂ PEC reduction.

Reference	SC	Co-catalyst	Reduction products and faradic efficiency (F.E.)	Photocurrent density (J_{ph}) ($\text{mA}\cdot\text{cm}^{-2}$)	Notes
[38]	Cu ₂ O	Re(bpy)(CO) ₃ Cl	CO (80-95%)	- 2.5 (@ - 1.9 V vs Fc/Fc ⁺)	Co-catalyst deactivation through structural changes; TiO ₂ protecting overlayer.
[46]	Cu ₂ O	Cu ⁺ species	CH ₃ OH (50.7%)	- 0.47 (@ 0.3 V vs RHE)	Cu ₂ O photocorrosion despite TiO ₂ protecting overlayer. Only 27.6% of J_{ph} after 30 min.
[36]	Si	Porous Au	CO (96%)	- 9.2 (@ - 1.0 V vs RHE); total current	Device stable for 4.5 h; thick Au layer selective for H ₂ , porous Au layer for CO.
[39]	Si	Porous SnO ₂	HCOOH (59.2%), CO (11.4%), H ₂ (29%)	- 10 (@ 0.25 V vs RHE)	≈ 90% J_{ph} after 3 h; E > - 0.4 V vs RHE afforded 95% F.E. in H ₂ .
[42]	GaP	Pyridine in buffered solution	CH ₃ OH (88-100%)	- 0.1 (@ - 0.4 V vs RHE)	Device stable up to 30 h; effect of two wavelength assessed.
[49]	Cu ₂ ZnGeS ₄	ZnS	CO (3.3%), H ₂ (80%)	Not reported for CO ₂ PEC test	Device stable up to 2 h; ZnS claimed to act as co-catalyst; predominant hydrogen evolution reaction (HER).
[52]	ZnTe	Au	CO (64%), H ₂ (32.5%)	- 3.14 (@ - 0.11 V vs RHE)	Stable up to 3 h; aggregation, Au NPs detachment, electrochemical corrosion of SC as suggested reasons of stability loss.
[53]	CuFeO ₂	CuO	HCOOH (90%)	- 0.3 (@ - 0.35 V vs RHE)	Stable up to 7 days; deactivation due to Cu(II) and Fe(III) reduction after prolonged utilization.

1.3. THE CASE OF COPPER-IRON DELAFOSSITE (CuFeO₂)

Cu(I)-based oxides have recently emerged as p-type SC materials in PEC devices, due to wide range of attainable band-gaps, the relative high carrier mobility and the high-lying E_c (Figure 3), that theoretically allows the facile reduction of both CO₂ and H₂O [55].

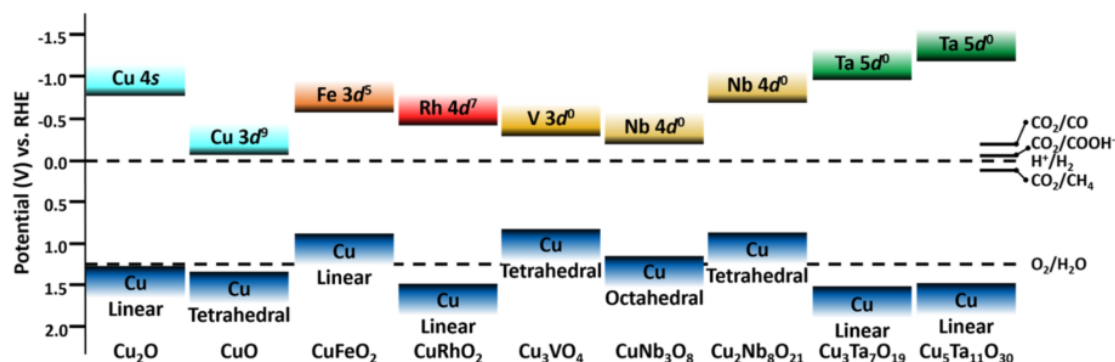


Figure 3. Band diagram of some CuO and some Cu(I)-based p-type SC [55].

Cu₂O is the simplest Cu(I)-based oxide, reported as effective photocathode in both water [14] and CO₂ [38] reduction, however suffering of poor photostability in water [46], thus requiring a protective overlayer [24]. An appealing class of Cu(I)-based materials is represented by copper delafossites, with a general formula CuMO₂, where M is a trivalent cation such as Fe³⁺, Al³⁺, Ga³⁺, Rh³⁺ or Cr³⁺ [56]. Most of these, like CuGaO₂, CuAlO₂ or CuCrO₂ have wide band-gaps ($E_g > 3$ eV), making them good candidate as transparent hole transporting material [57], but not as visible-light activated photocathodes. CuRhO₂ has been proposed as narrow band-gap SC (E_g 1.9 eV) for water splitting [58], however the expensiveness and rarity of Rh [59] makes economically unsustainable this material. CuFeO₂ is an appealing alternative to both Cu₂O and CuRhO₂, because:

1. Narrow band-gap (E_g 1.45 eV), allowing the harvesting of a large fraction of solar spectrum and a theoretical attainable photocurrent of 14.8 mA·cm⁻² [60]
2. Photostability in aqueous medium [53]
3. Composed of cheap and earth-abundant elements [61,62].

CuFeO₂ delafossite typically crystallizes with a rhombohedral structure [63], in which layer of octahedral FeO₆ are joined through linearly coordinated Cu(I), as represented in Figure 4. The CuFeO₂ phase can be obtained by thermal decomposition in inert atmosphere of Cu(II) and Fe(III) precursors at high temperature ($T > 650^\circ\text{C}$) [64], as well as through electrochemical deposition [53] or hydrothermal synthesis [63].

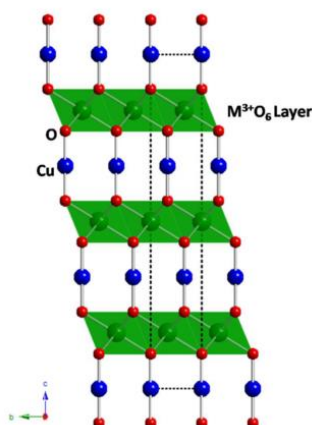


Figure 4. Rhombohedral R3m crystal structure of CuFeO₂ [55].

This material has been studied as photocathode for both water reduction [15] and CO₂ reduction [65]. Regarding the latter process, HCOOH has been often reported as the main CO₂ reduction product reaching high faradic efficiency (90%) with a CuO overlayer [66], while a lower one was observed on the bare surface (10%) [65], suggesting a competition of HER on pristine surface. Interestingly, C₂ carbon product such as acetic acid (CH₃COOH) and ethanol (C₂H₅OH) were detected as main reduction products by using a Fe-rich material [67] or titania nanotubes (TNT) scaffold [68], respectively. One of the most remarkable result in photocathode-based CO₂ PEC conversion is a CuFeO₂-based photoelectrode, achieving 1% of solar-to-fuel (STF) efficiency and, in particular, an impressive stability for one month [66]. However, several drawbacks still affect this material, such as the long term photostability [53,65], requiring periodic oxidative annealing to regenerate the photocathode [66], metal leaching [67] and the poor attainable photocurrent [68].

1.4. CuFeO₂ INSIGHTS: SURFACE STATES AND OVERLAYERS

Despite the promising mentioned features, this material suffers also of another important issue limiting its PEC performances: the surface states (SSs) [69]. These SSs cause the quasi-Fermi level (nE_F^*) to be pinned at the surface, acting as electron trap and allowing the SC/electrolyte charge transfer to occur only if the acceptor redox potential, E_{A/A^-} , lies at lower energy than the SSs; if it does not happen, the redox process cannot take place (Figure 5b) [2]. SSs in CuFeO₂ were assessed to be energetically located slightly above its E_V and thought to arise from a 10 nm layer composed of disordered Cu-Fe oxhydroxide [69]. These trap states, placed at + 0.65 V vs RHE, make in principle impossible both the water reduction ($E_{H^+/H_2}^0 = + 0.00 V vs RHE$) or CO₂ reduction, i.e. to CH₄ ($E_{CO_2/CH_4}^0 = + 0.17 V vs RHE$) or HCOOH ($E_{CO_2/HCOOH}^0 = - 0.20 V vs RHE$) [29].

A strategy to overcome the effect of SSs, is their passivation with a suitable overlayer that should possess some key features [70]:

1. Stability in the electrolyte
2. Uniform coating
3. Transparency in the absorbing region of the SC
4. Suitable band edge position to allow charge transfer to the electrolyte (i.e. only electrons in p-type SC)
5. Minimum lattice mismatch to minimize the creation of interfacial defects

A graphical representation of how an overlayer acts in SSs passivation is reported in Figure 5c. It has been proposed such overlayers to decrease the defects concentration on SC surface, responsible of SSs formation. For instance, Le Formal *et al.* proposed a thin overlayer of Al_2O_3 to saturate the oxygen vacancy, which was supposed to originate the SSs, on Fe_2O_3 photoanodes surface [71]. Similarly, on CuFeO_2 the overlayer would decrease the concentration of superficial defects, even if the nature of these defects is still unclear.

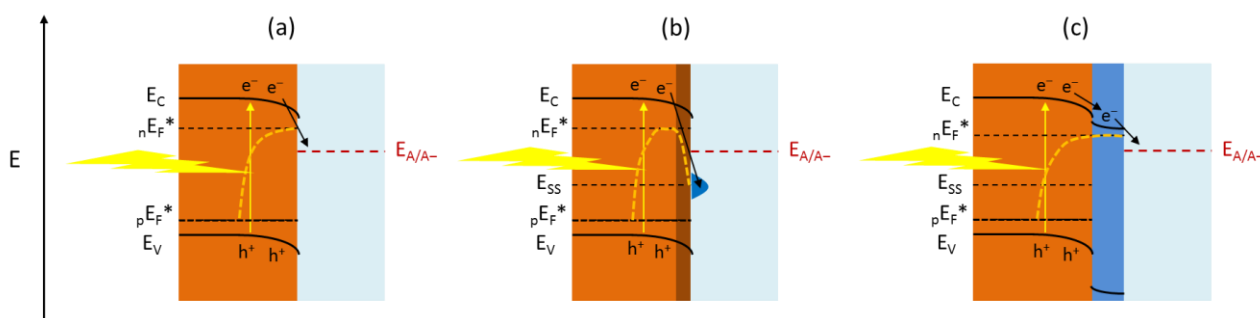


Figure 5. Band diagram of an irradiated p-type SC/electrolyte interface without (a), with SSs (brown layer) (b) and passivated with an overlayer (c).

A TiO_2 - ZnO overlayer was efficiently used to passivate CuFeO_2 SSs and, after surface functionalization with a co-catalyst, allows a stable H_2 evolution [60]. TiO_2 is the actual overlayer in this specific strategy, while ZnO was just enrolled as buffer layer to enable TiO_2 growth [24].

In the specific context of CO_2 PEC conversion ZnO is an interesting candidate as overlayer. Contrary to TiO_2 , being a basic SC, CO_2 adsorption can be remarkably improved on its surface [72]. A Cu-ZnO was already employed as co-catalyst on a Si/GaN photocathode, revealing a strong synergistic effect between Cu and ZnO in enhancing both the CO_2 reduction activity and selectivity [35]. Moreover, the chemical and electrical properties of ZnO can be tuned by heat treatments, aiming a higher crystallinity which improves the electrical conductivity [73] or an increased surface defects concentration to induce active sites for CO_2 activation [74] or improve ZnO basicity [75]. Finally, despite bare ZnO surfaces have been reported to be photo-catalytically active in CO_2 reduction [76], a co-catalyst is required to improve the conversion efficiency, and group 11 elements (Cu , Au , Ag) have been address as suitable materials acting in synergy with ZnO [35].

1.5. AIM OF THE CHAPTER

This work was performed in the Molecular Engineering of Optoelectronic Nanomaterials Laboratory (LIMNO), under the supervision of Professor Kevin Sivula, at the Ecole Polytechnique Fédérale de Lausanne (EPFL) (Lausanne, Switzerland) from May to October 2019. The aim of this chapter is to design ZnO overlayer as coating for CuFeO₂ photocathodes for CO₂ PEC conversion. Specifically, the chapter is divided in four sub-sections:

1. Optimization of ZnO thin films on a model non-conductive glass substrate. These films were prepared through a solution-based method aiming tunable thickness and structural properties (crystallinity, defects).
2. Preparation of a CFO photocathode through a vapor-phase synthetic technique, aiming an active photocathode with a sacrificial electron acceptor (sacrificial conditions).
3. Coating of CFO with optimized ZnO overlayers, assessing their effects on PEC performances in sacrificial conditions.
4. Loading of a co-catalyst (Cu) on the photocathodes, and assessing its activity in non-sacrificial conditions, namely with CO₂ as electron acceptor.

2. MATERIALS AND METHODS

2.1. REAGENTS

The following reagents were used as-received: zinc acetylacetonate hydrate ($\text{Zn}(\text{acac})_2 \cdot x\text{H}_2\text{O}$, Zn assay 23-26%, Sigma-Aldrich), iron (III) acetylacetonate ($\text{Fe}(\text{acac})_3$, assay > 97%, Sigma Aldrich), copper (II) nitrate trihydrate ($\text{Cu}(\text{NO}_3)_2 \cdot 3\text{H}_2\text{O}$, assay > 99%, Sigma Aldrich), copper (II) acetate monohydrate ($\text{Cu}(\text{OAc})_2 \cdot \text{H}_2\text{O}$, assay > 99.9%, Sigma Aldrich), sodium bicarbonate (NaHCO_3 , assay > 99.5%, Sigma Aldrich), sodium persulfate ($\text{Na}_2\text{S}_2\text{O}_8$, assay > 98%, Sigma Aldrich), sodium acetate (NaOAc , assay > 99%, Sigma Aldrich), europium (III) nitrate hexahydrate ($\text{Eu}(\text{NO}_3)_3 \cdot 6\text{H}_2\text{O}$, assay 99.9%, ABCR) and acetic acid (AcOH , assay > 99.7%, VWR).

The following solvents were used as-received: ethanol (EtOH , assay > 99.8%, VWR) and acetonitrile (MeCN , assay > 99.9%, Merck), Hellmanex solution (HelmaAnalytics), acetone (assay > 99.5%, Sigma Aldrich) and isopropanol (assay > 99.5%, Sigma Aldrich).

2.2. SYNTHESIS

2.2.1. SUBSTRATE PREPARATION

Borosilicate glass (Solaronix) or fluorine-doped tin oxide (FTO) coated aluminoborosilicate glass (Solaronix) slabs, were cut into 25 x 25 mm pieces. The substrates were then cleaned through successive ultrasound-assisted washing treatment with Hellmanex solution, acetone and isopropanol. The cleaned substrates were kept in isopropanol.

2.2.2. ZnO THIN FILMS SYNTHESIS

A proper amount of $\text{Zn}(\text{acac})_2 \cdot x\text{H}_2\text{O}$ was dissolved in a glass vial with a mixture of 8.5 mL of EtOH , 1.0 mL of deionized H_2O and 0.5 mL of AcOH . Different solutions with a Zn concentration ranging from 25 mM to 400 mM were prepared. The Zn solution was spin-coated with a WS-650MZ-23NPP (Laurell) spin-coater, pouring the Zn solution onto a cleaned glass substrate, at 2000 rpm for 1 minute, then air-dried on a heating pad at 110°C for 10 minutes. The as-coated substrates were finally annealed either in air at 300 °C for 1 hour, using a hotplate (ramp rate: 10 °C·min⁻¹) or under argon flow (ca. 300 mL·min⁻¹) at 400 °C or 600 °C for 1 hour (ramp: 10 °C·min⁻¹) with a OTF-1200X tubular oven. The annealed samples are labelled as follow:

1. XAZn, where X stands for the molar concentration of the Zn precursor solution (25, 50, 75, 100, 200, 300 or 400 mM). The samples were air annealed (A) at 300°C.
2. YArZn, where Y stand for the argon (Ar) annealing temperature, namely 400°C or 600°C. A 100 mM Zn precursor solution was spin-coated before annealing.

2.2.3. CuFeO₂ THIN FILM SYNTHESIS

Aerosol assisted chemical vapor deposition (AACVD) was used to prepare CuFeO₂ thin films. A solution of 0.06 M Fe(acac)₃ and 0.04 M Cu(NO₃)₂·3H₂O, was prepared by dissolving the proper amount of the precursors in 50 mL of MeCN. A vertically aligned nozzle was used to perform the deposition, equipped with an *in-situ* ultrasound generator to afford micrometer-sized droplets. The solution was then sprayed in atmospheric conditions (air, 101 kPa) through a lab-made spray-pyrolyzer, onto the conductive side of cleaned FTO substrate, on a hotplate at 550 °C, with a feeding rate of 1 mL·min⁻¹ for 20 minutes. The samples were then annealed under argon flow (ca. 300 mL·min⁻¹) at 700 °C for 1 hour (ramp: 10 °C·min⁻¹) with a OTF-1200X tubular oven. Finally, a mild air post-annealing at 300 °C for 1 hour using a hotplate (ramp rate: 10 °C·min⁻¹) was performed [60]. The sample is labelled CFO.

2.2.4. ZnO OVERLAYER COATING ON CuFeO₂ THIN FILMS

Zn(acac)₂·xH₂O solutions in EtOH/H₂O/AcOH were prepared, spin-coated onto CFO and air/Ar annealed as reported in section 2.2.2. The annealed samples are labelled as follow:

1. XAZn/CFO, where X stands for the molar concentration of the Zn precursor solution (0.5, 1.0, 2.5, 5, 10, 25, 50, 100, 200 mM). The samples were air annealed (A) at 300°C.
2. YArZn/CFO, where Y stand for the argon (Ar) annealing temperature, namely 400°C or 600°C. A 200 mM Zn precursor solution was spin-coated before annealing.

2.2.5. Cu CO-CATALYST LOADING ON CuFeO₂ THIN FILMS

A buffered solution of 1 mM Cu(OAc)₂ and 10 mM NaOAc was prepared by dissolving the proper amount of the precursors in 100 mL of deionized water. The resulting measured pH was 6.6. The photoelectrochemical deposition (PED) was performed with a three-electrode “cappuccino” cell configuration and a computer controlled SP-200 potentiostat (BioLogic). CFO or ZnO-coated CFO thin films were used as working electrodes, with an active geometric area of 0.238 cm², an Ag/AgCl/KCl (sat.) as reference electrode and a Pt wire as counter electrode. The PED was performed in an Ar purged Cu precursor solution, previously air-evacuated by bubbling Ar for 10 minutes, under front irradiation (electrolyte-side) and constant applied potential of 0.58 V vs RHE for 10 minutes. The as-deposited electrodes were finally rinsed with deionized water to remove residual ions. The Cu PED samples were labelled as Cu/P, where P is one of the previously mentioned photocathodes label, either CFO or the ZnO-coated ones.

2.3. STRUCTURAL AND OPTICAL CHARACTERIZATION

The optical absorbance was measured with an integration sphere equipped UV-vis-NIR UV-3600 spectrophotometer (Shimadzu). The bandgap (E_g) of the materials were determined by Equation 2 (Tauc

relation), where α is the absorption coefficient in cm^{-1} , h the Plank constant ($6.626 \cdot 10^{-34}$ J·s), ν the photon frequency in s^{-1} , C a constant and E_g the bandgap energy. For direct allowed optical transition the exponent is set to $n = \frac{1}{2}$, while for indirect transitions is set to $n = 2$. The E_g was determined as intercept plotting $(\alpha h\nu)^{1/n}$ vs $h\nu$ [77].

$$\alpha h\nu = C(h\nu - E_g)^n$$

Equation 2. Tauc relation [77].

Phase composition was measured using an Xplora Plus Raman microscope (Horiba Scientific), using a Ar laser (532.19 nm) as light excitation source.

Surface morphology was analyzed with a scanning electron microscopy (SEM) (Zeiss Merlin), using an in-lense detector for secondary electrons (SE).

Surface morphology was also examined using atomic force microscopy (AFM), while Fermi-level mapping was obtained through scanning Kelvin probe force microscopy (SKPM). Both analyses were carried out using an Cypher instrument (Asylum Researcher) and Pt:Ir-coated silicon tips (AC240TM, Olympus). For SKPM analyses, the work function of the tips was calibrated using reference sample of Pt, Cu and Mo.

Thickness of films was verified by a Dektak XT (Bruker) optical profilometer.

Surface composition and chemical states of elements were measured through X-ray photoelectron spectroscopy (XPS) using a PHI VersaProbe II scanning XPS microprobe. The analyses were performed using a monochromatic Al $K\alpha$ X-ray source of a beam diameter of 100 μm and a spherical capacitor analyzer at 45° take-off angle with respect to the sample surface. Charge shift was corrected by calibration with adventitious C 1s peak set at 284.8 eV. High-resolution XPS analyses were carried out after a mild Ar^+ sputtering to remove adventitious carbon interference. Peak deconvolutions were performed with Gauss function after Shirley-type baseline correction. Depth-profiling XPS spectra were acquired at different depths after Ar^+ beam sputtering.

Surface functional groups were analyzed through Fourier-transform IR (FTIR) spectroscopy using attenuated total reflectance (ATR) Perkin-Elmer spotlight 200i system. Clean uncoated substrates (FTO or glass) were taken as background spectrum.

2.4. PHOTOELECTROCHEMICAL CHARACTERIZATION

PEC measurements were carried out in a three-electrode cell setup connected to a computer-controlled SP-200 potentiostat (BioLogic). An Ag/AgCl/KCl sat. electrode was used as reference, a Pt wire as counter electrode and 12.5 x 25 mm coated-FTO as working electrodes, with an active geometric area of 0.238 cm^2 .

The applied potentials in all the PEC measurements were referred to the pH-independent reversible hydrogen electrode (RHE) (Equation 3).

$$V_{RHE} = V_{Ag/AgCl} + 0.059 \times pH + 0.197$$

Equation 3. RHE relation. $V_{Ag/AgCl}$ is the measured cell potential; $0.059 \cdot pH$ is a correction term due to electrolyte pH; 0.197 is the potential of the Ag/AgCl/KCl sat. electrode vs NHE.

The PEC cell configuration is the “cappuccino-type” (Figure 6), made of polyetheretherketone (Erta Peek), with a 20 mm fused silica spherical window (Robson Scientific) [78]. Specifically, reference and counter electrodes, were put on the lateral holders (blue arrow, Figure 6), while the working FTO-coated electrode was fixed in the central rectangular-shaped holder (red arrow, Figure 6), and the cell filled with an appropriate amount of electrolyte solution (ca. 10 mL).

The light source was provided by an array of RGBW Star LEDs (Cree) calibrated using a Si photodiode to provide a photon flux equal to the AM 1.5G spectrum ($1000 \text{ W} \cdot \text{m}^{-2}$) for $h\nu$ larger than the bandgap of CuFeO_2 .

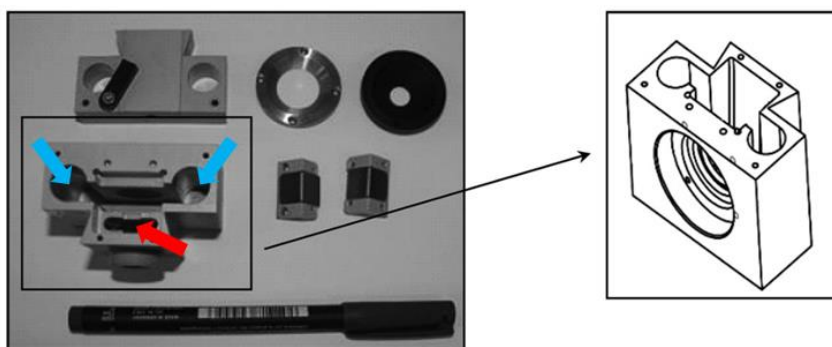


Figure 6. Cappuccino cell [78].

2.4.1. Linear Sweep Voltammetry (LSV) and Chronoamperometry (CA)

The photoelectrodes current-voltage (J-V) response under irradiation, was measured through linear sweep voltammetry (LSV), operating in a 0.0 – 1.0 V vs RHE scan range, with a $10 \text{ mV} \cdot \text{s}^{-1}$ scan rate using a chopped light irradiation (2 s light – 1 s dark). The analyses were carried either in sacrificial conditions (0.1 M NaHCO_3 , 0.1 M $\text{Na}_2\text{S}_2\text{O}_8$, pH = 8.4), using an aqueous electrolyte containing $\text{Na}_2\text{S}_2\text{O}_8$ as electron acceptor ($E_{\text{S}_2\text{O}_8^{2-}/\text{SO}_4^{2-}}^0 = + 2.1 \text{ V vs RHE}$) [79], or in non-sacrificial conditions, using an aqueous electrolyte (0.3 M NaHCO_3) purged by bubbling Ar (pH = 8.6) or CO_2 (pH = 7.4), previously air evacuated by bubbling the gases for 10 minutes. The onset potential (E_{ONSET}), potential in the J-V curve at which the current start to rise, was determined as the potential corresponding to a $5 \mu\text{A} \cdot \text{cm}^{-2}$ photocurrent density.

The photoelectrodes stability was assessed through chronoamperometry (CA), measuring the current density (J) under a constant applied potential of 0.2 V vs RHE, chopped light irradiation (30 s light – 10 s dark) and

using a CO₂-purged electrolyte (0.3 M NaHCO₃, pH = 7.4), previously air-evacuated by CO₂ bubbling for 10 minutes.

2.4.2. Open Circuit Potential (OCP)

The photo-induced voltage in open circuit conditions ($J = 0 \text{ mA}\cdot\text{cm}^{-2}$), namely the open circuit potential (OCP), was measured using a two electrodes configuration cell with coated-FTO as working electrodes and Ag/AgCl/KCl sat. as reference electrode. A 1.2 M Eu(NO₃)₃ aqueous solution (pH = 4.2) was used as electrolyte, involving the Eu^{3+/2+} redox couple as electrochemical probe due to its negative redox potential ($E_{Eu^{3+/2+}}^0 = -0.35 \text{ V vs RHE}$) and fast charge transfer kinetics [80].

2.4.3. Electrochemical Impedance Spectroscopy (EIS)

Information about the acceptor density (N_A) and flat-band potential (E_{FB}) of a SC, those are related to charge carrier mobility and the E_V position, respectively, were obtained through electrochemical impedance spectroscopy (EIS). Measurements were carried out in dark conditions, in a 0.6 – 1.2 V vs RHE scan range, 100 mHz – 1 MHz frequency range using non-sacrificial electrolyte (Ar-purged 0.1 M NaHCO₃), previously air-evacuated by bubbling Ar for 10 minutes.

The impedance (Z) is defined in Equation 4, where $E(t)$ is the applied voltage; $I(t)$ the measured current; E_0 and I_0 are the corresponding voltage and current amplitude; i is the imaginary unity; ω is the applied frequency; φ is the phase shift between $E(t)$ and $I(t)$; t is the time; Z' is the real part of impedance; Z'' is the imaginary part. Plotting the real part of impedance (Z') vs imaginary part (Z''), affords in the Nyquist plot.

$$Z(\omega) = \frac{E(t)}{I(t)} = \frac{E_0 e^{i\omega t}}{I_0 e^{i(\omega-\varphi)t}} = \frac{E_0}{I_0} e^{i\varphi} = Z'(\omega) e^{i\varphi} = Z'(\omega) Z''(\omega)$$

Equation 4. Impedance relation [81].

The space charge layer capacitance (C_{SC}) of the electrochemical system was obtained by fitting the Nyquist plot with an equivalent circuit already reported for CFO and reported in Figure 7. Specifically, R_s is the resistance related to the external circuit and the bulk of the semiconductor; C_{bulk} is the capacitance depending on the space-charge layer capacitance at the SC/electrolyte interface (C_{SC}) and the Helmholtz layer capacitance on the electrolyte side (C_H) (Equation 5); $R_{trapping}$ is the charge trapping/detrapping resistivity on SSS; C_{trap} is the capacitance due to SSS; $C_{ct,trap}$ is the resistivity associated to SSS-to-electrolyte charge transfer [69].

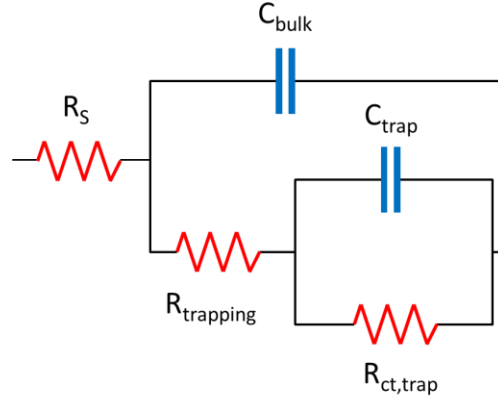


Figure 7. Equivalent circuit used for CuFeO₂ EIS modeling [69].

$$\frac{1}{C_{bulk}} = \frac{1}{C_{SC}} + \frac{1}{C_H}$$

Equation 5. Bulk capacitance (C_{bulk}) relation [69].

The acceptor density (N_A) and the flatband potential (E_{FB}) were obtained by plotting C_{SC} vs E (Mott-Schottky plot) and by fitting the linear part of the plot with the Mott-Schottky relation (Equation 6). In this equation, e is the elementary charge ($1.602 \cdot 10^{-19}$ C); ϵ the CFO relative permittivity ($\epsilon = 20$); ϵ_0 the vacuum permittivity ($8.854 \cdot 10^{-12}$ F·m⁻¹); N_A the acceptor density in cm⁻³; f_r the roughness factor, defined as the ratio between the actual electrode area (A) and the geometrical area (A_0) of the sample, and determined by AFM measurement (1.6); E and E_{FB} are the applied potential and the flatband potential, respectively, given as V vs RHE; k_B the Boltzmann constant ($1.38 \cdot 10^{-23}$ J·K⁻¹); T the absolute temperature in K [69].

$$\frac{1}{C_{SC}^2} = -\frac{2}{e\epsilon\epsilon_0 N_A f_r^2} \left(E - E_{FB} - \frac{k_B T}{e} \right)$$

Equation 6. Mott-Schottky equation [69].

3. RESULTS AND DISCUSSION

3.1. ZnO OVERLAYER

A solution-based method, namely spin-coating, followed by annealing to crystallize ZnO and remove organic residues [82], was chosen as simpler and safer procedure than the already reported atomic layer deposition (ALD) [60]. Air annealing is an effective thermal treatment for organic removal, however it must be carefully kept at $T < 300^\circ\text{C}$ to avoid over oxidation of p-type CuFeO_2 to n-type CuFe_2O_4 , that could negatively affect the PEC performances [60]. Annealing processes at higher temperature ($T > 300^\circ\text{C}$), exploited to tune the electrical properties (i.e. crystallinity and defect contents) of ZnO [73], were performed in inert atmosphere in order to avoid the oxidation of CuFeO_2 .

The UV-vis absorption spectra of the air annealed sample 100AZn compared to the bare glass substrate (Figure 8a), revealed an absorption band-edge in the UV region ($\lambda < 400\text{ nm}$). A direct band-gap (E_g) of 3.30 eV, determined through Tauc plot analysis (Figure 8b), is in good agreement with literature reports [83].

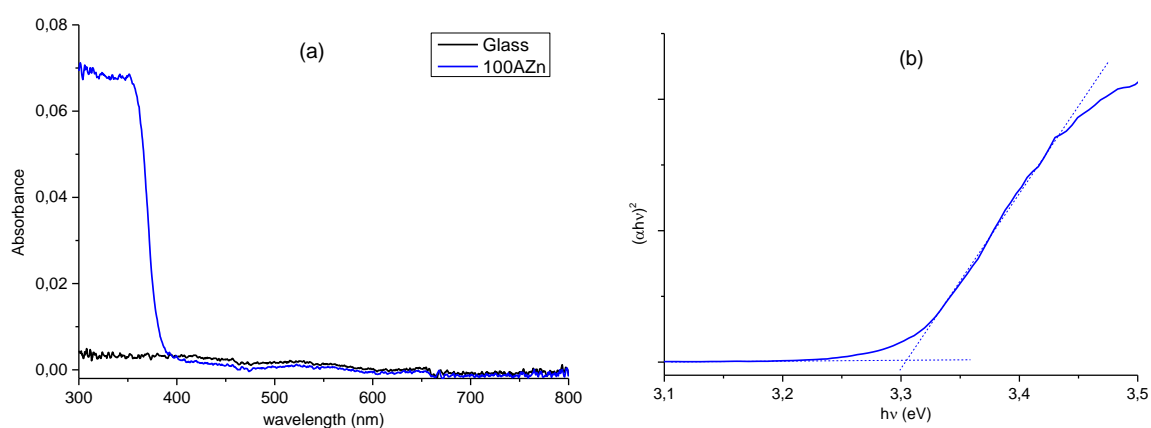


Figure 8. (a) UV-vis absorption spectra of 100AZn and glass; (b) Tauc plot of 100AZn.

The XPS analysis confirmed the presence of ZnO, through the Auger parameter (2010 eV, Equation 7), in agreement with literature reports of Zn^{2+} in ZnO lattice [84].

$$\alpha = E_K(\text{Zn LMM}) - E_{BE}(\text{Zn } 2p \ 3/2)$$

Equation 7. Auger parameter (α) relation. $E_K(\text{Zn LMM})$ is the kinetic energy of LMM Auger electrons; $E_{BE}(\text{Zn } 2p \ 3/2)$ is the binding energy of Zn 2p 3/2 line.

The O1s signal (Figure 9a) was composed of two main bands: one at 530 eV ascribable to lattice oxygen ions (O^{2-}) [85], and one at 531.5 eV, usually related to hydroxyl moiety (OH) [86] or O^{2-} ions within an oxygen-defective lattice [87]. C1s signal (Figure 9b) exhibited two bands: a stronger one at 284.7 eV, related to adventitious carbon (C-C bonds) and a weaker one, at ca. 288.7 eV, ascribable to carboxylate impurities from the precursor [88].

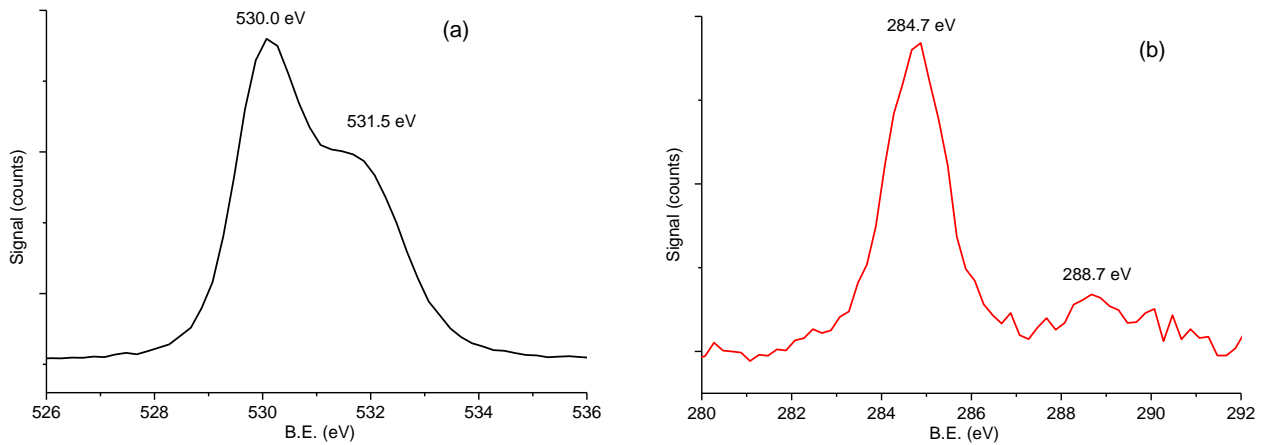


Figure 9. (a) O1s and (b) C1s high-resolution XPS signals of 100AZn.

The film thickness was tuned by changing the Zn concentration in the precursor solution. The actual thickness (t) was measured through profilometry and AFM profile on 400AZn, 300AZn and 200AZn. Through the Lambert-Beer relation (Equation 8), the absorption coefficient (α_{350}) was first extrapolated and assessed to be $5.0 \cdot 10^3 \text{ cm}^{-1}$. The film thicknesses were then determined for all samples through the Equation 8, knowing the α_{350} value and experimentally measuring A_{350} from UV-vis absorption spectra.

$$A_{350} = \alpha_{350}(\text{cm}^{-1}) \cdot t(\text{nm}) \cdot 10^7$$

Equation 8. Lambert-Beer relation [89]. A_{350} is the absorbance at 350 nm; α_{350} is the corresponding absorption coefficient; t is the film thickness.

A linear relationship was found between Zn concentration in the solution precursor and the film thickness, as reported in Figure 10: film thickness can be easily tuned from ca. 3 nm up to 60 nm by changing the Zn solution concentration.

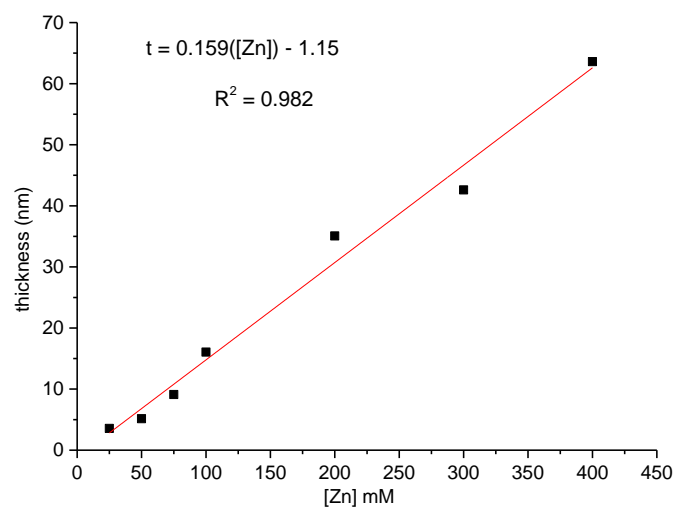


Figure 10. Thickness vs Zn precursor concentration dependence.

Besides the composition and thickness, film morphology, and in particular its roughness, is investigated. AFM images reveals that a lower precursor concentration affords in more flat films (Figure 11a and Figure 11b)

while increasing the concentration results in rougher surfaces (Figure 11c), as already observed also on ZnFe₂O₄ photoelectrodes [90].

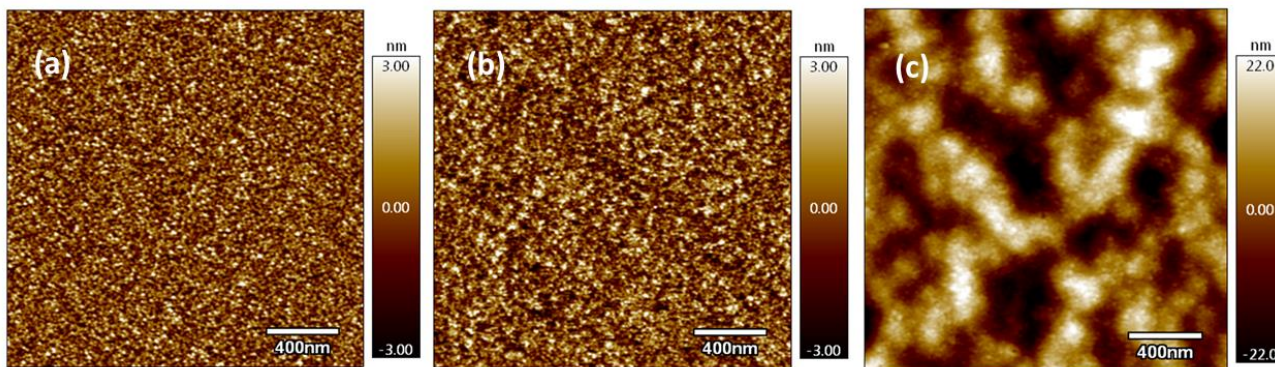


Figure 11. AFM images of (a) 50AZn; (b) 100AZn; (c) 400AZn.

The quantum confinement effect is known to affect the E_g of ZnO thin films [91], thus was extrapolated from Tauc plots (Figure S1). Furthermore, the conduction band edge (E_c) was determined through Equation 9, where χ is the electronegativity of ZnO (5.79 eV) and 4.5 is the energy of free electrons in RHE scale [92].

$$E_c = \chi - 4.5 - 0.5E_g$$

Equation 9. Empirical equation for E_c determination [92].

Plotting E_g and E_c vs film thickness (Figure 12) reveals an almost constant value above 35 nm. Conversely, thinner film exhibits quantum confinement, leading to a maximum increase of ca. 0.05 eV and -0.025 V vs RHE for E_g and E_c , respectively. A more negative E_c could be useful to enhance the reduction power of photoexcited electrons extracted from CFO. The quantum confinement effect is affected by ZnO crystallite size, which can differ from the film thickness [91], while the presence of intra-gap states due to intrinsic defects of ZnO are reported to do not significantly alter the E_g [93]. It can be supposed the ZnO grain size is decreased on the thinner films but, without further characterization (i.e. XRD or TEM), no quantitative assessment can be performed.

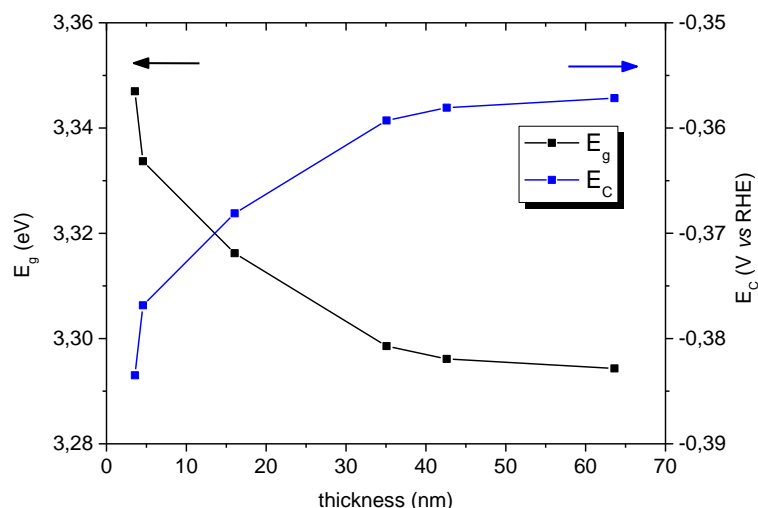


Figure 12. ZnO thin films E_g and E_c vs thickness.

The effect of different annealing treatments, aiming a tuning of thin films electrical properties, was then examined. In Figure 13a, the absorbance at 350 nm (A_{350}) on 400ArZn was observed similar to 100AZn, suggesting a comparable thickness (ca. 15 nm). Conversely, 600ArZn exhibited a halved A_{350} : this could be ascribed either to a partial diffusion of Zn^{2+} within glass, due to the reaction of silica with ZnO [94] and/or a partial evaporation of ZnO itself [95], resulting in a thinner film (ca. 8 nm). E_g and E_{CB} were determined as previously shown, and observed to decreased (ca. 0.01 eV and -0.005 V vs RHE, respectively) upon increasing the annealing temperature above 300°C , but keeping an almost constant value at the two used temperature (400°C or 600°C) (Figure 13b). As observed for ZnO film of different thickness, this was related to the enlargement of ZnO crystallite size [96].

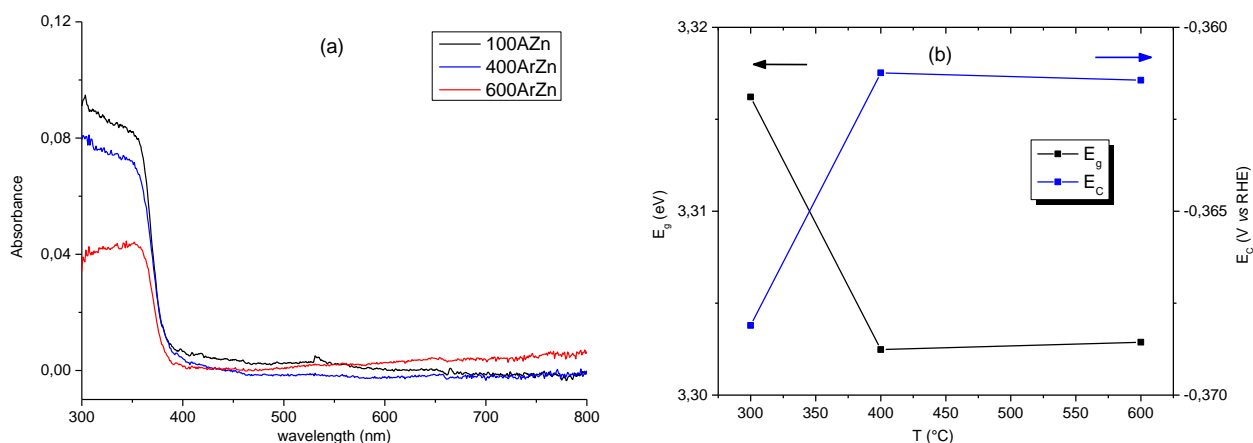


Figure 13. (a) UV-vis absorption spectra and (b) E_g and E_{CB} vs annealing temperature of ZnO samples annealed in different conditions.

The films morphology, examined through AFM, revealed a more flat surface upon inert annealing at 400°C (Figure 14b) compared to the air annealing at 300°C (Figure 14a), while further increase of the annealing temperature afforded a higher roughness of the film (Figure 14c). The flat surface on 400ArZn could be

ascribed to the crystallization and enlargement of ZnO crystallites, which resulted in a relatively smooth surface [97], while on 600ArZn the roughness was supposed to arise from a inhomogeneous evaporation of the ZnO [95], further supporting the thinning of ZnO through evaporative loss.

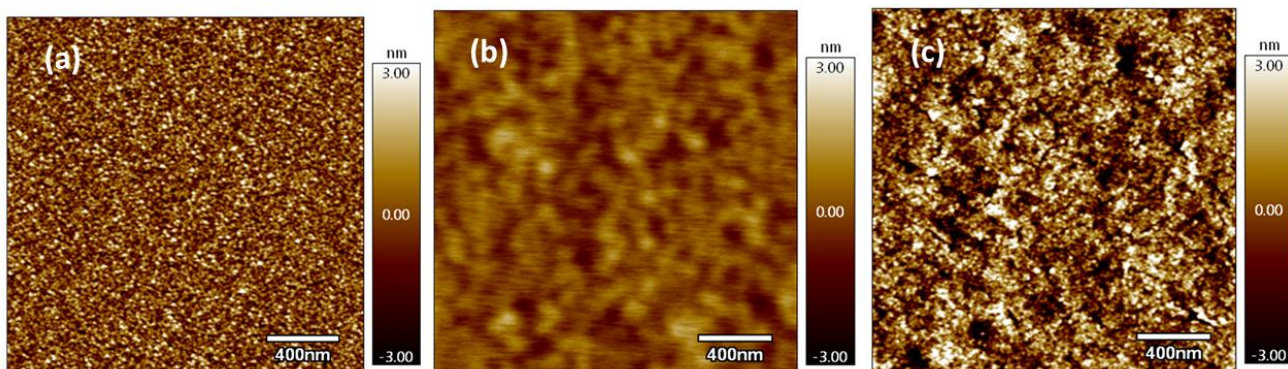


Figure 14. AFM images of (a) 100ArZn; (b) 400ArZn; (c) 600ArZn.

The chemical effect of different annealing conditions was evaluated by the O1s signal deconvolution (Figure S4 and Figure S6) of high-resolution XPS spectra. Three main O1s bands were recognized (Figure 15):

1. O_a line (530 eV), ascribable to O²⁻ lattice ions [85].
2. O_b line (531.5 eV), ascribable either to hydroxyl moiety [86] or O²⁻ within O-deficient lattice matrix [87].
3. O_c line (533 eV), mainly ascribable to adsorbed species such as H₂O, CO₂ or organic carboxylate [86]

The different contributions of these three bands, as atomic %, are summarized in Table 2. The annealing treatment had a remarkable effect on the O_a/O_b ratio, that can be ascribed to the crystallinity and defectivity of the films. The lowest value on 300ArZn, suggested a poorly crystallized material due to the low annealing temperature and a residual amount of organics from the precursors, as evidenced both on the C1s band (Figure 9b) and by the high amount of O_c (9%). Annealing treatment at 400°C (400ArZn) led to the highest O_a/O_b value, ascribable to the improved crystallinity of the material. Further increasing the annealing temperature (600ArZn) still maintain good crystallinity (67% O_a), but a decreased O_a/O_b ratio suggested an enhancement of defects concentration (i.e. oxygen vacancy), due to the preferential desorption of oxygen during the O₂-free thermal treatment [98].

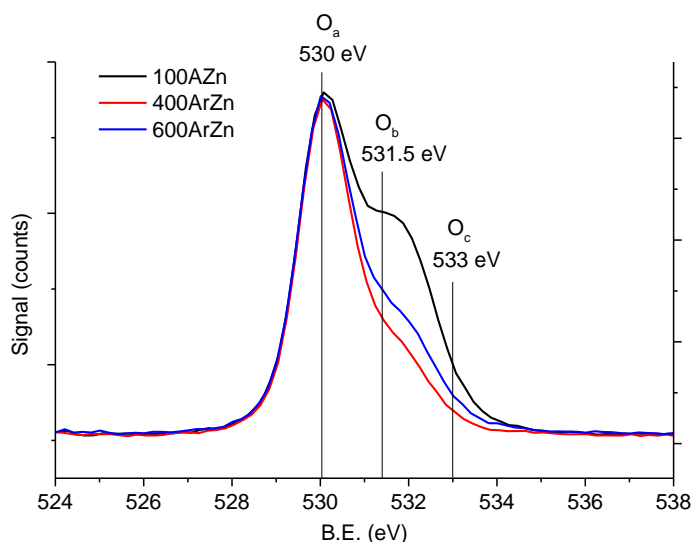


Figure 15. O 1s high resolution XPS signals of 100AZn, 400ArZn and 600ArZn.

Table 2. Contribution (atomic %) of O_a, O_b and O_c to the O 1s signal of 100AZn, 400ArZn and 600ArZn.

Sample	O _a (%)	O _b (%)	O _c (%)	O _a /O _b
100AZn	48	43	9	1.1
400ArZn	71	23	5	3.1
600ArZn	67	32	6	2.1

To summarize this section, the following conclusions can be drawn:

1. The thickness can be easily tuned from ca. 3 nm up to 60 nm by changing the Zn concentration in the solution precursor. The morphology is also changed affording in more rough films when using higher concentration Zn solutions. Quantum confinement effects can be finally observed in thinner films ($t < 30$ nm), exhibiting E_g increase up to 0.05 eV, with consequent increase of E_c .
2. The annealing conditions affected the morphology and chemical structure of ZnO thin films, as graphically represented in Figure 16. A rough, amorphous-rich and organic-impure film is obtained by air annealing at 300°C. A more flat and well-crystallized film was achieved by increasing the temperature to 400°C (inert atmosphere). Higher annealing temperature, was supposed to lead to

an enlargement of ZnO crystallites and a partial evaporation of ZnO, in turn affording a thinner and rougher film, with an improved concentration of intrinsic defects.

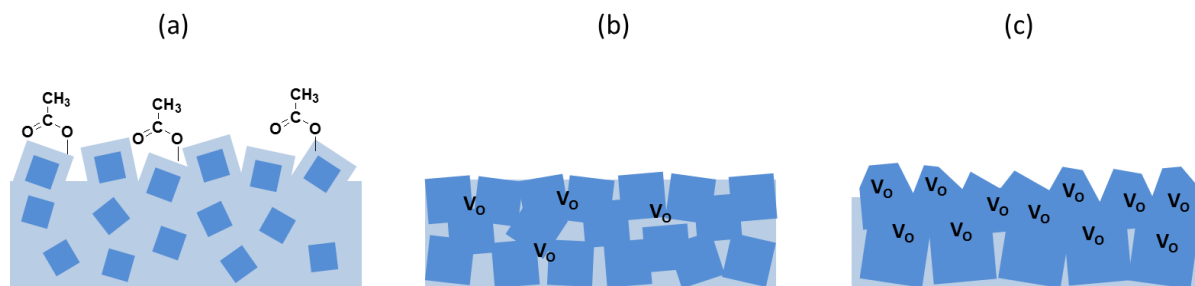


Figure 16. Scheme of the effect of annealing on ZnO thin film. (a) 300°C, air; (b) 400°C, Ar; (c) 600°C, Ar. Amorphous ZnO is represented as bright blue areas; crystalline ZnO as dark blue areas; defects (oxygen vacancy) as V_o .

3.2. CuFeO_2 PHOTOCATHODE

Chemical vapour deposition (CVD) was chosen as alternative CFO synthetic technique to the already reported sol-gel method [60,69], because homogeneous, dense films, with good adhesion to the substrate, can be achieved [99]. Aerosol-assisted chemical vapour deposition (AACVD) was utilized, because contrarily to traditional CVD: (i) avoid the utilization of volatile precursors, often reactive and harmful and (ii) allow a high mass transport of the precursor to the substrate [100].

Several parameters affect the AACVD process (i.e. precursor, solvent, spray flow etc.) [100], for this reason the procedure used in this work was previously optimized by Dr. F. Boudoire in order to get a phase-pure CFO, with a proper thickness and the best PEC performances. After the AACVD, an amorphous layer of Fe_2O_3 and CuO was obtained. The inert atmosphere annealing led to the reduction of Cu(II) to Cu(I) and the crystallization of the delafossite phase [64]. Finally, a mild air post-annealing was experimentally observed to improve the attainable photocurrent, probably due to improved p-type conductivity by oxygen intercalation [60]. A scheme of the overall synthetic process is reported in Figure 17.

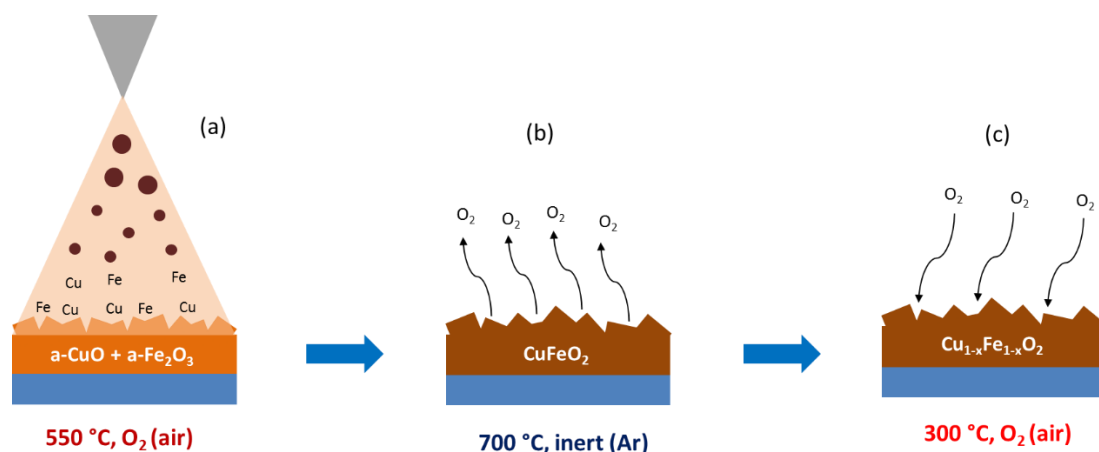


Figure 17. Scheme of the synthetic procedure of CFO thin films. (a) AACVD, a-CuO and a-Fe₂O₃ stand for the amorphous oxides; (b) Ar annealing, CuFeO₂ is the crystallized phase; (c) air post-annealing, Cu_{1-x}Fe_{1-x}O₂ is the oxygen-intercalated material.

The phase-purity was assessed through Raman spectroscopy (Figure 18a). The E_g (346 cm⁻¹) and A_{1g} (686 cm⁻¹) modes of CuFeO₂ delafossite, as well as disorder induced modes (187 cm⁻¹ and 502 cm⁻¹) [101], were detected confirming the phase-purity of the synthesized film. No other phases such as at 218 cm⁻¹, 290 cm⁻¹, 1300 cm⁻¹ can be detected, due to Cu₂O [102], CuO [103] and Fe₂O₃ [104], respectively. The latter, especially, was experimentally observed to negatively affect the PEC performance of CFO. The optical absorption (Figure 18b) revealed a broad band covering the whole visible region (400-800 nm). A 1.48 eV indirect E_g (Figure S5a) and a 3.18 eV direct E_g (Figure S5b) evaluated by means of Tauc plot analysis, were in good agreement with literature reports for CuFeO₂ [60].

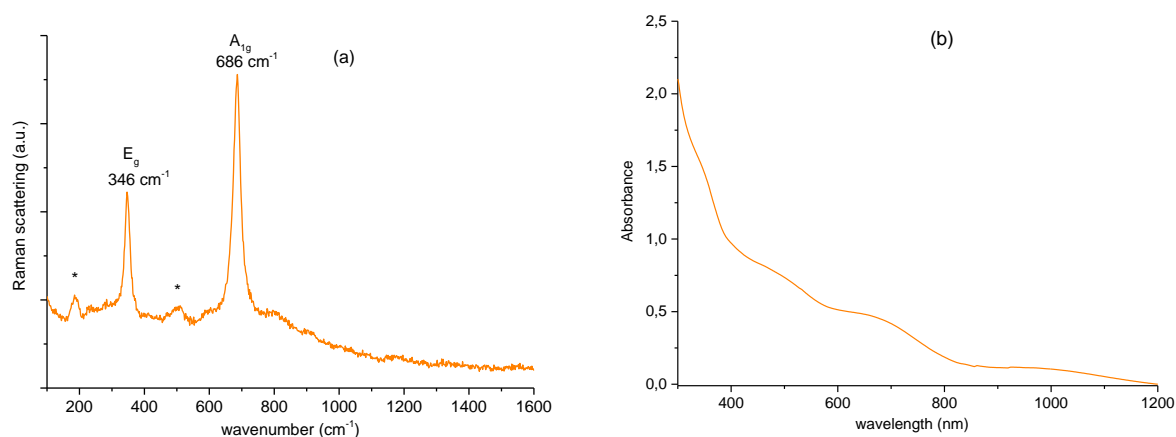


Figure 18. (a) Raman spectrum of CFO. Asterisks designates disordered induced non-zone centre modes [101]. (b) UV-vis absorption spectrum of CFO.

The thin film morphology examined through SEM reveals a rough surface (Figure 19b) composed of globular particles of average dimension between 100 and 200 nm (Figure 19a). The film thickness was estimated to be ca. 100 nm, as evidenced by the cross-sectional SEM (Figure 19).

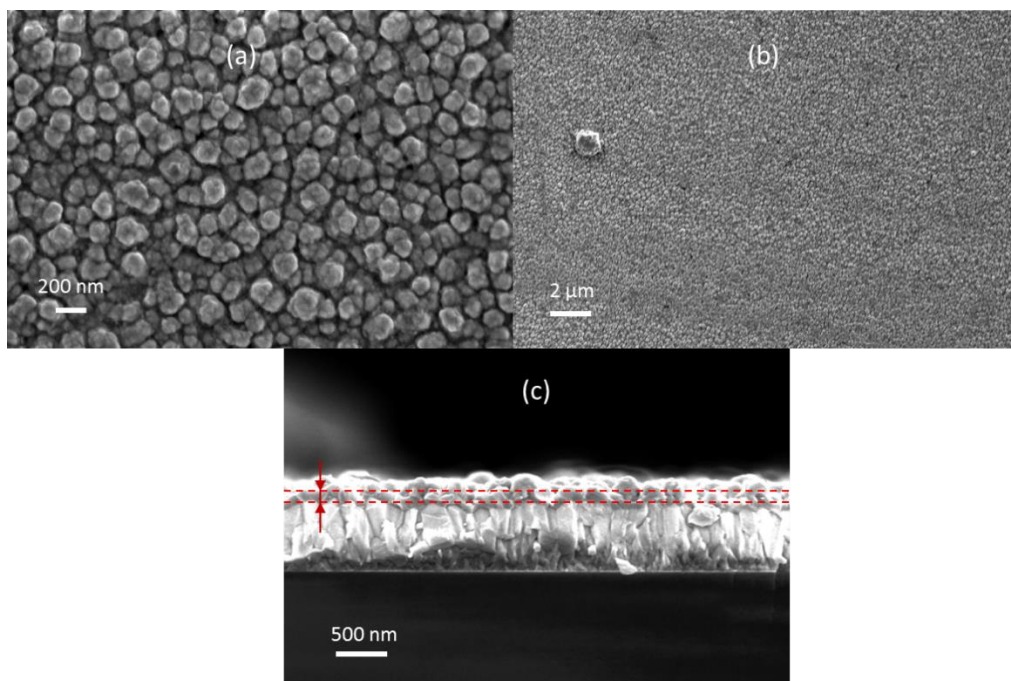


Figure 19. (a), (b) Top-view SEM images of CFO at different magnification; (c) cross-sectional SEM of the CFO photoelectrode. The CFO layer is highlighted by the two red dashed lines.

The PEC performance of CFO was evaluated by LSV using an electrolyte containing a sacrificial electron acceptor, namely $\text{Na}_2\text{S}_2\text{O}_8$, in order to maximize the attainable photocurrent by reducing kinetic charge transfer limitations [79] and avoiding the SSs issue [60]. A representative LSV of CFO photoelectrode is reported in Figure 20. The overall cathodic current (blue dashed line) is the sum of the dark current (black dashed line) and the photocurrent (J_{ph}). J_{ph} is the main parameter for performance assessment of a photoelectrode, directly representing the amount of photogenerated charge carriers can move toward the SC/electrolyte interface, usually referred to an arbitrary potential, chosen 0.2 V vs RHE in the present work. Another important parameter is the onset potential (E_{ONSET}), defined as the potential at which the photocurrent starts to rise. On an energetic point of view, this is the potential at which the electrolyte redox potential ($E^{\circ}_{\text{A/A}^-}$) and the SC Fermi level (E_{F}) align under irradiation, allowing the interfacial charge transfer to occur. This value is related both to kinetic limitations at SC/electrolyte charge transfer processes (overpotential), negligible if a sacrificial reagent (i.e. $\text{Na}_2\text{S}_2\text{O}_8$) is used, or to the presence of SSs [105]. Averaged value of J_{ph} @ 0.2 V vs RHE and E_{ONSET} , were assessed $1.4 \pm 0.2 \text{ mA}\cdot\text{cm}^{-2}$ and $+ 0.83 \pm 0.02 \text{ V vs RHE}$, respectively.

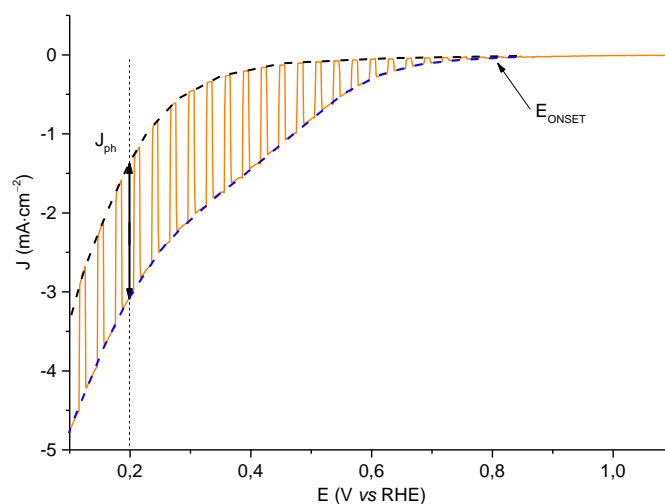


Figure 20. LSV of CFO in 0.1 M NaHCO₃ + 0.1 M Na₂S₂O₈.

The acceptor density (N_A), related to the hole mobility and thus to the bulk charge separation efficiency, and the flatband potential (E_{FB}), related to the E_V position, were determined as reported in Section 2.4.3, by fitting the C_{SC}^{-2} vs E plot (Figure 21a) with the Mott-Schottky relation. N_A was assessed to be $(7.1 \pm 0.4) \cdot 10^{18} \text{ cm}^{-3}$, while E_{FB} to $+0.934 \pm 0.006 \text{ V vs RHE}$, the former being comparable to sol-gel CFO, while the latter is slightly less positive [60]. The photovoltage (Equation 1) measured through OCP (Figure 21b) and affected by the presence of SSs, was assessed to be 0.11 V, a lower value than those reported for sol-gel CFO [69].

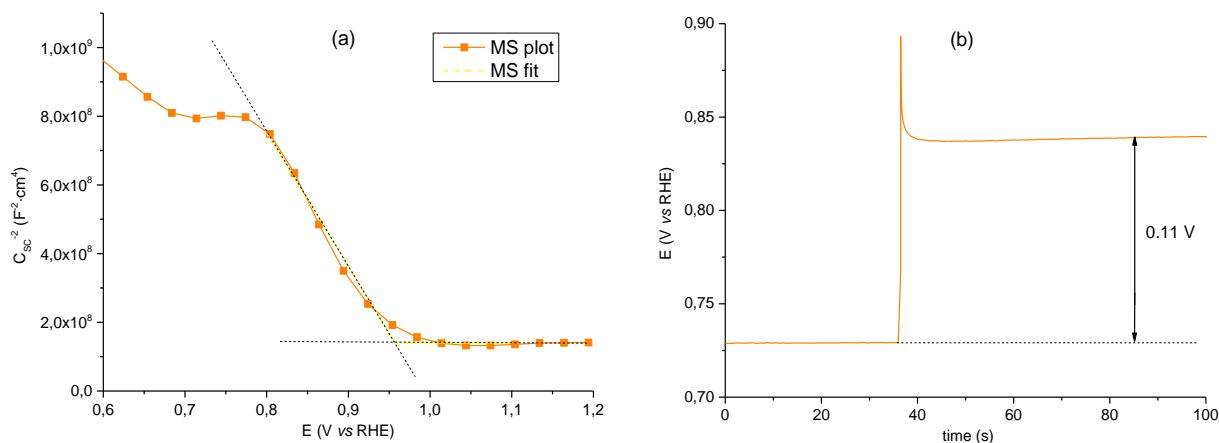


Figure 21. (a) Mott-Schottky (MS) plot and MS fit; (b) Open circuit potential (OCP) in 1.2 M Eu^{3+/2+} electrolyte.

UV-vis, EIS and OCP analyses allow to design the energetic picture of CFO reported in Figure 22. In details, E_{FB} ($\approx E_F$) is supposed to be located 60 meV above the E_V ($+0.99 \text{ V vs RHE}$) [69]; E_C (-0.49 V vs RHE) is assessed as difference between indirect E_g and E_V [60]; while the position of E_{SS} ($+0.82 \text{ V vs RHE}$) is determined as difference between E_{FB} and the measured OCP [69].

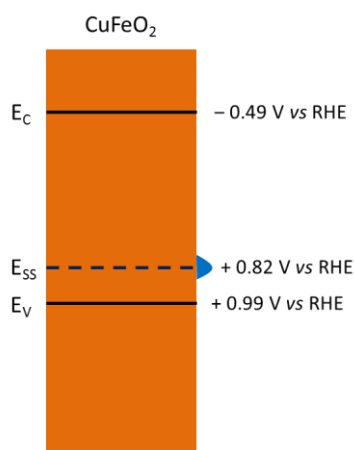


Figure 22. Energetic picture of CFO.

Summarizing the results of this section, a CFO thin film was prepared through AACVD and its phase composition, morphology and optical properties assessed. The opto-electronic performances in term of photocurrent and onset potential was evaluated and, coupling optical absorption measurements with EIS and OCP, and energetic picture of the CFO thin film was proposed.

3.3. ZnO/CuFeO₂ COMPOSITE PHOTOCATHODES

The procedures optimized for ZnO thin films (Section 3.2) were used to coat the AACVD-synthesized CFO photocathode (Section 3.3) and their PEC performance assessed in sacrificial conditions. Different amounts of ZnO were loaded onto the CFO photocathode, ranging from 0.5 mM to 200 mM of Zn precursor solution (0.5AZn/CFO and 200AZn/CFO samples, respectively), aiming to tune the overlayer thickness. No remarkable differences in term of phase composition and optical properties were observed on CFO upon loading the ZnO overlayer, as evidenced by Raman and UV-vis absorption spectra (Figure S6).

The film morphology examined by SEM reveals that the rough globular particles of CFO (Figure 23a) have been coated with an apparently smoother and uniform layer of ZnO on the sample with the highest Zn loading (200AZn/CFO, Figure 23b). Conversely, such differences cannot be clearly appreciate through AFM (Figure 24a, 27b and 27c), further supporting the quite homogeneous ZnO coating.

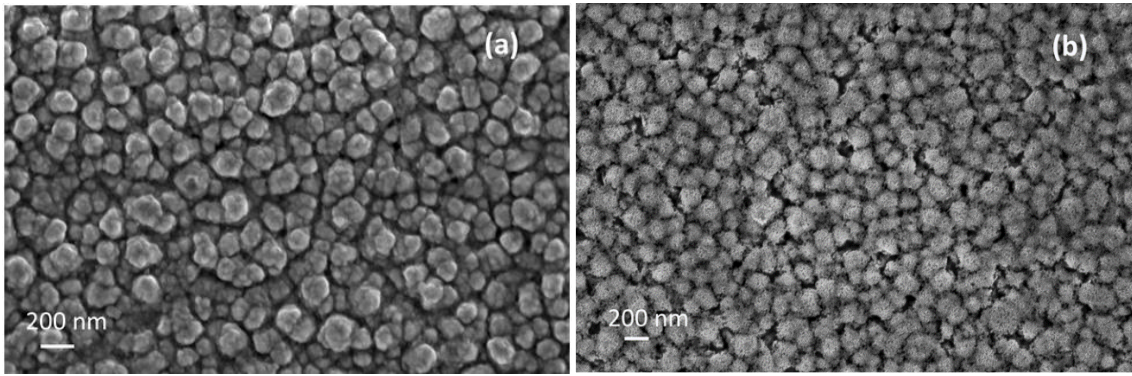


Figure 23. SEM images of (a) bare CFO; (b) 200AZn/CFO.

Being an n-type SC, the ZnO overlayer should induce a p-n heterojunction being coupled with a p-type SC [106]. Heterojunction formation was investigated through SKPM, probing the change in E_F at equilibrium in dark conditions [107]. As reported in Figure 24d, 27e, 27f, a shift of the average E_F value toward less negative value upon loading ZnO overlayer was observed, reaching the largest difference with the highest ZnO loading (200AZn/CFO, Figure 24f). No significant differences on topological distribution of E_F by SKPM came up. These results suggested that the ZnO overlayer, especially the thicker one, was effective in the generation of a p-n heterojunction.

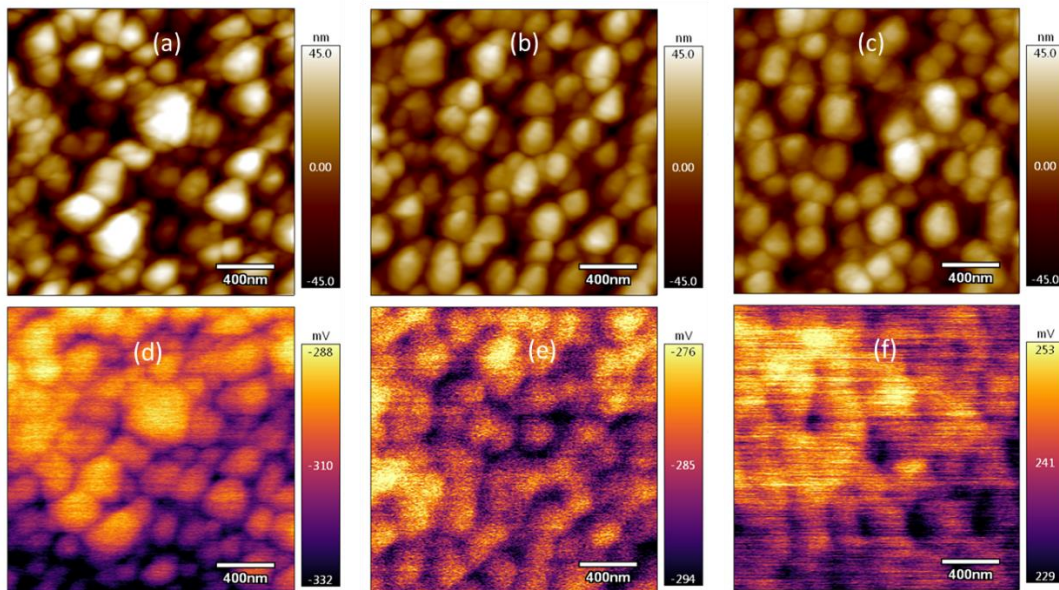


Figure 24. AFM of (a) CFO; (b) 5AZn/CFO; (c) 200AZn/CFO. SKPM of (d) CFO; (e) 5AZn/CFO; (f) 200AZn/CFO.

The film thickness was assessed through XPS depth-profiling and compared to ZnO/glass substrates. At low Zn loading (Figure 25a), ZnO was barely detected, suggesting a very thin layer actually covered the surface. At high Zn loading, namely on 200AZn/CFO, this element was still detected at 40 nm depth (Figure 25b). No sharp change in Zn signal vs Cu or Fe ones, ascribable to a discrete ZnO/CuFeO₂ bilayer structure, was observed (Figure 25b). This was motivated either as a preferential sputtering during depth profiling [108] or due to an inhomogeneous thickness of the ZnO overlayer. Nonetheless, depth profiling results on

200AZn/CFO can be considered in good agreement with thickness of 200AZn on glass (ca. 30 nm), confirming the reliability of ZnO thickness assessed on glass substrates.

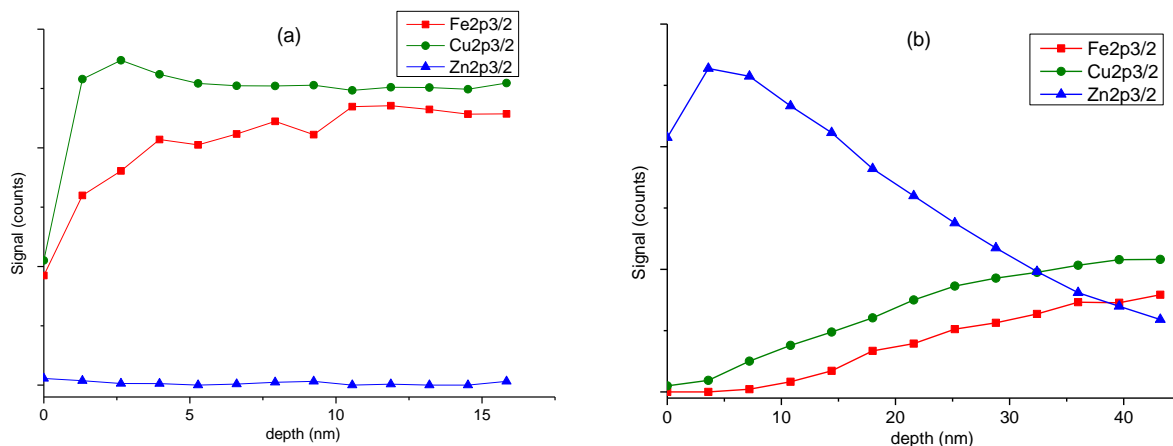


Figure 25. XPS depth profiling of Fe2p3/2, Cu2p3/2, Zn2p3/2 lines on (a) 5AZn/CFO and (b) 200AZn/CFO.

The PEC performances were evaluated through LSV in sacrificial conditions. As reported in Figure 26, the ZnO overlayer decreases the photocurrent, and such effect was more pronounced with increasing the Zn loading (light-blue to dark-blue curves). Moreover, the E_{ONSET} shifted toward less positive potentials.

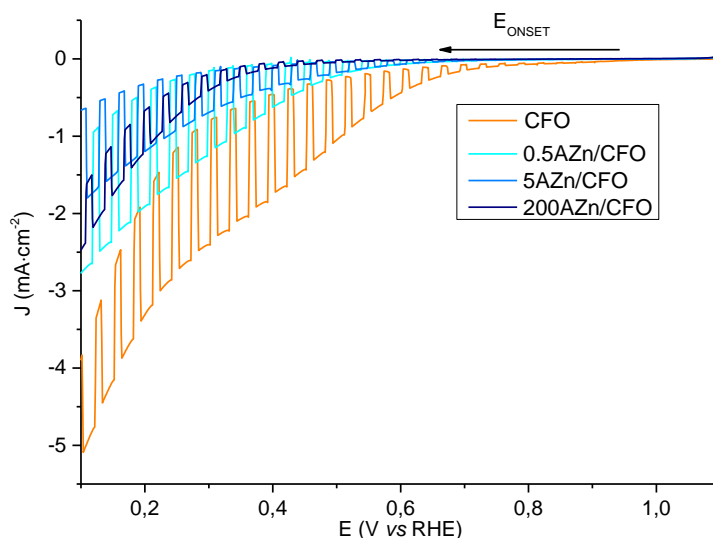


Figure 26. LSV of CFO and ZnO-coated CFO in 0.1 M NaHCO₃ + 1 M Na₂S₂O₈.

A more detailed screening of the impact of Zn loading on the attainable J_{ph} @ 0.2 V vs RHE is reported in Figure 27a. The J_{ph} slightly decreases respect to bare CFO can be observed up to 10 mM Zn in the spin-coating precursor solution. Further increases in Zn loading, have a remarkable effect in reducing the photocurrent ($J_{\text{ph}} < 0.3 \text{ mA/cm}^2$). Despite the formation of a p-n heterojunction observed through SKPM, that in principle should enhance charge carrier separation, no improvement in J_{ph} was observed upon loading ZnO. The overlayer thus acts by hindering charge transfer. The remarkable differences observed between low (< 10 mM) and high (> 10 mM) Zn loading, can be ascribed either to the formation of an overlayer homogeneously

covering the CFO surface or a layer thicker than ca. 3 nm, increasing the resistance in charge transfer at interfaces (CFO/ZnO and ZnO/electrolyte).

Another interesting effect was the shift of E_{ONSET} toward less positive potentials. As pictured in Figure 27b, the 0.5AZn/CFO sample, with the lower Zn loading (0.5 mM Zn), reveals no change in E_{ONSET} , supporting the idea of a very thin ZnO layer and/or incomplete surface coverage that barely affects the nature of the surface. Conversely, increasing the Zn loading afforded a shift of E_{ONSET} toward less positive potential, up to 0.24 V with the highest Zn loading (200AZn/CFO). The E_F , as previously observed through SKPM measurements, had shifted upon loading CFO with the ZnO overlayer and this was supposed to be reflected on the E_{ONSET} as well, since this value is related to the alignment between electrolyte redox potential ($E^{\circ}_{\text{A/A}^-}$) and the SC Fermi level (E_F). The heterojunction was thus hypothesized to dictate the energetic picture at SC/electrolyte interface of ZnO/CFO electrodes, while SSS on CFO were supposed to be passivated by the overlayer. New SSS at ZnO interface could occur and further complicate the data interpretation, however lacking in direct experimental evidence in this work, so they were neglected for simplicity.

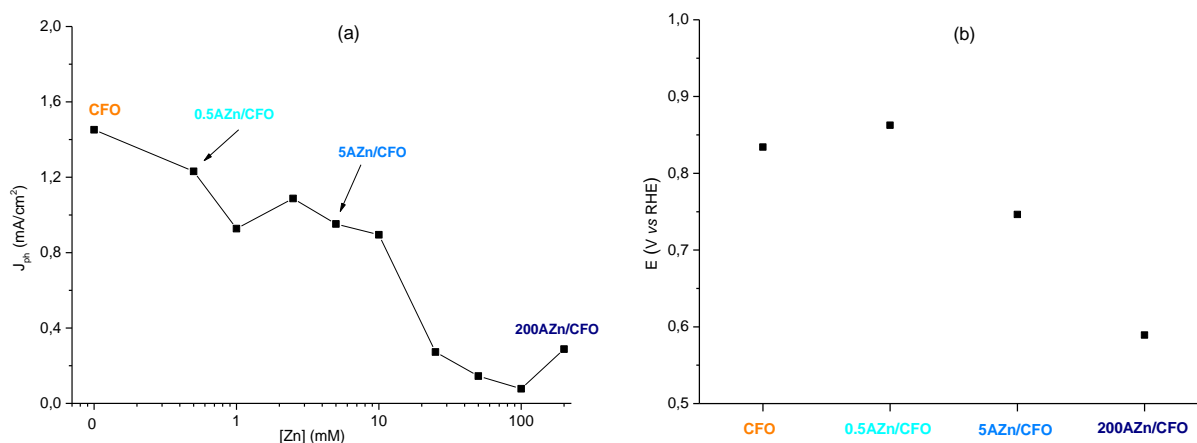


Figure 27. (a) J_{ph} @ 0.2 V vs RHE dependence on Zn concentration in the precursor solution; (b) E_{ONSET} on CFO and ZnO-coated CFO.

The effect of different annealing conditions was investigated on the highest ZnO loading. Despite the measured J_{ph} was still low compared to bare CFO, an improvement was gained by annealing at 400°C (400ArZn/CFO), reduced again by further increasing the annealing temperature at 600°C (600ArZn/CFO) (black trace, Figure 28). As observed in Section 3.3., Ar annealing at 400°C improves the crystallinity of ZnO, likely to improve the conductivity of the material [73]. Further increase of the annealing temperature increased the amount of defects within ZnO, probably decreasing the conductivity [109]. The E_{ONSET} (blue trace, Figure 28) exhibited a shift toward more positive potential by increasing the annealing temperature, in particular at 600°C where. On 600ArZn/CFO, as suggested in Section 3.1, thinning of the overlayer due to diffusion in the underlayer and/or evaporation of ZnO was also likely to occur. The change of E_{ONSET} was related to a shift of E_F as previously observed through SKPM measurements, and the different nature of ZnO

surfaces (Section 3.1), was hypothesized to affect the Fermi level equilibration within the p-n junction, even though further studies would be required for a better understanding of the phenomenon.

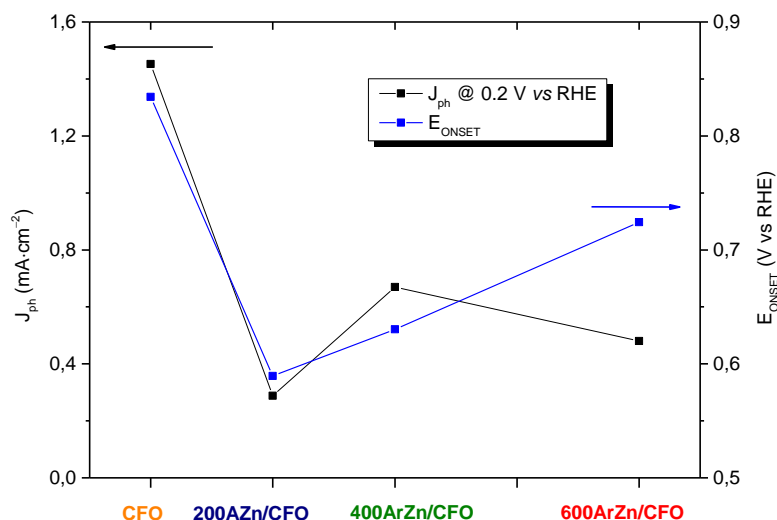


Figure 28. J_{ph} @ 0.2 V vs RHE and E_{ONSET} of samples annealed in different conditions.

On the basis of the shown results, the energetic pictures of ZnO-coated CFO are proposed in Figure 29. Bare CFO, being a p-type SC, was characterized by an E_F close to the E_V edge and SSs at 0.1 V above the latter (Figure 29a). When loading a thin overlayer of ZnO (less than 3 nm, Figure 29b), the overlayer experienced a quantum confinement effect as pointed out in Section 3.1, and the heterojunction E_F was supposed to be shift upward (ca. 0.35 eV) after the equilibration between CFO and ZnO. By thickening the overlayer (Figure 29c), the lack of a quantum confinement effects was suggested to move E_C toward less negative potentials (ca. 0.02 V), while E_F was further shifted upward probably due to the larger contribution of ZnO in the equilibration phenomena. Finally, the high temperature annealing (Figure 29d) did not afford a change in band edges position, due to the lack of quantum effects on large ZnO crystallites. A similar E_F was observed by annealing the overlayer at 400°C while going further (600ArZn/CFO, not shown in the picture), a thinner and defect-rich ZnO layer occurred, and the E_F decreased of ca. 0.1 V. In any case, upon loading ZnO the E_{ONSET} was hypothesized to be dictated by the Fermi level on the p-n heterojunction, and the original SSs on CFO were thus supposed to be passivated.

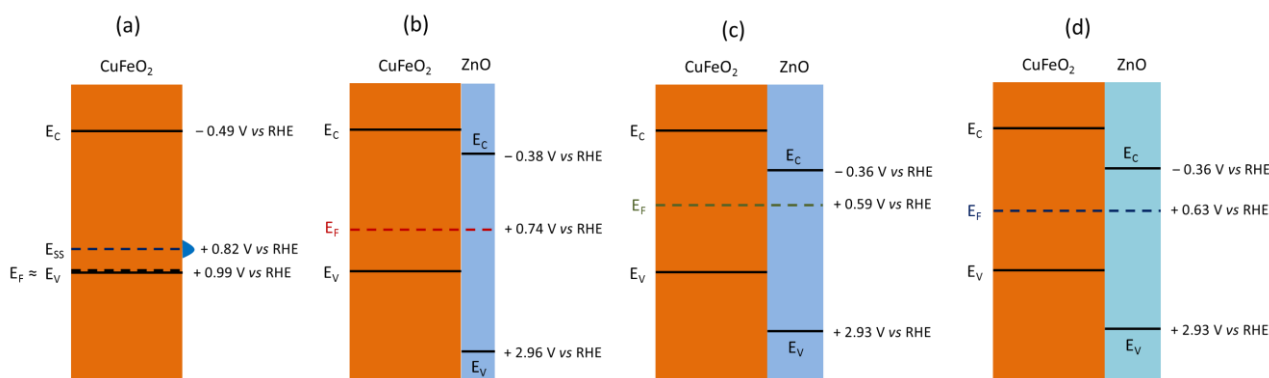


Figure 29. Energetic pictures of ZnO-coated CFO. (a) bare CFO; (b) 5AZn/CFO; (c) 200AZn/CFO; (d) 400ArZn/CFO. ZnO E_C and E_V band edges were determined in Section 3.1.

One of the aim of using a ZnO overlayer was also to improve the adsorption of CO_2 . To assess this property, ATR-FTIR spectra were measured on dry bare photoelectrode (CFO and 200AZn/CFO), after quick rinsing in the sacrificial electrolyte (0.1 M NaHCO_3 + 0.1 M $\text{Na}_2\text{S}_2\text{O}_8$) and after washing away the residual electrolyte. All samples exhibited two peaks at $800\text{-}820\text{ cm}^{-1}$ and at $508\text{-}517\text{ cm}^{-1}$ (Figure 30) ascribable to FeO_6 octahedra [110] and linearly coordinated Cu-O [111] vibrations, respectively. 200AZn/CFO reveals a new band at 561 cm^{-1} that, ascribable to Zn-O vibration in ZnO [112], supporting the composition previously observed by XPS. Some more interesting differences, were observed at higher wavenumber in samples rinsed in the electrolyte. In both, two weak overlapped bands at 1300 cm^{-1} and 1270 cm^{-1} , can be assigned to $\text{S}_2\text{O}_8^{2-}$ ions [113] while in 200AZn/CFO a new band at 1482 cm^{-1} can be assigned to CO_3^{2-} ions [114]. Interestingly, both bands disappear on both samples upon washing with water, suggesting a weak absorption of the ions on both surfaces.

These results confirm that the ZnO overlayer can enhance CO_2 adsorption, in form of CO_3^{2-} . Moreover, the competitive adsorption of both $\text{S}_2\text{O}_8^{2-}$ and CO_3^{2-} over ZnO-modified surfaces can afford in an increased resistance of ZnO/electrolyte charge transfer. This observation can suggest a relevant contribution of competitive adsorption to the observed decrease, at high Zn loading, of J_{ph} in Figure 27a, despite the presence of a p-n heterojunction that should in theory enhance the charge carrier separation.

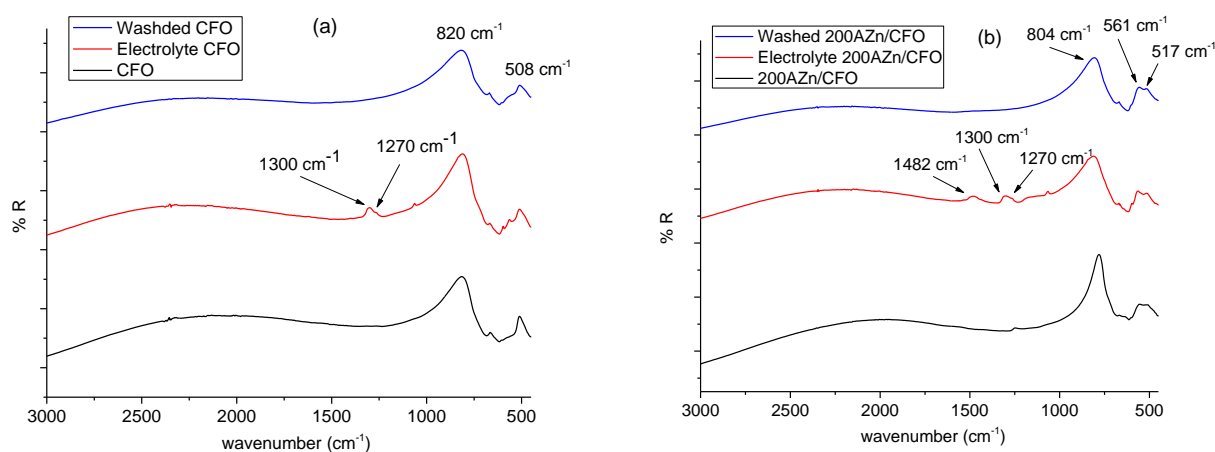


Figure 30. ATR-FTIR spectra of (a) CFO and (b) 200AZn/CFO. Bare thin film (black trace), electrolyte-rinsed (red trace) and water-washed (blue trace) spectra are reported.

Summarizing this section:

1. ZnO overlayers, coated with the procedure optimized in section 3.1., had a slightly effect on the morphology of the film, retaining the globular shape of bare CFO. The thickness was assessed to be comparable with that determined in section 3.1 and p-n heterojunctions formation were observed on ZnO/CFO samples.

- The PEC performances in term of J_{ph} revealed a slight decrease at moderate ZnO loading, becoming more pronounced at high ZnO loading. This effect can be related to charge-transfer resistance at CFO/ZnO interface and, in particular, to ZnO/electrolyte interface, the latter due to a competitive absorption of the sacrificial reagent and the bicarbonate ions in solution. The shift of E_{ONSET} was related to a shift of E_F , further supporting the formation of a p-n heterojunction and suggesting SSs on CFO to be passivated.
- The effect of the overlayer annealing was observed to affect both J_{ph} and the E_F position. Specifically, increasing the annealing temperature afforded on well crystallized ZnO overlayer that allow a more efficient charge transfer across ZnO/CFO interface and did not significantly alter the E_F position compared to the mild-annealed ZnO. Further enhancing the annealing temperature, a thinner and defect-rich overlayer was obtained, which increases the charge transfer resistance and slightly shift downward the E_F of the p-n heterojunction.

3.4. Cu CO-CATALYST LOADED PHOTOCATHODES

Aiming an improvement of CO_2 reduction kinetics [35], Cu co-catalyst was loaded on both CFO and ZnO-coated CFO. Photoelectrochemical deposition (PED) was selected as simple and fast loading technique, widely used for Pt deposition as HER co-catalyst [24,60], but not reported yet for Cu co-catalyst.

The PED was performed using a precursor solution of 1 mM $Cu(OAc)_2$, buffered to pH 6.6 with NaOAc: an almost neutral solution is required to limit the possible acidic dissolution of ZnO. The appropriate potential to run the PED was determined through an LSV using bare CFO as working electrode. As reported in Figure 31a, at 0.58 V vs RHE a total current density of $0.147 \text{ mA}\cdot\text{cm}^{-2}$ is obtained (red trace), with a negligible contribution of the buffer alone ($0.01 \text{ mA}\cdot\text{cm}^{-2}$, blue trace). In Figure 31b, the chronoamperometry of PED revealed a quite stable current density of $0.12 \text{ mA}\cdot\text{cm}^{-2}$ for 10 minutes, with an insignificant contribution of the buffer alone (blue trace), confirming what observed through LSV.

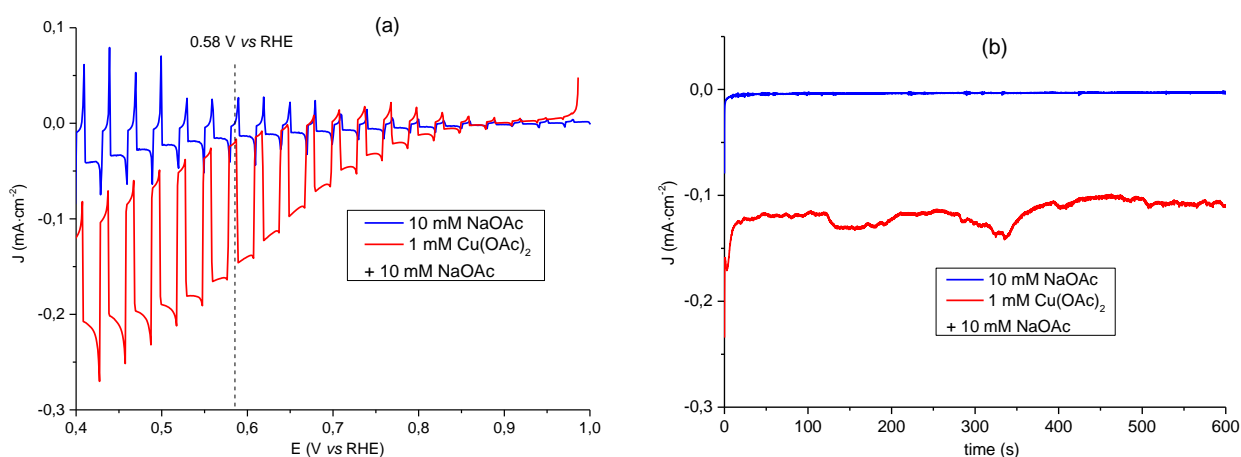


Figure 31. (a) LSV and (b) chronoamperometry of Cu and Cu-free buffered solution for PED on bare CFO.

The PEC performances in non-sacrificial conditions, aiming the actual CO₂ reduction, are known to be affected by the type of purging gas, inert or CO₂ [53]. Thus, LSV were performed on both Ar- and CO₂-purged electrolyte (0.3 M NaHCO₃). As reported in Figure 32, an anodic feature (above ca. 0.7 V vs RHE) is observed on the right side of both Ar-purged and CO₂-purged LSV graphs when using Cu/CFO, immediately followed by a cathodic light-induced, feature below such potential. This behaviour is likely to arise from the oxidation and immediate reduction of Cu co-catalyst on the surface. Far away from this weird redox feature, a noteworthy enhancement of J_{ph} is observed on both Ar- and CO₂-purged electrolytes, affording J_{ph} @ 0.2 V vs RHE of 0.12 mA·cm⁻² in both cases. No significant differences can be appreciated, suggesting the purging gas to do not play a crucial role on LSV measurements.

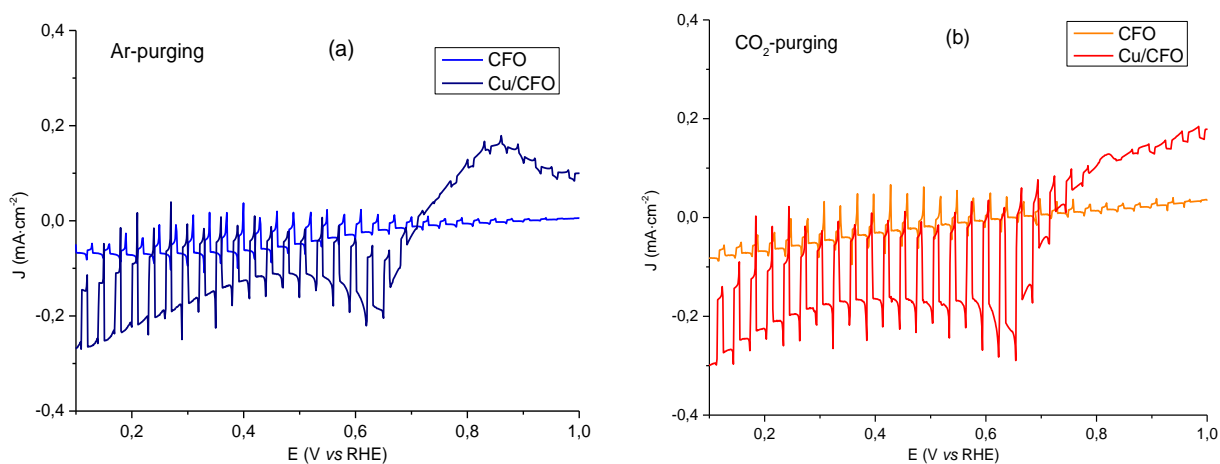


Figure 32. LSV of CFO and Cu/CFO in (a) Ar-purged and (b) CO₂-purged 0.3 M NaHCO₃ electrolyte. CO₂-purged LSV were run after Ar-purged experiment.

The next step was to assess the stability of the deposited Cu co-catalyst. Unfortunately, as reported in Figure 33, J_{ph} suddenly decreases almost to zero after one minute of stability test, both on Cu/CFO and Cu/200AZn/CFO, leaving only ca. 0.05 mA·cm⁻¹ contribution of dark current. The observed up and down spikes, arise from transient capacitive current due to charge accumulation at SC/electrolyte interface, when light is switched on or off, because slow charge transfer kinetics [60].

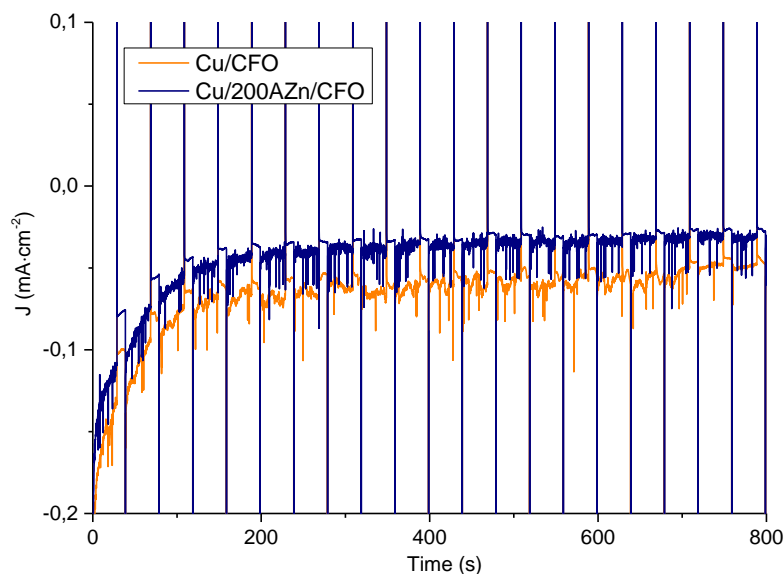


Figure 33. Chronoamperometry @ 0.2 V vs RHE on chopped light (10 s dark – 30 s light) of Cu/CFO and Cu/200AZn/CFO in CO₂-purged 0.3 M NaHCO₃.

Due to the poor stability and the very low attainable photocurrent, no further PEC tests were performed to identify and quantify the obtained reduction products.

The AFM image of as-deposited Cu/CFO revealed some small globular particles (Figure S7a) that revealed some differences in phase-contrast imaging as well (Figure S7b), an imaging technique that can highlight small features on rough surface, like differences in composition (i.e. second phase materials) [115], pointing out the actual surface decoration with Cu-based particles. After PEC utilization, these features disappeared from the surface (Figure S7d and Figure S7e). A slight change in the average E_F (ca. 50 mV) was also probed by SKPM (Figure S7c and Figure S7f). Metals on SC are known to induce a Schottky barrier which changes the E_F [116], so that this shift could further support the disappearance of the Cu-based particles observed on AFM images. A possible explanation relies on the physical detachment of the co-catalyst, as already reported on CFO [60], but a clear understanding of the phenomena would require further studies.

Nevertheless, it can be generally stated the co-catalyst to be weakly stabilized over the surface. This point out a careful selection of co-catalyst, its loading technique [15] and the utilization of a suitable overlayer [60] to be extremely important in affording a stable and effective co-catalysts.

Concluding this section, Cu co-catalyst was introduced over CFO-based photocathode and was observed to improve the photocurrent in non-sacrificial conditions, but fails in stability tests, likely due to a weak stabilization of the co-catalyst by the photoelectrode surface.

4. CONCLUSIONS

Through this work, earth-abundant oxide-based photocathodes were synthesized and their PEC performance in reduction reactions assessed. In details:

1. A solution-based method was developed to prepare ZnO thin films with tunable thickness, by changing the precursor concentration in solution, and structural properties (i.e. crystallinity and defectivity), by annealing the thin films in different conditions.
2. A vapour-phase process, namely AACVD, was used to prepare CFO photocathodes. A phase-pure CFO thin film composed of globular particles was obtained. Band edges (E_c and E_v) and SSs position were evaluated through spectroscopic and electrochemical techniques, to design an energetic picture of CFO.
3. ZnO thin films were coated, by the solution-based method, as overlayers on bare CFO photocathodes. A homogeneous coating of CFO surface and the formation of a p-n heterojunctions were achieved. Concerning PEC performance, low ZnO loading induces a slight decrease of J_{ph} in sacrificial conditions, becoming more pronounced at high loading due to a thicker film and/or a more uniform coating of CFO surface. The competitive ion adsorption is also supposed to increase SC/electrolyte charge transfer resistance at high ZnO loading. Different annealing conditions of ZnO change the electrical conductivity of the overlayer, reaching the highest charge-transfer efficiency by 400°C inert annealing.
4. Cu co-catalyst was introduced on both CFO and ZnO/CFO photocathodes to improve CO₂ reduction kinetics (non-sacrificial conditions). Despite a first J_{ph} enhancement was observed, the co-catalyst was not stable on the surface. This result suggested a careful selection of the co-catalyst, its loading technique and the overlayer to be essential to achieve effective and stable CO₂ PEC reduction.

5. SUPPLEMENTARY INFORMATIONS

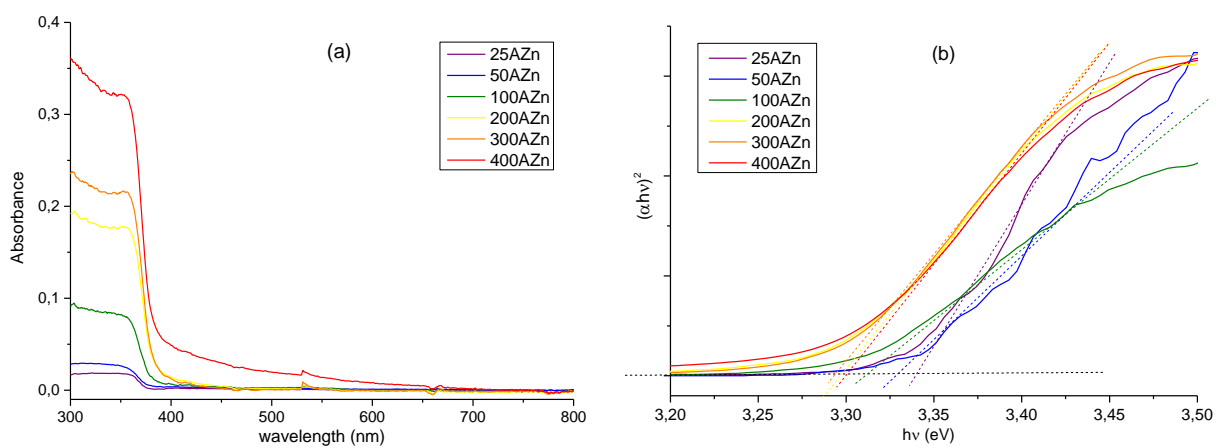


Figure S1. (a) UV-vis absorption spectra and (b) Tauc plots of ZnO thin films at different Zn precursor concentration.

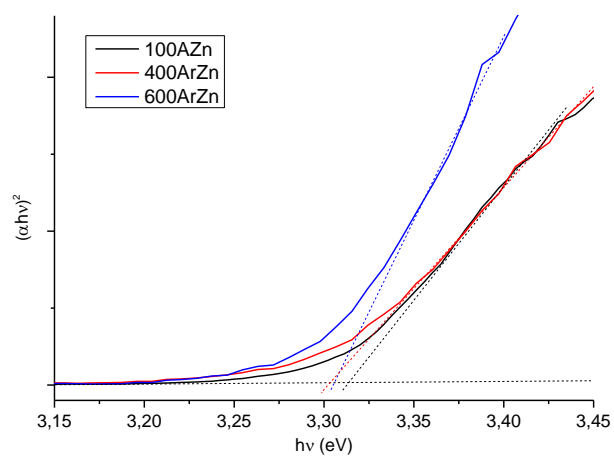


Figure S2. Tauc plots of ZnO thin films annealed in different conditions.

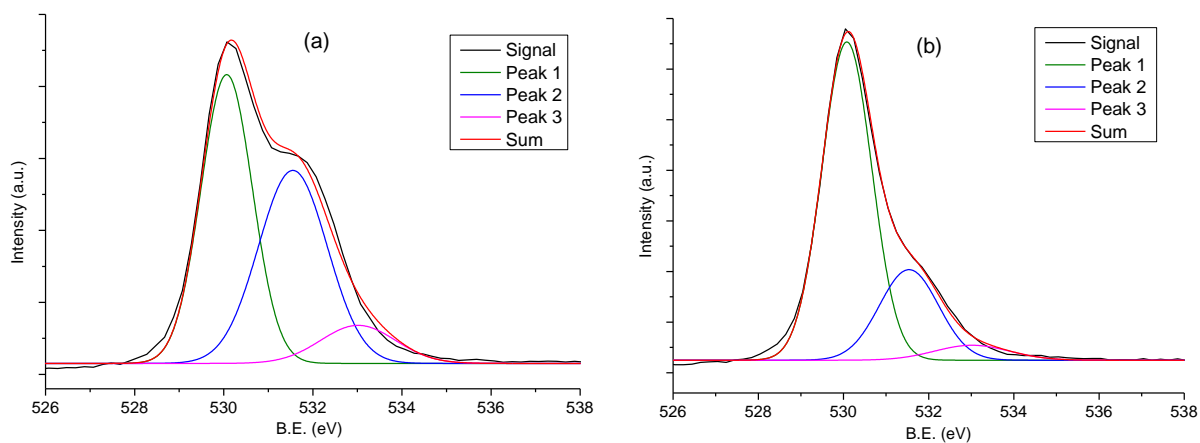


Figure S3. XPS O1s band deconvolution of (a) 100AZn and (b) 400ArZn.

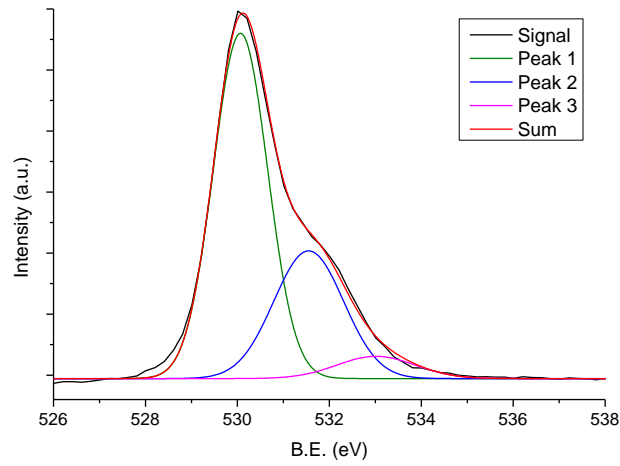


Figure S4. XPS O1s band deconvolution of 600ArZn.

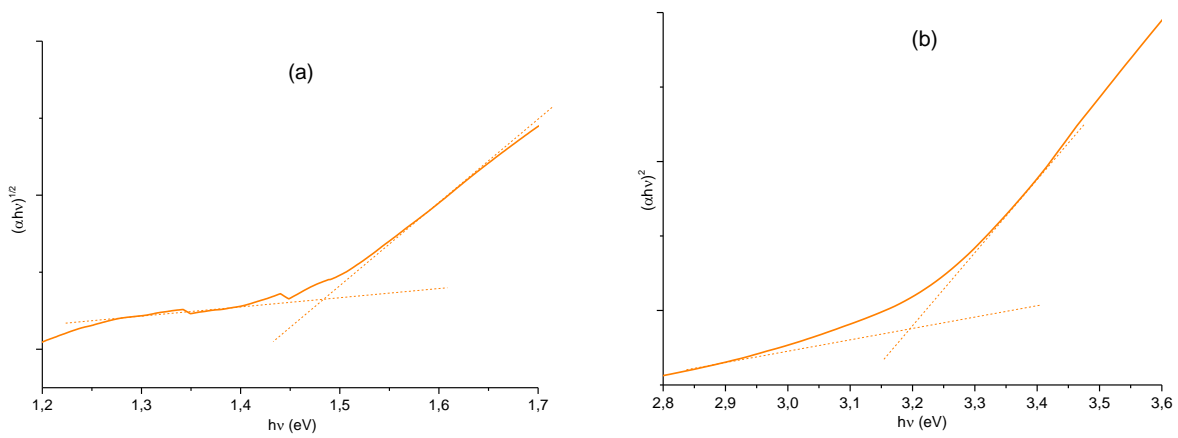


Figure S5. (a) Indirect and (b) direct Tauc plots of CFO.

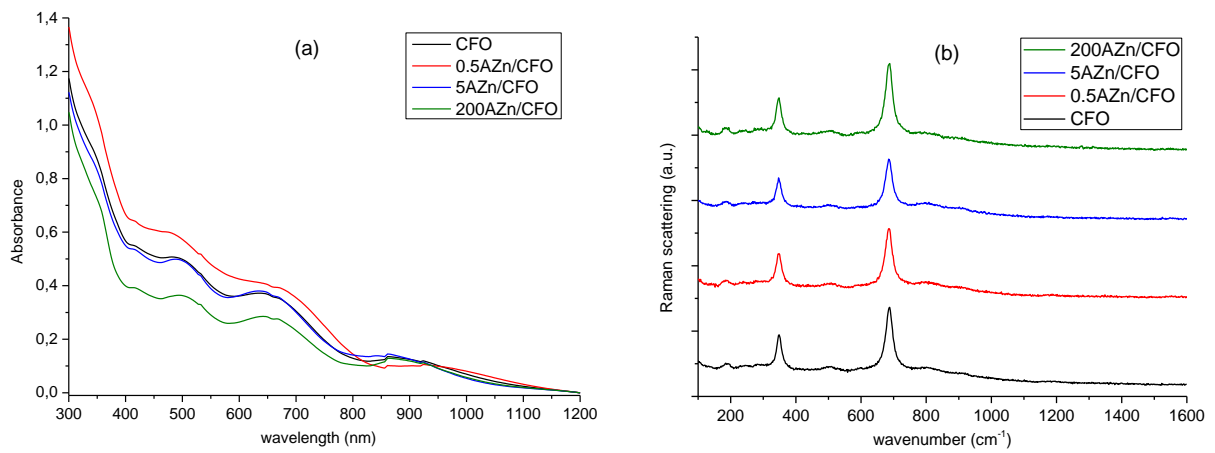


Figure S6. (a) UV-vis absorption spectra and (b) Raman spectra of CFO and ZnO/CFO photoelectrodes.

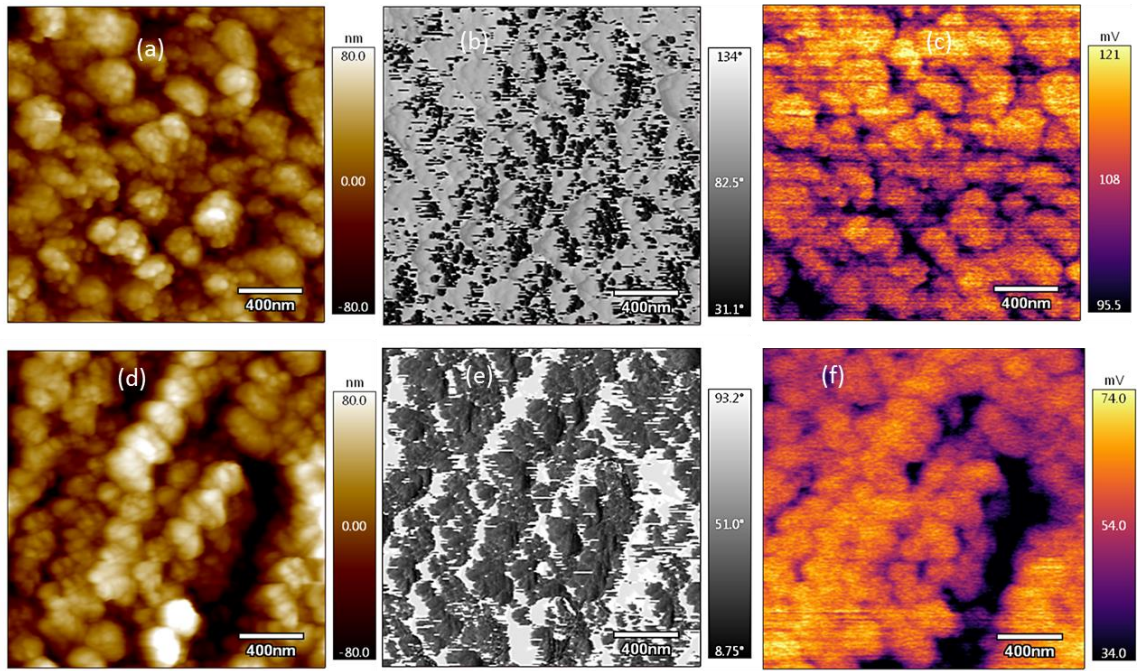


Figure S7. Figure 34. As-deposited Cu/CFO (a) AFM; (b) phase-contrast AFM; (c) SKPM. PEC-used Cu/CFO (d) AFM; (e) phase-contrast AFM; (f) SKPM.

6. REFERENCES

- ¹ H. Kisch, *Semiconductor photocatalysis*. Wiley-VCH Verlag GmbH & Co. KGaA: Weinheim (Germany), 2014. ISBN: 9783527335534.
- ² N. Sota, *Semiconductor Photoelectrodes in Electrochemistry at Material and Semiconductors Electrodes*. Elsevier Science B.V.: Amsterdam (The Netherlands), 1998. ISBN: 9780444828064.
- ³ T. Hisatomi, K. Domen, Recent advances in semiconductors for photocatalytic and photoelectrochemical water splitting. *Chem. Soc. Rev.* **2014**, *43*, 7520-7535, doi: 10.1039/c3cs60378d.
- ⁴ R. A. Afre, N. Sharma, M. Sharon, M. Sharon, Transparent Conducting Oxide Films for Various Applications: A Review. *Rev. Adv. Mater. Sci.* **2018**, *53*, 79-89, doi: 10.1515/rams-2018-0006.
- ⁵ M. S. Prévot, K. Sivula, Photoelectrochemical Tandem Cells for Solar Water Splitting. *J. Phys. Chem. C* **2013**, *117*, 17879-17893, doi: 10.1021/jp405291g.
- ⁶ A. Wolcott, W. A. Smith, T. R. Kuykendall, Y. Zhao, J. Z. Zhang, Photoelectrochemical Water Splitting Using Dense and Aligned TiO₂ Nanorod Arrays. *Small* **2009**, *5*(1), 104-111, doi: 10.1002/smll.200800902.
- ⁷ K. Sivula, F. Le Formal, M. Grätzel, WO₃-Fe₂O₃ Photoanodes for Water Splitting: A Host Scaffold, Guest Absorber Approach. *Chem. Mater.* **2009**, *21*, 2862-2867, doi: 10.1021/cm900565a.
- ⁸ S. Kishore Pilli, T. E. Furtak, L. D. Brown, T. G. Deutsch, J. A. Turner, A. M. Herring, Cobalt-phosphate (Co-Pi) catalyst modified Mo-doped BiVO₄ photoelectrodes for solar water oxidation. *Energy Environ. Sci.* **2011**, *4*, 5028-5034, doi: 10.1039/c1ee02444b.
- ⁹ C. R. Lhermitte, J. G. Verwer, B. M. Bartlett. Improving the stability and selectivity for the oxygen-evolution reaction on semiconducting WO₃ photoelectrodes with a solidstate FeOOH catalyst. *J. Mater. Chem. A*, **2016**, *4*, 2960-2968, doi: 10.1039/C5TA04747A.
- ¹⁰ R. S. Pessoa, M. A. Fraga, L. V. Santos, M. Massi, H. S. Maciel, Nanostructured thin films based on TiO₂ and/or SiC for use in photoelectrochemical cells: A review of the material characteristics, synthesis and recent applications. *Mater. Sci. Semicond. Process.* **2015**, *29*, 56-68, doi: 10.1016/j.mssp.2014.05.053.
- ¹¹ K. Sivula, F. Le Formal, M. Grätzel, Solar Water Splitting: Progress Using Hematite (α -Fe₂O₃) Photoelectrodes. *ChemSusChem* **2011**, *4*, 432-449, doi: 10.1002/cssc.201000416.
- ¹² Z.-F. Huang, L. Pan, J.-J. Zou, X. Zhanga, L. Wang, Nanostructured bismuth vanadate-based materials for solar-energy-driven water oxidation: a review on recent progress. *Nanoscale* **2014**, *6*, 14044-14063, doi: 10.1039/c4nr05245e.
- ¹³ T. Zhu, M. N. Chong, E. S. Chan, Nanostructured Tungsten Trioxide Thin Films Synthesized for Photoelectrocatalytic Water Oxidation: A review. *ChemSusChem* **2014**, *7*, 2974-2997, doi: 10.1002/cssc.201402089.
- ¹⁴ A. Paracchino, N. Mathews, T. Hisatomi, M. Stefik, S. D. Tilley, M. Grätzel, Ultrathin films on copper(I) oxide water splitting photocathodes: a study on performance and stability. *Energy Environ. Sci.* **2012**, *5*, 8673-8681, doi: 10.1039/c2ee22063f.
- ¹⁵ Y. Oh, W. Yang, J. Tan, H. Lee, J. Park, J. Moon, Boosting Visible Light Harvesting in p-Type Ternary Oxides for Solar-to-Hydrogen Conversion Using Inverse Opal Structure. *Adv. Funct. Mater.* **2019**, *29*, 1900194, doi: 10.1002/adfm.201900194.
- ¹⁶ U. A. Joshi, A. M. Palasyuk, P. A. Maggard, Photoelectrochemical Investigation and Electronic Structure of a p-Type CuNbO₃ Photocathode. *J. Phys. Chem. C* **2011**, *115*, 13534-13539, doi: 10.1021/jp204631a.
- ¹⁷ N. Guijarro, M. S Prévot, M. Johnson, X. Yu, W. S Bourée, X. A Jeanbourquin, P. Borno, F. Le Formal, K. Sivula, CuInGaS₂ photocathodes treated with SbX₃ (X = Cl, I): the effect of the halide on solar water splitting performance. *J. Phys. D* **2017**, *50*, 044003, doi:10.1088/1361-6463/aa524c.
- ¹⁸ Z. Xu, Z. Guan, J. Yang, Q. Li, Band Positions and Photoelectrochemical Properties of Solution-Processed Silver-Substituted Cu₂ZnSnS₄ Photocathode. *ACS Appl. Energy Mater.* **2019**, *2*, 2779-2785, doi: 10.1021/acsam.9b00116
- ¹⁹ X. Yu, M. S. Prévot, N. Guijarro, K. Sivula, Self-assembled 2D WSe₂ thin films for photoelectrochemical hydrogen production. *Nat. Commun.* **2015**, *6*, 7596, doi: 10.1038/ncomms8596.
- ²⁰ A. Standing, S. Assali, L. Gao, M. A. Verheijen, D. van Dam, Y. Cui, P. H. L. Notten, J. E.M. Haverkort, E. P.A.M. Bakkers, Efficient water reduction with gallium phosphide nanowires. *Nat. Commun.* **2015**, *6*, 7824, doi: 10.1038/ncomms8824.
- ²¹ Y. Lin, R. Kapadia, J. Yang, M. Zheng, K. Chen, M. Hettick, X. Yin, C. Battaglia, I. D. Sharp, J. W. Ager, A. Javey, Role of TiO₂ Surface Passivation on Improving the Performance of p-InP Photocathodes. *J. Phys. Chem. C* **2015**, *119*, 2308-2313, doi: 10.1021/jp5107313.
- ²² B. Seger, A. B. Laursen, P. C. K. Vesborg, T. Pedersen, O. Hansen, S. Dahl, I. Chorkendorff, Hydrogen Production Using a Molybdenum Sulfide Catalyst on a Titanium-Protected n+p-Silicon Photocathode. *Angew. Chem. Int. Ed.* **2012**, *51*, 9128-9131, doi: 10.1002/anie.201203585.
- ²³ M. J. Choi, J.-Y. Jung, M.-J. Park, J.-W. Song, J.-H. Lee, J. H. Bang, Long-term durable silicon photocathode protected by a thin Al₂O₃/SiO_x layer for photoelectrochemical hydrogen evolution. *J. Mater. Chem. A* **2014**, *2*, 2928-2933, doi: 10.1039/c3ta14443g.

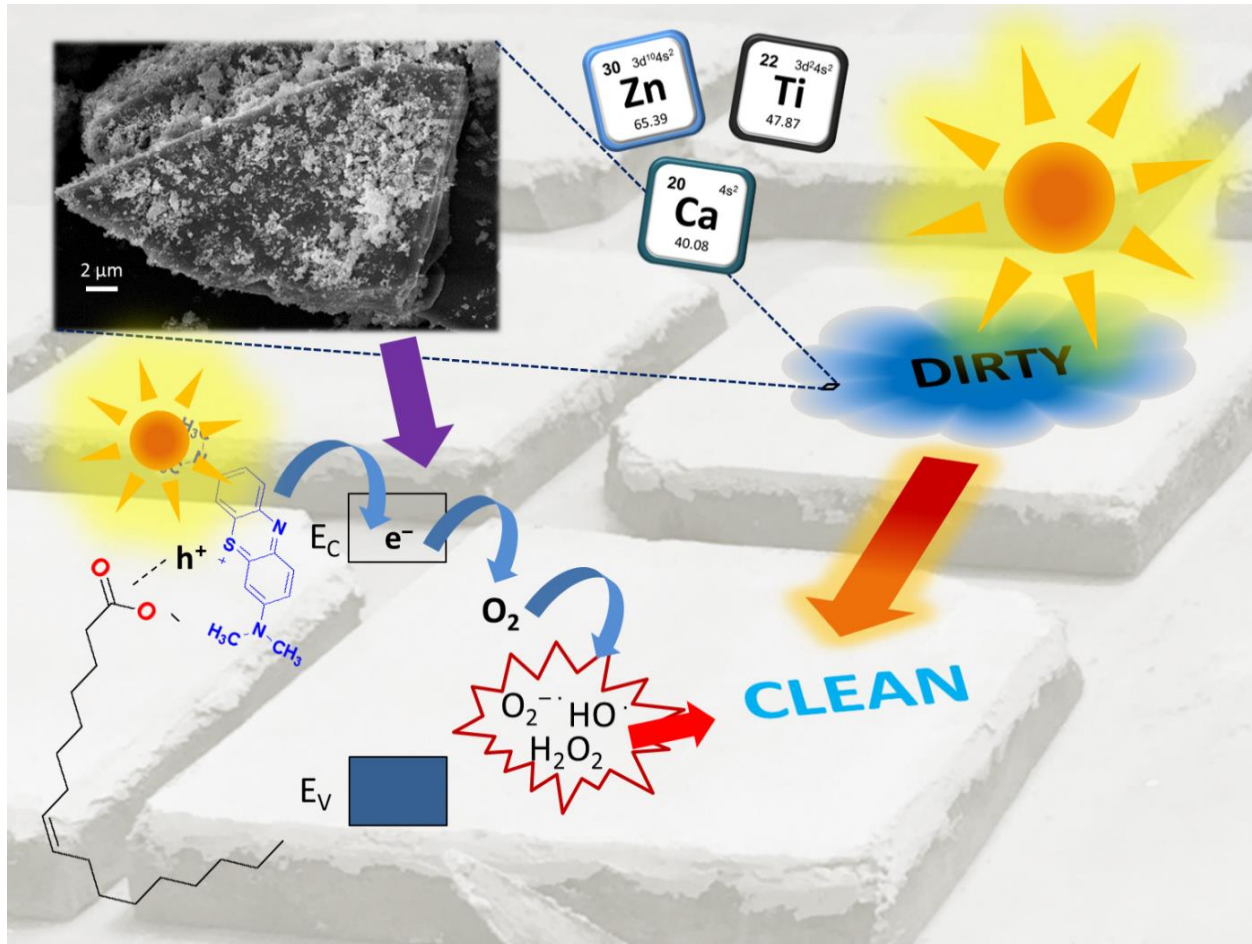
- ²⁴ A. Paracchino, V. Laporte, K. Sivula, M. Grätzel, E. Thimsen, Highly active oxide photocathode for photoelectrochemical water reduction. *Nat. Mater.* **2011**, *10*, 456-461, doi: 10.1038/nmat3017.
- ²⁵ M. Grätzel, Photoelectrochemical cells. *Nature* **2001**, *414*, 338-334, doi: 10.1038/35104607.
- ²⁶ M. G. Walter, E. L. Warren, J. R. McKone, S. W. Boettcher, Q. Mi, E. A. Santori, N. S. Lewis, Solar Water Splitting Cells. *Chem. Rev.* **2010**, *110*, 6446-6473, doi: 10.1021/cr1002326.
- ²⁷ R. B. Gupta, Transportation and Storage of Hydrogen. In *Hydrogen Fuel. Production, transport and storage*. CRC Press Taylor & Francis Group: Boca Raton (USA), 2009. ISBN: 9781420045758.
- ²⁸ Y. Wang, D. F. Ruiz Diaz, K. S. Chen, Z. Wang, X. C. Adroher, Materials, technological status, and fundamentals of PEM fuel cells – A review. *Mater. Today* **2020**, *32*, 178-203, doi: 10.1016/j.mattod.2019.06.005.
- ²⁹ E. Kalamaras, M. M. Maroto-Valer, Solar carbon fuel via photoelectrochemistry. *Catal. Today* **2018**, *317*, 56-57, doi: 10.1016/j.cattod.2018.02.045.
- ³⁰ G. A. Olah, A. Goepfert, G. K. Surya Prakash, The Hydrogen Economy and its Limitations. In *Beyond Oil and Gas: The Methanol Economy*. WILEY-VCH Verlag GmbH & Co. KGaA: Weinheim (Germany), 2009. ISBN: 9783527324224.
- ³¹ C. H. Bartholomew, R. J. Farrauto, Hydrogen Production and Synthesis Gas Reactions. In *Fundamental of Industrial Catalytic Processes*, 2nd ed. John Wiley & Sons, Inc.: Hoboken (USA), 2006. ISBN: 9780471457138.
- ³² K. Weissermel, H.-J. Arpe, *Industrial Organic Chemistry*, 3rd ed. WILEY-VCH Verlag GmbH & Co. KGaA: Weinheim (Germany), 1997. ISBN: 9783527614592.
- ³³ S. Xu, E. A. Carter, Theoretical Insights into Heterogeneous (Photo)electrochemical CO₂ Reduction. *Chem. Rev.* **2019**, *119*, 6631-6669, doi: 10.1021/acs.chemrev.8b00481.
- ³⁴ J. Zhao, X. Wang, Z. Xu, J. S. C. Loo, Hybrid catalysts for photoelectrochemical reduction of carbon dioxide: a prospective review on semiconductor/metal complex co-catalyst systems. *J. Mater. Chem. A* **2014**, *2*, 15228-15233, doi: 10.1039/c4ta02250e.
- ³⁵ S. Chu, S. Fan, Y. Wang, D. Rossouw, Y. Wang, G. A. Botton, Z. Mi, Tunable Syngas Production from CO₂ and H₂O in an Aqueous Photoelectrochemical Cell. *Angew. Chem. Int. Ed.* **2016**, *55*, 14262-14266, doi: 10.1002/anie.201606424.
- ³⁶ J. T. Song, H. Ryoo, M. Cho, J. Kim, J.-G. Kim, S.-Y. Chung, J. Oh, Nanoporous Au Thin Films on Si Photoelectrodes for Selective and Efficient Photoelectrochemical CO₂ Reduction. *Adv. Energy Mater.* **2017**, *7*, 1601103, doi: 10.1002/aenm.201601103.
- ³⁷ B. Kumar, J. M. Smieja, C. P. Kubiak, Photoreduction of CO₂ on p-type Silicon Using Re(bipy-But)(CO)₃Cl: Photovoltages Exceeding 600 mV for the Selective Reduction of CO₂ to CO. *J. Phys. Chem. C* **2010**, *114*, 14220-14223, doi: 10.1021/jp105171b.
- ³⁸ M. Schreier, J. Luo, P. Gao, T. Moehl, M. T. Mayer, M. Grätzel, Covalent Immobilization of a Molecular Catalyst on Cu₂O Photocathodes for CO₂ Reduction. *J. Am. Chem. Soc.* **2016**, *138*, 1938-1946, doi: 10.1021/jacs.5b12157.
- ³⁹ K. R. Rao, S. Pishgar, J. Strain, B. Kumar, V. Atla, S. Kumarib, J. M. Spurgeon, Photoelectrochemical reduction of CO₂ to HCOOH on silicon photocathodes with reduced SnO₂ porous nanowire catalysts. *J. Mater. Chem. A* **2018**, *6*, 1736-1742, doi: 10.1039/c7ta09672k.
- ⁴⁰ B. Weng, W. Wei, Yiliguma, H. Wu, A. M. Alenizib, G. Zheng, Bifunctional CoP and CoN porous nanocatalysts derived from ZIF-67 in situ grown on nanowire photoelectrodes for efficient photoelectrochemical water splitting and CO₂ reduction. *J. Mater. Chem. A* **2016**, *4*, 15353-15360, doi: 10.1039/c6ta06841c.
- ⁴¹ K. D. Yang, Y. Ha, U. Sim, J. An, C. W. Lee, K. Jin, Y. Kim, J. Park, J. S. Hong, J. H. Lee, H.-E. Lee, H.-Y. Jeong, H. Kim, K. T. Nam, Graphene Quantum Sheet Catalyzed Silicon Photocathode for Selective CO₂ Conversion to CO. *Adv. Funct. Mater.* **2016**, *26*, 233-242, doi: 10.1002/adfm.201502751.
- ⁴² E. E. Barton, D. M. Rampulla, A. B. Bocarsly, Selective Solar-Driven Reduction of CO₂ to Methanol Using a Catalyzed p-GaP Based Photoelectrochemical Cell. *J. Am. Chem. Soc.* **2008**, *130*, 6342-6344, doi: 10.1021/ja0776327.
- ⁴³ J. H. Kim, G. Magesh, H. J. Kang, M. Banu, J. H. Kim, J. Lee, J. S. Lee, Carbonate-coordinated cobalt co-catalyzed BiVO₄/WO₃ composite photoanode tailored for CO₂ reduction to fuels. *Nano Energy* **2015**, *15*, 153-163, doi: 10.1016/j.nanoen.2015.04.022.
- ⁴⁴ L.-X. Liu, J. Fu, L.-P. Jiang, J.-R. Zhang, W. Zhu, Y. Lin, Highly Efficient Photoelectrochemical Reduction of CO₂ at Low Applied Voltage Using 3D Co-Pi/BiVO₄/SnO₂ Nanosheet Array Photoanodes. *ACS Appl. Mater. Interfaces* **2019**, *11*, 26024-26031, doi: 10.1021/acsami.9b08144.
- ⁴⁵ G. Sahara, H. Kumagai, K. Maeda, N. Kaeffer, V. Artero, M. Higashi, R. Abe, O. Ishitani, Photoelectrochemical Reduction of CO₂ Coupled to Water Oxidation Using a Photocathode with a Ru(II)-Re(I) Complex Photocatalyst and a CoO_x/TaON Photoanode. *J. Am. Chem. Soc.* **2016**, *138*, 14152-14158, doi: 10.1021/jacs.6b09212.
- ⁴⁶ K. Lee, S. Lee, H. Cho, S. Jeong, W. D. Kim, S. Lee, D. C. Lee, Cu⁺-incorporated TiO₂ overlayer on Cu₂O nanowire photocathodes for enhanced photoelectrochemical conversion of CO₂ to methanol. *J. Energy Chem.* **2018**, *27*, 264-270, doi: 10.1016/j.jechem.2017.04.019.

- ⁴⁷ S. Kaneco, Y. Ueno, H. Katsumata, T. Suzuki, K. Ohta, Photoelectrochemical reduction of CO₂ at p-InP electrode in copper particle-suspended methanol. *Chem. Eng. J.* **2009**, *148*, 57-62, doi: 10.1016/j.cej.2008.07.038.
- ⁴⁸ T. Yoshida, A. Yamaguchi, N. Umezawa, M. Miyauchi, Photocatalytic CO₂ Reduction Using a Pristine Cu₂ZnSnS₄ Film Electrode under Visible Light Irradiation. *J. Phys. Chem. C* **2018**, *122*, 21695-21702, doi: 10.1021/acs.jpcc.8b04241.
- ⁴⁹ S. Ikeda, S. Fujikawa, T. Harada, T. H. Nguyen, S. Nakanishi, T. Takayama, A. Iwase, A. Kudo, Photocathode Characteristics of a Spray-Deposited Cu₂ZnGeS₄ Thin Film for CO₂ Reduction in a CO₂-Saturated Aqueous Solution. *ACS Appl. Energy Mater.* **2019**, *2*, 6911-6918, doi: 10.1021/acsaem.9b01418.
- ⁵⁰ J. Yuan, L. Zhenga, C. Hao, Role of pyridine in photoelectrochemical reduction of CO₂ to methanol at a CuInS₂ thin film electrode. *RSC Adv.* **2014**, *4*, 39435-39438, doi: 10.1039/c4ra06250g.
- ⁵¹ C. Cai, Y.-F. Xu, H.-Y. Chen, X.-D. Wang, D.-B. Kuang, Porous ZnO@ZnSe nanosheet array for photoelectrochemical reduction of CO₂. *Electrochim. Acta* **2018**, *274*, 298-305, doi: 10.1016/j.electacta.2018.04.108.
- ⁵² Y. J. Jang, J.-W. Jang, J. Lee, J. Hun Kim, H. Kumagai, J. Lee, T. Minegishi, J. Kubota, K. Domenc, J. Sung Lee, Selective CO production by Au coupled ZnTe/ZnO in the photoelectrochemical CO₂ reduction system. *Energy Environ. Sci.* **2015**, *8*, 3597-3604, doi: 10.1039/c5ee01445j.
- ⁵³ U. Kang, S. K. Choi, D. J. Ham, S. M. Ji, W. Choi, D. S. Han, A. Abdel-Wahabe, H. Park, Photosynthesis of formate from CO₂ and water at 1% energy efficiency via copper iron oxide catalysis. *Energy Environ. Sci.* **2015**, *8*, 2638-2643, doi: 10.1039/c5ee01410g.
- ⁵⁴ S. Kamimura, N. Murakami, T. Tsubota, T. Ohno, Fabrication and characterization of a p-type Cu₃Nb₂O₈ photocathode toward photoelectrochemical reduction of carbon dioxide. *Appl. Catal. B* **2015**, *174-175*, 471-476, doi: 10.1016/j.apcatb.2015.03.034.
- ⁵⁵ I. Sullivan, B. Zoellner, P. A. Maggard, Copper(I)-Based p-Type Oxides for Photoelectrochemical and Photovoltaic Solar Energy Conversion. *Chem. Mater.* **2016**, *28*, 5999-6016, doi: 10.1021/acs.chemmater.6b00926.
- ⁵⁶ A. B. Garg, R. Rao, Copper Delafossites under High Pressure—A Brief Review of XRD and Raman Spectroscopic Studies. *Crystals* **2018**, *8*, 255, doi:10.3390/cryst8060255.
- ⁵⁷ M. Yu, T. I. Draskovic, Y. Wu, Cu(I)-based delafossite compounds as photocathodes in p-type dye-sensitized solar cells. *Phys. Chem. Chem. Phys.* **2014**, *16*, 5026-5033, doi: 10.1039/c3cp55457k.
- ⁵⁸ J. Gu, Y. Yan, J. W. Krizan, Q. D. Gibson, Z. M. Detweiler, R. J. Cava, A. B. Bocarsly, p-Type CuRhO₂ as a Self-Healing Photoelectrode for Water Reduction under Visible Light. *J. Am. Chem. Soc.* **2014**, *136*, 830-833, doi: 10.1021/ja408876k.
- ⁵⁹ Platinum Group Metals, United States Geological Survey (USGS) summary, 2020. Pdf available online: <https://www.usgs.gov/centers/nmic/platinum-group-metals-statistics-and-information>. Accessed on 02/04/2020.
- ⁶⁰ M. S. Prévot, N. Guijarro, K. Sivula, Enhancing the Performance of a Robust Sol-Gel-Processed p-Type Delafossite CuFeO₂ Photocathode for Solar Water Reduction. *ChemSusChem* **2015**, *8*, 1359-1367, doi: 10.1002/cssc.201403146.
- ⁶¹ Iron Ore, United States Geological Survey (USGS) summary, 2020. Pdf available online: <https://www.usgs.gov/centers/nmic/iron-ore-statistics-and-information>. Accessed on 02/04/2020.
- ⁶² Copper, United States Geological Survey (USGS) summary, 2020. Pdf available online: <https://www.usgs.gov/centers/nmic/copper-statistics-and-information>. Accessed on 02/04/2020.
- ⁶³ D. Xiong, Y. Qi, X. Li, X. Liu, H. Tao, W. Chen, X. Zhao, Hydrothermal synthesis of delafossite CuFeO₂ crystals at 100 °C. *RSC Adv.* **2015**, *5*, 49280-49286, doi: 10.1039/c5ra08227g.
- ⁶⁴ H.-Y. Chen, J.-H. Wu, Characterization and optoelectronic properties of sol-gel-derived CuFeO₂ thin film. *Thin Solid Films* **2012**, *520*, 5029-5035, doi: 10.1016/j.tsf.2012.03.032.
- ⁶⁵ J. Gu, A. Wuttig, J. W. Krizan, Y. Hu, Z. M. Detweiler, R. J. Cava, A. B. Bocarsly, Mg-Doped CuFeO₂ Photocathodes for Photoelectrochemical Reduction of Carbon Dioxide. *J. Phys. Chem. C* **2013**, *117*, 12415-12422, doi: 10.1021/jp402007z.
- ⁶⁶ U. Kang, H. Park, A facile synthesis of CuFeO₂ and CuO composite photocatalyst films for the production of liquid formate from CO₂ and water over a month. *J. Mater. Chem. A* **2017**, *5*, 2123-2131, doi: 10.1039/c6ta09378g.
- ⁶⁷ X. Yang, E. A. Fugate, Y. Mueannern, L. R. Baker, Photoelectrochemical CO₂ Reduction to Acetate on Iron-Copper Oxide Catalysts. *ACS Catal.* **2017**, *7*, 177-180, doi: 10.1021/acscatal.6b0298.
- ⁶⁸ L. Zhang, H. Cao, Y. Lu, H. Zhang, G. Hou, Y. Tang, G. Zheng, Effective combination of CuFeO₂ with high temperature resistant Nb-doped TiO₂ nanotube arrays for CO₂ photoelectric reduction. *J. Colloid Interface Sci.* **2020**, *568*, 198-206, doi: 10.1016/j.jcis.2020.01.082.
- ⁶⁹ M. S. Prévot, X. A. Jeanbourquin, W. S. Bourée, F. Abdi, D. Friedrich, R. van de Krol, N. Guijarro, F. Le Formal, K. Sivula, Evaluating Charge Carrier Transport and Surface States in CuFeO₂ Photocathodes. *Chem. Mater.* **2017**, *29*, 4952-4962, doi: 10.1021/acs.chemmater.7b01284.
- ⁷⁰ N. Guijarro, M. S. Prévot, K. Sivula, Surface modification of semiconductor photoelectrodes. *Phys. Chem. Chem. Phys.* **2015**, *17*, 15655-15674, doi: 10.1039/c5cp01992c.

- ⁷¹ F. Le Formal, N. Tétreault, M. Cornuz, T. Moehl, M. Grätzel, K. Sivula, Passivating surface states on water splitting hematite photoanodes with alumina overlayers. *Chem. Sci.* **2011**, *2*, 737-743, doi:10.1039/c0sc00578a.
- ⁷² W. A. Thompson, A. Olivo, D. Zanardo, G. Cruciani, F. Menegazzo, M. Signoretto, M. M. Maroto-Valer, Systematic study of TiO₂/ZnO mixed metal oxides for CO₂ photoreduction. *RSC Adv.* **2019**, *9*, 21660-21666, doi: 10.1039/c9ra03435h.
- ⁷³ S. Benramache, B. Benhaoua, Influence of annealing temperature on structural and optical properties of ZnO: In thin films prepared by ultrasonic spray technique. *Superlattices Microst.* **2012**, *52*, 1062-1070, doi: 10.1016/j.spmi.2012.08.006.
- ⁷⁴ L. Liu, C. Zhao, Y. Li, Spontaneous Dissociation of CO₂ to CO on Defective Surface of Cu(I)/TiO_{2-x} Nanoparticles at Room Temperature. *J. Phys. Chem. C* **2012**, *116*, 7904-7912, doi: 10.1021/jp300932b.
- ⁷⁵ C. Drouilly, J.-M. Krafft, F. Averseng, H. Lauron-Pernot, D. Bazer-Bachi, C. Chizallet, V. Lecocq, G. Costentin, Role of oxygen vacancies in the basicity of ZnO: From the model methylbutynol conversion to the ethanol transformation application. *Appl. Catal. A* **2013**, *453*, 121-129, doi: 10.1016/j.apcata.2012.11.045.
- ⁷⁶ C. Xin, M. Hu, K. Wang, X. Wang, Significant Enhancement of Photocatalytic Reduction of CO₂ with H₂O over ZnO by the Formation of Basic Zinc Carbonate. *Langmuir* **2017**, *33*, 27, 6667-6676, doi: 10.1021/acs.langmuir.7b00620.
- ⁷⁷ J. Tauc, A. Menth, States in the gap. *J. Non-Cryst. Solids* **1972**, *8-10*, 569-585, doi: 10.1016/0022-3093(72)90194-9.
- ⁷⁸ T. Lopes, L. Andrade, H. Aguilar Ribeiro, A. Mendes, Characterization of photoelectrochemical cells for water splitting by electrochemical impedance spectroscopy. *Int. J. Hydrogen Energy* **2010**, *35*, 11601-11608, doi: 10.1016/j.ijhydene.2010.04.001.
- ⁷⁹ A. Mills, M. A. Valenzuela, The photo-oxidation of water by sodium persulfate, and other electron acceptors, sensitised by TiO₂. *J. Photochem. Photobiol. A* **2004**, *165*, 25-34, doi: 10.1016/j.jphotochem.2004.02.017.
- ⁸⁰ L. Yao, N. Guijarro, F. Boudoire, Y. Liu, A. Rahmanudin, R. A. Wells, A. Sekar, H.-H. Cho, J.-H. Yum, F. Le Formal, K. Sivula, Establishing Stability in Organic Semiconductor Photocathodes for Solar Hydrogen Production. *J. Am. Chem. Soc.* **2020**, *142(17)*, 7795-7802, doi: 10.1021/jacs.0c00126.
- ⁸¹ W. Schmickler, E. Santos, Experimental techniques for electrode kinetics – non stationary methods in *Interfacial Electrochemistry*, 2nd ed. Springer-Verlag: Berlin (Germany), 2010. ISBN: 9783642049378.
- ⁸² M.N. Kamalasanan, S. Chandra, Sol-gel synthesis of ZnO thin films. *Thin solid films* **1996**, *288*, 112-115, doi: 10.1016/S0040-6090(96)08864-5.
- ⁸³ Ü. Özgür, Ya. I. Alivov, C. Liu, A. Teke, M. A. Reshchikov, S. Doğan, V. Avrutin, S.-J. Cho, H. Morkoç, A comprehensive review of ZnO materials and devices. *J. Appl. Phys.* **2005**, *98*, 041301, doi: 10.1063/1.1992666.
- ⁸⁴ Auger parameters for Zn, NIST XPS database website, available on: https://srdata.nist.gov/xps/EngElmSrchQuery.aspx?ETType=AP&CSOpt=Retri_ex_dat&Elm=Zn. Accessed on 27/04/2020.
- ⁸⁵ O1s line, NIST XPS database website, available on: https://srdata.nist.gov/xps/EngElmSrchQuery.aspx?ETType=PE&CSOpt=Retri_ex_dat&Elm=O. Accessed on 27/04/2020.
- ⁸⁶ G. Ballerini, K. Ogle 1, M.-G. Barthés-Labrousse, The acid–base properties of the surface of native zinc oxide layers: An XPS study of adsorption of 1,2-diaminoethane. *Appl. Surf. Sci.* **2007**, *253*, 6860-6867, doi: 10.1016/j.apsusc.2007.01.126.
- ⁸⁷ J. C. C. Fan, J. B. Goodenough, X-ray photoemission spectroscopy studies of Sn-doped indium-oxide films. *J. Appl. Phys.* **1977**, *48*, 3524, doi: 10.1063/1.324149.
- ⁸⁸ C1s line, NIST XPS database website, available on: https://srdata.nist.gov/xps/EngElmSrchQuery.aspx?ETType=PE&CSOpt=Retri_ex_dat&Elm=C. Accessed on 27/04/2020.
- ⁸⁹ K. Jäger, O. Isabella, A. H. M. Smets, R. A. C. M. M. van Swaaij, M. Zeman, *Electrodynamic basis in Solar Energy. Fundamentals, Technology, and Systems*. Uit Cambridge Ltd.: Cambridge (UK), 2016. ISBN: 9781906860325.
- ⁹⁰ A. Polo, C. R. Lehrmitte, M. V. Dozzi, E. Selli, K. Sivula, Hydrogenation of ZnFe₂O₄ Flat Films: Effects of the Pre-Annealing Temperature on the Photoanodes Efficiency for Water Oxidation. *Surfaces* **2020**, *3*, 94-104, doi: 10.3390/surfaces3010009.
- ⁹¹ J. C. Nie, J. Y. Yang, Y. Piao, H. Li, Y. Sun, Q. M. Xue, C. M. Xiong, R. F. Dou, Q. Y. Tu, Quantum confinement effect in ZnO thin films grown by pulsed laser deposition. *Appl. Phys. Lett.* **2008**, *93*, 173104, doi: 10.1063/1.3010376.
- ⁹² Y. Xu, M. A. A. Schoonen, The absolute energy positions of conduction and valence bands of selected semiconducting minerals. *Am. Min.* **2000**, *85*, 543-556, doi: 10.2138/am-2000-0416.
- ⁹³ F. Yu, T. Song, B. Wang, B. Xu, H. Li, H. Hu, L. He, H. Duan, S. Wang, X. Tang, The effects of intrinsic defects on the structural and optical properties of ZnO thin film prepared via a sol-gel method. *Mater. Res. Express* **2019**, *6*, 115901, doi: 10.1088/2053-1591/ab4394
- ⁹⁴ P. Podbršček, G. Dražić, A. Anžlovar, Z.C. Orel, The preparation of zinc silicate/ZnO particles and their use as an efficient UV absorber. *Mater. Res. Bull.* **2011**, *46*, 2105-2111, doi: 10.1016/j.materresbull.2011.06.037.

- ⁹⁵ D. Kohl, M. Henzler, G. Heiland, Low temperature sublimation processes from clean cleaved polar surfaces of zinc oxide crystals during first heating. *Surf. Sci.* **1974**, *41*, 403-411, doi: 10.1016/0039-6028(74)90057-0.
- ⁹⁶ P. Sagar, P. K. Shishodia, R. M. Mehra, H. Okada, A. Wakahara, A. Yoshida, Photoluminescence and absorption in sol-gel-derived ZnO film. *J. Lumin.* **2007**, *126*, 800-806, doi: 10.1016/j.jlumin.2006.12.003.
- ⁹⁷ J. Lv, W. Gong, K. Huang, J. Zhu, F. Meng, X. Song, Z. Sun, Effect of annealing temperature on photocatalytic activity of ZnO thin films prepared by sol-gel method. *Superlattice Microst.* **2011**, *50(2)*, 98-106, doi: 10.1016/j.spmi.2011.05.003.
- ⁹⁸ X.Q. Wei, B.Y. Man, M. Liu, C.S. Xue, H.Z. Zhuang, C. Yang, Blue luminescent centers and microstructural evaluation by XPS and Raman in ZnO thin films annealed in vacuum, N₂ and O₂. *Physica B* **2007**, *388*, 145-152, doi: 10.1016/j.physb.2006.05.346.
- ⁹⁹ K. L. Choy, Chemical vapour deposition of coatings. *Prog. Mater. Sci.* **2003**, *48*, 57-170, doi: 10.1016/S0079-6425(01)00009-3.
- ¹⁰⁰ P. Marchand, I. A. Hassan, I. P. Parkin, C. J. Carmalt, Aerosol-assisted delivery of precursors for chemical vapour deposition: expanding the scope of CVD for materials fabrication. *Dalton Trans.* **2013**, *42*, 9406-9422, doi: 10.1039/c3dt50607j.
- ¹⁰¹ A. B. Garg, R. Rao, Copper Delafossites under High Pressure—A Brief Review of XRD and Raman Spectroscopic Studies. *Crystals* **2018**, *8*, 255, doi: 10.3390/cryst8060255.
- ¹⁰² Cuprite (Cu₂O) Raman spectra, RRUFF project, available on: <https://rruff.info/cuprite/display=default/>. Accessed on 01/05/2020.
- ¹⁰³ Tenorite (CuO) Raman spectra, RRUFF project, available on: <https://rruff.info/tenorite/display=default/>. Accessed on 01/05/2020.
- ¹⁰⁴ Hematite (Fe₂O₃) Raman spectra, RRUFF project, available on: <https://rruff.info/hematite/display=default/>. Accessed on 01/05/2020.
- ¹⁰⁵ K. Sivula, Metal Oxide Photoelectrodes for Solar Fuel Production, Surface Traps, and Catalysis. *J. Phys. Chem. Lett.* **2013**, *4*, 1624-1633, doi: 10.1021/jz4002983.
- ¹⁰⁶ C. de Melo, M. Jullien, Y. Battie, A. E. Naciri, J. Ghanbaja, F. Montaigne, J.-F. Pierson, F. Rigoni, N. Almqvist, A. Vomiero, S. Migot, F. Mücklich, D. Horwat, Semi-Transparent p-Cu₂O/n-ZnO Nanoscale-Film Heterojunctions for Photodetection and Photovoltaic Applications. *ACS Appl. Nano Mater.* **2019**, *2*, 4358-4366, doi: 10.1021/acsnm.9b00808.
- ¹⁰⁷ J.-H. Yum, S.-J. Moon, L. Yao, M. Caretti, S. Nicolay, D.-H. Kim, K. Sivula, Robust Electron Transport Layers via In Situ Cross-Linking of Perylene Diimide and Fullerene for Perovskite Solar Cells. *ACS Appl. Energy Mater.* **2019**, *2(9)*, 6616-6623, doi: 10.1021/acsaem.9b01154.
- ¹⁰⁸ Th. Albers, D. Lipinsky, L. Wiedmann, A. Benninghoven, Combined depth profile analysis with SNMS, SIMS and XPS: Preferential sputtering and oxygen transport in binary metal oxide multilayer systems. *Surf. Interface Anal.* **1994**, *22*, 9-13, doi: 10.1002/sia.740220105
- ¹⁰⁹ A. J. Leenheer, J. D. Perkins, M. F. A. M. van Hest, J. J. Berry, R. P. O'Hayre, D. S. Ginley, General mobility and carrier concentration relationship in transparent amorphous indium zinc oxide films. *Phys. Rev. B* **2008**, *77*, 115215, doi: 10.1103/PhysRevB.77.115215.
- ¹¹⁰ H. Dai, F. Ye, T. Li, Z. Chen, X. Cao, B. Wang, Impact of Li doping on the microstructure, defects, and physical properties of CuFeO₂ multiferroic ceramics. *Ceram. Int.* **2019**, *45*, 24570-24577, doi: 10.1016/j.ceramint.2019.08.186.
- ¹¹¹ S. Bassaid, M. Chaib, S. Omeiri, A. Bougueliac, M. Trari, Photocatalytic reduction of cadmium over CuFeO₂ synthesized by sol-gel. *J. Photochem. Photobiol. A* **2009**, *201*, 62-68, doi: 10.1016/j.jphotochem.2008.09.015.
- ¹¹² S. Muthukumar, R. Gopalakrishnan, Structural, FTIR and photoluminescence studies of Cu doped ZnO nanopowders by co-precipitation method. *Opt. Mater.* **2012**, *34*, 1946-1953, doi: 10.1016/j.optmat.2012.06.004.
- ¹¹³ F. A. Miller, C. H. Wilkins, Infrared Spectra and Characteristic frequencies of Inorganic Ions. *Anal. Chem.* **1952**, *24*, 1253-1294, doi: 10.1021/ac60068a007.
- ¹¹⁴ A. Gankanda, D. M. Cwiertny, V. H. Grassian, Role of Atmospheric CO₂ and H₂O Adsorption on ZnO and CuO Nanoparticle Aging: Formation of New Surface Phases and the Impact on Nanoparticle Dissolution. Role of Atmospheric CO₂ and H₂O Adsorption on ZnO and CuO Nanoparticle Aging: Formation of New Surface Phases and the Impact on Nanoparticle Dissolution. *J. Phys. Chem. C* **2016**, *120*, 19195-19203, doi: 10.1021/acs.jpcc.6b05931.
- ¹¹⁵ G. K. H. Pang, K. Z. Baba-Kishi, A. Patel, Topographic and phase-contrast imaging in atomic force microscopy. *Ultramicroscopy* **2000**, *81*, 35-40, doi: 10.1016/S0304-3991(99)00164-3.
- ¹¹⁶ B. L. Sharma, Physics of Schottky Barrier Junctions in *Metal-Semiconductor Schottky Barrier Junctions and Their Applications*. Plenum Press: New York (US), 1984. ISBN: 9781468446555.

CHAPTER 4: SELF-CLEANING PROPERTIES ON ZnO AND TiO₂-MODIFIED VENETIAN MARMORINO



1. INTRODUCTION

1.1 THE SURFACE DEGRADATION OF CULTURAL HERITAGE

The cultural heritage is largely composed of stone-based materials, which are affected by several kinds of damaging processes, such as physical [1,2], chemical [3] or biological [4] ones. Such effects have a negative impact on its aesthetic value and potentially affecting the local economy as well. For this reason, it is essential to understand the mechanism of damaging processes [5] and to develop appropriate remediation strategies [6,7].

Physical damage often affords morphological alterations [8], due to a change of the shape of the artifact (Figure 1a), and could be very harmful because affecting the structural integrity of the artifacts itself. Chemical [9] and biological [10] phenomenon, despite potentially affect the stone structure and morphology as well, usually induces chromatic alterations by changing the color of the artifact (Figure 1b). Despite having less serious effects, such alterations still negatively affect the aesthetic value of a material involved part of the cultural heritage.

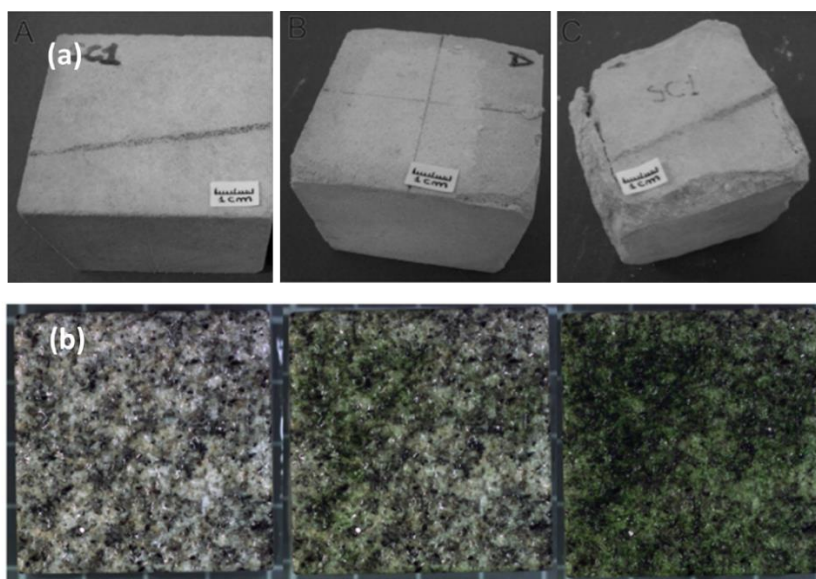
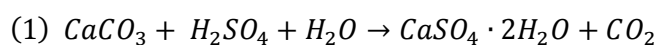


Figure 1. (a) Morphological alteration due to salt crystallization [8] and (b) Chromatic alteration due to algae growth [10]. Increasing exposure time from left to right.

A well-known chromatic alteration on cultural-heritage is the formation of black crusts due to gypsum formation (Reaction 1), especially on limestone or mortars [11]. Gypsum does not absorb in the visible light, but undergoes dissolution and re-precipitation phenomenon which incorporate carbonaceous particulate matter, giving the typical colour of such gypsum-based crust [9].



Another important chromatic alteration is the growth of cyanobacteria or green algae, which form a biofilm staining the stone material [12]. Beside the chromatic effect, this biofilm can also allow the growth of other

microorganism, such as bacteria and fungi, which have a minor role in staining, but cause more severe damaging due to acid metabolites and mechanical effects [12,13].

The climatic and environmental changes that our planet is experiencing, affect also the deterioration of stone cultural heritages. Smith *et al.* pointed out a change in the staining phenomenon of stones, due to the decrease amount of sulfur oxides (SO_x) responsible of gypsum-based black crusts, and the improvement of algae-based staining due to an increase in nitrogen oxides (NO_x), representing a source of nutrient for the microorganisms [5]. The rise of CO_2 concentration and humidity in the atmosphere, further stimulate the growth of algae, and the consequent staining of stone materials [10].

Finally, anthropogenic staining (i.e. *graffiti* vandalism, Figure 2) is another form of chromatic alteration of stone materials, due to the intentional coating with an organic material (i.e. paints) [14].



Figure 2. Graffiti vandalism with a red paint on a lion statue in Venice in 2018 [15].

1.2. CULTURAL HERITAGE REMEDIATION: LIGHT-DRIVEN SELF-CLEANING

The removal of superficial deposits causing chromatic alteration of cultural heritage, can rely on different methods, such as mechanical [16], physical (i.e. laser) [17], chemical [18,19], biological [19,20] or combined approaches (i.e. physical-chemical) [21]. All these techniques, however, have the drawback to be effective only once the material has been already damaged.

An alternative method is to prevent the formation and accumulation of these deposits, namely modifying the surface aiming to get it a self-cleaning property. This feature can rely on a physical effect, allowing the deposits to be easily washed away (i.e. superhydrophobicity or superhydrophilicity), but also on a chemical one, through a chemical attack that oxidizes the deposit to simple and safe molecules (i.e. CO_2 and H_2O) [22]. Photocatalysis is an appealing choice to achieve such chemical self-cleaning feature, because able to operate in very mild conditions (r.t. and atmospheric pressure), using the atmospheric O_2 as bleacher and the light as energy source, even with a low intensity such as in indoor environment [23], ideal conditions to easily and cheaply prevent stain deposits on cultural heritage.

The mechanism of the photocatalytic self-cleaning is pictured in Figure 3. As for other photocatalytic reaction, it involves the generation of photoexcited charge carriers, electrons and holes, upon absorption of photon of suitable energy by the semiconductor. Then, a superficial charge transfer occurs by the reaction of photoexcited electrons with a suitable electron acceptor, O_2 in the case of a photo-oxidation, and holes with an electron donor, organic compounds (RH) composing the stain deposit, which are eventually oxidized (pathway 4) [24].

The organics oxidative decomposition occurs also through another pathway. Indeed, O_2 undergoes a multi-step reduction by the photoexcited electrons (pathway 2) affording different intermediates such as superoxide ions ($O_2^{\cdot -}$), hydrogen peroxide (H_2O_2) and hydroxyl radical (HO^{\cdot}), the so-called reactive oxygen species (ROS), finally involved in the oxidative degradation of organics (pathway 3) [25].

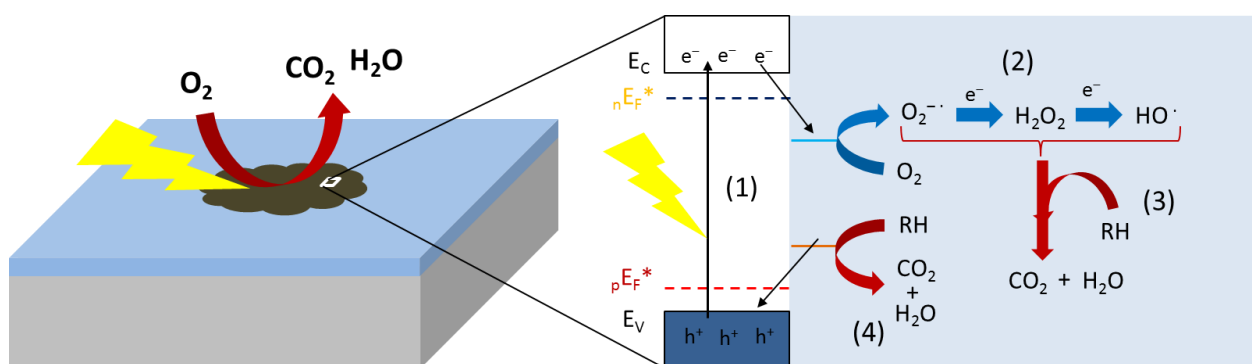


Figure 3. Mechanism of photocatalytic self-bleaching surface. (1) Excitation of the semiconductor (SC); (2) oxygen reduction reaction to ROS; (3) Organic compounds (RH) oxidation by ROS; (4) Organic compounds oxidation by photoexcited holes. The energy levels are labelled according to the Preface section.

Different materials have been used in the photooxidation of organic compounds. Titanium dioxide (TiO_2) [26], zinc oxide (ZnO) [27] and strontium titanate ($SrTiO_3$) [28] have been involved as wide-bandgap semiconductor (SC), capable of harvesting UV photons only, while materials such as tungsten trioxide (WO_3) [29], bismuth vanadate ($BiVO_4$) [30], hematite (Fe_2O_3) [31], cadmium sulphide (CdS) [32] or graphitic carbon nitride ($g-C_3N_4$) [33], having a narrower bandgap, are able to exploit also the visible light photons, more abundant in sunlight. Besides pure materials, heterostructures such as TiO_2/ZnO [34], Cu_2O/ZnO [35] or $g-C_3N_4/WO_3$ [36], have been reported too. These composites take advantages of the interfacial charge transfer (heterojunction) from one material to another, reducing the photoexcited charge carrier recombination and eventually boosting up the photocatalytic activity [34].

Despite the large amount of photocatalytic material available for organic photodegradation, few reports can be found in literature (Table 1) concerning the exploitation of photocatalysis, mainly pristine TiO_2 , as self-cleaning tool for stone-like materials in the cultural heritage field [37-39], making this appealing application of photocatalysis a relatively unexplored field. In this context, an interesting candidate is a plaster, in which

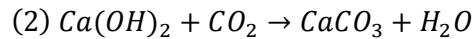
a photocatalyst could be incorporated easily in the formulation, like *marmorino*, a material used in Venice building and part of the cultural heritage of the city.

Table 1. Examples of photocatalytic materials used for self-cleaning surfaces.

Ref.	Surface	Photocatalyst	Conditions	Comments
[37]	Portland cement mortar and silicate-coated mortar	TiO ₂ (P25, Evonik)	r.t. and 0.1 MPa; UVA light (315-400 nm); 3.7 W·m ⁻² ; Rhodamine B as reactant; 25 h irradiation; 2 – 4 wt. % TiO ₂ within the mortar and 5 – 20 wt. % TiO ₂ in the silicate coating	Comparable activity TiO ₂ bulk (within the mortar) vs TiO ₂ coating; loss in activity upon recycling the former (detrimental effect of reaction intermediates uptake), activity enhancement in the latter (decomposition of organic additives in the silicate coating, acting as inhibitors).
[38]	White cement – metakaolin – glass (inert) mortar	TiO ₂ (pure anatase and P25 Evonik)	25 – 40 °C and 0.1 MPa; UVA light (3.1 – 3.4 W·m ⁻²) and visible (0.5 – 0.6 W·m ⁻²); Rhodamine B as reactant; 4 or 26 h of irradiation; weathering with 12 h of wet dark (pumping water) and dry daylight (UVA light source) conditions for 1 or 2 weeks	Best performance with the coated TiO ₂ (ca. 50% dye removal); activity loss upon weathering, more pronounced with P25 suspension probably due to catalyst physical detachment; activity either on UVA (direct excitation) or visible (indirect excitation) light
[39]	Travertine blocks (limestone)	Colloidal anatase TiO ₂	r.t. and 0.1 MPa; UVA (3.5 W·m ⁻²) 26 h of irradiation for Rhodamine B degradation; UVA (20 W·m ⁻²) for NO _x photooxidation (0.6 ppmv NO in air, flow 1.5 L·min ⁻¹)	Comparable activity toward dye removal using a single layer or a three-layer spray-coated TiO ₂ ; slight better NO removal with the three layers deposited TiO ₂ (35% vs 25%)

1.3. CASE OF STUDY: VENETIAN *MARMORINO*

Marmorino is a plaster traditionally used in Venice city as a coating for both inside and outside walls. This stone-based material differs from other plaster due to its composition, being a mixture of marble powder (CaCO_3) and hydrated lime ($\text{Ca}(\text{OH})_2$), and the *fresco su fresco* coating technique, in which each layer of plaster is applied over the previous one without waiting the full carbonatation process of $\text{Ca}(\text{OH})_2$. This process (Reaction 2) converts the hydrated lime into a solid layer of CaCO_3 , bounding the marble particles each other, and gives both mechanical resistance and good water vapor permeability [40].



Historically, plaster with marble powders dates back to the ancient Rome, testified in the 1st century BC by Vitruvius in the *De Architectura* book. During the Renaissance, along with the rediscovery of classical culture, a revival of this material occurred, in particular in the *Serenissima* (Venetian Republic), dating back to the seventeenth century AD. This material is still used nowadays in Venice (Figure 4), both in new buildings as well as in the restoration of many buildings. A superficial treatment with of lime water, soaps, natural waxes or vegetable oils is usually involved to protect *marmorino* against weathering [41].

As other stone-based material, this material suffers of several types of surface damaging phenomena affording a chromatic alteration, as described in Section 1.1. This affects its aesthetic values and requires a cleaning procedure to restore the original surface, or an appealing alternative procedure such as the photocatalytic self-cleaning process. Nonetheless, to the best of our knowledge, no reports concerning the addition of photocatalytic material in Venetian *marmorino* formulation, aiming a self-cleaning property, have been reported yet.



Figure 4. (a) Indoor and (b) outdoor example of marmorino wall coating.

1.4. AIM OF THE CHAPTER

The aim of this chapter is to develop some ZnO- and TiO₂-modified Venetian *marmorino* aiming to obtain a self-cleaning property on this material, while preserving its aesthetic features. The preparation of the *marmorino* was performed in collaboration with Mr. Giorgio Berto (Uni.S.Ve company, Venice, Italy) and Arch. L. Scappin (IUAV University of Venice, Venice, Italy). In details, the work is divided in two sub-sections:

1. Evaluation of how the main structural, morphological, optical and surface properties of Venetian *marmorino* are modified by the addition of ZnO- and TiO₂-based material.
2. Assessment of the photocatalytic self-cleaning property and the impact of the above-mentioned properties on the material photoactivity.

2. MATERIALS AND METHODS

2.1. REAGENTS

The following reagents were used as-received: zinc oxide (ZnO, assay > 99.99%, Carlo Erba) zinc nitrate hexahydrate ($\text{Zn}(\text{NO}_3)_2 \cdot 6\text{H}_2\text{O}$, assay > 99%, Sigma Aldrich), sodium carbonate (Na_2CO_3 , assay > 99.5%, Sigma Aldrich), titanium isopropoxide ($\text{Ti}(\text{O}^i\text{Pr})_4$, assay > 97%, Sigma Aldrich), titanium (IV) oxysulphate sulphuric acid hydrate ($\text{TiOSO}_4 \cdot x\text{H}_2\text{O} \cdot \gamma\text{H}_2\text{SO}_4$, Ti assay > 29%, Sigma Aldrich), ammonia NH_3 aqueous solution (assay 30-33%, Sigma Aldrich), isopropanol (assay 99.8%, Sigma Aldrich), methylene blue chloride (dye content > 82%, Sigma Aldrich), gallic acid monohydrate (assay > 98%, Sigma-Aldrich), iron (III) nitrate nonahydrate ($\text{Fe}(\text{NO}_3)_3 \cdot 9\text{H}_2\text{O}$, assay > 98%, Sigma-Aldrich) and sodium oleate (fatty acid > 82%, Sigma Aldrich).

The material required for the preparation of the Venetian *marmorino*, quicklime (CaO), *spolverone* marble powder (CaCO_3 , grain size 1 – 3 mm), *impalpabile* marble powder (CaCO_3 , grain size 0.07 mm) and Aleppo soap, were supplied by Uni.S.Ve company (Venice, Italy).

2.2. SYNTHESIS

2.2.2. PHOTOCATALYTS SYNTHESIS

Laboratory-made TiO_2 , was prepared through a wet chemistry approach (precipitation) according to the literature [42]. A 1.2 M TiOSO_4 solution was added dropwise to a beaker containing deionized water under vigorous stirring. The pH was kept constant at 5.5 by the addition of a 9 M NH_3 aqueous solution. The as-obtained suspension was aged at 60°C for 20 hours, then vacuum filtered, washed with deionized water to remove dissolved ions and air-dried at 110°C for 18 hours. The dried product was finally annealed at 400°C for 4 hours (ramp: 2 °C·min⁻¹) in air flow (30 mL·min⁻¹). The sample was labelled LAB-Ti.

Laboratory-made ZnO, was prepared through a wet chemistry method (precipitation). A 1.1 M $\text{Zn}(\text{NO}_3)_2$ aqueous solution was added dropwise to a beaker containing deionized water under vigorous stirring. The pH was kept constant at 9 by the addition of a 1.0 M Na_2CO_3 aqueous solution. The as-obtained suspension was aged at 60°C for 20 hours, then vacuum filtered, washed with deionized water to remove dissolved ions and air-dried at 110°C for 18 hours. The dried product was finally annealed at 400°C or 600°C for 4 hours (ramp: 2 °C·min⁻¹) in air flow (30 mL·min⁻¹). The sample was labelled LAB-Zn.

A laboratory-made TiO_2 -ZnO composite was prepared by wetness impregnation of TiO_2 . In details, $\text{Ti}(\text{O}^i\text{Pr})_4$ precursor was dissolved in i-PrOH and added dropwise either to LAB-ZnO powder, to afford a 6 wt. % Ti loading. The impregnated powder was air dried at 110°C for 18 hours and finally annealed at 400°C for 4 hours (ramp: 2 °C·min⁻¹) in air flow (30 mL·min⁻¹). The sample was labelled LAB-TiZn.

2.2.3. MARMORINO PREPARATION

The Venetian *marmorino* was coated on a 20 x 20 cm cotto (fired clay) brick. A first underlayer composed of coarse sand and lime putty (1:3 weight ratio) was applied onto a moisten brick. Then, two layers of *marmorino* were coated. They are composed of *impalpabile*, a tiny-sized marble powder (0.07 mm), *spolverone*, a coarser marble powder (1-3 mm) and lime putty in 2:1:1 weight ratio. The third layer of *marmorino*, prepared mixing 16 g of calcium-based mixture previously mentioned either with 4 g of photocatalysts (20 wt. %) or 4 g of *impalpabile*. The coated bricks were let in air at r.t. for 20 days, in order to dry them and allow the carbonatation of $\text{Ca}(\text{OH})_2$ to occur. The as-prepared marmorino-coated brick appeared as in Figure 5.



Figure 5. Freshly-prepared marmorino coated-brick.

The samples were labelled as following:

- M, pristine *marmorino*
- M-COM-Ti, 20 wt. % benchmark TiO_2 (P25, Evonik) in the upper layer
- M-LAB-Ti, 20 wt. % LAB- TiO_2 in the upper layer
- M-COM-Zn, 20 wt. % benchmark ZnO (Carlo Erba) in the upper layer
- M-LAB-Zn, 20 wt. % LAB-ZnO in the upper layer
- M-LAB-TiZn, 20 wt. % LAB-TiZnO in the upper layer

2.3. CHARACTERIZATIONS

The phase composition and crystallite size were measured by X-ray diffraction (XRD) using a Bruker D8 Advance DaVinci powder diffractometer using a sealed X-ray tube (copper anode; operating conditions, 40 kV and 40 mA) and a linear array detector (LynxEye), set to discriminate the $\text{Cu K}\alpha$ radiation, coupled with a Ni filter to completely remove the $\text{Cu K}\beta$ component. Data scans were performed in the 2θ range 5–90° with

0.02° step size and point-detector equivalent counting times of 5 s/step. Quantitative phase analysis and crystallite size determination were performed using the Rietveld method as implemented in the TOPAS v.5 program (Bruker AXS) using the fundamental parameters approach for line-profile fitting. The determination of the crystallite size was accomplished by the Double-Voigt approach and calculated as volume-weighted mean column heights based on integral breadths of peaks.

The specific surface area (SSA) was determined using nitrogen (N₂) physisorption with a TriStar II Plus (Micromeritics) analyzer. The samples were outgassed at 200°C in vacuum for 2 hours to clean the surface before the analysis. The N₂ adsorption-desorption isotherms were then acquired at – 196 °C and the SSA determined by the Brunauer-Emmet-Teller (BET) equation [43] fitted in the 0.04 – 0.3 P/P° range.

The morphology was evaluated with a field emission electron scanning microscopy (FE-SEM) LEO 1525 ZEISS equipped with in-lense detector. The chemical composition was determined using a Bruker Quantax EDS. The samples were deposited onto conductive carbon adhesive tape and metallized with chromium.

The optical absorbance was measured by diffuse-reflectance spectroscopy (DRS), through an integration sphere equipped Cary100 UV-vis spectrophotometer (Agilent). The spectra was reported through the Kubelka-Munk function (Equation 1), where R_∞ is the reflectance at an infinite thick layer of the sample [44].

$$f(R_\infty) = \frac{(1 - R_\infty)^2}{2R_\infty}$$

Equation 1. Kubelka-Munk function.

The bandgap (E_g) of the material was determined by the Tauc relation (Equation 2), where the Kubelka-Munk function ($f(R_\infty)$) is used in place of the absorption coefficient (α), h the Plank constant ($6.626 \cdot 10^{-34}$ J·s), ν the photon frequency in s^{-1} , C a constant and E_g the bandgap energy. For direct allowed optical transition the exponent is set to $n = \frac{1}{2}$, while for indirect transitions is set to $n = 2$. The E_g was determined as intercept plotting $(f(R_\infty)h\nu)^{1/n}$ vs $h\nu$ [45].

$$f(R_\infty)h\nu = C(h\nu - E_g)^n$$

Equation 2. Tauc relation.

The Urbach energy (E_U), related to the density of states of defects [46], was assessed by the Urbach relation (Equation 3), where $f(R_\infty)$ is used in place of the optical absorption coefficient (α), h the Plank constant ($6.626 \cdot 10^{-34}$ J·s), ν the photon frequency in s^{-1} , α_0 and E_0 are temperature-dependent constants.

$$f(R_\infty) = \alpha_0 \exp\left(\frac{h\nu - E_0}{E_U}\right)$$

Equation 3. Urbach relation.

The E_U is assessed from the near absorption-edge slope of $\ln(\alpha)$ vs $h\nu$ [47].

The optical emission (photoluminescence, PL) was measured at r.t. using a Fluorolog F2 Horiba/ Jobin-Yvon spectrofluorometer in the 350-750 nm range, using a 320 nm excitation source.

The surface functional groups were evaluated through Fourier-transform IR (FTIR) spectroscopy using attenuated total reflectance (ATR), by means of a Bruker Vertex 70 spectrophotometer equipped the Harrick MVP2 ATR cell, with resolution 4 cm⁻¹.

2.3.1. SOAP CHARACTERIZATION

The optical absorbance of Aleppo soap was measured by dissolving the soap in milliQ water (0.5 g·L⁻¹), and the resulting solution was analyzed with a Cary100 UV-vis spectrophotometer (Agilent).

The functional groups were evaluated through Fourier-transform IR (FTIR) spectroscopy, dispersing the sample in a KBr pellet, by means of a Bruker Vertex 70 spectrophotometer equipped the Harrick MVP2 ATR cell, with resolution 4 cm⁻¹.

The metal content (Fe and Cu) was analyzed by means of inductively-coupled plasma mass spectrometry (ICPS-MS), using a Perkin-Elmer ICP NexION 350X instrument. The sample was first digested with concentrated HNO₃ and H₂O₂ in Ethos 1600 (Milestone) microwave oven. Before the analysis, the sample was diluted with milliQ water and an internal standard aqueous solution (Re) was added. The metal concentration was quantified by means of calibration curves from standard Cu and Fe solutions.

2.4. PHOTOACTIVITY ASSESSMENT

2.4.1. SELF-CLEANING PHOTOACTIVITY ON MARMORINO

The photocatalytic self-cleaning properties of the modified *marmorino*, were assessed using methylene blue (MB), usually involved as model staining compound [48]. Since a superficial top-coating (i.e. soaps, waxes or lime water) is usually applied on the surface of this material as protective overlayer [41] some samples were coated with Aleppo soap, which is made by the saponification of olive and laurel berry oil. The coating procedure relied on the brushing of 2.5 mL of a 20 g·L⁻¹ aqueous solution of Aleppo soap, on some of the *marmorino* samples and dried at r.t. for 18 h in dark.

The MB was applied on both bare or Aleppo-coated samples by brushing 0.5 mL of a 0.56 mM aqueous solution of MB and air-dried at r.t. for 3 h (Figure 6, steps 1 and 2). The stained samples were covered with a black paperboard mask, equipped with three well-spaced circular holes (20 mm diameter) as probing spots and irradiated with a 42 W Lexman halogen table lamp (Figure 6, step 3). The lamp emission spectrum, compared to the absorption band of MB, is reported in Figure S1. The light intensity was set to 140 W·m⁻², and measured with a Delta Ohm HD 2302.2 photoradiometer and a LP 471 probe for visible (400-1000 nm) light irradiation, and. The dye bleaching was evaluated through colorimetric analysis (Figure 1, step 4) [38,49]

each 30 minutes using a Konica Minolta CM-2006d portable colorimeter with D65 standard illuminant and specular component excluded (SCE), recording the b^* parameter (yellow-to-blue coordinate).

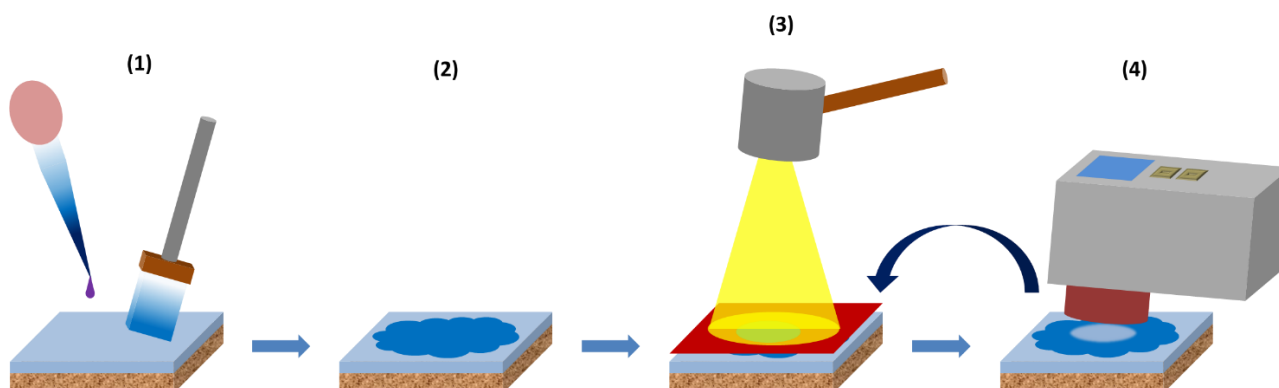


Figure 6. Procedure scheme for dye application and photodegradation assessment.

The dye degradation was probed each 30 min for 3 h, and reported as dye degradation percentage (Equation 4), where $b^*(t_0)$ is the b^* value of the stained surface before starting the self-cleaning, $b^*(0)$ before the staining with the dye and $b^*(t)$ after a given time t .

$$\% MB \text{ degradation} = \frac{b^*(t_0) - b^*(t)}{b^*(0) - b^*(t_0)}$$

Equation 4. Determination of dye degradation.

2.4.2. LIQUID PHASE DYE PHOTODEGRADATION

The dye degradation was evaluated in the liquid phase using a lab-made equipment. A 0.056 mM aqueous solution of MB (100 mL), was put in a crystallizing dish and top-irradiated at r.t. with a 42 W Lexman halogen table lamp, with a $170 - 240 \text{ W} \cdot \text{m}^{-2}$ light intensity, probed through a Delta Ohm HD 2302.2 photoradiometer and a LP 471 probe for visible light (400-1000 nm). The reaction was monitored by sampling 2 mL of solution each 30 minutes for 3 h and analyzed through a UV-vis Cary100 spectrophotometer (Agilent), in the 400-800 nm range. The results were graphed as A/A_0 vs time, where A is the maximum absorbance at a given time, and A_0 is the absorbance at $t = 0$.

The photoactivity was assessed with different additives in the MB aqueous solution, as summarized in Table 2.

Table 2. Composition of the liquid reaction mixture. All the blends contains 0.056 mM of MB.

Test	Aleppo soap (g·L ⁻¹)	Sodium oleate (g·L ⁻¹)	Gallic acid (mM)	Iron (III) nitrate (mM)
Blank	-	-	-	-
Aleppo soap	5.0	-	-	-
Oleate	-	5.0	-	-
GA	-	-	3	-
Oleate + GA	-	5.0	3	-
Fe	-	-	-	3
Oleate + Fe	-	5.0	-	3

3. RESULTS AND DISCUSSION

3.1. MATERIALS CHARACTERIZATION

The XRD analyses (Figure 7a) revealed all the samples to contain portlandite (Ca(OH)_2 , ICDD PDF card no. 05-0586) and calcite (CaCO_3 , ICDD PDF card no. 01-1079), as expected since the raw materials used in *marmorino* formulation. The TiO_2 -modified materials, namely M-COM-Ti and M-LAB-Ti, exhibited in both case a weak peak at 25° , corresponding to the (101) reflection plane of anatase (TiO_2 , ICDD PDF card no. 21-1272), and being more sharper in M-COM-Ti pointing out an higher crystallinity of TiO_2 in such sample. On ZnO-modified materials, two phase were detected: zincite (ZnO , ICDD PDF card no. 36-1451) and calcium zinc hydroxide ($\text{CaZn(OH)}_6 \cdot 2\text{H}_2\text{O}$, ICDD PDF card no. 24-0222), labelled as CZH and known to arise from the reaction of ZnO in a strongly Ca-based alkaline medium [50]. The amount and the crystallite size of the Zn-base phases changed depending on the starting material, as summarized in Table 3. The ZnO crystallites size resulted narrower in the case of lab-made materials added to *marmorino* (M-LAB-Zn and M-LAB-TiZn). On M-LAB-TiZn, no TiO_2 peaks were observed, suggesting its higher dispersion and/or amorphous nature within the matrix, but played a role in the partial protection of ZnO against alkaline corrosion, due to the higher amount of this phase and the lower concentration of CZH.

Table 3. Amount and average crystallite size of ZnO and CZH in ZnO-modified *marmorino*.

Sample	CZH wt. %	CZH crystallite size (nm)	ZnO wt. %	ZnO crystallite size (nm)
M-COM-Zn	54	2200	11	40
M-LAB-Zn	49	4900	11	18
M-LAB-TiZn	13	6200	15	19

The N_2 physisorption analyses (Figure 7b) evidenced the presence of a hysteresis loop at $P/P^0 > 0.6$ and ending up at $P/P^0 = 1$, indicating the presence of both macro and mesopores in all the materials. The specific surface area (SSA) is observed to be higher for TiO_2 -modified samples compared to the unpromoted one: $8 \text{ m}^2/\text{g}$, $17 \text{ m}^2/\text{g}$, $25 \text{ m}^2/\text{g}$ for M, M-COM-Ti and M-LAB-Ti, respectively. Conversely, all ZnO-promoted *marmorino* exhibited no differences compared to the bare one. This suggested TiO_2 materials to partially change the *marmorino* microstructure, while ZnO has no effect.

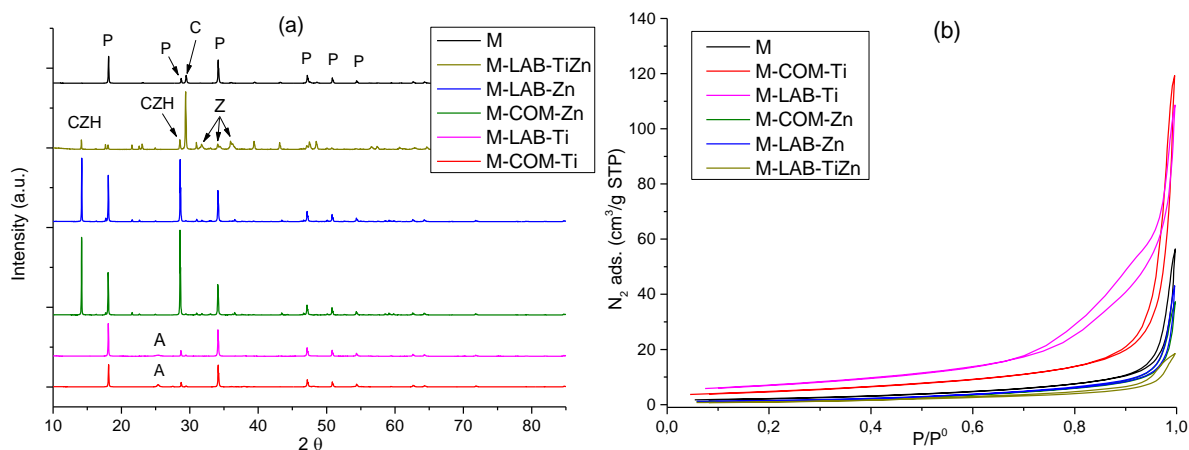


Figure 7. (a) XRD diffractograms and (b) N_2 physisorption isotherms of marmorino-based samples. Crystal phases: P = portlandite [$Ca(OH)_2$], C = calcite [$CaCO_3$], A = anatase [TiO_2], CZH = calcium hydroxyzincate hydrate [$CaZn_2(OH)_6 \cdot 2H_2O$], Z = zincite (ZnO).

The bare *marmorino*, M, was composed of roughly globular micrometer-sized particles (Figure 8a) and contained Ca and O (Figure 8b), as evidenced by the EDX spectrum, uniformly composing such particles (Figure 8c).

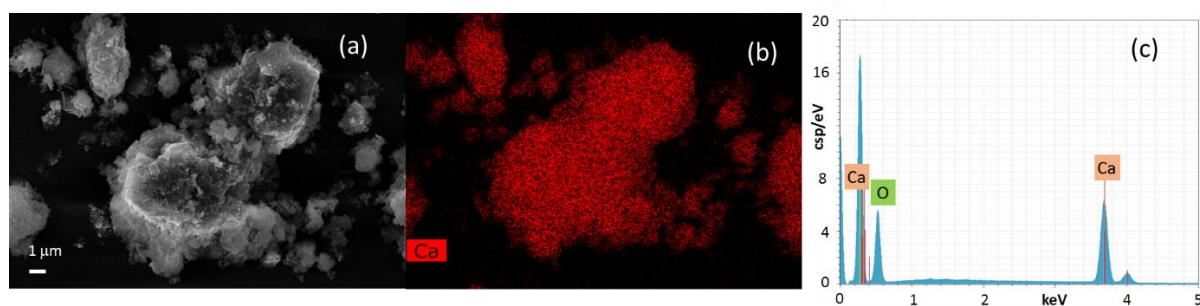


Figure 8. (a) SEM image, (b) Ca EDX elemental mapping and (c) EDX spectrum of bare *marmorino* (M).

The TiO_2 -modified samples exhibited a slightly different morphology. M-COM-Ti revealed tiny TiO_2 particles quite uniformly coating the surface of *marmorino* globular ones (Figure 9a, Figure 9b and Figure 9c). On M-LAB-Ti, on the contrary, some dense micrometer-sized polyhedral particles of almost pure TiO_2 were observed (Figure 9d, Figure 9e and Figure 9f).

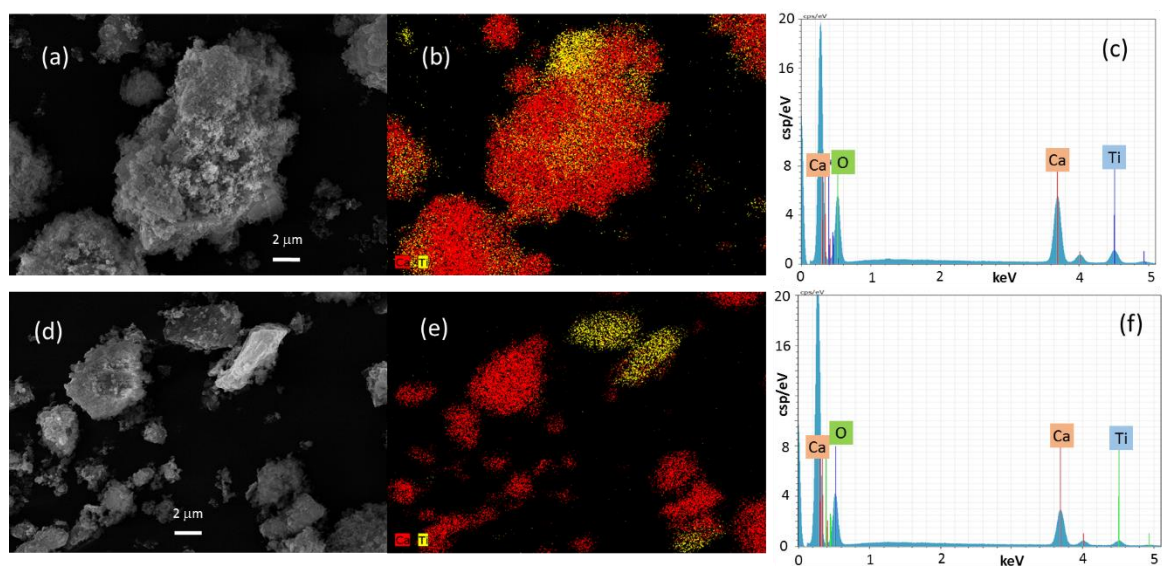


Figure 9. (a) SEM image, (b) Ca and Ti EDX elemental mapping, (c) EDX spectrum of M-COM-Ti. (d) SEM image, (e) Ca and Ti EDX elemental mapping, (f) EDX spectrum of M-LAB-Ti.

The ZnO-modified materials contained micrometer-sized triangular-shaped particles (Figure 10a, Figure 10b and Figure 10c). Lozenge-like morphology, that have been previously ascribed to the CZH phase [51], thus it was suggested the observed triangular particles to be fragments of lozenge ones. The plate-like shape is also consistent with the strong preferred orientation exhibited by the CZH phase on the XRD patterns. From the elemental mapping, Ca was found in Zn-rich zones (Figure S2 and Figure S3), further supporting the formation of the CZH phase. On M-LAB-TiZn, TiO₂ was observed to be heterogeneously dispersed over the particles, affording some Ti-rich spots (Figure S3d). These spots are overlapped by Zn-rich region, and this could further support the protective role of TiO₂ against ZnO alkaline corrosion.

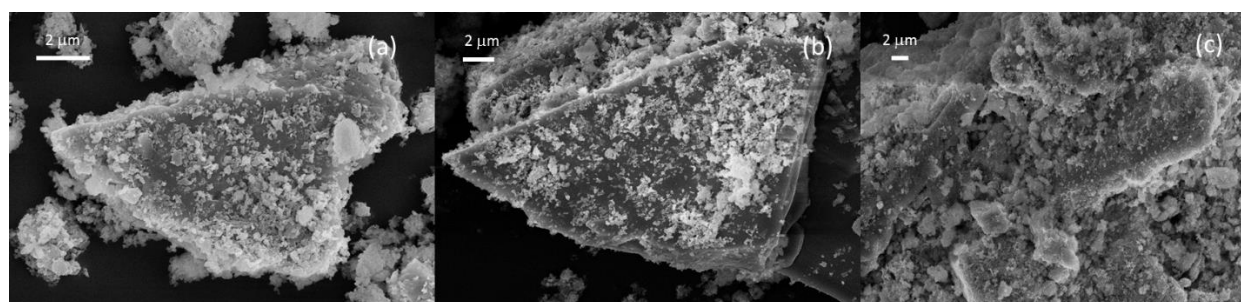


Figure 10. SEM images of (a) M-COM-Zn, (b) M-LAB-Zn and (c) M-LAB-TiZn.

The ZnO-modified samples exhibited a quite comparable morphology and composition, and further spectroscopic characterization were performed to highlight some more differences.

The surface moiety were evaluated by means of FTIR spectroscopy (Figure 11a). The bare *marmorino* (M) exhibited the signals ascribable to calcite (CaCO₃), in particular the carbonate stretching modes at 1410 cm⁻¹ (asymmetric ν₃), 872 cm⁻¹ (asymmetric ν₂), and 712 cm⁻¹ (symmetric ν₄) [52,53]. The signal at 3644 cm⁻¹ (O–H stretching in Ca–OH moiety, ν_{CaOH}), was ascribed to portlandite (Ca(OH)₂), while the on ZnO-modified

materials some new signals at in the low-wavenumber region can be related to the CZH phase. In details, the peak at 564 cm^{-1} , was ascribed to Zn–O vibrations in $\text{Zn}(\text{OH})_4^{2-}$ units ($\nu_{\text{Zn-O}}$), and the peak at 1065 cm^{-1} , ascribed to hydroxyl bending mode in Zn–OH moiety (δ_{ZnOH}) [54].

Some more differences concerning the surface composition can be drawn from the high-wavenumber region (Figure 11b): the bands at 2895 , 3020 and 3170 cm^{-1} were assigned to stretching modes of OH moiety involved in H-bonding, and were virtually absent on bare *marmorino* surface, pointing out a surface poorer in hydroxyl groups. The two bands at 3616 cm^{-1} and 3490 cm^{-1} on ZnO-modified samples were attributable to bridges hydroxyl modes of Ca–OH–Zn and Zn–OH–Zn respectively [54], and could be related to the CZH surface. Comparing these two modes with that of portlandite (ν_{CaOH}), the CZH/ $\text{Ca}(\text{OH})_2$ intensity ratio decreased in the order: M-LAB-Zn > M-COM-Zn > M-LAB-TiZn. These observations suggested a different amount on CZH to compose the surface: the richest one on M-LAB-Zn, decreasing on M-COM-Zn due to a partial coverage by $\text{Ca}(\text{OH})_2$, and further decreasing on M-LAB-TiZn. On the latter, the presence of superficial TiO_2 nanoparticles (NPs) “masking” the CZH surface, cannot be totally excluded.

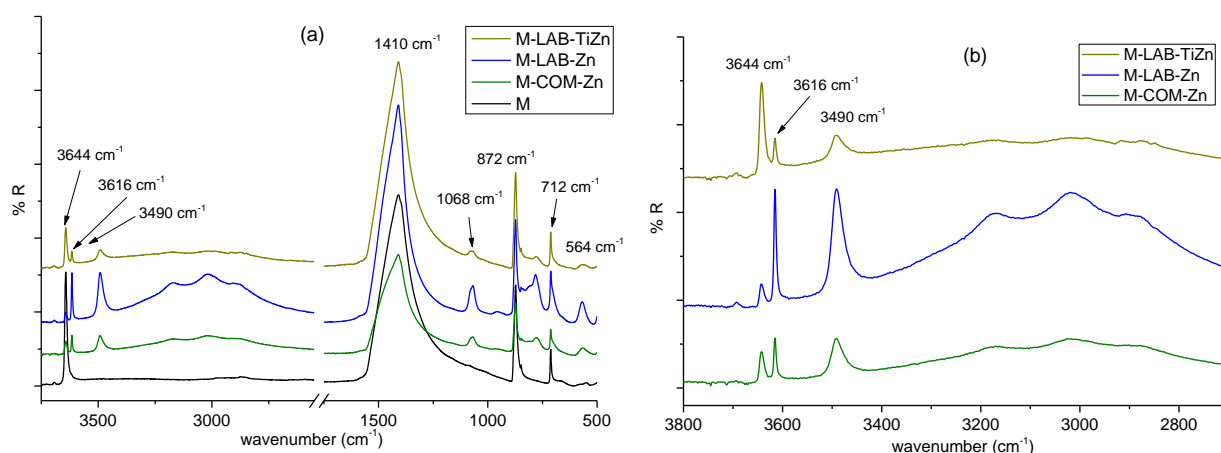


Figure 11. (a) ATR spectra of M and ZnO-modified materials and (b) high-wavenumber region of ZnO-modified material ATR spectra.

The absorption optical properties were evaluated through DRS. The reflectance spectra of ZnO-modified samples (Figure 12), revealed the absence of features in the visible range ($\lambda > 400\text{ nm}$), while a sharp edge appeared in the UV range ($\lambda < 400\text{ nm}$). This supported the presence of wide-bandgap SCs that did not alter the aesthetic value of *marmorino*. Different materials previously detected, however, could contribute to the UV adsorption edge: TiO_2 and ZnO, as shown in Chapter 1 and 3, as well as CZH [51].

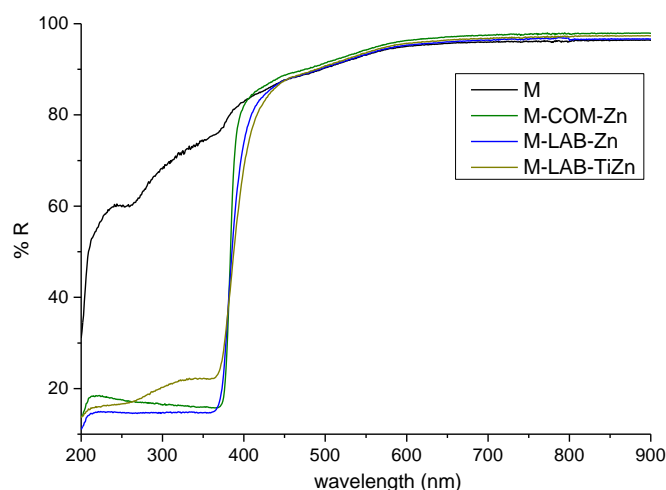


Figure 12. UV-vis reflectance spectra of M and ZnO-modified materials.

The E_g extrapolated from Tauc plots analysis (Figure S4a) and listed in Table 4, are almost comparable for all the ZnO-modified materials. More relevant differences were observed through the Urbach plots analysis (Figure S4b). The E_U value is usually related to the density of intra-gap states [55] and was observed to decrease in the order M-LAB-TiZn > M-LAB-Zn > M-COM-Zn (Table 4). Comparing M-COM-Zn with M-LAB-Zn, the lowest density of such states on the former, could be ascribed both to the larger amount of Zn–OH moiety on the latter and the narrower ZnO NPs, evidenced by XRD analysis, which in turn improving the ZnO/CZH interface. Both the superficial Zn–OH groups and the ZnO/CZH interface was thus supposed to originate such intra-gap states. On M-COM-Zn, the presence of larger ZnO crystallites and an insulating $\text{Ca}(\text{OH})_2$ overlayer supposed to passivate the Zn–OH moiety, were likely to decrease the intra-gap states density. On M-LAB-TiZn, the narrow and abundant ZnO NPs and the presence of TiO_2 NPs were likely to increase the interfaces among the SC materials (ZnO, TiO_2 and CZH), eventually enhancing the amount of surface states.

Table 4. E_g and E_U values for ZnO-modified samples.

Sample	E_g (eV)	E_U (meV)
M-COM-Zn	3.26	29
M-LAB-Zn	3.26	57
M-LAB-TiZn	3.25	80

Further differences were found on the optical emission of the ZnO-modified materials. As reported in Figure 13, both the intensities and the position of the emission bands changed. M-COM-Zn exhibited the a peak at $\lambda < 400$ nm, which is defined as the near band-edge emission (NBE) due to a direct E_c -to- E_v relaxation of photoexcited electrons [56]. The strong band in the visible region centred at 520 nm (green emission), was ascribable intra-gap defects states [57]. M-LAB-Zn exhibited a strong decrease in the emission intensity along

with a redshift of the band to yellow emission (568 nm), while M-LAB-TiZn experienced a further luminescence quench of such band. Both M-LAB-Zn and M-LAB-TiZn, had no NBE.

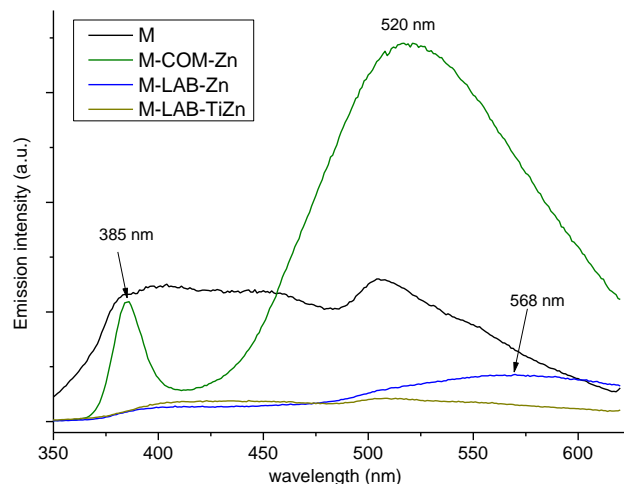


Figure 13. Photoluminescence spectra ($\lambda_{\text{exc}} = 320 \text{ nm}$) of M and ZnO-modified materials.

On M-COM-Zn, the surface $\text{Ca}(\text{OH})_2$ layer was supposed to act as insulating layer blocking the excited charge carriers flow [58], and allowing them to recombine in sub-surface defects (Figure 14a). Furthermore, the presence of large ZnO crystallites within this material, was hypothesized to induce the observed NBE [57], as already observed in Chapter 2. Moving to M-LAB-Zn, the presence of a Zn–OH-rich surface and the larger ZnO/CZH interface were supposed to reduce the radiative recombination. This was suggested to arise, respectively, from surface trapping of excited charge carriers on hydroxyl moiety with a subsequent non-radiative relaxation [59] (Figure 14b) and interfacial charge carriers separation at the ZnO/CZH interface (heterojunction) [60], which was enhanced due to the narrower ZnO NPs. The redshift of the emission band was ascribed to the radiative recombination phenomena occurring at the surface of CZH, likely on some Zn–OH sites, contrary to the sub-surface one occurring on M-COM-Zn: probably, different types of defect states were involved in these transitions. Finally on M-LAB-TiZn, despite the $\text{Ca}(\text{OH})_2$ -rich insulating surface, the further quench in the luminescence, in particular the yellow band, was ascribed to heterojunctions formation on a large extent. Indeed, the ZnO/CZH interface was supposed to be enlarged due to the higher ZnO/CZH wt. ratio (Table 3), while the presence of TiO_2 afforded new interfaces with both ZnO and CZH, further contributing to the interfacial charge carriers separation and consequent quench in the luminescence (Figure 14c) [60].

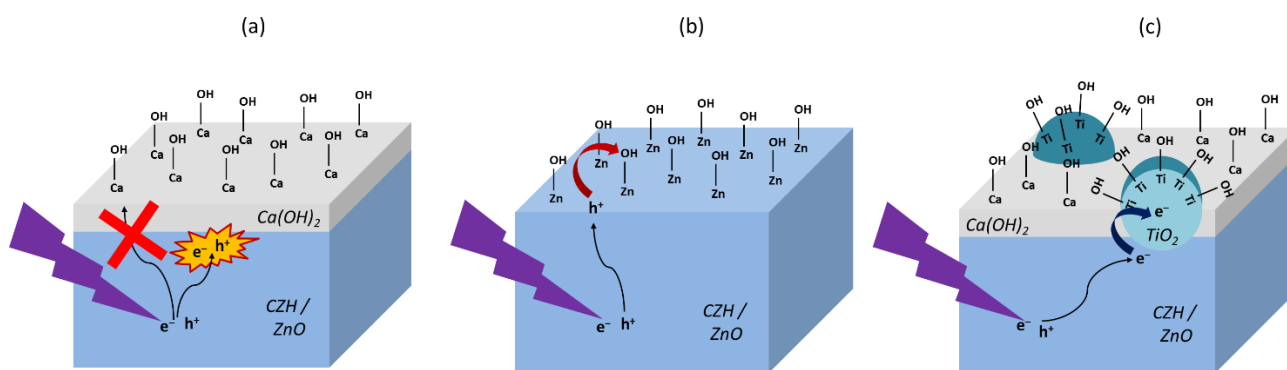


Figure 14. Schemes of photoexcited charge carriers recombination processes on (a) M-COM-Zn, (b) M-LAB-Zn and (c) M-LAB-TiZn. CZH/ZnO interfaces were neglected for simplicity.

Summarizing this section, the addition of TiO₂ materials within the *marmorino* formulation, had an effect in the structural properties, increasing the porosity of the plaster, while preserving the anatase phase. On the contrary, the addition of ZnO did not enhance the SSA, but a partial reaction of the photocatalyst with the Ca(OH)₂ afforded a new phase, namely CZH. More differences in term of surface and optical properties were observed on ZnO-modified *marmorino*, depending on the type of added ZnO (M-COM-Zn, M-LAB-Zn or M-LAB-TiZn). These features eventually affect the photoexcited charge carrier recombination processes, due to the presence of heterojunctions or surface insulating layers.

3.2. PHOTOCATALYTIC SELF-CLEANING ACTIVITY ASSESSMENT

The photocatalytic materials were added within the *marmorino* (upper layer) because the higher reported stability against physical detachment of the catalyst [27]. The photocatalytic self-cleaning was then evaluated using a model molecule, namely methylene blue (MB), which mimicked a stain deposit over the surface. Under irradiation, the bare surfaces (Figure 15a) gave a comparable performance with the bare *marmorino*, able to remove up to 20% of the dye after 4 h. Only one sample, M-LAB-TiZn, allowed an almost doubled efficiency in dye removal, with 40% dye degradation after 4 h.

Since a protective top-coating is usually used in traditional *marmorino* once applied on a wall, a natural soap (Aleppo soap) was used and compared to the bare surface. As reported in Figure 15b, an improved efficiency in dye bleaching was obtained upon using the soap top-coating, even for the un-promoted *marmorino* (ca. 47% dye removal). Two samples experienced a further enhancement: M-LAB-Zn and M-LAB-TiZn, which were able to degrade 78% and 100% of the loaded dye in 4 h, respectively.

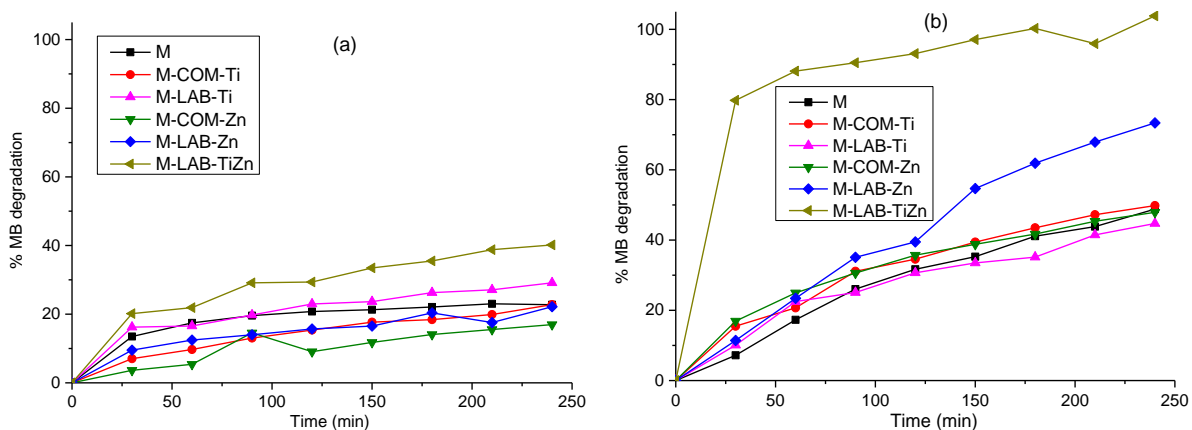


Figure 15. Photocatalytic self-cleaning with visible-light of bare and photocatalyst-modified *marmorino* on (a) bare surfaces and (b) Aleppo soap top-coated surfaces.

Both TiO_2 -modified samples (M-COM-Ti and M-LAB-Ti), despite the unaltered anatase phase detected within the formulation and the enhancement of the SSA of the material, experienced no remarkable enhancement on self-cleaning activity, either with or without the soap top-coating. The improved porosity of these materials probably inhibited the light exposure [61] and/or reactant (atmospheric oxygen) mass transfer [62] deep into the *marmorino* layer, in turn negatively affecting the photodegradation of the dye, which penetrate deeply in the material during the staining, but it can be efficiently removed mainly in the outermost layer. A scheme of this hypothesis is represented in Figure 16.

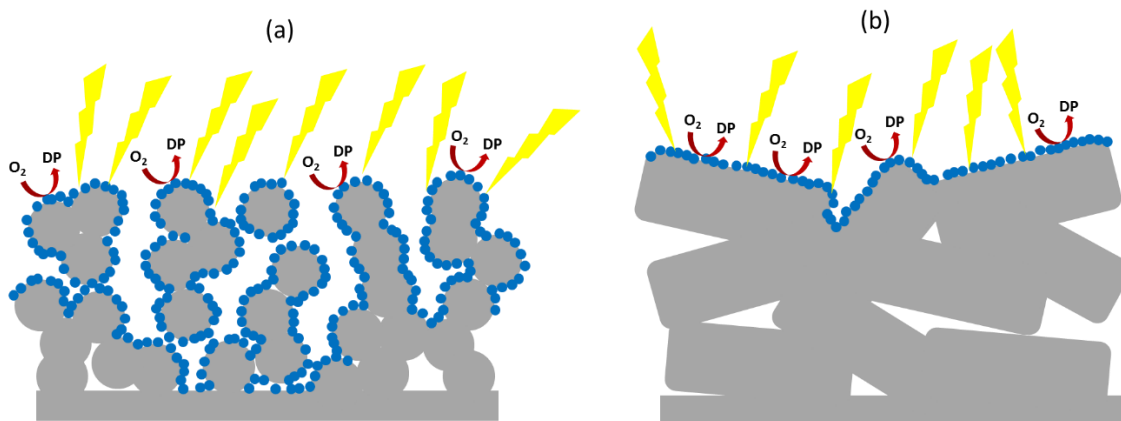


Figure 16. Proposed effect of the porosity on the photodegradation efficiency on (a) TiO_2 -modified (higher SSA) and (b) ZnO -modified (lower SSA) *marmorino*. Blue spots = methylene blue dye; DP = degradation products.

ZnO -modified materials revealed a different behaviour. The superior performances of M-LAB-TiZn, with or without the soap top-coating, were ascribed to the multiple heterojunction within this material (ZnO/CZH , ZnO/TiO_2 and CZH/TiO_2), allowing a more efficient charge carriers interfacial separation and harvesting, in turn boosting up the reaction [60]. M-LAB-Zn exhibited an improved performance compare to the reference sample, M, only when using the soap top-coating. The hydroxyl-rich semiconductive surface (CZH) of this sample probably hinder the photoactivity by trapping the excited charge carriers [63], but, upon using the soap, a passivation of these detrimental OH group was supposed to occur, making the semiconductive

surface active toward the dye degradation. On M-COM-Zn the $\text{Ca}(\text{OH})_2$ insulating overlayer was hypothesized to hinder surface charge transfer process, resulting in no enhancement of the photoactivity.

The soap top-coating had a remarkable effect in enhancing the self-cleaning activity, and to shed light in the reason of such improvement, the Aleppo soap was first characterized.

The FTIR spectra (Figure 17a) revealed the presence of aliphatic C–H stretching vibration ($\nu_{\text{C-H}}$) at 2955 cm^{-1} , 2918 cm^{-1} and 2850 cm^{-1} , as well as the bending vibrations ($\delta_{\text{C-H}}$) at 1462 and 1455 cm^{-1} . The carboxylate (COO^-) group was ascribed to the band at 1558 cm^{-1} and 1423 cm^{-1} . The large band at $\nu > 3000\text{ cm}^{-1}$ was ascribed to water within the sample, while unsaturated C=C bonds, pointing out the presence of unsaturated fatty acids, were suggested due to the weak band at 3008 cm^{-1} and the shoulder at ca. 1650 cm^{-1} [64]. The spectra resembled those reported in literature for sodium oleate [65], likely to be the main component of the soap. The UV-vis spectra (Figure 17b) revealed an intense band in the UV region at $\lambda < 250\text{ nm}$, which is ascribable to the carboxylic moiety of the soap [66]. A shoulder at higher wavelength (ca. $\lambda = 275\text{ nm}$) was observed in sodium oleate reference and, especially, in Aleppo soap where it end up at ca. 450 nm . This feature can be ascribed to electronic transitions of polyunsaturated molecules such as polyphenols, usually contained in the olive oil used for Aleppo soap manufacturing [67].

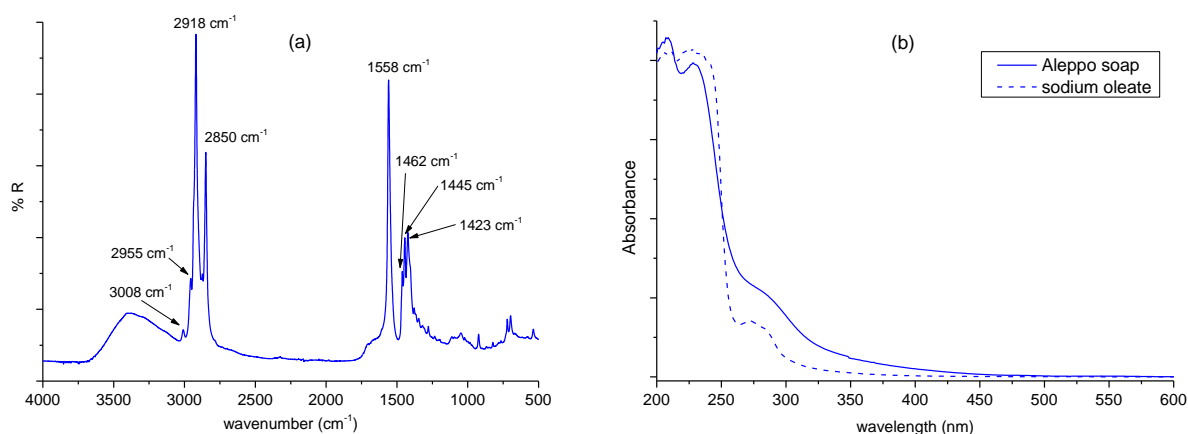


Figure 17. (a) FTIR spectrum of solid Aleppo soap; (b) UV-vis absorption spectra of $5.0\text{ g}\cdot\text{L}^{-1}$ Aleppo soap aqueous solution (straight line) compared with a $5.0\text{ g}\cdot\text{L}^{-1}$ sodium oleate aqueous solution (dashed line).

Besides the organic constituents, the vegetable oils used as raw materials for soap manufacturing usually contains transition metal ions such as iron (Fe) and copper (Cu) [68], which are known to be active as redox catalysts in oxidation reactions [69,70]. These metals were thus analyzed through ICP-MS, finding both Fe ($0.202\text{ g}\cdot\text{kg}^{-1}$) and Cu ($0.016\text{ g}\cdot\text{kg}^{-1}$) within the Aleppo soap used for this work.

Some photodegradation tests of MB in liquid phase were then carried out (Figure 18), as described in Section 2.4.2, aiming a better understanding of the soap's role. Aleppo soap (black line, Figure 18) was observed to be able to bleach MB even in solution. The pure sodium oleate (blue line, Figure 18) was even more active than Aleppo soap. Next, attempting to mimic the natural soap composition, a test with oleate and a model

polyphenol compound (gallic acid or GA), was carried out (green straight line, Figure 18). The MB photodegradation kinetic was slower than the pure oleate, due to the well-known anti-oxidant activity of phenol derivatives [71], but was similar to Aleppo soap, pointing out a detrimental role of these compounds in MB bleaching. The effect of a metal salt (Fe^{3+}) was also evaluated: in this case, a faster photodegradation kinetics was obtained (red straight line, Figure 18), in agreement with the well-known activity as redox catalyst. However, it is worth to remind that the used amount of Fe (3 mM) was two magnitude order higher than the Fe from dissolved soap (ca. 0.01 mM): this ruled out the role of redox active metal ions in the MB degradation enhancement. Both GA and Fe^{3+} without oleate (dashed green and red lines, respectively), had no remarkable effect in MB photodegradation.

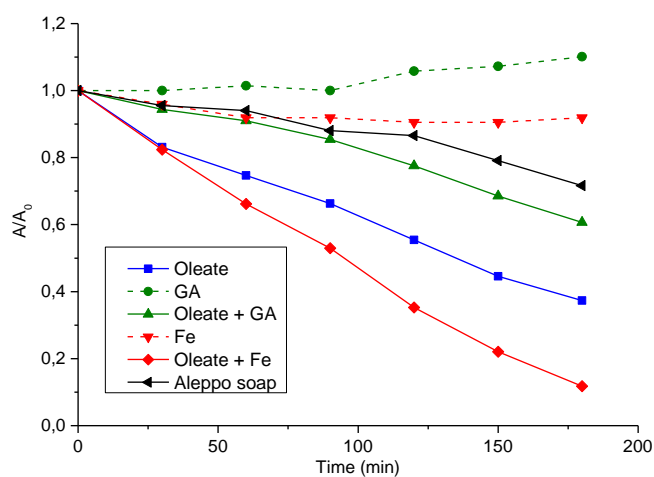


Figure 18. Liquid-phase MB photodegradation tests. GA = gallic acid; Fe = iron (III) nitrate. The pure MB solution was stable against photodegradation (not shown).

These liquid-phase tests suggested oleate, the main component of Aleppo soap, to be the responsible of the enhancement of photodegradation ruling out the effect of transition metal ions.

The anionic surfactant (sodium oleate) was supposed to have to different effect. An electrostatic interaction between the positively charged dye and the negatively charged surfactant occurred in both solution and air/solid interface of *marmorino*, leading however to two different effect. Indeed, a remarkable improvement of actual dye concentration, due to the adsorption on micelles surface, was hypothesized to occur in solution experiments [72], while a better dispersion of the dye at air/solid interface, due to the well known ability of surfactant-modified oxides to adsorb dyes [73], was supposed. In both cases, the final effect was likely to be a better exposure of the dye to the incoming light.

Beside this physical effect, also a chemical one was hypothesized. Indeed, anions are known to enhance the charge carrier separation in solar cells, by interaction with excited holes [74]. Similarly, it can be supposed

the anionic carboxylate head of the oleate to stabilize the holes, allowing a facile transfer of photoexcited electrons to the acceptor (O_2) or to the semiconductors, and limiting the charge carriers recombination.

The mechanism of self-cleaning reported in this study, relied on the excitation of the dye under visible light irradiation, which thus act both as reactant and photosensitizer (or light harvester) [75]. In details (Figure 19), the methylene blue adsorbed a photon yielding an excited state (item 1). In the presence of a suitable SC material (M-LAB-Zn or M-LAB-TiZn), the photoexcited electron was extracted by the SC (CZH, ZnO and/or TiO_2) (item 3), and potentially being further transferred from a SC to another thanks to heterojunctions (not shown in the picture). The excited electron then underwent a surface charge transfer process that reduced the adsorbed molecular O_2 to reactive oxygen species (ROS) such as $O_2^{\cdot-}$, H_2O_2 and HO^{\cdot} (item 4), which were finally involved in the oxidative degradation of the dye. The excited hole left on the dye, was supposed to be stabilized, or transferred, by the anionic carboxyl moiety of the surfactant (item 2).

If no suitable SC were present, like in the case of bare *marmorino*, a direct electron transfer from excited MB to O_2 occurred and was hypothesized to be assisted by the anionic surfactant, which stabilized the excited holes and, somehow, could push the excited electron away. This mechanism allowed the soap to enhance the dye bleaching even in the absence of SCs.

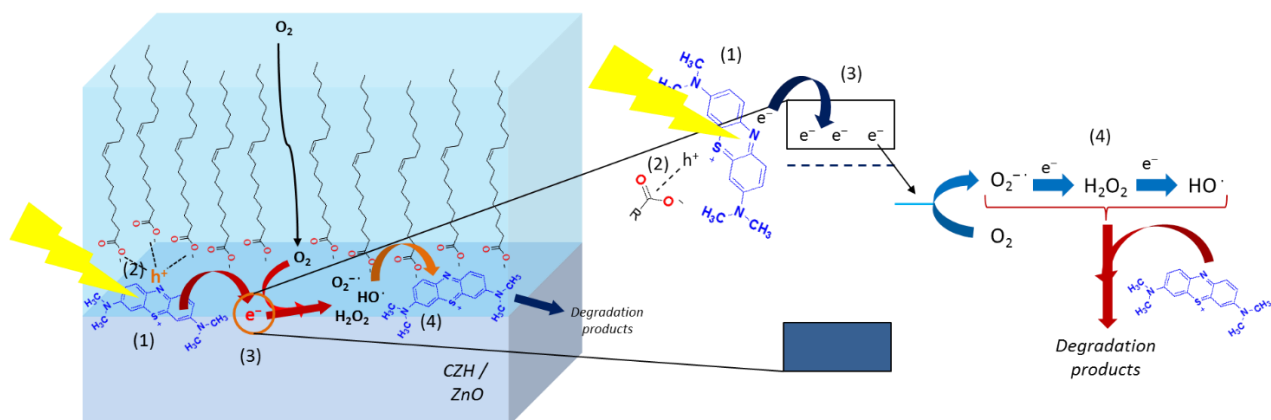


Figure 19. Soap-assisted photodegradation mechanism on ZnO-modified marmorino. TiO_2 was not reported for simplicity.

Summing up this section, the structural and surface feature of the prepared materials were observed to have a huge impact on the photocatalytic self-cleaning properties. The improved SSA of TiO_2 -modified materials was unuseful for the activity enhancement, probably limiting an efficient light exposure and/or oxygen mass transfer phenomena. On ZnO-modified materials the surface played an important role in determining the photoactivity: an insulating surface or a hydroxyl-rich one hindered the self-cleaning, probably by inhibiting the surface charge-transfer processes or boosting the charge trapping, respectively. The presence of semiconductive phase on the surface, as well as a large amount of heterojunctions, improved the dye photodegradation due to a more efficient charge transfer process, on the surface and at SC/SC interfaces.

The soap top-coating, traditionally used as protective layer for *marmorino*, revealed a remarkable effect in enhancing the self-cleaning activity, even without a photocatalyst in the formulation. Its effect was hypothesized to arise, on one side to a better exposure of the dye to the incoming light, on the other to the stabilization of excited holes by the anionic carboxylate moiety. On two sample, a synergistic effect between the soap and the SC was observed, reaching an almost complete dye removal on the best one (M-LAB-TiZn).

Finally, the overall mechanism did not rely on the direct excitation of the SC, acting as a “traditional” photocatalyst, rather through a photosensitization by the dye itself, which act both as reactant and light harvester. Nevertheless, a material with good photo-induced self-cleaning ability was obtained in this work, opening the way to further studies such as the long-term stability assessment, or the evaluation of the activity under different light source (i.e. solar or UVA) and using different stains.

4. CONCLUSIONS

In this work, the traditional Venetian *marmorino* formulation was modified with ZnO and TiO₂-based photocatalyst, in collaboration with Uni.S.Ve company (Venice, Italy), and the photocatalytic self-cleaning properties of these modified materials were assessed. In details:

1. The addition of TiO₂ has a notable effect in enhancing the porosity of the *marmorino*, while ZnO affect mainly the surface properties. On M-COM-Zn, where a benchmark ZnO was used, a Ca(OH)₂-rich insulating surface was achieved, while when a lab-made ZnO was used (M-LAB-Zn), an hydroxyl-rich semiconductive surface was obtained. Modifying the lab-made ZnO with TiO₂, afforded a material with a TiO₂-decorated surface and a large amount of heterojunctions.
2. The photocatalytic self-cleaning properties did not take advantages of the high porosity, probably due to light and mass transfer limitations. No activity enhancement was also observed on ZnO-modified material if insulating-rich (M-COM-Zn) or hydroxyl-rich (M-LAB-Zn) surfaces were present, likely because hampering the charge transfer processes or improving the charge carriers trapping, respectively. Surface TiO₂ SC NPs and improved interfaces between the SCs, were supposed to boost up the charge carriers transfer, and thus the dye blanching.
3. The soap top-coating exhibited a remarkable improvement in dye removal, even without any SC. This effect was ascribed on one side to the better dye exposure to the incoming light, on the other side to a stabilization effect on the excited holes due to the anion moiety of the surfactant. In two cases, a synergistic soap-SC effect was found, achieving an activity surface able to completely bleach the dye in less than 4 h.
4. A mechanism of the self-cleaning was finally proposed. The light was absorbed by the dye itself, acting thus as both photosensitizer and reactant, transferring the excited electrons to the SC(s), finally affording O₂ reduction to ROS, which were involved in the oxidative degradation of the dye. On the other side, the excited holes on the dye molecules were stabilized by the surfactant, further improving the charge separation efficiency.

5. SUPPLEMENTARY INFORMATION

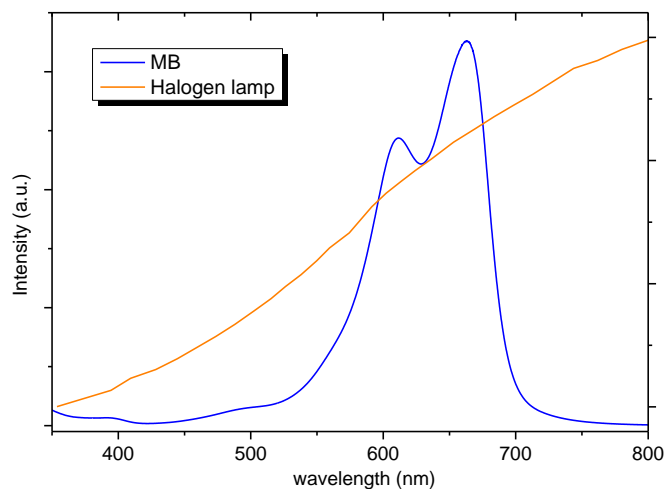


Figure S1. Emission spectra of the halogen lamp (orange line), compared with the absorption spectrum of MB (0.056 mM aqueous solution). The spectra intensities are not in scale.

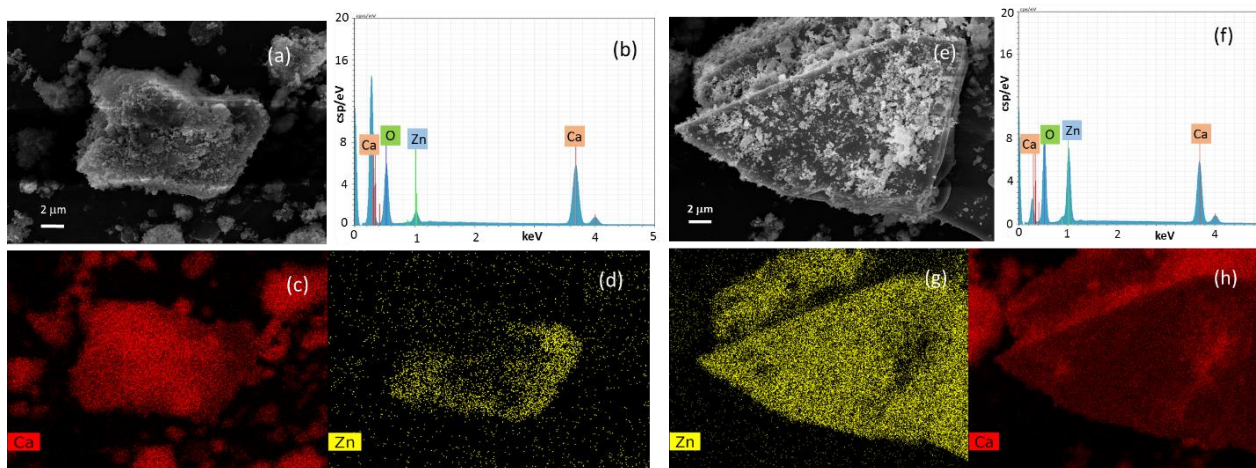


Figure S2. (a) SEM image, (b) EDX spectrum, (c) Ca and (d) Zn elemental mapping of M-COM-Zn. (e) SEM image, (f) EDX spectrum, (g) Ca and (d) Zn elemental mapping of M-LAB-Zn.

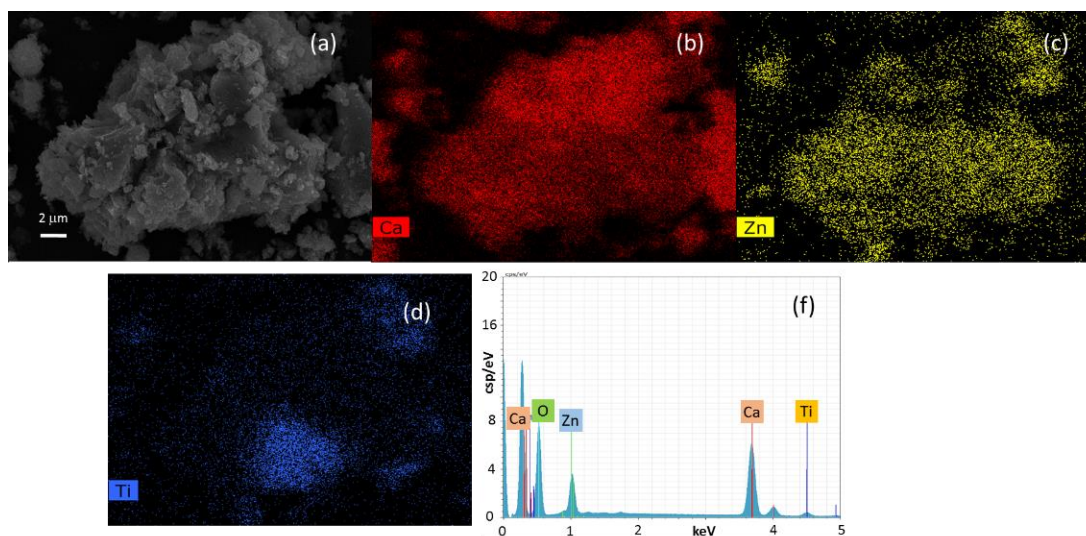


Figure S3. (a) SEM image, (b) Ca, (c) Zn, (d) Ti EDX elemental mapping and (f) EDX spectrum of M-LAB-TiZn.

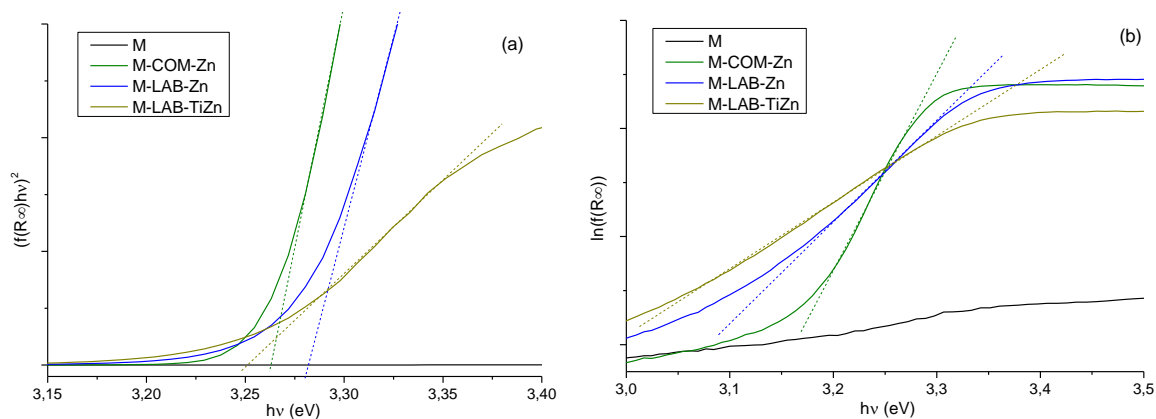


Figure S4. (a) Tauc plots and (b) Urbach plots of M and ZnO-modified materials.

6. REFERENCES

- ¹ N. Tsui, R.J. Flatt, G.W. Scherer, Crystallization damage by sodium sulfate. *J. Cult. Herit.* **2003**, *4*, 109-115, doi:10.1016/S1296-2074(03)00022-0.
- ² C.M. Grossi, P. Brimblecombe, I. Harris, Predicting long term freeze-thaw risks on Europe built heritage and archaeological sites in a changing climate. *Sci. Total Environ.* **2007**, *377*, 273-281, doi:10.1016/j.scitotenv.2007.02.014.
- ³ D. De la Fuente, J.M. Vega, F. Viejo, I. Díaz, M. Morcillo, Mapping air pollution effects on atmospheric degradation of cultural heritage. *J. Cult. Herit.* **2013**, *14*, 138-145, doi:10.1016/j.culher.2012.05.002
- ⁴ P.S. Griffin, N. Indictor, R.J. Koestler, The biodeterioration of stone: a review of deterioration mechanisms, conservation case histories, and treatment. *Int. Biodeterior.* **1991**, *28*, 187-207, doi:10.1016/0265-3036(91)90042-P.
- ⁵ B.J. Smith, M. Gomez-Heras, S. McCabe, Understanding the decay of stone-built cultural heritage. *Prog. Phys. Geogr.* **2008**, *32*, 439-461, doi:10.1177/0309133308098119.
- ⁶ J. Delgado Rodrigues, A.P. Ferreira Pinto, R. Nogueira, A. Gomes, Consolidation of lime mortars with ethyl silicate, nanolime and barium hydroxide. Effectiveness assessment with microdrilling data. *J. Cult. Herit.* **2018**, *29*, 43-53, doi:10.1016/j.culher.2017.07.006.
- ⁷ A. Polo, F. Cappitelli, L. Brusetti, P. Principi, F. Villa, L. Giacomucci, G. Ranalli, C. Sorlini, Feasibility of removing surface deposits on stone using biological and chemical remediation methods. *Microb. Ecol.* **2010**, *60*, 1-14, doi:10.1007/s00248-009-9633-6.
- ⁸ G. Barbera, G. Barone, P. Mazzoleni, A. Scandurra, Laboratory measurement of ultrasound velocity during accelerated aging tests: Implication for the determination of limestone durability. *Constr. Build. Mater.* **2012**, *36*, 977-983, doi:10.1016/j.conbuildmat.2012.06.029.
- ⁹ C. Rodriguez-Navarro, E. Sebastian, Role of particulate matter from vehicle exhaust on porous building stones (limestone) sulfation. *Sci. Total Environ.* **1996**, *187*, 79-91, doi:10.1016/0048-9697(96)05124-8.
- ¹⁰ B. Prieto, D. Vázquez-Nion, E. Fuentes, A.G. Durán-Román, Response of subaerial biofilms growing on stone-built cultural heritage to changing water regime and CO₂ conditions. *Int. Biodeterior. Biodegrad.* **2020**, *148*, 104882, doi:10.1016/j.ibiod.2019.104882.
- ¹¹ O. Farkas, S. Siegesmund, T. Licha, Á. Török, Geochemical and mineralogical composition of black weathering crusts on limestones from seven different European countries. *Environ. Earth Sci.* **2018**, *77*, 1-20, doi:10.1007/s12665-018-7384-8.
- ¹² N. Cutler, H. Viles, Eukaryotic microorganisms and stone biodeterioration. *Geomicrobiol. J.* **2010**, *27*, 630-646, doi:10.1080/01490451003702933.
- ¹³ L.K. Herrera, C. Arroyave, P. Guiamet, S.G. De Saravia, H. Videla, Biodeterioration of peridotite and other constructional materials in a building of the Colombian cultural heritage. *Int. Biodeterior. Biodegrad.* **2004**, *54*, 135-141, doi:10.1016/j.ibiod.2004.06.001.
- ¹⁴ V. Gomes, A. Dionísio, J.S. Pozo-antonio, Progress in Organic Coatings Conservation strategies against graffiti vandalism on Cultural Heritage stones: Protective coatings and cleaning methods. *Prog. Org. Coatings* **2017**, *113*, 90-109, doi:10.1016/j.porgcoat.2017.08.010.
- ¹⁵ La voce del trentino website, available on: <https://www.lavocedel trentino.it/2018/10/05/leone-imbrattato-a-venezia-la-ragazza-trentina-sara-espulsa-dallaccademia/>. Accessed on 04/11/2020.
- ¹⁶ J.S. Pozo-Antonio, T. Rivas, A.J. López, M.P. Fiorucci, A. Ramil, Effectiveness of granite cleaning procedures in cultural heritage: A review. *Sci. Total Environ.* **2016**, *571*, 1017-1028, doi:10.1016/j.scitotenv.2016.07.090.

- ¹⁷ S. Pozo, P. Barreiro, T. Rivas, P. González, M.P. Fiorucci, Effectiveness and harmful effects of removal sulphated black crust from granite using Nd:YAG nanosecond pulsed laser. *Appl. Surf. Sci.* **2014**, *302*, 309-313, doi:10.1016/j.apsusc.2013.10.129.
- ¹⁸ E. Boccalon, M. Nocchetti, M. Pica, A. Romani, M. Casciola, Layered double hydroxide and zirconium phosphate as ion exchangers for the removal of "black crusts" from the surface of ancient monuments. *Dalt. Trans.* **2018**, *47*, 2976-2985, doi:10.1039/c7dt03957c.
- ¹⁹ A. Polo, F. Cappitelli, L. Brusetti, P. Principi, F. Villa, L. Giacomucci, G. Ranalli, C. Sorlini, Feasibility of removing surface deposits on stone using biological and chemical remediation methods. *Microb. Ecol.* **2010**, *60*, 1-14, doi:10.1007/s00248-009-9633-6.
- ²⁰ F. Cappitelli, E. Zanardini, G. Ranalli, E. Mello, D. Daffonchio, C. Sorlini, Improved methodology for bioremoval of black crusts on historical stone artworks by use of sulfate-reducing bacteria. *Appl. Environ. Microbiol.* **2006**, *72*, 3733-3737, doi:10.1128/AEM.72.5.3733-3737.2006.
- ²¹ C. Ricci, F. Gambino, M. Nervo, A. Piccirillo, A. Scarcella, F. Zenucchini, A. Ramil, J.S. Pozo-Antonio, Enhancement of graffiti removal from heritage stone by combining laser ablation and application of a solvent mixture. *Constr. Build. Mater.* **2020**, *262*, 119934, doi:10.1016/j.conbuildmat.2020.119934.
- ²² I.P. Parkin, R.G. Palgrave, Self-cleaning coatings. *J. Mater. Chem.* **2005**, *15*, 1689-1695, doi:10.1039/b412803f.
- ²³ A. Fujishima, T.N. Rao, D.A. Tryk, Titanium dioxide photocatalysis. *J. Photochem. Photobiol. C* **2000**, *1*, 1-21, doi:10.1016/S1389-5567(00)00002-2.
- ²⁴ M.R. Hoffmann, S.T. Martin, W. Choi, D.W. Bahnemann, Environmental Applications of Semiconductor Photocatalysis. *Chem. Rev.* **1995**, *95*, 69-96, doi:10.1021/cr00033a004.
- ²⁵ Y. Nosaka, A.Y. Nosaka, Generation and Detection of Reactive Oxygen Species in Photocatalysis. *Chem. Rev.* **2017**, *117*, 11302-11336, doi:10.1021/acs.chemrev.7b00161.
- ²⁶ G.M. Zuo, Z.X. Cheng, H. Chen, G.W. Li, T. Miao, Study on photocatalytic degradation of several volatile organic compounds. *J. Hazard. Mater.* **2006**, *128*, 158-163, doi:10.1016/j.jhazmat.2005.07.056.
- ²⁷ G.S. Pozan, A. Kambur, Significant enhancement of photocatalytic activity over bifunctional ZnO-TiO₂ catalysts for 4-chlorophenol degradation. *Chemosphere* **2014**, *105*, 152-159, doi:10.1016/j.chemosphere.2014.01.022.
- ²⁸ X. Wei, G. Xu, Z. Ren, C. Xu, G. Shen, G. Han, PVA-assisted hydrothermal synthesis of SrTiO₃ nanoparticles with enhanced photocatalytic activity for degradation of RhB. *J. Am. Ceram. Soc.* **2008**, *91*, 3795-3799, doi:10.1111/j.1551-2916.2008.02716.x.
- ²⁹ T. Arai, M. Yanagida, Y. Konishi, Y. Iwasaki, H. Sugihara, K. Sayama, Promotion effect of CuO co-catalyst on WO₃-catalyzed photodegradation of organic substances. *Catal. Commun.* **2008**, *9*, 1254-1258, doi:10.1016/j.catcom.2007.11.012.
- ³⁰ Z. Zhang, W. Wang, M. Shang, W. Yin, Photocatalytic degradation of rhodamine B and phenol by solution combustion synthesized BiVO₄ photocatalyst. *Catal. Commun.* **2010**, *11*, 982-986, doi:10.1016/j.catcom.2010.04.013.
- ³¹ J.C. Wang, J. Ren, H.C. Yao, L. Zhang, J.S. Wang, S.Q. Zang, L.F. Han, Z.J. Li. Synergistic photocatalysis of Cr(VI) reduction and 4-Chlorophenol degradation over hydroxylated α-Fe₂O₃ under visible light irradiation. *J. Hazard. Mater.* **2016**, *311*, 11-19, doi:10.1016/j.jhazmat.2016.02.055.
- ³² Y. Bessekhoud, D. Robert, J. V. Weber, Bi₂S₃/TiO₂ and CdS/TiO₂ heterojunctions as an available configuration for photocatalytic degradation of organic pollutant. *J. Photochem. Photobiol. A* **2004**, *163*, 569-580, doi:10.1016/j.jphotochem.2004.02.006.
- ³³ N.F.F. Moreira, M.J. Sampaio, A.R. Ribeiro, C.G. Silva, J.L. Faria, A.M.T. Silva, Metal-free g-C₃N₄ photocatalysis of organic micropollutants in urban wastewater under visible light. *Appl. Catal. B* **2019**, *248*, 184-192, doi:10.1016/j.apcatb.2019.02.001.
- ³⁴ X. Zheng, D. Li, X. Li, J. Chen, C. Cao, J. Fang, J. Wang, Y. He, Y. Zheng, Construction of ZnO/TiO₂ photonic crystal heterostructures for enhanced photocatalytic properties. *Appl. Catal. B* **2015**, *168-169*, 408-415, doi:10.1016/j.apcatb.2015.01.001.
- ³⁵ J. Ma, K. Wang, L. Li, T. Zhang, Y. Kong, S. Komarneni, Visible-light photocatalytic decolorization of Orange II on Cu₂O/ZnO nanocomposites. *Ceram. Int.* **2015**, *41*, 2050-2056, doi:10.1016/j.ceramint.2014.09.137.
- ³⁶ K. ichi Katsumata, R. Motoyoshi, N. Matsushita, K. Okada, Preparation of graphitic carbon nitride (g-C₃N₄)/WO₃ composites and enhanced visible-light-driven photodegradation of acetaldehyde gas. *J. Hazard. Mater.* **2013**, *260*, 475-482, doi:10.1016/j.jhazmat.2013.05.058.
- ³⁷ P. Krishnan, M. Zhang, L. Yu, H. Feng, Photocatalytic degradation of particulate pollutants and self-cleaning performance of TiO₂-containing silicate coating and mortar. *Constr. Build. Mater.* **2013**, *44*, 309-316, doi:10.1016/j.conbuildmat.2013.03.009.
- ³⁸ M. Guo, A. Maury-ramirez, C. Sun, Self-cleaning ability of titanium dioxide clear paint coated architectural mortar and its potential in field application. *J. Clean. Prod.* **2016**, *112*, 3583-3588, doi:10.1016/j.jclepro.2015.10.079.

- ³⁹ E. Quagliarini, F. Bondioli, G.B. Goffredo, C. Cordoni, P. Munafò, Self-cleaning and de-polluting stone surfaces: TiO₂ nanoparticles for limestone. *Constr. Build. Mater.* **2012**, *37*, 51-57, doi:10.1016/j.conbuildmat.2012.07.006.
- ⁴⁰ L. Falchi, D. Slanzi, E. Balliana, G. Driussi, E. Zendri. Rising damp in historical buildings: A Venetian perspective. *Build. Environ.* **2018**, *131*, 117-127, doi:10.1016/j.buildenv.2018.01.004.
- ⁴¹ F. Doglioni, L. Scappin, A. Squassina, F. Trovò. *Conoscenza e restauro degli intonaci e delle superfici murarie esterne di Venezia. Campionature, esemplificazioni, indirizzi di intervento*. Il prato: Saonara (Italy), 2017. ISBN: 9788863364033.
- ⁴² V. Trevisan, M. Signoretto, F. Pinna, G. Cruciani, G. Cerrato, Investigation of titania synthesis for photocatalytic NO_x abatement. *Chem. Today* **2012**, *30*, 25-28.
- ⁴³ S. Brunauer, P.H. Emmett, E. Teller, Adsorption of Gases in Multimolecular Layers. *J. Am. Chem. Soc.* **1938**, *60*, 309-319, doi:10.1021/ja01269a023.
- ⁴⁴ P. Kubelka; F. Munk, Ein Beitrag zur Optik der Farbanstriche. *Zeitschrift Technische Physik* **1931**, *12*, 593-601.
- ⁴⁵ J. Tauc, A. Mentis, States in the gap. *J. Non-Cryst. Solids* **1972**, *8-10*, 569-585, doi:10.1016/0022-3093(72)90194-9.
- ⁴⁶ W.F. Lim, H.J. Quah, Z. Hassan, R. Radzali, N. Zainal, F.K. Yam, Alteration of structural and optical properties in quaternary Al_{0.1}In_{0.1}Ga_{0.8}N films using ultraviolet assisted photo-electrochemical etching route. *J. Alloys Compd.* **2015**, *649*, 337-347, doi:10.1016/j.jallcom.2015.07.114.
- ⁴⁷ I. Studenyak, M. Kranjčec, M. Kurik, Urbach Rule in Solid State Physics. *Int. J. Opt. Appl.* **2014**, *4(3)*, 76-83, doi: 10.5923/j.optics.20140403.02.
- ⁴⁸ V.P. Singh, K. Sandeep, H.S. Kushwaha, S. Powar, R. Vaish, Photocatalytic, hydrophobic and antimicrobial characteristics of ZnO nano needle embedded cement composites. *Constr. Build. Mater.* **2018**, *158*, 285-294, doi:10.1016/j.conbuildmat.2017.10.035.
- ⁴⁹ A. Gilchrist, J. Nobbs, Colorimetry, Theory. In *Encyclopedia of Spectroscopy and Spectrometry*. Academic Press, Cambridge (US), 2016. ISBN: 9780128032251.
- ⁵⁰ M. Lackhoff, X. Prieto, N. Nestle, F. Dehn, R. Niessner, Photocatalytic activity of semiconductor-modified cement— influence of semiconductor type and cement ageing. *Appl. Catal. B* **2003**, *43*, 205-216, doi: 10.1016/S0926-3373(02)00303-X.
- ⁵¹ C.S. Xavier, J.C. Sczancoski, L.S. Cavalcante, C.O. Paiva-Santos, J.A. Varela, E. Longo, M. Siu Li, A new processing method of CaZn₂(OH)₆·2H₂O powders: Photoluminescence and growth mechanism. *Solid State Sci.* **2009**, *11*, 2173-2179, doi:10.1016/j.solidstatesciences.2009.09.002.
- ⁵² K. Nakamoto, *Infrared and Raman Spectra of Inorganic and Coordination Compounds, sixth ed.* John Wiley & Sons: Hoboken (USA), 2009. ISBN: 9780471743392.
- ⁵³ S. Gunasekaran, G. Anbalagan, S. Pandi, Raman and infrared spectra of carbonates of calcite structure. *J. Raman Spectrosc.* **2006**, *37*, 892-899, doi:10.1002/jrs.1518.
- ⁵⁴ Lin, M. Y.A. Mollah, R. K. Vempati, D. L. Cocke, Synthesis and Characterization of Calcium Hydroxyzincate Using X-ray Diffraction, FT-IR Spectroscopy, and Scanning Force Microscopy. *Chem. Mater.* **1996**, *7*, 1974-197, doi:10.1021/cm00058a031.
- ⁵⁵ R.A. Wahyuono, F. Hermann-Westendorf, A. Dellith, C. Schmidt, J. Dellith, J. Plentz, M. Schulz, M. Presselt, M. Seyring, M. Rettenmeyer, B. Dietzek, Effect of annealing on the sub-bandgap, defects and trapping states of ZnO nanostructures. *Chem. Phys.* **2017**, *483-484*, 112-121, doi: 10.1016/j.chemphys.2016.12.002.
- ⁵⁶ T. Andelman, Y. Gong, M. Polking, M. Yin, I. Kuskovsky, G. Neumark, S. O'Brien, Morphological Control and Photoluminescence of Zinc Oxide Nanocrystals. *J. Phys. Chem. B* **2005**, *109*, 14314-14318, doi:10.1021/jp050540o.
- ⁵⁷ I. Shalish, H. Temkin, V. Narayanamurti, Size-dependent surface luminescence in ZnO nanowires. *Phys. Rev. B* **2004**, *69*, 245401, doi:10.1103/PhysRevB.69.245401.
- ⁵⁸ M. S. Prévot, Y. Li, N. Guijarro, K. Sivula, Improving charge collection with delafossite photocathodes: a host-guest CuAlO₂/CuFeO₂ approach. *J. Mater. Chem.* **2016**, *4*, 3018-3026, doi:10.1039/c5ta06336a
- ⁵⁹ R. Nakamura, T. Okamura, N. Ohashi, A. Imanishi, Y. Nakato, Molecular mechanisms of photoinduced oxygen evolution, PL emission, and surface roughening at atomically smooth (110) and (100) n-TiO₂ (rutile) surfaces in aqueous acidic solutions. *J. Am. Chem. Soc.* **2005**, *127*, 12975-12983, doi: 10.1021/ja053252e.
- ⁶⁰ S. Hu, B. Wang, M. Zhu, Y. Ma, Z. Lv, H. Wang, High-performance 1D type-II TiO₂@ZnO core-shell nanorods arrays photoanodes for photoelectrochemical solar fuel production. *Appl. Surf. Sci.* **2017**, *403*, 126-132, doi:10.1016/j.apsusc.2017.01.093.
- ⁶¹ H. Lin, K. T. Valsaraj, Development of an optical fiber monolith reactor for photocatalytic wastewater treatment. *J. Appl. Electrochem.* **2005**, *35*, 699-708, doi:10.1007/s10800-005-1364-x
- ⁶² T. Van Gerven, G. Mul, J. Moulijn, A. Stankiewicz, A review of intensification of photocatalytic processes. *Chem. Eng. Process.* **2007**, *46*, 781-789, doi:10.1016/j.cep.2007.05.012
- ⁶³ K. Kobayakawa, Y. Nakazawa, M. Ikeda, Y. Sato, A. Fujishima, Influence of the Density of Surface Hydroxyl Groups on TiO₂ Photocatalytic Activities. *Phys. Inorg. Chem.* **1990**, *94*, 1439-1443, doi:10.1002/chin.199112023

-
- ⁶⁴ R.M. Silverstein, F.X. Webster, D.J. Kiemle, Infrared Spectrometry. In *Spectrometric identification of organic compounds*, 7th ed. John Wiley & Sons, Inc.: Hoboken (USA), 2005. ISBN: 0471393622.
- ⁶⁵ Oleic acid sodium salt, NIST chemistry webbook website, available on: <https://webbook.nist.gov/cgi/cbook.cgi?ID=B6005865&Mask=80>. Accessed on 14/11/2020.
- ⁶⁶ Acetic acid, NIST chemistry webbook website, available on: <https://webbook.nist.gov/cgi/cbook.cgi?ID=C64197&Mask=400#UV-Vis-Spec>. Accessed on 14/11/2020.
- ⁶⁷ A. Carrasco-Pancorbo, L. Cerretani, A. Bendini, A. Segura-Carretero, T. Gallina-Toschi, A. Fernández-Gutiérrez, Analytical determination of polyphenols in olive oils. *J. Sep. Sci.* **2005**, *28*, 837-858, doi:10.1002/jssc.200500032.
- ⁶⁸ M. Martín-Polvillo, T. Albi, A. Guinda, Determination of trace elements in edible vegetable oils by atomic absorption spectrophotometry. *J. Am. Oil Chem. Soc.* **1994**, *71*, 347-353, doi:10.1007/BF02540512.
- ⁶⁹ D. Mantzavinos, M.I. Maldonado, S. Malato, A. Zapata, T. Velegraki, J.A. Sa, Applied Catalysis B : Environmental Solar photo-Fenton treatment of pesticides in water : Effect of iron concentration on degradation and assessment of ecotoxicity and biodegradability. *Appl. Catal. B* **2009**, *88*, 448-454, doi:10.1016/j.apcatb.2008.10.024.
- ⁷⁰ H. Lee, H. Lee, C. Lee, Degradation of diclofenac and carbamazepine by the copper (II)-catalyzed dark and photo-assisted Fenton-like systems. *Chem. Eng. J.* **2014**, *245*, 258-264, doi: 10.1016/j.cej.2014.02.037.
- ⁷¹ C. Kröhnke, O. Schacker, M. Zäh, Antioxidants. In, *Ullmann's Encyclopedia of Industrial Chemistry*. Wiley-VCH Verlag GmbH & Co. KGaA: Weinheim (Germany), 2015. Doi: 10.1002/14356007.a03_091.pub2.
- ⁷² M.S. Tunuli, J.H. Fendler, Aspects of Artificial Photosynthesis. Photosensitized Electron Transfer across Bilayers, Charge Separation, and Hydrogen Production in Anionic Surfactant Vesicles. *J. Am. Chem. Soc.* **1981**, *103*, 2507-2513, doi:10.1021/ja00400a002.
- ⁷³ P. Zhang, I. Lo, D. O'Connor, S. Pehkonen, H. Cheng, D. Hou, High efficiency removal of methylene blue using SDS surface-modified ZnFe₂O₄ nanoparticles. *J. Colloid Interface Sci.* **2017**, *508*, 39-48, doi:10.1016/j.jcis.2017.08.025.
- ⁷⁴ C.Z. Li, C.C. Chueh, F. Ding, H.L. Yip, P.W. Liang, X. Li, A.K.Y. Jen, Doping of fullerenes via anion-induced electron transfer and its implication for surfactant facilitated high performance polymer solar cells. *Adv. Mater.* **2013**, *25*, 4425-4430, doi:10.1002/adma.201300580.
- ⁷⁵ M. Styliidi, D. I. Kondarides, X. E. Verykios, Visible light-induced photocatalytic degradation of Acid Orange 7 in aqueous TiO₂ suspensions. *Appl. Catal. B* **2004**, *47*, 189-201, doi:10.1016/j.apcatb.2003.09.014.

CONCLUDING REMARKS

The climate change currently threatening the human society could be faced through adaptation strategies, in which the production systems, settlements and lifestyles are adapted to such change through several approaches.

Chemical reactions are involved in several aspects of human society, from industrial to household application, from fuel or chemicals production, to environmental remediation (i.e. pollutants or pathogens removal). In the concept of adaptation strategies, these reactions could be run exploiting the sunlight as energy source, with several advantages. Light-driven chemical reaction can be run in mild conditions of temperature and pressure, potentially increasing the overall energy efficiency and requiring simpler and cheaper equipment. Furthermore, besides avoiding the use of fossil fuels, being sunlight is abundant, widespread and cheap, light-driven chemical reactions could be run even in remote regions and poor countries, key targets in sustainable and equal adaptation strategies. Due to the poor optical absorption features, several reactions require a light-activated catalyst (photocatalyst) in order to occur, able to both absorb the incoming light and efficiently catalyze the desired reaction.

The aim of this work was to prepare, characterize and assess earth-abundant oxide-based materials, more robust and cheaper than other (i.e. sulphides or carbon-based), in different kind of photocatalyzed reactions. Specifically, the impact of the materials physical-chemical properties on a given reaction was assessed, aiming to understand how to design an effective photocatalyst.

In Chapter 1, the effect of non-noble co-catalysts on a TiO₂-based photocatalyst was evaluated in hydrogen production by liquid-phase glucose photoreforming. CuO co-catalysts were observed to improve the photoactivity, likely due to the favorable electronic properties of Cu-derived intra-gap states, allowing an efficient charge transfer process with reduced recombination phenomenon. Furthermore, these co-catalysts were observed to afford a selective improvement of the hydrogen evolution reaction (HER), playing an important role in directing the reaction selectivity.

In Chapter 2, ZnO-based materials were assessed in gas-phase CO₂ photoreduction, evaluating the impact of structural, surface and optical properties on the reactivity. Crystallinity and phase-purity were observed to be a key parameter in allowing an efficient charge transfer to the reactants, minimizing recombination processes or interference with reaction intermediates. Furthermore, types and amount of defects, the nature of the surface (photoactive exposed facets and hydroxyl vs carbonate superficial moiety) can further contribute in the enhancement of photoactivity, by improving charge transfer processes and the relative amount of reduction/oxidation surface sites. Due to its basicity, ZnO photocatalysts were also able to capture CO₂ from diluted stream and photoconvert it in a CO₂-free reaction medium, showing its capability to act as hybrid capture-photoreducing system.

In Chapter 3, it was tried to improve visible-light photons harvesting of ZnO, while keeping its CO₂ adsorption properties, by coupling it with another material, CuFeO₂ delafossite, in a photoelectrochemical (PEC) setup. Thin film composites of CuFeO₂ as light-absorbing layer and a ZnO as surface overlayer were prepared. The impact of ZnO layer thickness and defectivity in the charge transfer across the electrode/reaction medium interface was assessed, observing a decrease of photocurrent by increasing ZnO layer thickness, while it increases by achieving a more crystalline material. Attempts in CO₂ photoreduction, by a co-catalyst (Cu-based), however failed probably due to weak interaction with the surface.

In Chapter 4, ZnO and TiO₂-based material were introduced as photocatalytic additives in the formulation of a plaster used traditionally in Venice, *marmorino*, and the photocatalytic self-cleaning capability was assessed. In a such mixture of insulators (calcium hydroxide and carbonate) and semiconductors, key parameter for a photoactive material was found to be the presence of a semiconductor at the air-material interface, and the presence of semiconductor-semiconductor interfaces (heterojunction), both allowing facile charge transfer processes. Furthermore, top-coating the surface with a soap was observed further enhance the photoactivity, likely by improving light exposure and charge transfer, synergistically acting with some semiconductors.

In conclusion, as previously highlighted, light-driven catalyzed chemical reactions have appealing potential application but several issues still affect a reliable and feasible large-scale application. Through this research work, despite having involved different materials and reactions, an important consideration can be drawn: the importance of both solid/reaction medium and solid/solid interfaces. A comprehensive knowledge of how the opto-electronic, chemical and morphological properties of an interface affect both the solid/solid and the solid/reagent charge transfer processes is a key point for the design of an active, selective and stable photocatalyst, aiming to maximize an efficient exploitation of the photogenerated charge carriers. Future perspectives should be thus oriented on interface design, focusing on strategies like nature of the pristine surfaces (i.e. surface moiety, defects, facets), heterojunctions and co-catalysts.

CURRICULUM VITAE

I was born in 1992 and I got the high-school diploma in agricultural studies in July 2012, with a specialization in vine-growing and wine-making. I got the Bachelor degree in Sustainable Chemistry and Technology (*curriculum* Industrial Chemistry) at Ca' Foscari University of Venice (Venice, Italy) in October 2015, with an experimental thesis on homogeneous supramolecular catalysis, under the supervision of Prof. Alessandro Scarso and Prof. Giorgio Strukul. Then, I acquired the Master degree in Sustainable Chemistry and Technology (*curriculum* Industrial Chemistry), in the same university, in October 2017, with an experimental thesis on solid-gas heterogeneous photocatalysis, in CATMAT group under the supervision of Prof. Michela Signoretto and Dr. Alberto Olivo. In November 2017, I started the Ph.D. in Chemistry in the Ca' Foscari University of Venice (Venice, Italy) and University of Trieste (Trieste, Italy) joint Ph.D. program, under the supervision of Prof. Michela Signoretto and Dr. Federica Menegazzo (CATMAT group, Ca' Foscari University of Venice). My project dealt with the development and assessment of oxide-based materials as catalysts for light-driven fuel production (CO₂ production, H₂ reduction), environmental and cultural heritage remediation. During my Ph.D. program, I worked on a PRIN project concerning the photocatalytic H₂ production from biomass, funded by the Italian Ministry of education, university and research, in collaboration with Prof. Ilenia Rossetti (University of Milan, Milan, Italy). I worked on a project relying on the application of photocatalysis in cultural heritage remediation, in collaboration with Mr. Giorgio Berto (Uni.S.Ve company, Venice, Italy) and Arch. Luca Scappin (IUAV University of Venice, Venice, Italy). I collaborated with Dr. Warren A. Thompson and Prof. M. Mercedes Maroto-Valer (Heriot-Watt University, Edinburgh, UK) for a project relying mixed metal oxides for CO₂ photoreduction. From May 2019 to October 2019, I spent a period at the EPFL (Lausanne, Switzerland) for a research project relying on the development of oxide-based photocathodes for photoelectrochemical CO₂ reduction, under the supervision of Prof. Kevin Sivula (LIMNO group). During my Ph.D. program, I was also involved in guidance activities for high-school students and tutoring activities in educational laboratory for undergraduates. My research activity was often aided by undergraduates, that I trained to work within my projects. I also have been co-supervisor of three Bachelor degree theses, in Sustainable Chemistry and Technology and in Technology for Conservation and Restoration. Since 2017, I have been a member of the Italian Chemical Society.

PUBLISHED WORKS

CHAPTER 1

E. Bahadori, G. Ramis, D. Zanardo, F. Menegazzo, M. Signoretto, D. Gazzoli, D. Pietrogiacomini, A. Di Michele, I. Rossetti, Photoreforming of Glucose over CuO/TiO₂. *Catalysts* **2020**, *10*, 477, doi:10.3390/catal10050477.

CHAPTER 2

D. Zanardo, G. Forghieri, E. Ghedini, F. Menegazzo, A. Giordana, G. Cerrato, E. Cattaruzza, I. Concina, A. Di Michele, G. Cruciani, M. Signoretto, CO₂ photoreduction with ZnO-based materials: a wet chemistry approach, **2021**. In preparation.

CHAPTER 4

F. Menegazzo, M. Signoretto, D. Zanardo, L. Scappin, Fotocatalizzatori fissati mediante le finiture tradizionali del marmorino: una strategia ecologica tra chimica e restauro per rendere più pulite le nostre città, *Lo Stato dell'Arte 18 IGIC*, **2020**. Publication in congress proceedings.

D. Zanardo, E. Ghedini, F. Menegazzo, A. Giordana, G. Cerrato, A. Di Michele, G. Cruciani, M. Signoretto. Traditional Venetian *marmorino*: Effect of zinc-based oxides on self-bleaching properties, **2020**. Submitted.

OTHER PUBLICATIONS

D. Zanardo, G. Forghieri, E. Ghedini, F. Menegazzo, A. Di Michele, G. Cruciani, M. Signoretto. Effect of SiO₂-based scaffolds in TiO₂-photocatalyzed CO₂ reducti, **2021**. In preparation.

G. Forghieri, D. Zanardo, E. Ghedini, F. Menegazzo, Federica Menegazzo, A. Landström, G. Solomon, R. Mazzaro, A. Vomiero, I. Concina, M. Signoretto, The photoelectrochemical behavior of thin-layer coated TiO₂ and ZnO nanorods for water splitting application, **2021**. In preparation.

G. Forghieri, D. Zanardo, E. Ghedini, F. Menegazzo, A. Giordana, G. Cerrato, M. Signoretto, Structural and functional behavior of Ce-doped wide-bandgap semiconductors for photocatalytic application, **2021**. In preparation.

E. Ghedini, L. Longo, M. Pizzolato, D. Zanardo, F. Menegazzo, M. Signoretto. Which are the main surface disinfection approaches at the time of SARS-CoV-2? *Front. Chem. Eng.* **2021**, doi: 10.3389/fceng.2020.589202.

D. Zanardo, E. Ghedini, F. Menegazzo, E. Cattaruzza, M. Manzoli, G. Cruciani, M. Signoretto, Titanium dioxide-based nanocomposites for enhanced gas-phase photodehydrogenation. *Materials* **2019**, *12(19)*, 3093, doi:10.3390/ma12193093.
W.A. Thompson, A. Olivo, D. Zanardo, G. Cruciani, F. Menegazzo, M. Signoretto, M.M. Maroto-Valer, Systematic study of TiO₂/ZnO mixed metal oxides for CO₂ photoreduction. *RSC Adv.* **2019**, *9*, 21660, doi:10.1039/C9RA03435H.

A. Olivo, D. Zanardo, E. Ghedini, F. Menegazzo, M. Signoretto Solar Fuels by Heterogeneous Photocatalysis: From Understanding Chemical Bases to Process Development. *ChemEngineering* **2018**, *2(3)*, 42, doi:10.3390/chemengineering2030042.

F. Menegazzo, C. Pizzolitto, M. Signoretto, D. Zanardo, C. Buysschaert, G. Bény, A. Di Michele, Hydrogen production by ethanol steam-reforming on Ni-based catalysts: effect of the support and of CaO and Au doping. *Chemistry Select* **2017**, *2*, 9523-9531, doi:10.1002/slct.201702053.

CONGRESSES AND CONGRESS PROCEEDINGS

CHAPTER 2

Europacat 2019. August **2019**, Aachen (Germany). Congress Abstract: *“Advanced in CO₂ photoreduction: ZnO as photocatalytic adsorbent”* D. Zanardo, G. Cruciani, F. Menegazzo, M. Signoretto. Poster presentation.

MEYCS (Merck Elsevier Young Chemist Symposium). November **2018**, Rimini (Italy). Congress Abstract: *“ZnO photocatalysts for enhanced CO₂ conversion”* D. Zanardo, F. Menegazzo, M. Signoretto, G. Cruciani. Oral presentation.

CHAPTER 4

MYCS (Merck Young Chemist Symposium). November **2019**, Rimini (Italy). Congress Abstract: *“Technology meets tradition: photocatalysts development for self-cleaning Venetian marmorino”* Danny Zanardo, Federica Menegazzo, Alessandro Di Michele, Giuseppe Cruciani, Luca Scappin, Giorgio Berto, Michela Signoretto. Oral presentation.

OTHER CONGRESS PROCEEDINGS

XXI Congress of the Industrial Chemistry Division of Società Chimica Italiana. August **2019**, Salerno (Italy). Congress Abstract: *“Materials for CO₂-to-valuable-products photoconversion: efficiency optimization in mild reaction conditions”*. G. Forghieri, D. Zanardo, F. Menegazzo, M. Signoretto. Poster presentation.

Advanced Inorganic Materials: Green and Unconventional Synthesis Approaches and Functional Assessment. September **2018**, Padova (Italy). Congress Abstract: *“Synthesis of CuO/TiO₂ photocatalytic nanocomposites by a modified precipitation technique”* D. Zanardo, E. Ghedini, M. Signoretto, M. Manzoli, G. Cruciani. Oral presentation.

XX National Congress of Catalysis and Industrial Chemistry Division of Società Chimica Italiana. September **2018**, Milan (Italy). Congress Abstract: *“Boosting up renewable hydrogen: efficient titania-based photocatalysts for gas phase photoreforming”* D. Zanardo, A. Olivo, E. Ghedini, M. Signoretto, M. Manzoli, G. Cruciani. Oral presentation.

MYCS (Merck Young Chemist Symposium). November **2017**, Milano Marittima (Italy). Congress Abstract: *“CuO promoted TiO₂ catalysts for ethanol photoreforming”* D. Zanardo, M. Signoretto, A. Olivo, G. Cruciani. Poster presentation.

XXVI National Congress of Società Chimica Italiana. September **2017**, Paestum (Italy). Congress Abstract: *“Methane Dry Reforming: effect of lanthanum oxide in Ni/CeO₂ catalyst”* C. Pizzolitto, M. Signoretto, F. Menegazzo, D. Zanardo, G. Cruciani. Poster presentation.

TEACHING AND GUIDANCE ACTIVITIES

Tutoring activity, Laboratory of Formulation, given by prof. M. Signoretto. A.Y. **2017/2018**.

Tutoring activity, Laboratory of Industrial and Chemical Technologies, given by prof. M. Signoretto. A.Y. **2018/2019** and **2019/2020**.

Tutoring activity, Laboratory of Industrial Chemistry II, given by prof. M. Signoretto. A.Y. **2020/2021**.

Thesis co-supervision, *“Studio dei test di invecchiamento accelerato dei materiali lapidei”*, Arianna De Luca, October **2020**. Bachelor degree in Technologies for Conservation and Restoration of Cultural Heritage.

Thesis co-supervision, *“Sviluppo delle proprietà di self-cleaning di nuove formulazioni per il marmorino veneziano”*, Federica Brunello, July **2020**. Bachelor degree in Technologies for Conservation and Restoration of Cultural Heritage.

Guidance activity, Giornate 2018 dell'Università ed ITS. March **2018**, Conegliano (Italy). Presentation: *“A better life through chemistry”*.

Guidance activity, Festival Carta Carbone 2018. September **2018**, Treviso (Italy). Presentation: "*Chimicapisce??? La chimica delle formulazioni nella vita di tutti I giorni*", D. Zanardo, C. Pizzolitto, G. Bortolomiol, S. Zancanaro.

Guidance activity, Open days. March **2018** and March **2019**, Ca' Foscari University of Venice, Venezia (Italy).

ACKNOWLEDGMENTS

First, a special acknowledgment goes to my research group, CATMAT (Ca' Foscari University of Venice, Italy). I would like to thank my supervisor, Prof. Michela Signoretto, and my co-supervisor, Prof. Federica Menegazzo, for the opportunity to join to the team, discussions and support. I would like to thank Ms. Tania Fantinel for her technical assistance in AAS analyses, Dr. Elena Ghedini and Sebastiano Tieuli for N₂ physisorption measurements. I would also like to thank all the rest of the group, especially bachelor and master students those worked in my research project.

I would like to thank Prof. Ilenia Rossetti and Dr. Elanaz Bahadori (University of Milan, Italy) for the liquid-phase reactivity tests on hydrogen production; Prof. Giuseppe Cruciani (University of Ferrara, Italy) for XRD analyses and data interpretation; Dr. Alessandro Di Michele (University of Perugia, Italy) for SEM images acquisition; Prof. Giuseppina Cerrato and Dr. Alessia Giordana (University of Turin, Italy) for FTIR and PL measurements; Dr. Maela Manzoli (University of Turin) for HR-TEM images acquisition; Prof. Isabella Concina and Giulia Forghieri (Luleå Institute of Technology, Sweden) for PL analyses; Prof. Elti Cattaruzza (Ca' Foscari University of Venice, Italy) for XPS measurements and data interpretation; Prof. Giancarlo Rampazzo and Flavia Visin (Ca' Foscari University of Venice, Italy) for ICP-MS analyses; Giorgio Berto (Uni.S.Ve company, Venice, Italy) for the technical assistance in *marmorino* preparation and Arch. Luca Scappin (IUAV University of Venice) for *marmorino* historical and cultural background.

Another important acknowledgment goes to LIMNO (EPFL, Switzerland), where I spent six months during my Ph.D. research program. I would like to thank, for the opportunity to join LIMNO and for discussions on my research project, prof. Kevin Sivula; Dr. Jun-Ho Yum for AFM and SKPM measurements and interpretation; Dr. Florent Boudoire for the technical assistance concerning the AACVD synthesis and EIS data elaboration; Connor R. Firth and Yongpeng Liu for SEM images acquisition, and Dr. Mounir Mensi for XPS measurements.

Finally, last but not least, a special thank goes to my family and all my friends, for their support within these three years.